INTEGRATED MODELLING FOR EVALUATION OF CLIMATE CHANGE IMPACTS ON AGRICULTURAL DOMINATED BASIN

Rong Zhang

Tese apresentada à Universidade de Évora
para obtenção do Grau de Doutor em
Ciências da Engenharia do Território e Ambiente
Especialidade: Engenharia Civil

ORIENTADORES: *Prof.ª Dr.ª Maria Madalena Vitório Moreira Vasconcelos*
Prof. Dr. João Alexandre Medina Corte-Real

ÉVORA, 2015

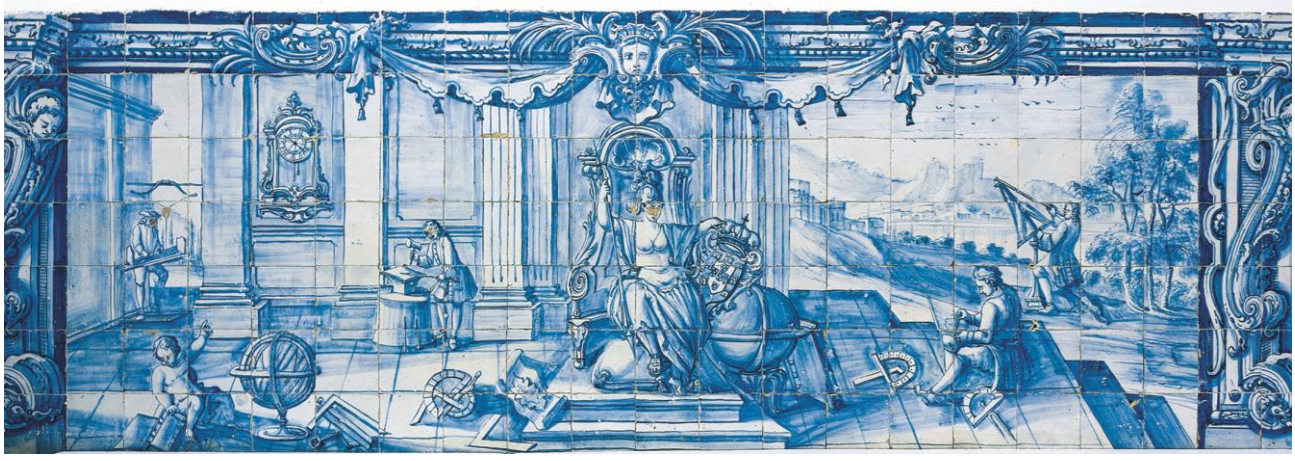

INSTITUTO DE INVESTIGAÇÃO E FORMAÇÃO AVANÇADA

Tese de Doutoramento financiada pelo Ministério da Educação e Ciência
Fundação para a Ciência e a Tecnologia
Bolsa de Doutoramento SFRH/BD/48820/2008

Centro de Investigação da Universidade de Évora, de acolhimento da Bolseira

致我父亲和母亲：感谢您们让我的梦想变成了现实

致我叔叔和婶婶：感谢您们永无止境的支持和鼓励

To Professors Cui GuangBai and João Corte-Real:

Thank you for having opened a door to a wonderful world

Ao meu amor Sandro:

Obrigada por fazer parte da minha vida

Acknowledgments

I would like to thank my supervisors, Prof. Madalena Moreira and Prof. João Corte-Real, for their invaluable guidance and support throughout the period of this research.

This thesis was made possible by a PhD grant of Portuguese national funding agency for science, research and technology (SFRH/BD/48820/2008). I am very grateful to Prof. Francisco Sepúlveda Texeira, vice-president of FCT in 2008, and Mrs. Gertrudes Almeida for the opportunity of fellowship.

I wish to thank the support from the projects ERLAND (PTDC/AAC-AMB/100520/2008), CLIPE (PTDC/AAC-CLI/111733/2009) and KLIMHIST (PTDC/AAC-CLI/119078/2010), the observed data from SNIRH, SAGRA/COTR and IPMA and the climate model data provided by the EU-FP6 project ENSEMBLES.

I am deeply grateful to Prof. Cui Guangbai, my previous supervisor in Hohai University, China, for his great advice, encouragement and support to the opportunity of this research.

I very much appreciate the twice opportunities offered by Prof. Chris Kilsby for me to visit Newcastle University to have training courses on SHETRAN model and development of weather generator applications. I would like to thank him and his colleagues, Dr. James Bathurst, Prof. John Ewen, Dr. Stephen Birkinshaw, Dr. Isabella Bovolo, Prof. Hayley Fowler, Dr. Aidan Burton, Dr. Stephen Blenkinsop, Dr. Greg O'Donnell and Dr. Nathan Forsythe, for the observed data, great assistance and helpful discussions.

I would like to thank Prof. Celso Santos and Dr. Paula Freire for their valuable visit to University of Évora. The collaboration was very helpful and fruitful.

I would further like to thank Prof. Ricardo Serralheiro, Prof. Lúcio Santos, Prof. Elsa Sampaio, Prof. Shakib Shahidian, Dr. Qian Budong, Dr. Sandra Mourato, Dr. Célia Toureiro and Dr. Júlio Lima for help, comments and scientific discussions during the elaboration of this thesis.

I would like to thank my friends at University of Évora, Hohai University and Newcastle University for making my stay so enjoyable. Special Thanks go to Prof. José Peça, Regina Corte-Real, Isilda Menezes, Susana Mendes, Luiz Tadeu Silva, Cláudia Vicente, Clarisse Brígido, Guilhermina Pias, Maria João Vila Viçosa, Ana Canas, Lígia Justo, Elisete Macedo, Véronica Moreno, Cláudia Furtado, Marco Machado, Amaia Nogales, Daniel Malet and Lemos Djata.

I want to thank my family for all their love and support. I would like to thank Sandro Veiga and his family for all the encouragement and support.

Integrated Modelling for Evaluation of Climate Change Impacts on Agricultural Dominated Basin

Abstract

This study evaluated future climate change impacts on water resources, extreme discharges and sediment yields for the medium-sized (705-km^2) agriculture dominated Cobres basin, Portugal, in the context of anti-desertification strategies. We applied the physically-based spatially-distributed hydrological model—SHETRAN, obtaining the optimized parameters and spatial resolution by using the Modified Shuffled Complex Evolution (MSCE) method and the Non-dominated Sorting Genetic Algorithm II (NSGA-II), to simulate the hydrological processes of runoff and sediment transport. We used the model RanSim V3, the rainfall conditioned weather generator—ICAAM-WG, developed in this study, based on the modified Climate Research Unit daily Weather Generator (CRU-WG), and SHETRAN, to downscale projections of change for 2041–2070, from the RCM HadRM3Q0 with boundary conditions provided by the AOGCM HadCM3Q0, provided by the ENSEMBLES project, under SRES A1B emission scenario.

We found future climate with increased meteorological, agricultural and hydrological droughts. The future mean annual rainfall, actual evapotranspiration, runoff and sediment yield are projected to decrease by the orders of magnitude of respectively ~88 mm (19%), ~41 mm (11%), ~48 mm (50%) and ~1.06 t/ha/year (45%). We also found reductions in extreme runoff and sediment discharges, for return periods smaller than 20 years; however for return periods in the range of 20–50 years, future extremes are of the same order of magnitude of those in the reference climate.

Modelação integrada para avaliação dos impactos das alterações climáticas sobre bacias hidrográficas com uso predominantemente agrícola

Resumo

Neste estudo são avaliados os impactos futuros das alterações climáticas nos recursos hídricos e em extremos do escoamento e transporte de sedimentos, na bacia hidrográfica do rio Cobres, Portugal, agrícola, de dimensão média (705 Km^2), no contexto do combate à desertificação. Foi aplicado o modelo hidrológico fisicamente baseado e espacialmente distribuído SHETRAN, tendo sido obtidos os valores optimizados de parâmetros e da resolução espacial, utilizando o método "Modified Shuffled Complex Evolution" (MSCE) e o algoritmo "Non-dominated Sorting Genetic Algorithm II" (NSGA-II), para simular os processos hidrológicos de escoamento e transportes de sedimentos. Foram utilizados o modelo de RainSim V3, o gerador de tempo ICAAM-WG, desenvolvido neste estudo, baseado no CRU-WG, e o SHETRAN, para o "downscaling" das projecções climáticas para 2041 – 2070, geradas pelo MRC HadRM3Q0 com condições de fronteira fornecida pelo MCG HadCM3Q0, projecto ENSEMBLES, sob o cenário SRES A1B.

O clima futuro é caracterizado por um número crescente de secas meteorológicas, agrícolas e hidrológicas. Os valores médios anuais da precipitação, evapotranspiração real, escoamento superficial e transporte de sedimentos, revelam decréscimos com ordens de grandeza respectivamente de ~88 mm (19%), ~41 mm (11%), ~48 mm (50%) e ~1.06 t/há/ano (45%). Encontraram-se ainda reduções nos valores extremos do escoamento superficial e do transporte de sedimentos para períodos de retorno inferiores a 20 anos; contudo, para períodos de retorno no intervalo 20–50 anos, os valores extremos futuros apresentam a mesma ordem de grandeza que os relativos ao período de referência mas mantendo níveis equivalentes para os com 20–50 anos.

气候变化对农业为主流域的影响的综合模拟

摘要

水资源短缺和沙漠化是葡萄牙南部地区面临的主要问题。为了给沙漠化防治对策提供科学依据，本文评估了气候变化对葡萄牙南部以农业为主的科布热斯流域(Cobres，面积约705 km^2)的水资源、暴雨径流和泥沙流失的影响。采用基于物理机制的分布式水文模型SHETRAN 模拟径流和泥沙迁移的水文过程，并运用 MSCE(Modified Shuffled Complex Evolution)方法和 NSGA-II(Non-dominated Sorting Genetic Algorithm II)算法优化模型参数和空间步长.采用奈曼－斯科特时空矩形脉冲（STNSRP）模型 RainSimV3，本研究开发的基于改进的英国气候研究所（Climate Research Unit）天气发生器(CRU-WG)的雨控天气发生器 ICAAM-WG，对由 ENSEMBLES 项目提供的基于 SRES A1B 温室气体排放情景下由全球气候模式 HadCM3Q0 提供边界条件的区域气候模式 HadRM3Q0 所模拟的 2041-2070 年间的气候变化情景做降尺度分析。结果表明，未来该地区的气象干旱、农业干旱和水文干旱都有加重趋势。未来平均年降雨、蒸散发量、径流和产沙量预计将比现在分别减少数量级约 88 毫米（19%）、41 毫米（11%）、48 毫米（50%）和 1.06 吨/公顷/年（45%）。并且，我们预计重现期在 20 年以下的极端径流和输沙量都将减少,重现期在20－50 年范围内极端径流和输沙量将保持与基准气候模式相同数量级。

Index

List of Figures

List of Tables

List of Symbols and Abbreviations

List of Symbols

a	Coefficient of the Yalin equation
A	Flow cross sectional area (m^2)
AET	Actual Evapotranspiration (mm) or (mm/s)
$AETPET_{FC1}$	The AET/PET ratio at field capacity for crop
$AETPET_{FC2}$	The AET/PET ratio at field capacity for agroforestry
AII	Average dry day precipitation (DP < 10 mm) (mm)
α	van Genuchten α parameter (cm^{-1})
α_1	van Genuchten α parameter of V_x soil (cm^{-1})
α_2	van Genuchten α parameter of P_x soil (cm^{-1})
α_3	van Genuchten α parameter of E_x soil (cm^{-1})
$\alpha_{g,i}$	Change factor for the statistic *g* and the calendar month *i*
$\alpha_{T,i}$	Change factor for the temperature statistic *T* and the calendar month *i*
b	Drainage parameter
B	Channel flow width (m) or active bed width for which there is sediment transport (m)
c_i	Sediment concentration in size group *i* (m^3/m^3)
c_P	Specific heat of air at constant pressure (J/kg/K)
C	Depth of water on canopy (mm)
CDD	Maximum number of consecutive dry days (DP < 1.0 mm) (day)
C_c	Percentage canopy cover (%)
C_g	Proportion of ground shielded by near ground cover (decimal fraction) or percentage ground cover (%)
C_r	Proportion of ground shielded by ground level cover (decimal fraction)
C_R	Storm runoff coefficient (%)
D_{50}	Sediment particle diameter greater than the diameter of 50% of the particles (m);
D_n	The largest absolute difference between empirical and fitted cumulative probabilities
δ	Coefficient of the Yalin equation
δ_e	Vapour pressure deficit of air (Pa)

Δ	Rate of increase with temperature of the saturation vapour pressure of water at air temperature (Pa/K)
ΔS	Change of subsurface water storage (mm)
D_i	Representative sediment particle diameter for the size group *i* (m).
DP	Daily precipitation (mm)
D_q	Rate of detachment of soil per unit area (kg/m^2/s)
D_r	Rate of detachment of soil (kg/m^2/s);
e_i	White noise on the day *i* for the equations 7.10–7.24 and A2.1–A2.13
η	Storage coefficient (m^{-1})
η_c	Crossover distribution index
η_m	Mutation distribution index
E_b	Rate of detachment of material per unit area of river bank (kg/m^2/s)
E_x	Lithosols from semi-arid and sub-humid climate of Schist or Greywacke origin
FDD	Number of dry spells (consecutive period with at least 8 dry days, DP < 1.0 mm) (freq.)
η_c	Crossover distribution index
η_m	Mutation distribution index
ϕ	Bed sediment porosity (m^3/m^3)
F_w	Effect of surface water layer in protecting the soil from raindrop impact (dimensionless)
g	Acceleration due to gravity (m/s^2)
γ	Psychrometric constant (~66 Pa/K)
g_i^{Fut}, g_i^{Con}	The statistic *g* for the calender month i under the future (^{Fut}) and control (^{Con}) conditions
g_i^{Obs}, g_i^{Est}	The observed (^{Obs}) and estimated (^{Est}) statistic *g* for the calender month *i*
$G_{gr,i}$	Dimensionless sediment transport rate for sediment size group *i*
G_i	Volumetric sediment transport rate for particles in size group *i* (m^3/s)
G_{tot}	The capacity particulate transport rate for overland flow (including all sediment size groups) (m^3/s)
g_x, g_y	Volumetric sediment transport rates per unit width in the x and y directions respectively (m^3/s/m)

h	Water depth (m) or top soil depth (m)
H	Flow depth of channel flow (m)
HP	Hourly precipitation (mm)
I_{mean}	Mean rainfall intensity (mm/h)
I_{max}	Max rainfall intensity (mm/h)
k	Drainage parameter
k_b	Bank erodibility coefficient ($kg/m^2/s$)
k_f	Overland flow soil erodibility coefficient ($kg/m^2/s$)
k_r	Raindrop impact soil erodibility coefficient (J^{-1}) or relative hydraulic conductivity (-)
K_1 ($m^{1/3}/s$)	Strickler overland flow resistance coefficient for crops
K_2 ($m^{1/3}/s$)	Strickler overland flow resistance coefficient for agroforestry
K_s	Saturated hydraulic conductivity (m/day)
K_{s1}	Saturated hydraulic conductivity of V_x soil (m/day)
K_{s2}	Saturated hydraulic conductivity of P_x soil (m/day)
K_{s3}	Saturated hydraulic conductivity of E_x soil (m/day)
K_x, K_y and K_l	Strickler coefficients ($m^{1/3}/s$), which are the inverse of the Manning coefficient, in the x, y and l directions
K_x, K_y and K_z	Saturated hydraulic conductivities in the x, y and z directions (m/s)
l	Width of the flow (m)
$L1AC_{DP}$	Lag-1 autocorrelation (-)
λ	Loose sediment porosity (decimal fraction) or latent heat of vaporization of water (J/g)
M_d	Momentum squared of leaf drips reaching the ground per unit time per unit area (kg^2/s^3)
M_{DP}	Daily mean rainfall for a specified month (mm)
M_{DT}	Mean of daily mean 2-m air temperature for a specified month (°C)
$M_{\Delta DT}$	Mean of daily 2-m air temperature range for a specified month (°C)
M_r	Momentum squared of raindrops reaching the ground per unit time per unit area (kg^2/s^3)
n	Porosity (m^3/m^3) or van Genuchten n parameter (-)
n_1	van Genuchten n parameter of V_x soil (-)
n_2	van Genuchten n parameter of P_x soil (-)
n_3	van Genuchten n parameter of E_x soil (-)

n_i	The transition exponent for sediment size group *i* for the Ackers-White equation for Channel flow sediment transport
O_i	Observed watershed responses at time point *i*
$\bar{O}$	The mean values of observed watershed responses
PET	Potential Evapotranspiration (mm)
Ψ	Soil moisture tension (m)
Ψ_w	Soil moisture tension at wilting point (m)
Ψ_L	Soil moisture tension at which soil water begins to limit plant growth and water uptake is considered to take place at the potential rate (m)
P	Precipitation (mm) or non-exceedance probabilities (-)
$Pdry_{DP1.0}$	Proportion of dry days (less than 1.0 mm) (-)
$Pdry_{HP0.1}$	Proportion of dry hours (less than 0.1 mm) (-)
P_i	Daily precipitation (mm) for the day *i*
P_{obs}	Observed precipitation (mm)
P_x	Brown Mediterranean soil of Schist or Greywacke origin
q	Specific volumetric flow rate out of the medium (s^{-1})
q_{si}	Sediment input from bank erosion and overland flow supplies per unit channel length for size fraction *i* ($m^3/s/m$)
q_w, q_{sp} and q_t	Specific volumetric fluxes (s^{-1}) out of abstraction well, spring discharges and transpiration losses respectively
Q	Net rate of rainfall supply to canopy (mm/hour) or water flow rate (m^3/s)
Q_b	Baseflow (at the start of the flood) (m^3/s)
Q_i	Lateral influx (m^3/s)
Q_{obs}	Observed discharge (m^3/s)
Q_p	Peakflow (maximum peakflow for processes with multiple peaks) (m^3/s)
Q_R	Net vertical input to the element (m^3/s)
Q_{obs}	Observed discharge (m^3/s)
Q_{sim}	Simulated discharge (m^3/s)
Q_{obs}^{pk}	Observed peak discharges (m^3/s)
Q_{sim}^{pk}	Simulated peak discharges (m^3/s)
r_a	Aerodynamic resistence to water vapour transport (s/m)
r_c	Canopy resistance to water vapour transport (s/m).
ρ	Water density (kg/m^3) or density of air (kg/m^3)

ρ_s	Density of sediment particles (kg/m^3)
R	Daily 2-m air temperature range (°C) or runoff (mm) or Pearson correlation coefficient (-)
R5D	Highest consecutive 5-day precipitation total (mm)
R30	Number of days with daily precipitation totals above or equal to 30 mm (day)
R_i	Daily 2-m air temperature range for the day *i* (°C)
R_n	Net radiation (W/m^2)
R_{obs}	Observed runoff (mm)
R_{sim}	Simulated runoff (mm)
s	Sediment specific gravity (decimal fraction)
S	Water surface slope in the direction of flow (m/m) or canopy storage capacity (mm)
S_i	Simulated watershed responses at time point *i*
$\bar{S}$	The mean values of simulated watershed responses
SDII	Average wet day precipitation (DP >= 1.0 mm) (mm)
S_{fx}, S_{fy} and S_{fl}	Friction slopes in the x, y and l directions respectively (m/m)
σ_e	Standard deviation of the white noise on the day *i* for the equations 7.10–7.24 and A2.1–A2.13
$Skew_{DP}$	Skewness of daily rainfall for a specified month (-)
$Skew_{HP}$	Skewness of hourly rainfall for a specified month (-)
S_s	Specific storage (m^{-1})
SS	Sunshine duration (hours)
SS_i	Sunshine duration for the day *i* (hours)
SY	Sediment Yield (t ha^{-1} year^{-1})
t	Time (hour or second)
T	Daily mean 2-m air temperature (°C) or return period (year)
θ	Volumetric soil water content (m^3/m^3)
θ_s	Saturated soil water content (m^3/m^3)
θ_{s1}	Saturated soil water content of V_x soil (m^3/m^3)
θ_{s2}	Saturated soil water content of P_x soil (m^3/m^3)
θ_{s3}	Saturated soil water content of E_x soil (m^3/m^3)
θ_r	Residual soil water content (m^3/m^3)
θ_{r1}	Residual soil water content of V_x soil (m^3/m^3)
θ_{r2}	Residual soil water content of P_x soil (m^3/m^3)
θ_{r3}	Residual soil water content of E_x soil (m^3/m^3)
T_i	Daily mean 2-m air temperature for the day *i* (°C)

T_i^{Fut}, T_i^{Con}	The temperature statistic *T* for the calender month i under the future (^{Fut}) and control (^{Con}) conditions
T_i^{Obs}, T_i^{Est}	The observed (^{Obs}) and estimated (^{Est}) temperature statistic *T* for the calender month *i*
T_{max}	Daily maximum 2-m air temperature (°C)
T_{min}	Daily minimum 2-m air temperature (°C)
τ	Shear stress due to overland flow (N/m^2)
τ_b	Shear stress acting on the bank (N/m^2);
τ_{bc}	Critical shear stress for initiation of motion of bank material (N/m^2)
τ_{ec}	Critical shear stress for initiation of sediment motion (N/m^2)
TSS	Total suspended solid (mg/l)
Turb	Turbidity (NTU)
u_x, u_y and u_l	Flow velocities in the x, y and l directions (m/s)
u_*	Shear velocity of channel flow (m/s)
U	Water velocity of channel flow (m/s)
Var_{DP}	Variance of daily rainfall for a specified month (mm^2)
Var_{DT}	Variance of daily mean 2-m air temperature for a specified month (°C^2)
$Var_{\Delta DT}$	Variance ($Var_{\Delta DT}$) of daily 2-m air temperature range for a specified month (°C^2)
Var_{HP}	Variance of hourly rainfall for a specified month (mm^2)
VP	Vapour pressure (kPa)
VP_i	Vapour pressure for the day *i* (kPa)
V_x	Yellow Mediterranean soil of Schist origin
WS	Wind speed (m/s)
WS_i	Wind speed for the day *i* (m/s)
XC_{DP}	Spatial cross correlation between the rain gauges (-)
X(Pdry)	The invertible transformation *X* that can be applied to the proportional dry variable *Pdry*
Y(L1AC)	The invertible transformation *Y* that can be applied to the lag-1 autocorrelation variable *L1AC*
z	Depth of loose soil (m) or z = depth of bed sediment (m)
z_g	Ground or channel bed level (m)

List of Abbreviations

A1B	A balanced emphasis on all energy sources

Additive Ɛ-indicator	The largest distance required to translate the approximation set solution to dominate its nearest neighbor in the best known approximation set
Alb	Albernoa
Alm	Almodôvar
AOGCM	Atmposphere-ocean coupled general circulation model
Bej	Beja
Cas	Castro verde
CDF	Cumulative distribution function
CF	Change Factor
CLEMDES	Clearing house mechanism on desertification for the Northern Mediterranean region, an European project with the aim of setting up an Internet based network devoted to the improvement of the diffusion of information among public.
CORDEX	COordinated Regional climate Downscaling Experiment, a WCRP (World Climate Research Programme) sponsored program to produce regional climate change scenarios globally, contributing to the IPCC's fifth Assessment Report (AR5) and to the climate community beyond the AR5.
CORINE	Coordination of information on the environment
$Crit_{0.05}$	The critical value at a significance level of 5%
CRU-WG	Climate Research Unit daily Weather Generator
CTL	Control
CV	Coefficient of Variation
DEM	Digital Elevation Model
DesertWATCH	An European Space Agency (ESA) project aiming at developing a user-oriented Information System based on EO technology to support national and local authorities in responding to the reporting obligations of the UNCCD and in monitoring land degradation trends over time.
DESERTLINKS	An European, international and interdisciplinary research project funded by the European Commission under Framework Programme 5, with the aim of developing a desertification indicator system for Mediterranean Europe
DeSurvey	A project funded by the European Commission under the Framework Programme 6 and contributing to the implementation of the actions 'Mechanisms of desertification' and 'Assessment of

	the vulnerability to desertification and early warning options' within the 'Global Change and Ecosystems priority'
DISMED	Desertification Information System for the Mediterranean, an European project to improve the capacity of national administrations of Mediterranean countries to effectively program measures and policies to combat desertification and the effects of drought.
E	Exponential distribution
EEA	European Environment Agency, www.esa.int
ENSEMBLES	An EU-FP6 financed project. The value, and core, of the ENSEMBLES project is in running multiple climate models (‘ensembles’); a method known to improve the accuracy and reliability of forecasts.
ERLAND	A research project financed by FCT for estimating the impacts of climate change on soil erosion in representative Portuguese agroforestry watersheds, due to changes in rainfall, runoff generation and vegetation cover.
ESA	European Space Agency
EU-FP6	European Union Sixth Framework Programme, http://ec.europa.eu/research/fp6/index_en.cfm
EV	Gumbel or Extreme Value distribution
EXP	Expected
FAO	Food and Agriculture Organization, www.fao.org
FCT	Fundação para a Ciência e a Tecnologia, http://www.fct.pt/, (Portuguese national funding agency for science, research and technology)
FUT	Future
G	Gumbel distribution
GA	Genetic Algorithm
GCM	Global Climate Model
GDP	Gross domestic product
Generational distance	The average Euclidean distance of points in an approximation set to their nearest corresponding points in the best known approximation set.
GEV	Generalized Extreme Value
GHGs	Green House Gases
GLO	The generalized logistic distribution

GNO	The generalized normal distribution
GPA	The generalized Pareto distribution
GW	Groundwater model
HydroGeoSphere	A fully integrated, physically based hydrological model
Hypervolume	The ratio of volume of objective space dominated by an approximation set to that dominated by the best known approximation set
HH:MM	Hours:Minutes
ICAAM-WG	The Institute of Mediterranean Agricultural and Environmental Sciences daily Weather Generator
IHERA	Instituto de Hidráulica, Engenharia Rural e Ambiente (Institute of Hydraulics, Rural Engineering and Environment)
ln3	Three-parameter lognormal distribution
IOA	Index of agreement
IP	Iberian Peninsula
IPCC	Intergovernmental Panel on Climate Change, http://www.ipcc.ch/
IPMA	Instituto Português do Mar e da Atmosfera, www.ipma.pt, (Portuguese Institute for the Ocean and Atmosphere)
IQRs	Interquartile Ranges
ISD	Indicator of Susceptibility to Desertification
L	Logistic distribution
LADAMER	Land Degradation Assessment in Mediterranean Europe, an European project with the aim of providing an assessment of the degradation status of Mediterranean lands on small scales, and the identification of Hot Spot areas subject to high desertification and land degradation risk
LAMs	Limited-area models
LHS	Latin hypercube sampling
LOG	Logarithm
LOGE	LOG transformed Error
LUCINDA	Land care in desertification affected areas: from science towards application, an European project with aim of promoting and facilitating the dissemination, transfer, exploitation and broad take-up of past and present research programme results in the theme of combating desertification in Mediterranean Europe.
MBE	Mass Balance Error
MCCE	Modified Competitive Complex Evolution

MEDACTION	An European Commission funded 5th Framework Program research project that aims to address the main issues underlying the causes, effects and mitigation options for managing land degradation and desertification in the North Mediterranean region of Europe.
MEDALUS	Mediterranean Desertification and Land Use, an international research project with the general aim to investigate the relationship between desertification and land use in Mediterranean Europe.
MCCE	Modified Competitive Complex Evolution
METO-HC_HadRM3Q0	The Met Office Hadley Centre regional climate model HadRM3Q0 with normal sensibility
MIKE SHE	An integrated hydrological modelling system for building and simulating surface water flow and groundwater flow
MOEA	Multi-Objective Evolutionary Algorithms
Monte Ponte	Monte da Ponte gauging station
MOSCEM-UA	Multi-Objective Shuffled Complex Evolution Metropolis global optimization algorithm
MRC	Modelo Regional Climático
MSCE	Modified Shuffled Complex Evolution
N	Normal distribution
NAO	North Atlantic Oscillation
NOPT	The number of optimization parameters
NSE	Nash-Sutcliffe Efficiency
NSGA-II	Non-dominated sorting genetic algorithm II
OBS	Observation or observed
Opt-indicator	The smallest distance required to translate the approximation set solution to dominate its nearest neighbor in the best known approximation set
PBSD	Physically-based spatially-distributed
PDF	Probability density function
PE3	The Pearson type III distribution
PKE	Peak Error
PM	Polynomial mutation
PMCC	Coefficient of determination
PRJ	Projected

PRUDENCE	Prediction of Regional scenarios and Uncertainties for Defining EuropeaN Climate change risks and Effects, an European Union project with the aim of providing high resolution climate change scenarios for Europe at the end of the twenty-first century by means of dynamic downscaling (regional climate modelling) of global climate simulations.
$q_{0.05}$, $q_{0.25}$, $q_{0.50}$, $q_{0.75}$, $q_{0.95}$ $q_{0.98}$ and $q_{0.99}$	5^{th}, 25^{th}, 50^{th}, 75^{th}, 95^{th}, 98^{th} and 99^{th} percentile
RainSim V3	Rainfall simulation version 3 model
RCM	Regional Climate Model
RCPs	Representative Concentration Pathways, which are four greenhouse gas concentration trajectories adopted by the IPCC for its fifth Assessment Report (AR5) in 2014
REACTION	Restoration actions to combat desertification in the Northern Mediterranean, an European project with its general objective of facilitating access to high quality information for forest managers, scientists, policy-makers and other stakeholders, providing tools for the promotion of techniques and initiatives for sustainable mitigation actions
RMSE	Root Mean Square Error
SAC-SMA	Sacramento Soil Moisture Accounting model, a conceptual hydrological model that attempts to represent soil moisture characteristics to effectively simulate runoff that may become streamflow in a channel
SAGRA/COTR	Sistema Agrometeorológico para a Gestão da Rega no Alentejo/ Centro Operativo e de Tecnologia de Regadio, http://www.cotr.pt/cotr/sagra.asp, (the Portuguese Agrometeorological System for the Management of Irrigation in the Alentejo/Irrigation Technology and Operative Center)
Sao	São Marcos da Ataboeira
SAO MDA	São Marcos da Ataboeira station
Sbp	Santa Barbara de Padrões
SBX	Simulated binary crossover
SCE	Shuffled Complex Evolution
SCE-UA	Shuffled Complex Evolution method developed at the University of Arizona
SHE	Système Hydrologique Européen

SHETRAN	Système Hydrologique Européen TRANsport, a physically-based spatially-distributed modelling system for water flow and sediment and contaminant transports in river catchments, http://research.ncl.ac.uk/shetran/
SIM	Simulation or simulated
SNIRH	Sistema Nacional de Informação de Recursos Hídricos, www.snirh.pt, (Portuguese national water resources information system)
SPEA2	The Strength Pareto Evolutionary Algorithm 2
SRES	Special Report on Emissions Scenarios
STD	Standard deviation
STNSRP	Spatial Temporal Neyman-Scott Rectangular Pulse
SWAT	Soil and Water Assessment Tool, a river basin scale model developed to quantify the impact of land management practices in large, complex watersheds
Trindade	Tri
U	Uniform distribution
UNCCD	United Nations Convention to Combat Desertification, www.unccd.int
Vdc	Vale de Camelos
WESP	Watershed Erosion Simulation Program
WetSpa	Water and Energy Transfer between Soil, Plants and Atmosphere, a distributed hydrological model for prediction of river discharges
WS	Wind speed
Ɛ-NSGA-II	Epsilon dominance non-dominated sorting genetic algorithm II

1. Introduction and Objectives

Semi-arid (EEA 2012), large intra- and inter-annual variability in precipitation (Corte-Real *et al.*, 1998; Mourato *et al.*, 2010; Guerreiro *et al.*, 2014), drought (*Santos et al.*, 2010), land abandonment, land degradation (Pereira *et al*., 2006) and desertification (Rubio and Recatalà 2006) have been the highlights of southern Portugal since the early 1990s (Bathurst *et al.*, 1996; Thornes 1998). Water shortage and desertification processes are the main problems the region is confronting. The persistence of temperature rise and precipitation decrease has exacerbated the situation (EEA 2012; IPCC 2013), which will continue to be at stake in the 21st century (Kilsby and Tellier *et al.*, 2007; Mourato 2010; EEA 2012; IPCC 2013). Mitigation strategies are urgently required to make the region sustainable for the future climate change impacts (IPCC 2012); and a step of utmost importance is the accurate quantification of water availability and extreme events for both current and future climates. Recent studies from EEA 2012, Feyen *et al.* (2012), Rojas *et al.* (2012), Rojas *et al.* (2013), Rajczak *et al.* (2013) and Schneider *et al.* (2013) have dealt with the issues at a spatial level of European continent; however, their results cannot be extracted for a direct use at a catchment scale of southern Portugal due to the considered coarse spatial resolutions. Among investigations on climate change impacts of the region, some regarded only the changes in precipitation (Corte-Real *et al.* 1995b, 1998, 1999a and 1999b), and others have not included recent progresses in regional climate modelling, downscaling methods and hydrological models as well as observation data with temporal resolution higher than a day (Bathurst *et al.*, 1996; Bathurst and Bovolo 2004; Kilsby and Tellier *et al.*, 2007; Mourato 2010). The present study attempts to fill the mentioned gaps.

The objective of this study is to investigate the climate change impacts on the agricultural dominated Cobres basin in southern Portugal in terms of water resources, extreme events as well as sediment transport, considering the importance of sediment yield in the risk of desertification which has been demonstrated by Vanmaercke *et al.* (2011). The selection of Cobres basin as the study area can be justified by the problems of southern Portugal described in Section 2.1 as well as by previous studies of MEDALUS and MEDACTION projects. The study, sets 1981–2010 as the control period, due to the data availability, and 2041–2070 as the future period for practical purpose. Considering the size and topography of the Cobres basin, hourly precipitation and daily potential evapotranspiration (PET) are enough for getting better representation of hydrological and sediment transport processes under both control

and future climates. The state-of-the-art climate projections derived from the RCM HadRM3Q0 output, provided by the ENSEMBLES project (van der Linden *et al.*, 2009), together with the advanced version of the Spatial-Temporal Neyman-Scott Rectangular Pulses (STNSRP) model RainSim V3 (Burton *et al.*, 2008) are used to downscale synthetic hourly precipitation series. Daily PET is calculated based on the FAO Penman-Monteith equation (Allen *et al.*, 1998) and the variables, namely daily maximum and minimum 2-m air temperatures, sunshine duration hours, vapour pressure and wind speed, are generated by the rainfall conditioned weather generator—ICAAM-WG, developed in this study, based on the modified Climate Research Unit daily Weather Generator (CRU-WG) (Kilsby and Jones *et al.*, 2007). Temperature variables are projected to change based on the RCM HadRM3Q0 output; other variables are assumed not to change for future, because maximum sunshine duration cannot increase, and vapour pressure and wind speed are projected with large uncertainties, differing largely from the different RCM integrations (van der Linden *et al.*, 2009). Bias of RCMs statistics for precipitation and temperature are corrected based on the change factor approach described in Kilsby and Jones *et al.* (2007) and Jones *et al.* (2009). The physically-based spatially-distributed model SHETRAN (Ewen *et al.*, 2000) is used for the simulations of hydrological and sediment transport processes. A global optimization method is used for automatically getting the best parameter setting in their physically constrained ranges; and the effects of spatial resolutions on SHETRAN performance are also investigated. Finally, three series of 1000-year hydrological and sediment transport processes are developed, respectively for control and future climates, to provide a robust conclusion.

The structure of the thesis is as follows: Chapter 2 shows the scientific background of the present study. Chapters 3 and 4 respectively introduce the study area and data preparation processes and the SHETRAN hydrological modelling system. Chapters 5 and 6 provide the bases of SHETRAN model set-up. To be specific, Chapter 5 demonstrates automatic calibrations of SHETRAN model by using two global optimization methods; and Chapter 6 investigates the effects of spatial resolution on SHETRAN model performance. Chapter 7 is dedicated to prepare the series of synthetic hourly precipitation and daily PET for both control and future climates. Chapter 8 assesses future climate change impacts on Cobres basin. Finally, Chapter 9 concludes the study and suggests recommendations for further research.

2. Scientific Background

A short review of relevant literature and state-of-the-art, which motivated the researches of the present study are introduced in this chapter. First, the problems of southern Portugal are presented together with the justifications for the hydrological impacts assessments of climate change for an agricultural dominated basin of the region; then, a review of hydrological impacts assessments is given as well as the cutting-edge climate model data, downscaling methods and hydrological models; and finally, problems involved in the use of physically-based spatially-distributed (PBSD) hydrological models, such as determinations of model parameters and spatial resolution, are also described. This review has a general character, since the detailed reviews are given in the following chapters for individual subjects.

2.1 Problems of Southern Portugal

Previous studies from observation (Corte-Real *et al.*, 1998; Rodrigo and Trigo 2007; IPCC 2007; de Lima *et al*., 2013; Guerreiro *et al.*, 2014; IPCC 2013) and climate model simulations (IPCC 2007; van der Linden *et al.*, 2009; Costa *et al.*, 2012; Majone *et al.*, 2012; Rajczak *et al.*, 2013; IPCC 2013) have unequivocally indicated a substantial temperature rise and rainfall decrease over the Iberian Peninsula for the recent past and projected the same changes or worse for future decades. Vicente-Serrano *et al*. (2014) have concluded that the drought severity in the Iberian Peninsula (IP) has increased in the past five decades due to the greater atmospheric evaporative demand resulting from temperature rise. These changes of climate can exacerbate the desertification processes in the region to a great extent (Nunes 2007). According to UNCCD 2004, around 60% of the land in Portugal has been identified with the risk of desertification due to the semi-arid climatic condition, seasonal droughts, very high rainfall variability, and sudden and high-intensity rainfall (Rubio and Recatalà 2006). The DesertWATCH project applied the Indicator of Susceptibility to Desertification (ISD) to the mainland Portugal for the year of 2005 and confirmed that one third of the country was suffering from desertification processes which mainly occur in the southern part of the country (ESA 2012).

Southern Portugal, particularly the Alentejo region, is a drought prone area with rainfall of ~400–800 mm/year and runoff or water availability of <200 mm/year (Ramos and Reis 2002; Pereira *et al.*, 2006). The factors associated with desertification in the region are high frequency of moderate to extreme droughts (~3.6 years, *Santos et al.*,

2010), increase of aridity and extreme rainfall variability (Costa and Soares 2009) along with others such as land abandonment and soil degradation (Pereira *et al.*, 2006; ESA 2012). Studies related to the combat of desertification in southern Europe can be found from projects such as MEDALUS, MEDACTION, DESERTLINKS, DeSurvey, DISMED, LADAMER, REACTION, CLEMDES, LUCINDA and DesertWATCH; a literature review of desertification and land degradation can be found in Baartman *et al*. (2007). These studies have started the monitoring evaluation or surveillance of the desertification processes, establishing indicators considering climate, soil, vegetation and land management and the assessments for impacts of climate and land-use changes by using hydrological and ecological modelling (Bathurst and Bovolo 2004). In the recent 30 years, the rapid development of microcomputer processing power has facilitated the great leaps forward in the high-resolution climate simulations, the improvements in techniques and technologies for downscaling GCM or RCM model to a catchment scale and the physically based hydrologic modelling with high spatial and temporal resolutions. Under the circumstances, this study is intended to update the hydrological impacts assessments for an agricultural dominated basin in southern Portugal by using state-of-the-art regional climate simulations, a statistic downscaling method and a fully physically-based spatially-distributed hydrological model.

2.2 Hydrological Impacts Assessments

IPCC 2013 has concluded, with high confidence, that human influence has been one of the causes of the observed temperature rise since 1950 and the increased concentrations of greenhouse gases (GHGs) from anthropogenic activities have contributed to the observed climate variations in the period. Solomon *et al*. (2009) has demonstrated that climate change due to carbon dioxide emissions can be irreversible for 1000 years after emissions stop. Climate anomalies has significantly affected the global and regional hydrological cycles. In southern Europe, decrease in river flows and increase in the frequency and intensity of droughts have already been observed (EEA 2012; IPCC 2013); climate model simulations have also suggested the continued trends in the 21st century (Kilsby and Tellier *et al*., 2007; Hagemann *et al*., 2013; IPCC 2013; Rajczak *et al*., 2013). In this region, precipitation has displayed large intra- and inter-annual variations (Corte-Real *et al.*, 1998; Durão *et al.*, 2009; Mourato *et al.*, 2010; Guerreiro *et al.*, 2014; Santo *et al.*, 2013), which have led to severe consequences (Santos *et al.*, 2007). Natural climate variability plays an important role in the magnitude and frequency of extreme precipitation events (Corte-Real *et al.*, 1995a and 1995b; Qian *et al.*, 2000; Zhang *et al.*, 1997; Santo *et al.*, 2013) and the consequent

flood events (Benito *et al.*, 2004; Ortega and Garzón 2004; Salgueiro *et al.*, 2013; Vaquero 2004). However, the temperature increase can enhance the water-holding capacity of the atmosphere and evaporation into the atmosphere, which will increase climate variability, with more intense precipitation and high frequent droughts (Trenberth *et al.*, 2003); as a result, the hydrological cycle accelerates (Huntington 2006; Kundzewicz *et al.*, 2007). The higher water temperature and variations in runoff can facilitate the adverse changes in water quality of rivers, lakes and reservoirs etc. (Environment Canada 2001; Hall *et al.*, 2002; Robarts *et al.*, 2005; Kundzewicz *et al.*, 2007). Furthermore, the increased rainfall amounts and intensities can lead to larger rates of erosion if none adaptation measures are made (Kundzewicz *et al.*, 2007). These aspects should be taken into consideration for the existing water quality problems, e.g., for the Alqueva reservoir (Palma *et al.*, 2014).

Simulations by atmosphere-ocean coupled general circulation models (AOGCMs) are required to provide the long-term climate change projections to consider the possible human activities and natural effects that may alter climate over decades and centuries. Nakicenovic and Swart (2000) developed altogether 40 SRES scenarios (story lines), based on the relationships between driving forces of GHGs and sulfur emissions, such as demographic development, socio-economic development, technological changes, and their evolutions are story lines, corresponding to the GHG emission scenarios (e.g. A1, A2, B1 and B2). Recently, Representative Concentration Pathways (RCPs) were developed (Moss *et al*., 2010) to supersede SRES projections for facilitating the inclusion of climate change mitigation and adaptation measures in climate change impacts studies. Outputs of AOGCMs cannot be directed used in hydrological impact assessments because of the existence of model bias (Corte-Real *et al*., 1999a) and discrepancies in spatial and temporal resolutions (Kilsby and Jones *et al.*, 2007; Burton *et al.*, 2008). Therefore, downscaling is necessary to correct the bias on one hand and to transform climate model data into hydrological model inputs on the other hand.

The AOGCMs output can be downscaled to a finer spatial resolution by two fundamental approaches: dynamic downscaling and statistical-stochastic downscaling (Fowler *et al.*, 2007). Dynamical downscaling refers to the use of regional climate models (RCMs), or limited-area models (LAMs) (Fowler *et al.*, 2007), whose lateral boundary conditions are provided by an AOGCM (Schoof 2013). Statistical-stochastic downscaling can be classified as scaling methods, regression-based methods, weather pattern-based methods and weather generators (Schoof 2013), which are based on the assumption of a strong and stationary relationship between the predictor variable(s)

and the predictand. Both downscaling approaches have their own advantages and disadvantages (Fowler *et al.*, 2007), studies comparing the downscaling methods have not reached a general consensus; instead, the end-users are suggested to combine advantages of the two approaches and to choose the predictors and methods best suitable for their applications (Burton *et al*. 2008; Maraun *et al.*, 2010). For Europe, the largest coordinated dynamical downscaling experiments have been the ended projects PRUDENCE (Christensen *et al*., 2007) and ENSEMBLES (van der Linden and Mitchell 2009) and the on-going one CORDEX (Giorgi *et al*., 2009).

Hydrological impact assessments involve uncertainties from various aspects such as GCMs (Chien *et al*., 2013; Demaria *et al.*, 2013; Das *et al*., 2013; Li *et al.*, 2013), RCMs (van Vliet *et al*., 2012; Wang *et al.*, 2013), GHGs emission scenario or RCPs (Koutroulis *et al*., 2013; Xu *et al.*, 2013), downscaling methods (Haylock *et al.*, 2006; Chen *et al.*, 2012), hydrological models (Haddeland *et al.*, 2011; Hagemann *et al*., 2013) and observed data. Theoretically, all these uncertainties should be considered; however, this is not the case due to the limitations of computational resources and the availabilities of climate model data and observed data. In this thesis, the aforementioned uncertainties are not considered being left for further study; instead, more efforts are dedicated to get better simulations of synthetic rainfall series and hydrological processes in accordance with the final objectives of the research. As indicated in the beginning of this section, accurate evaluations of water resources and extreme events are of highest importance for future hydrological impact assessments in southern Europe. Therefore, the better simulations of synthetic rainfall series is designed to be achieved by considering rainfall statistics most related to evaluations of water resources and extreme events; and the better representations of hydrological processes are to be realized by considering spatial resolution and parameter setting best suitable for a PBSD model.

2.3 Problems Involved in the Use of Physically-Based Spatially-Distributed Hydrological Models

Physically-based spatially-distributed hydrological models have been developed for around 30 years with the aim of explicitly considering spatial variability to a level of model grid scales (Abbott *et al*., 1986a,b; Beven *et al*., 1980; Ewen *et al*., 2000; Therrien *et al*., 2006; Refsgaard *et al*., 2010; Brunner and Simmons 2012). Due to the physically-based property, the model has the capacity for evaluations of climate and land-use changes impacts (Bathurst and O'Connell 1992; Bathurst *et al.*, 2004;

Bathurst *et al.*, 2007; Goderniaux *et al.*, 2009; Goderniaux *et al.*, 2011; Bathurst 2011; Birkinshaw *et al*., 2011); and it is also an indispensable tool for diffuse pollution controls (Lutz *et al*., 2013) due to the spatially-distributed characteristics. However, these models are difficult to apply due to the requirements of massive data input and large number of parameters (Leavesley 1994); among others, model calibration and overparameterization (Beven and O'Connell 1982; Bathurst 1986; Bathurst and O'Connell 1992; Refsgaard 1997; Refsgaard *et al*., 2010), scaling problems (Beven 1989; Bathurst *et al*., 1996), spatial discretization (Bathurst and O'Connell 1992; Refsgaard 1997; Wildemeersch *et al*., 2014) and uncertainties (Beven and Binley 1992; Lukey *et al.*, 2000; Nasr *et al*., 2007; Ewen *et al.*, 2006) are the main problems. Because of the high level of computational requirements, model calibration (Zhang *et al.*, 2013), spatial discretization and uncertainties cannot be tackled appropriately; as a consequence, best model performances cannot be achieved. To avoid this situation, global optimization algorithms are used in the study for model calibration and spatial discretization to get best configuration of the PBSD model; and parameter uncertainties are also considered by validating the optimized parameter settings with equally good performances and comparing their validation results.

3. Cobres Basin

3.1 Geographical and Climatological Context

This study is carried out on the part of the Cobres river basin situated upstream of the Monte da Ponte gauging station. The basin is, semi-arid, middle-sized with area of 705 km^2, located in the Alentejo province of southern Portugal (37°28′N–37°57′N, 8°10′W–7°51′W, Fig. 3.1), an area suffering from desertification (Bathurst *et al*. 1996).

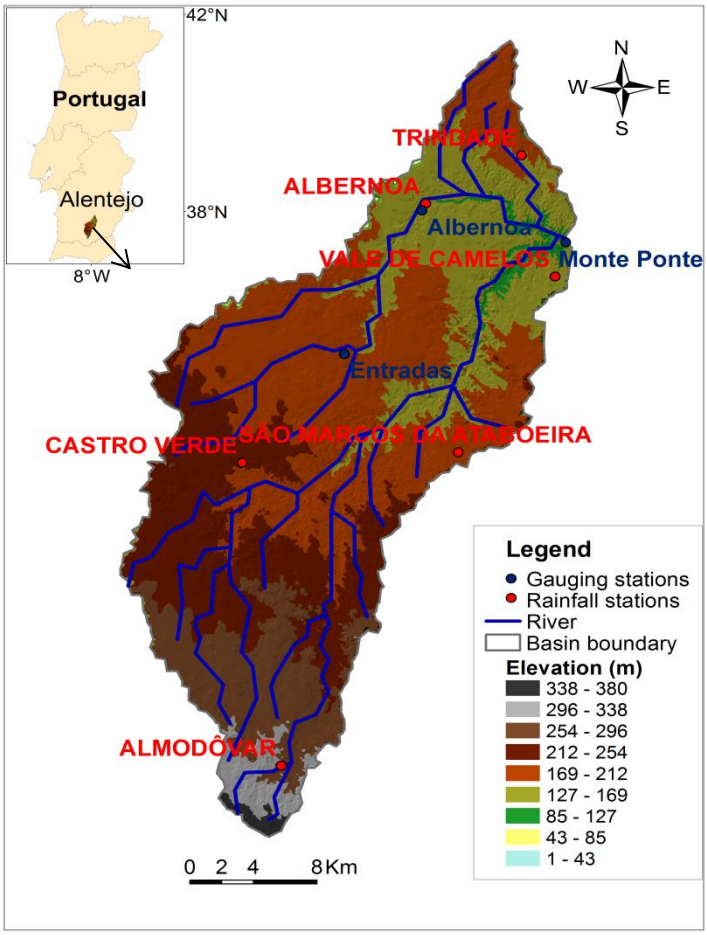

Fig. 3.1 Map showing elevations, gauging stations, rainfall stations and watercourses of the Cobres basin.

It is a region of relatively low relief, with the elevation varying from 103 to 308 m above sea level. Based on the 1:25000 soil map provided by the Institute of Hydraulics, Rural Engineering and Environment (IHERA), nine types of soil are identified, of which the main types are red or yellow Mediterranean soil of Schist origin (V_x soil), brown Mediterranean soil of Schist or Greywacke origin (P_x soil) and lithosols from semi-arid and sub-humid climate of Schist or Greywacke origin (E_x soil), occupying respectively

20 %, 45 % and 26 % of the basin area. The soils are thin with depths varying from 10 to 50 cm. Based on the 1:100000 CORINE Land Cover 2006 (Caetano *et al*. 2009), four types of land-use are identified, of which the predominant types are crop (70 %) and agroforestry (27 %). Details of soil and land-use characteristics are shown in Chapter 5. The climate in this region is characteristically Mediterranean and Continental, with moderate winters and hot and dry summers, high daily temperature range, and a weak and irregular precipitation regime; mean annual precipitation of rain gauge stations in the region varies between 400 and 900 mm, with around 50 to 80 rainy days per year (Ramos and Reis 2002). The mean annual potential evapotranspiration (PET) is around 1300 mm. For the control period 1981–2010, Table 7.1 (page 94) indicates the mean annual precipitation of rain gauge stations of Cobres basin varying between 410 and 550 mm and Fig. 7.2 (page 96) displays the annual cycle of mean daily precipitation, of daily maximum and daily minimum 2-m air temperature, of FAO Penman-Monteith potential evapotranspiration. Details of climatological characteristics, for the control period 1981–2010, can be found in Chapter 7.

3.2 Hydrological Data

Hourly dischage and rainfall data were provided by SNIRH for the stations indicated in Fig. 3.1 (page 9) respectively for the periods from October 2004 to September 2008 and from March 2001 to September 2008. The data gaps of hourly rainfall are required to be filled in for SHETRAN hydrological simulations. Three steps are needed: (1) analysis of data availability; (2) filling of the missing data; and (3) Validation of the filled missing data. Two types of missing data are considered: no registration and no consistency. No registration is a result of the data logger's problems such as breakdown and out of memory or battery, and no consistency means the data are not consistent with those registered from the nearby stations, which is identified by the double-mass curve method (Searcy and Hardison 1960) for this study. The results of data availability analysis are indicated in Fig. 3.2 (page 11) for the 6 rainfall stations at Cobres basin.

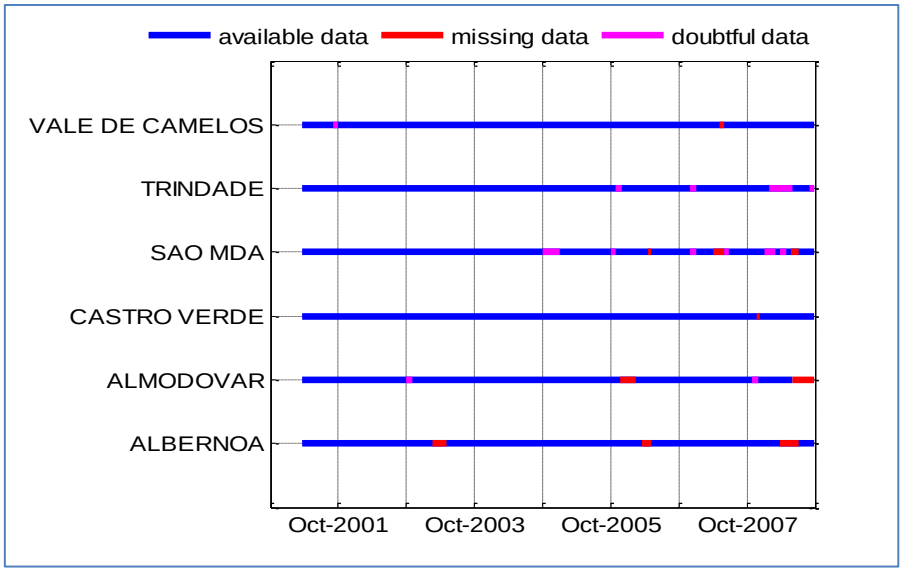

Fig. 3.2 Data availability analysis for hourly rainfall series at stations in the Cobres basin (SAO MDA denotes the São Marcos da Ataboeira station).

The missing data are filled firstly at monthly scale and then at daily and hourly scales. The monthly double-mass curves are applied to get monthly rainfalls; and the method of fragments described in Srikanthan and Mcmahon (1980) is used to downscale the filled monthly rainfall to daily, and further to hourly, scales. Fig. 3.3 indicates the double-mass curves of monthly rainfall for the 6 stations after completion of the filling procedure. The method of fragments is validated to 6 monthly rainfalls, with observed values in the range of [13.3, 165.0] mm, to daily scale, and the root mean square errors in the range of [0.8, 12.6] mm.

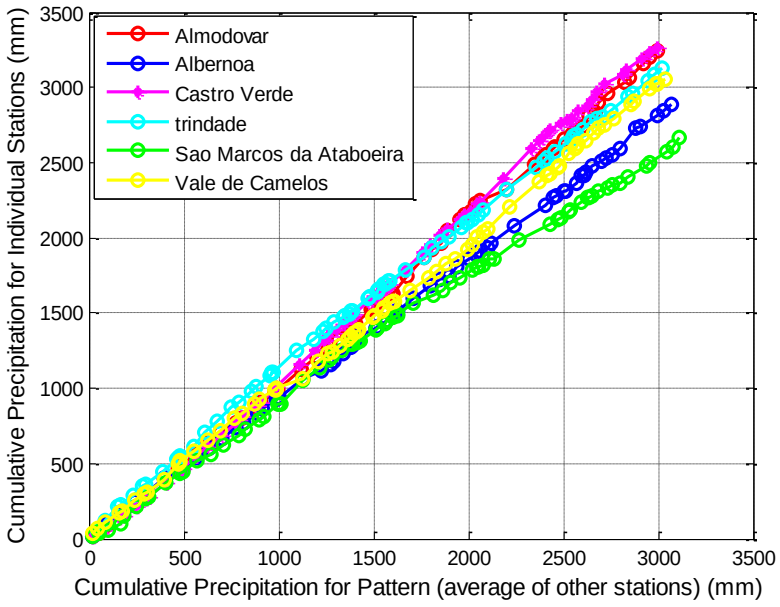

Fig. 3.3 Double mass curve for monthly rainfall of 6 stations from January 2001 to September 2009.

3.3 Sediment Data

In this study, the observed sediment discharge data is not directly measured. Instead, it is derived from the observed discharge and turbidity and the rating curve between turbidity and sediment concentration. Hourly turbidity, hourly discharge and 29 samples of total suspended solid (TSS) are available at the Portuguese national water resources information system (SNIRH) respectively for the periods from July 2001 to October 2006, from October 2004 to September 2008 and from July 2001 to March 2006 for the basin outlet Monte da Ponte gauging station. Table 3.1 (page 13) displays the 29 time points with the available data of turbidity, TSS and discharge, and Table 3.2 (page 14) presents the summary statistics of these data. As one may see, the hourly discharges showed in Table 3.1 are in the range of [0.4, 51.0] m^3/s, so careful interpretation should be made when the relationship between TSS and turbidity derived from data of Table 3.1 is applied to discharges with values much higher than 51.0 m^3/s. However, since no other alternative sediment data was made available, Table 3.1 is used to get the observed sediment discharges.

According to Sun *et al.* (2001) and Rasmussen *et al.* (2009), the relationship between TSS and turbidity is often expressed as a linear regression equation, like equation 3.1, a non-linear equation, like equation 3.2, or a polynomial function like equation 3.3.

$$TSS = a \times Turb + b \tag{3.1}$$

$$TSS = a \times Turb^b \tag{3.2}$$

$$TSS = a_0 + a_1 \times Turb + a_2 \times Turb^2 + a_3 \times Turb^3 + \cdots + a_n \times Turb^n \tag{3.3}$$

Where TSS is in mg/l, Turb is turbidity in NTU, with a, b, a_0, a_1, …, and a_n being coefficient to be calculated.

Pearson and Kendall's tau tests were conducted for the available pairs of TSS and turbidity shown in Table 3.1. Pearson's correlation test indicated strong positive relation between TSS and turbidity (r = 0.96, α = 3.5986e-17) and Kendall's tau test also indicated a positive relation (r = 0.39, α = 0.0036) between TSS and turbidity. Three regression analyses were carried out between TSS and turbidity by using matlab R2012a: linear and quadratic regressions to original TSS and turbidity; linear regression to log10TSS and log10turbidity. The results show that the linear regression between log10TSS and log10turbidity produces larger residuals for high flows than those from the linear and quadratic regressions between TSS and turbidity. From Fig. 3.4 (page14), the quadratic regression "TSS = 0.32599 × Turb + 0.0011818 ×

$Turb^2$" is adopted. The observed sediment discharges are then obtained by applying the regression to the observed turbidity and discharge. Finally, the periods with observed sediment transport discharges are: (1) From December 26th, 2005 15:00 to December 29th, 2005 05:00; (2) From January 29th, 2006 22:00 to February 1st, 2006 02:00; (3) From March 18th, 2006 13:00 to March 23rd, 2006 17:00; (4) From October 23rd, 2006 05:00 to October 28th, 2006 07:00; and (5) From November 3rd, 2006 02:00 to November 4th, 2006 22:00.

Table 3.1 Available TSS, turbidity and hourly discharge at Monte da Ponte gauging station

Date	HH:MM	Turbidity (NTU)	TSS (mg/l)	Q_{obs} (m^3/s)
10-07-2001	10:10	21.2	7.0	0.6
09-10-2001	09:45	44.0	5.0	0.6
13-11-2001	09:15	12.0	1.2	0.7
11-12-2001	09:55	40.0	2.6	0.7
15-01-2002	09:30	54.0	14.5	2.7
13-02-2002	09:40	29.0	7.0	2.5
12-03-2002	09:20	24.0	6.5	3.0
09-04-2002	09:30	266.0	148.0	27.0
14-05-2002	09:30	24.0	9.8	0.9
11-06-2002	09:30	17.0	7.0	0.8
05-11-2002	10:00	54.0	31.0	1.7
03-12-2002	10:30	19.5	9.7	7.2
14-01-2003	09:30	89.0	43.0	9.0
11-02-2003	09:30	40.5	2.6	4.7
11-03-2003	10:00	40.0	11.0	5.6
08-04-2003	09:45	6.3	7.5	2.7
13-05-2003	09:50	20.5	13.0	0.7
11-06-2003	09:50	7.2	9.4	0.4
11-11-2003	09:30	58.0	14.0	2.1
09-12-2003	10:00	237.0	172.0	51.0
20-01-2004	10:40	17.0	3.2	1.3
17-02-2004	10:00	28.0	3.1	1.2
16-03-2004	09:40	12.3	5.0	3.7
13-04-2004	10:00	27.0	8.2	0.7
11-05-2004	10:00	13.0	6.8	0.6
08-06-2004	09:30	5.0	3.1	0.5
17-01-2006	10:30	51.5	37.0	1.3
14-02-2006	10:00	14.0	6.0	0.7
14-03-2006	10:00	4.0	7.8	0.4

Data origin: SNIRH.

Table 3.2 Summary statistics for the data sets shown in Table 3.1

Statistic[a]	Turbidity (NTU)	TSS (mg/l)	Q_{obs} (m^3/s)
Minimum	4.0	1.2	0.4
Mean	44.0	20.8	4.7
Maximum	266.0	172.0	51.0
N	29	29	29
STD	60.8	40.0	10.3

Note: [a]N is number of samples and STD is the standard deviation of samples.

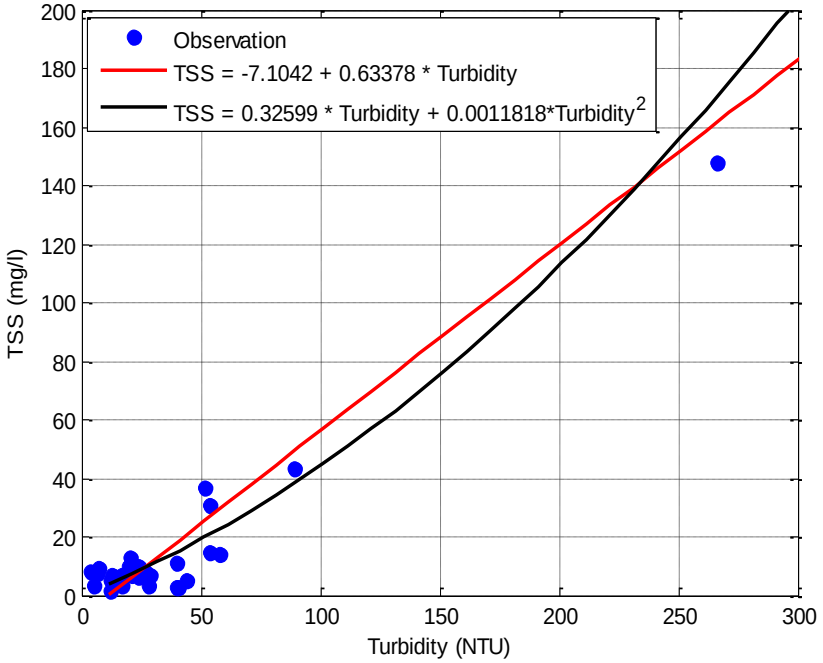

Fig. 3.4 Plot for comparison between linear and quadratic regressions.

4. SHETRAN Modelling System

SHETRAN (http://research.ncl.ac.uk/shetran/) is a Physically-based Spatially-distributed modelling system for water flow and sediment and contaminant transports in river catchments (Ewen *et al*. 2000; Birkinshaw *et al*. 2010). The physical processes are modelled by finite difference representations of the partial differential equations of mass, momentum and energy conservation and by empirical equations. The basin is discretized by an orthogonal grid network in the horizontal view and by a column of layers at each grid square in the vertical view; the river network is simplified as the links run along the edges of the grid squares.

Herein, the present study considers the water flow component (v4.301) and sediment transport component (v4.2.7) of SHETRAN. The model represents the physical processes of the hydrological cycle through: (1) the interception calculated from the modified Rutter model; (2) the actual evapotranspiration (AET) calculated from FAO Penman-Monteith PET and a prescribed ratio of AET/PET as a function of soil water potential; (3) the overland and channel flow processes based on the diffusive wave approximation of the Saint-Venant equations and (4) the subsurface flow processes calculated from 3D variably saturated flow equation. SHETRAN model simulates the physical processes of sediment transport through: (1) soil detachment by raindrop impact, leaf drip impact and overland flow; and (2) sediment transports by overland flow and channel flow based on the comparisons between sediment transport capacities and the available sediment loads (Wicks 1988; Bathurst *et al.*, 1995; Lukey *et al.*, 1995; Wicks and Bathurst 1996).

4.1 Water Flow Component

4.1.1 Interception and Evapotranspiration Module

All vegetation (trees and grass) are considered to have a surface storage capacity, which can receive intercepted rainfall and release it through evaporation and drainage. A modified Rutter model (Rutter *et al.,* 1971–1972 and 1975) is used to calculate net rainfall reaching the ground through canopy. The rate of change of storage is calculated as:

$$\frac{\partial C}{\partial t} = \mathrm{Q} - \mathrm{k}e^{b(C-S)} \qquad 4.1$$

Where C = depth of water on canopy (mm); Q = net rate of rainfall supply to canopy (mm/hour); S = canopy storage capacity (mm); k and b are drainage parameters; t = time (hour).

AET is controlled by the soil/plant/atmosphere system. In this study, AET is calculated by the approach presented by Feddes *et al.* (1976). Under conditions drier than wilting point Ψ_w (where Ψ is soil moisture tension), plant cannot live and therefore does not take up water from the soil and AET is 0; under conditions wetter than the pressure head Ψ_L at which soil water begins to limit plant growth, water uptake is considered to take place at the potential rate, so AET is equal to PET; and for $\Psi_w < \Psi < \Psi_L$ it is assumed that AET varies linearly as a proportion of the PET according to soil moisture tension Ψ. In SHETRAN model, other options are allowed for calculating the evapotranspiration, such as using the Penman-Monteith equation (Monteith 1965).

$$AET = \frac{R_n\Delta + \frac{\rho c_P \delta_e}{r_a}}{\lambda\left[\Delta + \gamma\left(1 + \frac{r_c}{r_a}\right)\right]} \qquad 4.2$$

Where AET = actual evapotranspiration (mm/s); R_n = net radiation (W/m^2); Δ = rate of increase with temperature of the saturation vapour pressure of water at air temperature (Pa/K); ρ = density of air (kg/m^3); c_P = specific heat of air at constant pressure (J/kg/K); δ_e = vapour pressure deficit of air (Pa); r_a = aerodynamic resistence to water vapour transport (s/m); λ = latent heat of vaporization of water (J/g); γ = psychrometric constant (~66 Pa/K); r_c =canopy resistance to water vapour transport (s/m).

4.1.2 Overland and Channel Flow Module

Overland and channel flows are represented by the diffusion wave approximation of the Saint-Venant equations. The involved equations are the mass conservation equation 4.3, the momentum conservation equations 4.4, 4.5 and 4.6 and the Manning-type law formulas 4.7, 4.8 and 4.9 (SHETRAN water flow equations).

$$\frac{\partial h}{\partial t} = \frac{1}{A}\left(\sum_{i=1}^{4} Q_i + Q_R\right) \qquad 4.3$$

Where h = water depth (m); A = surface area of the element (grid square, bank element, or channel link) (m^2); Q_i = lateral influx (m^3/s); Q_R = net vertical input to the element (m^3/s), which is calculated as net precipitation plus saturated flows to the surface less infiltration and evaporation.

$$S_{fx} + \frac{\partial(z_g + h)}{\partial x} = 0 \qquad 4.4$$

$$S_{fy} + \frac{\partial(z_g+h)}{\partial y} = 0 \qquad 4.5$$

$$S_{fl} + \frac{\partial(z_g+h)}{\partial l} = 0 \qquad 4.6$$

Where equations 4.4, 4.5 and 4.6 are respectively for overland flow at x and y directions and channel flow; x and y = Cartesian coordinates; l =distance along the channel; z_g = ground or channel bed level (m); and S_{fx}, S_{fy} and S_{fl} = friction slopes (Henderson 1966) in the x, y and l directions respectively (m/m).

$$S_{fx} = \frac{u_x^2}{K_x^2 h^{4/3}} \qquad 4.7$$

$$S_{fy} = \frac{u_y^2}{K_y^2 h^{4/3}} \qquad 4.8$$

$$S_{fl} = \frac{u_l^2}{K_l^2 h^{4/3}} \qquad 4.9$$

Where u_x, u_y and u_l = flow velocities in the x, y and l directions (m/s); K_x, K_y and K_l = Strickler coefficients ($m^{1/3}/s$), which are the inverse of the Manning coefficient, in the x, y and l directions.

4.1.3 Variably Saturated Subsurface Module

The variably saturated subsurface flow is represented by equation 4.10 (Parkin 1996).

$$\eta \frac{\partial \psi}{\partial t} = \frac{\partial}{\partial x}\left[K_x k_r \frac{\partial \psi}{\partial x}\right] + \frac{\partial}{\partial y}\left[K_y k_r \frac{\partial \psi}{\partial y}\right] + \frac{\partial}{\partial z}\left[K_z k_r \frac{\partial \psi}{\partial z}\right] + \frac{\partial (k_r K_z)}{\partial z} - q \qquad 4.10$$

Where η = storage coefficient (m^{-1}), which is defined by equation 4.11; ψ = pressure potential (m); K_x, K_y and K_z are saturated hydraulic conductivities in the x, y and z directions (m/s); k_r = relative hydraulic conductivity (-); q = specific volumetric flow rate out of the medium (s^{-1}), given by equation 4.12.

$$\eta = \frac{\theta S_s}{n} + \frac{d\theta}{d\psi} \qquad 4.11$$

Where θ = volumetric soil water content (m^3/m^3); S_s = specific storage (m^{-1}); and n = porosity (m^3/m^3).

$$q = q_w + q_{sp} + q_t \qquad 4.12$$

Where q_w, q_{sp} and q_t are specific volumetric fluxes (s^{-1}) out of abstraction well, spring discharges and transpiration losses respectively.

Description of water flow component is based on Parkin (1996).

4.2 Sediment Transport Component

4.2.1 Hillslope Sediment Transport Module

Soil particles are assumed to be detached from soil mass composing the ground mainly by raindrop, lead drip and overland flow; and then the eroded materials are transported towards the basin outlet by overland flow.

Raindrop and Leaf Drip Impact Erosion

The rate of soil erosion by raindrop and leaf drip impact is determined by the following empirical equation (Wicks 1988).

$$D_r = k_r F_w \left(1 - C_g - C_r\right)(M_r + M_d) \qquad 4.13$$

Where D_r = rate of detachment of soil (kg/m^2/s); k_r = raindrop impact soil erodibility coefficient (J^{-1}); F_w = effect of surface water layer in protecting the soil from raindrop impact (dimensionless); C_g = proportion of ground shielded by near ground cover (decimal fraction); C_r = proportion of ground shielded by ground level cover (decimal fraction); M_r = momentum squared of raindrops reaching the ground per unit time per unit area (kg^2/s^3); M_d = momentum squared of leaf drips reaching the ground per unit time per unit area (kg^2/s^3).

Overland Flow Erosion

Soil detachment by overland flow is determined by the approach of Ariathurai and Arulanandan (1978), considering the uniform sheet erosion on the hillslopes of a catchment.

$$D_q = \begin{cases} k_f(1 - C_r)\left[\frac{\tau}{\tau_{ec}} - 1\right] & if\ \tau > \tau_{ec} \\ 0 & otherwise \end{cases} \qquad 4.14$$

Where D_q = the rate of detachment of soil per unit area (kg/m^2/s); k_f = overland flow soil erodibility coefficient (kg/m^2/s); τ = shear stress due to overland flow (N/m^2); τ_{ec} = critical shear stress for initiation of sediment motion (N/m^2).

Capacity for Overland Transport

Both the Yalin equation (Yalin 1963, Equation 4.15) and the Engelund-Hansen equation (Engelund and Hansen, 1967, Equation 4.16) are available in SHETRAN model to be selected to calculate the total volumetric transport capacity of sediment

particles in the overland flow across the hillslope. These equations were recommended by the studies of Julien and Simons (1985) and Park *et al.* (1982).

$$G_{tot} = 0.635\sqrt{\frac{\tau}{\rho}} l D_{50} \delta \left[1 - \frac{1}{a\delta} ln(1 + a\delta)\right] \qquad 4.15$$

$$G_{tot} = \begin{cases} \frac{0.05 Q^2 S^{\frac{3}{2}}}{\sqrt{gh}\left(\frac{\rho_s}{\rho} - 1\right)^2 D_{50} l} & if\ h > 0 \\ = 0 & otherwise \end{cases} \qquad 4.16$$

Where G_{tot} = the capacity particulate transport rate for overland flow (including all sediment size groups) (m^3/s); ρ = water density (kg/m^3); l = width of the flow; D_{50} = sediment particle diameter greater than the diameter of 50% of the particles (m); δ and a are defined in equations 4.17 and 4.18 respectively; Q = water flow rate (m^3/s); g = acceleration due to gravity (m/s^2); S = water surface slope in the direction of flow (m/m); ρ_s = density of sediment particles (kg/m^3).

$$\delta = max\left[0, \frac{\tau}{\tau_{ec}} - 1\right] \qquad 4.17$$

$$a = 2.45\sqrt{\frac{\tau_{ec}}{[(\rho_s - \rho) g D_{50}]}} \left(\frac{\rho_s}{\rho}\right)^{-0.4} \qquad 4.18$$

Routing Overland Sediment Transport

The following two-dimensional mass conservation equation is applied to each sediment size fraction in turn to calculate overland sediment transport.

$$\frac{\partial (c_i h)}{\partial t} + (1 - \lambda)\frac{\partial z_i}{\partial t} + \frac{\partial g_{xi}}{\partial x} + \frac{\partial g_{yi}}{\partial y} = 0 \qquad 4.19$$

Where h = water depth (m); c = sediment concentration (m^3/m^3); λ = loose sediment porosity (decimal fraction); z = depth of loose soil (m); g_x and g_y = volumetric sediment transport rates per unit width in the x and y directions respectively ($m^3/s/m$); t = time (s); and *i* = size fraction.

The actual rate of transport of sediment is limited by the carrying capacity determined by equations 4.15 or 4.16, and the speed of sediment particles moving in the flow is assumed to equal the speed of the water flow. The portion of the sediment that cannot be carried by the flow is left on the hillslope as loose sediment. The hillslope process is assumed to have no effect on sediment particle size distribution.

4.2.2 Channel Sediment Transport Module

Channel Bank Erosion

The rate of erosion by channel flow at one of the two channel banks is determined by the following equation (Osman and Thorne 1988).

$$E_b = \begin{cases} k_b \left[\frac{\tau_b}{\tau_{bc}} - 1\right] & if\ \tau_b > \tau_{bc} \\ 0 & otherwise \end{cases} \qquad 4.20$$

Where E_b = rate of detachment of material per unit area of river bank (kg/m^2/s); k_b = bank erodibility coefficient (kg/m^2/s); τ_b = shear stress acting on the bank (N/m^2); and τ_{bc} = critical shear stress for initiation of motion of bank material (N/m^2).

Sediment load in channel link mainly comes from the channel bed material, eroded sediment transported from the hillslopes by overland flow, bank erosion and sediment transported from the upstream link. The available bed material for a time step is given by the depth of active bed layer.

Capacity for Sediment Transport

The sediment particles with diameters less than 0.25 mm (fine sediment) are assumed to travel at the speed of the water flow (Wicks 1988) and the transported quantities are not constrained. For sediment particles with larger sizes (non-fine sediment), either the Engelund-Hansen equation (Engelund and Hansen, 1967, Equation 4.21), the Ackers-White equation (Ackers and White 1973, Equation 4.22) or the Day modified Ackers-White equation (Day 1980, not shown) can be selected to calculate the transport capacity.

$$G_i = \frac{0.05BU^2H^{1.5}S^{1.5}}{(s-1)^2 D_i g^{0.5}} \qquad 4.21$$

Where G_i = volumetric sediment transport rate for particles in size group *i* (m^3/s); B = flow width (m); U = water velocity (m/s); H = flow depth (m); S = water surface slope (m/m); s = sediment specific gravity (decimal fraction); D_i = representative sediment particle diameter for the size group *i* (m).

$$G_i = Q \frac{D_i}{H} \left(\frac{U}{u_*}\right)^{n_i} G_{gr,i} \qquad 4.22$$

Where u_* = shear velocity (m/s); n_i = the transition exponent for sediment size group *i*; and $G_{gr,i}$ = dimensionless sediment transport rate for sediment size group *i*.

Routing Channel Sediment Transport

The transport of both fine and non-fine sediment is simulated with the following one-dimensional equation for conservation of sediment mass (Bennett 1974).

$$\frac{\partial(Ac_i)}{\partial t} + (1-\phi)B\frac{\partial z_i}{\partial t} + \frac{\partial G_i}{\partial x} = q_{si} \qquad 4.23$$

Where A = flow cross sectional area (m^2); c_i = concentration of sediment particles in size group i (m^3/m^3); ϕ = bed sediment porosity (m^3/m^3); B = active bed width for which there is sediment transport (m); z = depth of bed sediment (m); G_i = volumetric sediment transport rate for the sediment size fraction *i* (m^3/s); q_{si} = sediment input from bank erosion and overland flow supplies per unit channel length for size fraction I ($m^3/s/m$).

Description of sediment transport component is based on Wicks (1988).

5. Calibration of SHETRAN Model

The model set-up and calibration is described in this chapter. After a brief literature review, this chapter firstly presents calibration parameters of SHETRAN model as well as the model set-up and objective functions; secondly, it introduces the automatic calibration of SHETRAN model by MSCE for a single objective function; then, it describes multi-objective calibration of SHETRAN model by NSGA-II; finally, a short discussion concludes this chapter.

5.1 Introduction

One of the major difficulties of applying SHETRAN model is the evaluation of the most important parameters to represent a particular basin. Theoretically, these parameters should be accessible from catchment data; however, in practice, this is not the case due to unaffordable cost, experimental constraints or scaling problems (Beven *et al*. 1980). Calibration is necessary for river basin planning and management studies. Like other PBSD models, the calibration of SHETRAN model is complex and expensive due to the sophisticated model structure, heavy computation requirements and large number of calibration parameters. Successful manual calibration requires rigorous and purposeful parameterisation (Refsgaard 1997) and well-trained modeller. It is subjective, tedious and very time-consuming, which makes an extensive analysis of the model calibration quite difficult. This thesis therefore proposes the use of two automatic methods (respectively based on the Shuffled Complex Evolution and the non-dominated sorting genetic algorithm II) to calibrate the SHETRAN model.

Ewen and Parkin (1996) proposed a “blind” validation procedure for this model, with no calibration allowed, to quantify the uncertainty of predicted features for a particular application. In practice, there are various approximations in the model designs which degrade the physical bases, so that some level of adjustment in the model parameters is required. SHETRAN model is mostly calibrated manually by adjusting the principal calibration parameters on the basis of physical reasoning (Lukey *et al*. 2000; Mourato 2010; Bathurst *et al*. 2011; Birkinshaw *et al*. 2011). This can be easily handled in basins with homogenous characteristics respecting parameters, such as elevation, slope, land-use, and soil type, and small size, but it would be much more complicated for large basins with more heterogeneous characteristics.

Studies have shown that population-evolution-based algorithms might be the right solutions due to their effectiveness and efficiency in complex optimization problems

involving nonlinear, non-convex, and noisy functions (Schwefel 1995; Madsen 2003; Bekele and Nicklow, 2007). Because of their robustness and ease of implementation, the shuffled complex evolution (SCE) algorithm (Madsen 2003; Santos *et al*., 2003; Brath *et al*., 2004; Blasone *et al*., 2007; Francés *et al*., 2007) and non-dominated sorting genetic algorithm II (NSGA-II) (Bekele and Nicklow, 2007; Zhang *et al*., 2008; Shafii and Smedt, 2009; Dumedah *et al*., 2010; Zhang *et al*., 2010) are the most popular global optimization methods and have been successfully applied to automatic calibration of PBSD models like MIKE SHE, WESP and GW and semi physically based model SWAT.

The SCE method has a great potential to solve the problems accompanying the automatic calibration of PBSD models, due to its robustness in the presence of different parameter sensitivities and parameter interdependence and its capacity for handling high-parameter dimensionality. Santos *et al*. (2003) introduced new evolution steps in SCE-UA, which speed up the parameter searching processes. They also demonstrated that the final results from the Modified Shuffled Complex Evolution (MSCE) are independent of the initial parameter values, which facilitates its application. NSGA-II algorithm is one of the first Pareto-based multi-objective evolutionary algorithms (MOEA) capable of searching for the entire Pareto front in a single run (Deb *et al*. 2002). Although there are many improved versions available, the availability of its source code, the ease of use and parallelization, and the success of its application in multi-objective calibration of PBSD models still make it attractive for the first attempt of multi-objective calibration of SHETRAN model.

This chapter aims to demonstrate the applicability and efficiency of the MSCE and NSGA-II algorithms in calibration of SHETRAN model when applied to a semi-arid middle-sized basin in an area of active desertification processes. The SHETRAN simulations are considered with spatial resolution of 2.0 km and temporal resolution of 1.0 hour, taking into account the available data, computational resources as well as size and reduced heterogeneity of the Cobres basin. To reduce the complexity, the calibration parameters are split into hydrological parameters, which are the key parameters that have great influences on runoff generation and transport processes, and sediment parameters, which mainly control sediment erosion and transport processes. The calibration starts with hydrological parameters and the results are used in the following calibration of sediment parameters. As explained in Chapter 3, the available observed sediment discharge data are not of high quality; therefore, the automatic calibration of sediment parameters are carried out by the NSGA-II algorithm

only as a demonstration of the methodology. As for NSGA-II, the simulated binary crossover (SBX) and polynomial mutation (PM) are used as GA operators; the crossover distribution index (η_c) and mutation distribution index (η_m) are parameters to be adjusted. In most hydrological applications, the (η_c, η_m) are normally configured with values of (20., 20.) for NSGA-II during the optimization processes. In this study, two settings of (η_c, η_m) smaller than (20., 20.) are proposed to find out the effect of their values on the efficiencies of optimization. Considering the reasons explained in Section 5.6.4, the hydrological parameters calibrated by MSCE algorithm and the sediment parameters optimized by NSGA-II method are used, in chapter 8, for projecting the future climate change impacts on hydrology and soil erosion in the Cobres basin.

5.2 Calibration Parameters

Model parameterisation and choice of calibration parameters are based on model structure and previous studies. Bathurst (1986) carried out sensitivity analysis of the SHE model, SHETRAN's precursor, for an upland catchment in mid-Wales and found out that soil and Strickler overland flow resistance coefficients are the parameters to which the runoff generation and transport processes are most sensitive. Studies by Parkin *et al*. (1996), Bathurst *et al*. (2004, 2011), Mourato (2010) and Birkinshaw *et al*. (2011) have indicated that parameters such as Strickler overland flow resistance coefficient, AET/PET ratio and soil parameters namely top soil depth, saturated hydraulic conductivity, soil water retention and hydraulic conductivity functions are the key hydrological parameters required to be specified using field or calibrated data for flow simulations. As for sediment parameters, studies from Wicks (1988), Wicks *et al*. (1992), Wicks and Bathurst (1996) and Lukey *et al*. (2000) have shown that the soil erodibility coefficients and sediment transport capacity equations are main parameters contributing great uncertainties in sediment yield simulations. The selection of sediment transport equations can be made based on trial-and-error method using the observed sediment yield data (Wicks 1988; Wicks *et al*., 1992; Wicks and Bathurst 1996). The raindrop impact erodibiliy and overland flow erodibility are sediment parameters to be calibrated for sediment transport simulations (Bathurst *et al.*, 1996; Bathurst *et al*., 1998; Bathurst *et al*., 2002; Bathurst 2011; Birkinshaw *et al*., 2011; Elliott *et al*., 2012).

5.3 SHETRAN Model Set-Up

The input data comprise rainfall and PET, whilst the model parameters comprise rainfall station distribution, ground surface elevations, land-use and soil type distributions as

well as river links with associated cross-section information. Hourly precipitation data and basin runoff are available at SNIRH for the stations indicated in Fig. 5.1.

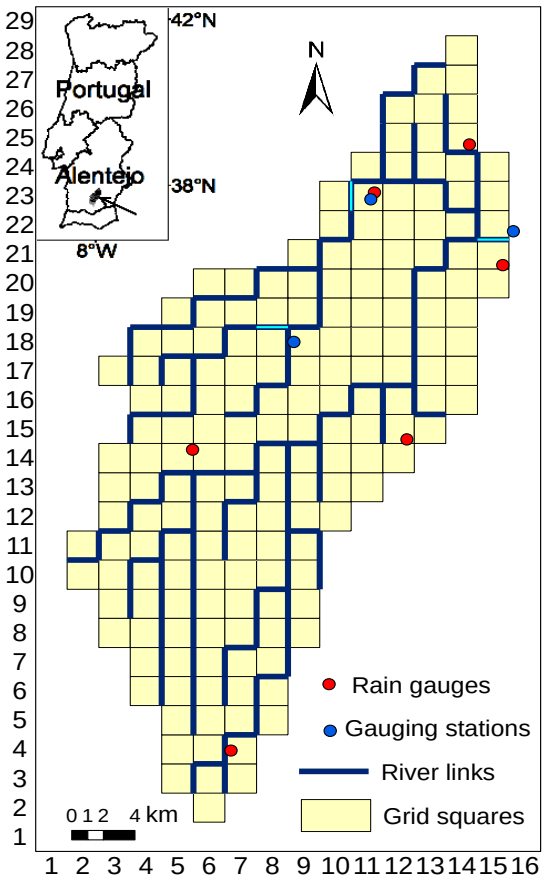

Fig. 5.1 Location map, SHETRAN grid network (abscissa and ordinate indicate grid cell number) and channel system (the *heavy blue lines*, representing all channel links, and the *light blue lines*, representing the links used to extract simulated discharges at basin outlet and internal gauging stations) for the Cobres basin, showing the rain gauges (the *red circles*) and gauging stations (the *blue circles* at outlet, northern and central parts of the basin, are respectively Monte da Ponte, Albernoa and Entradas gauging stations). The *grid squares* have dimensions 2 × 2.0 km^2.

Daily FAO Penman-Monteith PET from Quinta da Saúde meteorological station (38°02′15″N, 07°53′06″W) at Beja is provided by the Agrometeorological System for the Management of Irrigation in the Alentejo/Irrigation Technology and Operative Center (SAGRA/COTR). Hourly PET is also available for Vale de Camelos station (37°48′43″N, 07°52′11″W) from SNIRH for the study period; however its annual PET is around 1000 mm, which seems to be too low for the region (semi-arid with hot summer); in fact values reported in the literature are always higher (see Bathurst *et al.* 1996 where values are higher by 200−300 mm and Ramos and Santos (2009) who reports value as high as Bathurst *et al.* 1996). Preliminary analysis has indicated that the lower annual PET might have resulted from the higher relative humidity and the lower wind velocity measurements. Since hourly distribution of PET during the day is mainly influenced by

solar radiation in the semi-arid southern Portugal region, hourly PET proportion during the day from Vale de Camelos station may not have been affected much, and it is assumed to be the same for stations under the same climate condition. Therefore, the daily PET from Beja is disaggregated into hourly intervals, according to the proportions of hourly PET at Vale de Camelos, to serve as input. A comprehensive geospatial dataset is available including topographic data with a scale of 1:25000 at 10 m intervals, digital maps of land-use type (Caetano *et al*. 2009) with a scale of 1:100000 and soil types (from Institute of Hydraulics, Rural Engineering and Environment, IHERA) with a scale of 1:25000. Here, model calibration and validation are carried out respectively from October 1st 2004 to September 30th 2006 and from October 1st 2006 to September 30th 2008. The calibration excludes the first 10 months considered as a warm-up period; the validation excludes the period from November 4th 2006 to November 8th 2006, due to the existence of missing data. SHETRAN is applied to the study basin with spatial resolution of 2.0 km grid and temporal resolution of 1.0 hour. However, we attempted the simulations of other resolutions, such as 0.5 and 1.0 km, just for the purposes explained on page 34 and Chapter 6.

To effectively reduce the number of calibration parameters, the key parameters are considered for calibration of only the two main types of land-use and the three main types of soil, while those for the other types of land-use and soil maintain their baseline values. AET is determined by PET, crop characteristics and soil water stress conditions (Allen *et al*. 1998). The AET/PET ratio is considered to be maximal at soil field capacity declining linearly with increasing soil suction. The AET/PET ratio at soil field capacity and Strickler overland flow resistance coefficient are to be calibrated for the main types of land-use. Anisotropy of soil physical properties is not considered, so vertical saturated conductivity is assumed to be the same as the lateral saturated conductivity. The soil water retention and hydraulic conductivity functions are defined by van Genuchten *et al*. (1991). The saturated hydraulic conductivity, saturated water content, residual water content, van Genuchten n and α parameters, and top soil depth are to be calibrated for the main types of soil for the runoff generation and transport processes. Consequently, twenty-two hydrological parameters are to be calibrated by MSCE or NSGA-II algorithm. As for the sediment erosion and transport processes, six parameters, derived from the raindrop impact erodibiliy and overland flow erodibility for the main types of soil, are to be calibrated by NSGA-II method.

As automatic calibration does not use physical reasoning, the parameter values are constrained within physically realistic ranges according to field measurements and

literature data to produce results that can be justified on physical grounds. The measured and estimated soil parameters are shown in Table 5.1 (page 29). The key hydrological parameters for automatic calibration of the SHETRAN model, with spatial resolution of 2.0 km grid and temporal resolution of 1.0 hour, are finalized in Table 5.2 (page 31), with specified ranges and baseline values based on literature (Cardoso 1965; Bathurst *et al*. 1996, 2002; Saxton and Rawls 2006), sensitivity analysis (Appendix 1) and personal communication with Dr. Birkinshaw at Newcastle University. According to Allen *et al*. (1998), the AET/PET ratio at field capacity is considered to be in the range of [0.5, 0.9] for crop and [0.6, 0.8] for agroforestry; it is set to 0.6 for crop and 0.7 for agroforestry in baseline simulation. Ramos and Santos (2009) found that the AET/PET ratio is around 0.7 at field capacity for olive orchard in southern Portugal, which confirmed our AET/PET ratio setting. Based on Engman (1986) and Bathurst *et al*. (1996, 2002), the Strickler overland flow resistance coefficient is set to be in the ranges of [2.5, 10] and [0.5, 5.0] $m^{1/3}/s$ respectively for crop and agroforestry; it is set to 5.0 and 2.0 $m^{1/3}/s$ respectively for crop and agroforestry in baseline simulation. Based on Chow (1959), the Strickler channel flow resistance coefficient is set to 30 $m^{1/3}/s$. In Appendix 1, sensitivity analysis is carried out on the key hydrological parameters in terms of model outputs such as total runoff and Nash-Sutcliffe Efficiency (NSE). It is shown that the results are most sensitive to top soil depth and van Genuchten α, sensitive to AET/PET ratio, Strickler overland flow resistance coefficient, saturated water content, van Genuchten n and residual water content, and not so much sensitive to saturated hydraulic conductivity. As for sediment parameters, the raindrop impact erodibiliy and overland flow erodibility are set to be in the respective ranges of [0.01, 10.0] J^{-1} and [0.01, 20.0] $mg/m^2/s$, for all the three main types of soil, based on previous studies of Bathurst (2011) and Birkinshaw *et al*. (2011). As described in Section 5.6.4, further set-up of sediment parameters are based on the calibrated hydrological parameters from MSCE optimization.

Table 5.1 Comparison of model performances from manual and MSCE calibrations at basin outlet (Monte da Ponte gauging station)

Soil type	Soil sample	Soil texture		K_s[a] (m/day)	θ_s[a] (m^3/m^3)	θ_r[a] (m^3/m^3)	n[a] (-)	α[a] (cm^{-1})	h[a] (m)
		Sand %	Clay %						
V_x	V_x-459[b]	17.3[b]	46.8[b]	0.110[b]	0.506[b]	0.065[c]	1.221[c]	0.0250[c]	0.50[b]
	V_x-460[b]	28.0[b]	38.5[b]	0.192[b]	0.517[b]	0.073[c]	1.403[c]	0.0055[c]	0.65[b]
P_x	P_x-455[b]	58.3[b]	20.6[b]	0.191[b]	0.418[b]	0.041[c]	1.345[c]	0.0225[c]	0.40[b]
	P_x-457[b]	40.8[b]	22.3[b]	0.425[b]	0.519[b]	0.053[c]	1.422[c]	0.0075[c]	0.35[b]
E_x	E_x-140[b]	50.2[b]	25.6[b]	0.233[d]	0.446[d]	0.120[d,e]	1.311[d,e]	0.0250[d,e]	0.10[b]
	E_x-144[b]	82.9[b]	6.1[b]	2.221[d]	0.457[d]	0.051[d,e]	1.557[d,e]	0.0690[d,e]	0.10[b]

Note: [a]K_s, θ_s, θ_r, n, α and h are respectively saturated hydraulic conductivity, saturated water content, residual water content, van Genuchten n, van Genuchten α and top soil depth; [b]Measured by Cardoso (1965); [c]Fitted parameters of the Mualem-van Genuchten model for soil water retention and hydraulic conductivity curves derived from field capacity and wilting point measured by Cardoso (1965); [d]Parameters evaluated from soil texture based on Saxton *et al*. 2006; [e]Fitted parameters of the Mualem-van Genuchten model for soil water retention and hydraulic conductivity curves derived from field capacity and wilting point evaluated from Saxton *et al*. 2006.

5.4 The Objective Function

The objective function of MSCE algorithm is the root mean square error (RMSE), equation 5.1, between observed and simulated hourly discharges at basin outlet, which must be minimized for calibration and validation of the SHETRAN model. Other functions such as LOG transformed Error (LOGE) (Bekele and Nicklow 2007), equation 5.2, Nash-Sutcliffe Efficiency (NSE) (Nash and Sutcliffe 1970), equation 5.3, coefficient of determination (PMCC) (Rodgers and Nicewander 1988), equation 5.4, and index of agreement (IOA) (Willmott 1981), equation 5.5, are also calculated to evaluate comprehensively the model performances. In addition, visual fitting of hydrographs is performed in manual calibration.

$$RMSE = \sqrt{\frac{\sum_{i=1}^{n}(O_i - S_i)^2}{n}} \qquad 5.1$$

$$LOGE = \sqrt{\frac{1}{n} \times \sum_{i=1}^{n}(Log(\frac{O_i}{S_i}))^2} \qquad 5.2$$

$$NSE = 1.0 - \frac{\sum_{i=1}^{n}(O_i - S_i)^2}{\sum_{i=1}^{n}(O_i - \overline{O})^2} \qquad 5.3$$

$$PMCC = \frac{\sum_{i=1}^{n}(O_i - \overline{O})(S_i - \overline{S})}{\sqrt{\sum_{i=1}^{n}(O_i - \overline{O})^2}\sqrt{\sum_{i=1}^{n}(S_i - \overline{S})^2}} \quad 5.4$$

$$IOA = 1.0 - \frac{\sum_{i=1}^{n}(O_i - S_i)^2}{\sum_{i=1}^{n}(\left|S_i - \overline{O}\right| + \left|O_i - \overline{O}\right|)^2} \quad 5.5$$

Where O_i and S_i are respectively observed and simulated watershed responses; n is the total number of data; $\overline{O}$ and $\overline{S}$ are respectively the mean values of observed and simulated watershed responses.

RMSE emphasizes fitting of the higher or peak discharges due to the square of errors greater than 1.0 and LOGE is designed to emphasize fitting of the lower discharges through the introduction of logarithms. Both of them range between 0 (perfect match) and +∞. NSE is a measure of goodness-of-fit and it ranges from −∞ to 1 (perfect fit). NSE is linearly related to $RMSE^2$ and the relation for the calibration of the study is indicated in equation 5.6.

$$(1 - NSE) = \frac{n \times RMSE^2}{\sum_{i=1}^{n}(O_i - \overline{O})^2} = 0.015934 \times RMSE^2 \quad 5.6$$

PMCC measures the variability of observed flow that is explained by the model. It ranges from −1 (fully negative correlation) to +1 (fully positive correlation). IOA makes cross-comparisons between models or model performances and it varies between 0 and 1 (perfect fit). As for NSGA-II algorithm, the objective functions for calibration of SHETRAN hydrological parameters are RMSE, LOGE and NSE. As NSE is commonly used in the evaluations of hydrological simulations, the inclusion of it would facilitate the comparison of the SHETRAN simulations from this study to previous studies. Because our optimization intends to minimize errors, the NSE is introduced to the objective of NSGA-II as “1-NSE”. The objective functions for calibration of SHETRAN sediment parameters are RMSE and LOGE, derived from comparisons between observed and simulated hourly sediment discharges.

Table 5.2 Description of SHETRAN key hydrological parameters, feasible ranges, baseline setting (in bracket) and values derived from manual and MSCE calibrations for different scenarios (I, II, III and IV) as explained in the Section 5.5.2

Parameters (unit)	Description	Range	Manual		MSCE			
			I	II	I	II	III	IV
K_1 ($m^{1/3}/s$)	Strickler overland flow resistance coefficient for crops	2.5–10.0 (5.0)	**10.0**[a]	**10.0**[a]	**10.0**[b]	**10.0**[b]	**10.0**[b]	**10.0**[b]
K_2 ($m^{1/3}/s$)	Strickler overland flow resistance coefficient for agroforestry	0.5–5.0 (2.0)	**5.0**[a]	**5.0**[a]	**5.0**[b]	**5.0**[b]	**3.7**[b]	**4.9**[b]
K_{s1} (m/day)	Saturated hydraulic conductivity of V_x soil	0.110–0.192 (0.160)	0.160	0.160	0.160	0.160	0.160	**0.168**[b]
θ_{s1} (m^3/m^3)	Saturated water content of V_x soil	0.506–0.517 (0.513)	0.513	0.513	0.513	0.513	0.513	**0.513**[b]
θ_{r1} (m^3/m^3)	Residual water content of V_x soil	0.065–0.073 (0.073)	0.073	0.073	0.073	0.073	0.073	**0.068**[b]
n_1 (-)	van Genuchten n of V_x soil	1.221–1.403 (1.324)	1.324	1.324	1.324	1.324	1.324	**1.221**[b]
α_1 (cm^{-1})	van Genuchten α of V_x soil	0.0055–0.0250 (0.0140)	0.0140	0.0140	0.0140	0.0140	0.0140	**0.0123**[b]
h_1 (m)	Top soil depth of V_x soil	0.30–0.65 (0.40)	0.40	0.40	0.40	0.40	0.40	**0.30**[b]
K_{s2} (m/day)	Saturated hydraulic conductivity of P_x soil	0.191–0.425 (0.200)	0.200	0.200	0.200	0.200	**0.353**[b]	**0.215**[b]
θ_{s2} (m^3/m^3)	Saturated water content of P_x soil	0.418–0.519 (0.418)	0.418	0.418	0.418	0.418	**0.418**[b]	**0.418**[b]
θ_{r2} (m^3/m^3)	Residual water content of P_x soil	0.041–0.053 (0.053)	0.053	0.053	0.053	0.053	**0.051**[b]	**0.052**[b]
n_2 (-)	van Genuchten n of P_x soil	1.345–1.422 (1.345)	1.345	1.345	1.345	1.345	**1.345**[b]	**1.345**[b]
α_2 (cm^{-1})	van Genuchten α of P_x soil	0.0075–0.0225 (0.0075)	0.0075	0.0075	0.0075	0.0075	**0.0080**[b]	**0.0080**[b]
h_2 (m)	Top soil depth of P_x soil	0.30–0.40 (0.30)	0.30	0.30	0.30	0.30	**0.31**[b]	**0.31**[b]
K_{s3} (m/day)	Saturated hydraulic conductivity of E_x soil	0.233–2.221 (1.227)	1.227	1.227	1.227	1.227	1.227	**0.679**[b]
θ_{s3} (m^3/m^3)	Saturated water content of E_x soil	0.446–0.457 (0.446)	0.446	0.446	0.446	0.446	0.446	**0.446**[b]
θ_{r3} (m^3/m^3)	Residual water content of E_x soil	0.051–0.120 (0.120)	0.120	0.120	0.120	0.120	0.120	**0.079**[b]
n_3 (-)	van Genuchten n of E_x soil	1.311–1.557 (1.311)	1.311	1.311	1.311	1.311	1.311	**1.311**[b]
α_3 (cm^{-1})	van Genuchten α of E_x soil	0.0250–0.0690 (0.0250)	0.0250	0.0250	0.0250	0.0250	0.0250	**0.0250**[b]
h_3 (m)	Top soil depth of E_x soil	0.05–0.10 (0.10)	0.10	0.10	0.10	0.10	0.10	**0.07**[b]
$AETPET_{FC1}$ (-)	The AET/PET ratio at field capacity for crop	0.50–0.90 (0.60)	0.60	**0.50**[a]	0.60	**0.50**[b]	**0.50**[b]	**0.50**[b]
$AETPET_{FC2}$ (-)	The AET/PET ratio at field capacity for agroforestry	0.60–0.80 (0.70)	0.70	**0.60**[a]	0.70	**0.60**[b]	**0.60**[b]	**0.60**[b]

Note: [a]The bold figures are derived from the respective manual calibration in the expected ranges, [b]The bold figures are derived from the respective MSCE calibration in the expected ranges; others are fixed baseline values indicated in parentheses.

We now describe the application of MSCE and NSGA-II optimization algorithms to the automatic calibration of SHETRAN in the period from October 1st 2004 to September 30th 2006.

5.5 Automatic Calibration of SHETRAN Model by MSCE

5.5.1 The MSCE Optimization Algorithm

The SCE-UA method, proposed by Duan *et al*. (1992), is an effective and efficient global optimization method in calibration of lumped and distributed models (Madsen 2000, 2003; Eckhardt and Arnold 2001; Blasone *et al*. 2007). It is based on the simplex downhill search scheme (Nelder and Mead 1965). Santos *et al*. (2003) introduced new evolution steps to improve its efficiency by making the simplex expand in a direction of more favourable conditions, or contract if a move is taken in a direction of less favourable conditions. The MSCE optimization algorithm was tested successfully for calibration of the physically-based erosion model WESP in a semi-arid watershed in Brazil (Santos *et al*., 2003).

MSCE is a population-based algorithm in the sense that offspring population is generated by several parent populations together. It starts with random generation of parent population of potential solutions. The parent population is then ranked from the best solution to the worst solution and divided into several complexes (Duan *et al*., 1992). Then complexes evolve independently according to the Modified Competitive Complex Evolution (MCCE) algorithm (Santos *et al*., 2003). For each MCCE step, a subcomplex is selected out of the complex and its worst solution is substituted by a better one generated by at most five evolution steps. The evolution steps used in original SCE-UA are based on Nelder and Mead (1965): reflection, contraction and mutation. Based on this, Santos *et al.* (2003) introduced a new evolution step expansion and extended old evolution step contraction to positive contraction and negative contraction to efficiently accelerate the optimization process. After, the new subcomplex is replaced into the complex, and the complex is arranged in order of increasing function values for the following MCCE step. The MCCE step is to be repeated until convergence criteria have been met. The complexes are then shuffled and separated to start the new MCCE step if the convergence criteria are not satisfied. In this study, the optimization is terminated if the model simulation has been tried 10 000 times, if the change of the best function value in 10 shuffling loops is less than 0.01% or if the normalized geometric mean of parameter ranges is less than 0.001.

The selection of algorithmic parameters is important, since otherwise it might lead to the premature termination of the automatic program or it might delay the converging of optimum parameter searching process (Madsen 2000; Santos *et al*. 2003). In this study, the number of complexes is set to 2, considering the long-time requirement for a single SHETRAN simulation (3 min). As suggested by Santos *et al*. (2003), the number of populations in each complex is set to be 2NOPT+1, in which NOPT is the number of optimization parameters, the number of populations in a subcomplex is set to be NOPT+1, and the number of evolution steps required before complexes are shuffled is set to be 2NOPT+1. The initial parameter values are selected randomly from the feasible hypercube search space.

5.5.2 MSCE Calibration of SHETRAN Hydrological Parameters

To compare the difference of results between manual and automatic calibrations, scenario I considers only calibration of Strickler overland flow resistance coefficient for the two main types of land-use (two parameters), scenario II considers calibration of Strickler overland flow resistance coefficient and the AET/PET ratio at field capacity for the two main types of land-use (four parameters). The differences among MSCE calibration schemes with different parameterizations are compared: scenarios I and II; scenario III, considers key parameters for two main types of land-use and P_x soil (ten parameters), and scenario IV (the previously proposed MSCE calibration of 22 parameters).

MSCE Calibration of SHETRAN Model (Scenario IV)

Scenario IV provides the best set of hydrological parameters (Table 5.2, page 31). The parameter values are well consistent with literature data. Bathurst *et al*. (1996) carried out a SHETRAN simulation of the Cobres basin for the period from 1977 to 1985; they characterized the basin land-use as crop (at least 90 % occupation) and the soil type as a thin, poor quality, red Mediterranean soil overlying schists (corresponding to the V_x soil of this study) with measured saturated hydraulic conductivity values between 0.03 and 0.4 m/day and depth of A and B horizons between 13 and 33 cm thick. Their calibration indicated that the soil depth is 0.4 m, saturated hydraulic conductivity is 0.05 m/day and Strickler overland flow resistance coefficient is 6 $m^{1/3}/s$. Here, we carried out hydrological simulation for the period from 2004 to 2008, and characterized the basin as two main types of land-use (crop and agroforestry) and three main types of soil (V_x, P_x and E_x soil). Scenario IV determined that soil depth is 0.30 m, saturated hydraulic conductivity is 0.168 m/day for V_x soil, which is in agreement with Bathurst *et al*. (1996).

Strickler overland flow resistance coefficient for crop is 10 $m^{1/3}/s$, which is larger than that derived by Bathurst *et al*. (1996) and at the highest limit of its physically realistic range. Experiment of scenario IV with spatial resolution of 1.0 km suggests a value of 7.0 $m^{1/3}/s$, which indicates that by using the larger spatial resolution the resulting value of Strickler overland flow resistance coefficient may become smaller than the highest limit of its physically realistic range. However, further studies are required to clarify this point.

The result of prescribed AET/PET ratio as a function of soil water potential can also be properly interpreted by physical reasoning. Scenario IV suggests values of 0.50 and 0.60 respectively for crop and agroforestry at field capacity. The AET/PET ratio was assigned to decline linearly with increasing soil suction. It is 0 at wilting point. Specifically, we assumed −3.3 m at field capacity, −150.0 m at wilting point; then, the AET/PET ratios for crop and agroforestry with soil water potential of −10.0 m are respectively 0.165 and 0.198. Taking the P_x soil as an example, the calibrated soil water retention curve, Fig 5.2 (page 35), indicates that soil water contents at field capacity, soil water potential of −10.0 m and wilting point are respectively 0.298, 0.228 and 0.122 m^3/m^3. The available water at field capacity and soil water potential of −10.0 m are respectively 0.176 and 0.106 m^3/m^3. To access the available water, plants need to exert 3.3 and 10.0 m soil suction respectively at field capacity and soil water potential of −10.0 m. Consequently, the AET/PET ratio at soil water potential of −10.0 m is 0.33 times at field capacity.

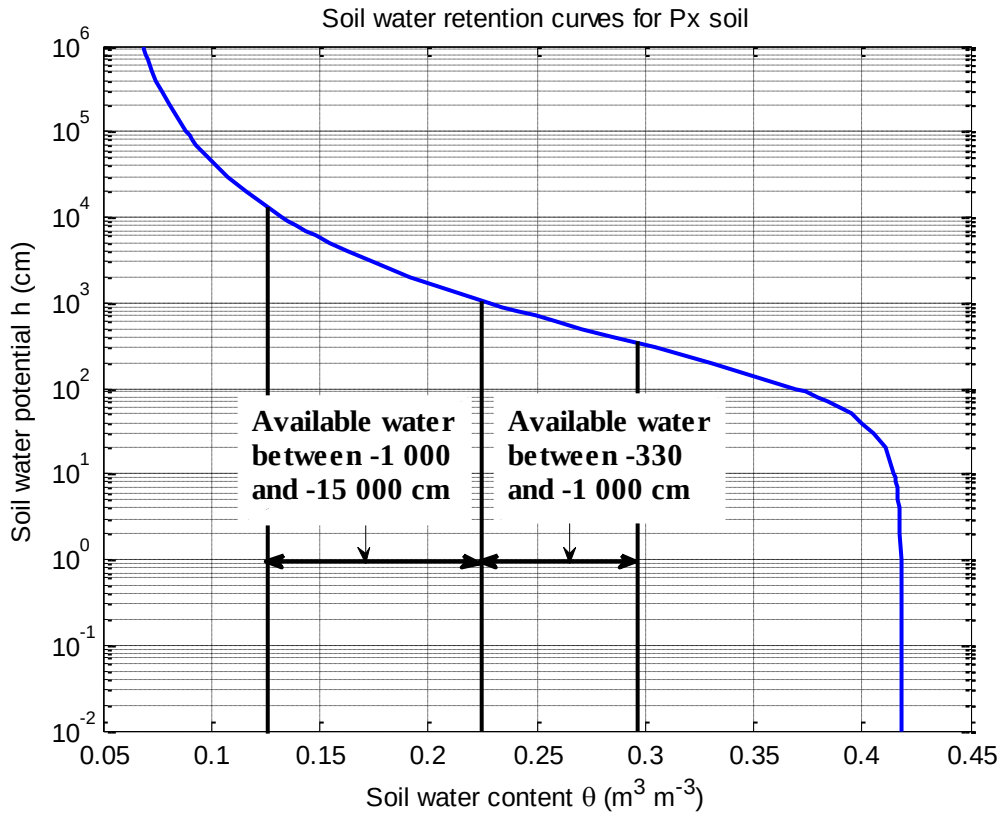

Fig. 5.2 Soil water retention curve for P_x soil in Cobres basin (result from MSCE calibration scenario IV).

Model performance under scenario IV is shown in Table 5.3 (page 36); annual mass balance analysis of it is shown in Table 5.4 (page 37) for basin outlet and internal gauging stations. For basin outlet, the NSE is 0.86 for calibration and 0.74 for validation; the NSE is respectively 0.65 and 0.82 for calibration, 0.69 and 0.63 for validation, respectively for internal gauging stations Albernoa and Entradas. The simulation underestimated annual runoff at basin outlet, around 11 % (year 2007) to 35 % (year 2006). The graphical comparison between observed and simulated discharges at basin outlet, displayed in Figs 5.3a−b (page 38) for the main runoff periods, during the calibration and validation phases, indicates that the model could not catch well the peak discharge for most of the storm events.

To find out the reason for this mismatch, we plotted the monthly water balance components for the simulation in Fig 5.4 (page 39). It is shown that, during the entire period, (1) rainfall mainly concentrates in the period from October to May of the following year; (2) runoff mainly appeared in 4 months, namely November 2005, October 2006, November 2006 and December 2006. It is clear that the two main runoff generation periods are respectively preceded by 12 and 6 months' drought. Therefore, the runoff underestimation may also be explained by the reduced soil infiltration

resulting from the occurrence of surface sealing and crust formation, physical processes that are not embodied in SHETRAN model, due to the existence of forcing factors such as dry initial soil moisture content, gentle basin slope, P_x and E_x soils (loam and sandy loam) and moderate rainfall intensity. Studies conducted in this region (Silva 2006; Pires *et al*., 2007) have shown that Mediterranean soils are characterized by having crust formation problems and low infiltration capacity. Soil sealing and crusting are recognized as common processes in cultivated soils of semi-arid and arid regions. Since the study basin is mainly occupied by crops, the crusting formation problems might have been very important in this region. However, the crust formation problem is not considered in this study due to the lack of information for quantifying how much infiltration would be reduced by soil crust considering the nature of the rain, the soil's physical and chemical properties of the Cobres basin during the study period. Experiments show that the overall model performance would not be improved by arbitrarily reducing saturated hydraulic conductivity for the whole simulation period.

Table 5.3 Comparison of model performances from manual and MSCE calibrations at basin outlet (Monte da Ponte gauging station)

Cobres simulation	Indicator	Manual		MSCE			
		Scenario I	Scenario II	Scenario I	Scenario II	Scenario III	Scenario IV
Calibration	RMSE (m^3/s)	**3.48**[a]	**2.98**[a]	**3.48**[b]	**2.98**[b]	**3.13**[b]	**3.00**[b]
	LOGE (-)	2.17	2.07	2.17	2.07	2.03	2.07
	NSE (-)	0.81	0.86	0.81	0.86	0.84	0.86
	PMCC (-)	0.93	0.94	0.93	0.94	0.93	0.94
	IOA (-)	0.93	0.95	0.93	0.95	0.95	0.95
Validation	RMSE (m^3/s)	**6.15**[a]	**5.60**[a]	**6.15**[b]	**5.60**[b]	**5.71**[b]	**4.96**[b]
	LOGE (-)	2.71	2.69	2.71	2.69	2.67	2.70
	NSE (-)	0.60	0.67	0.60	0.67	0.65	0.74
	PMCC (-)	0.89	0.90	0.89	0.90	0.89	0.91
	IOA (-)	0.80	0.85	0.80	0.85	0.84	0.90

Note:
[a]The bold figures are objective values from the respective manual calibration.
[b]The bold figures are objective values from the respective MSCE calibration.

Table 5.4 Statistics for the MSCE calibration scenario IV at Cobres basin

Simulation	Year[a]	Rainfall (mm)[b]	PET (mm)[c]	AET (mm)	ΔS (mm)[d]	Monte da Ponte (Basin outlet)			Albernoa (Internal gauging station)			Entradas (Internal gauging station)		
						R_{obs}	R_{sim}	NSE	R_{obs}	R_{sim}	NSE	R_{obs}	R_{sim}	NSE
Calibration	2004-05[e]	1.8 (194.2)	358.2 (1475.7)	31.9 (256.7)	-30.1 (-64.5)	0.0 (11.6)	0.0 (1.9)	-	0.0 (0.1)	0.0 (1.1)	-	0.0 (0.0)	0.0 (1.4)	-
	2005-06	502.5	1345.8	386.3	69.5	55.1	46.6	-	50.5	36.3	-	44.8[g]	31.8[g]	-
	2004-06[e]	504.3	1704.0	418.2	39.4	55.1	46.6	0.86	50.5	36.3	0.65	44.8[g]	31.8[g]	0.82[g]
Validation	2006-07[f]	447.2 (532.2)	1267.6 (1272.9)	373.2 (378.3)	6.0 (18.2)	104.5 (-)	68.0 (135.5)	-	79.6 (-)	71.6 (138.4)	-	130.1 (-)	104.0 (195.1)	-
	2007-08	421.4	1274.1	383.4	14.4	25.6	22.9	-	12.5	22.8	-	5.3	12.3	-
	2006-08[f]	868.7	2541.7	756.6	20.4	130.1	90.9	0.74	92.1	94.4	0.69	135.4	116.3	0.63

Note:

[a]Years are defined from October to September.

[b]Basin mean rainfall based on six rain gauges indicated in Fig. 5.1 (page 26) (SNIRH).

[c]FAO Penman-Monteith PET from the meteorological station at Beja, provided by SAGRA/COTR.

[d]Change of Subsurface water storage calculated by SHETRAN model.

[e]Only August and September in 2005 are considered for calibration, and annual statistics of the year are presented in parenthesis.

[f]Data missing period, from November 4th 2006 23:00 to November 8th 2006 16:00, is not included, and annual statistics of the year are presented in parenthesis.

[g]Data missing, from November 19th 2005 09:00 to November 25th 2005 09:00, is not included.

(a)

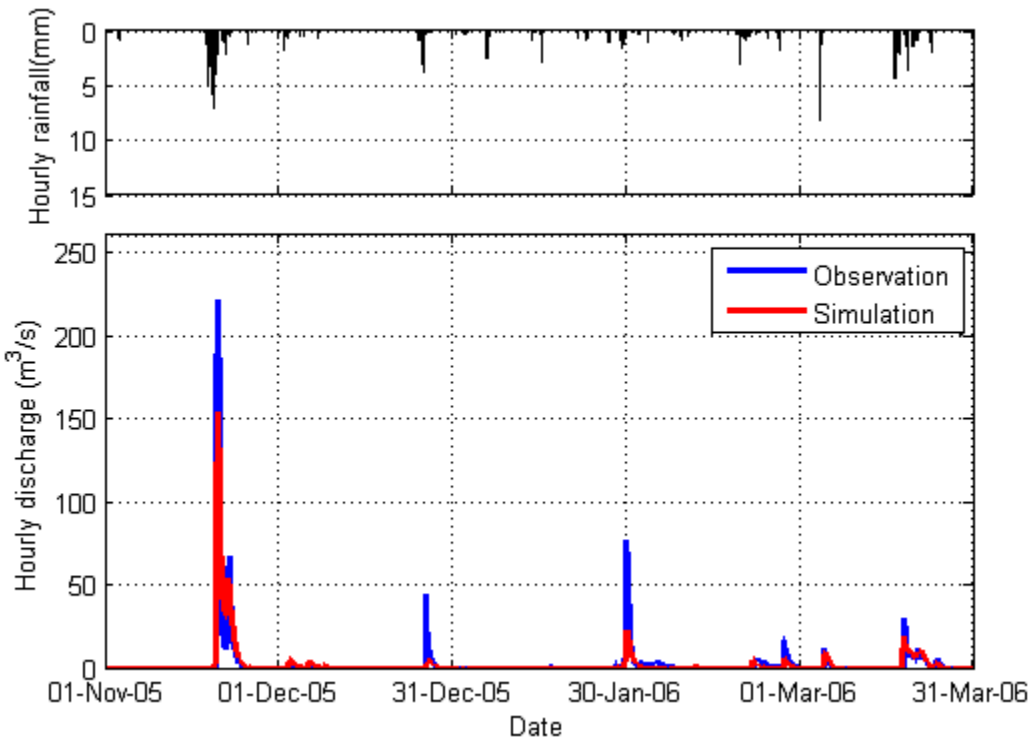

(b)

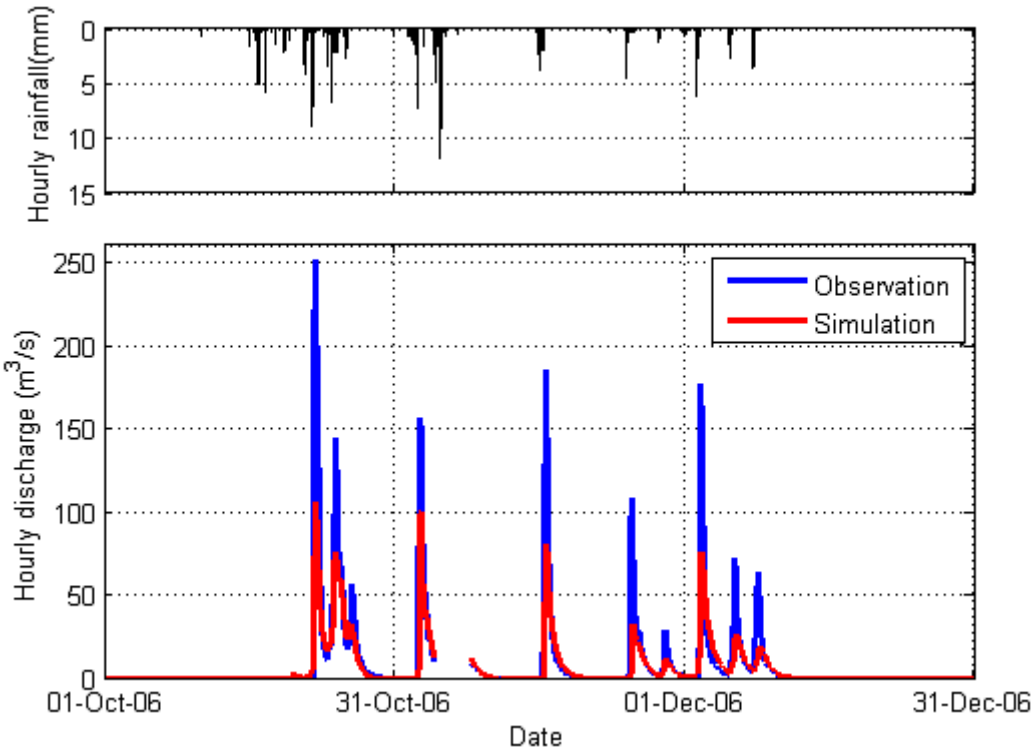

Fig. 5.3 Comparison of observed and simulated discharges from MSCE calibration scenario IV for the Cobres basin with spatial resolution of 2.0 km grid and temporal resolution of 1.0 hour, for main periods of (a) calibration and (b) validation processes.

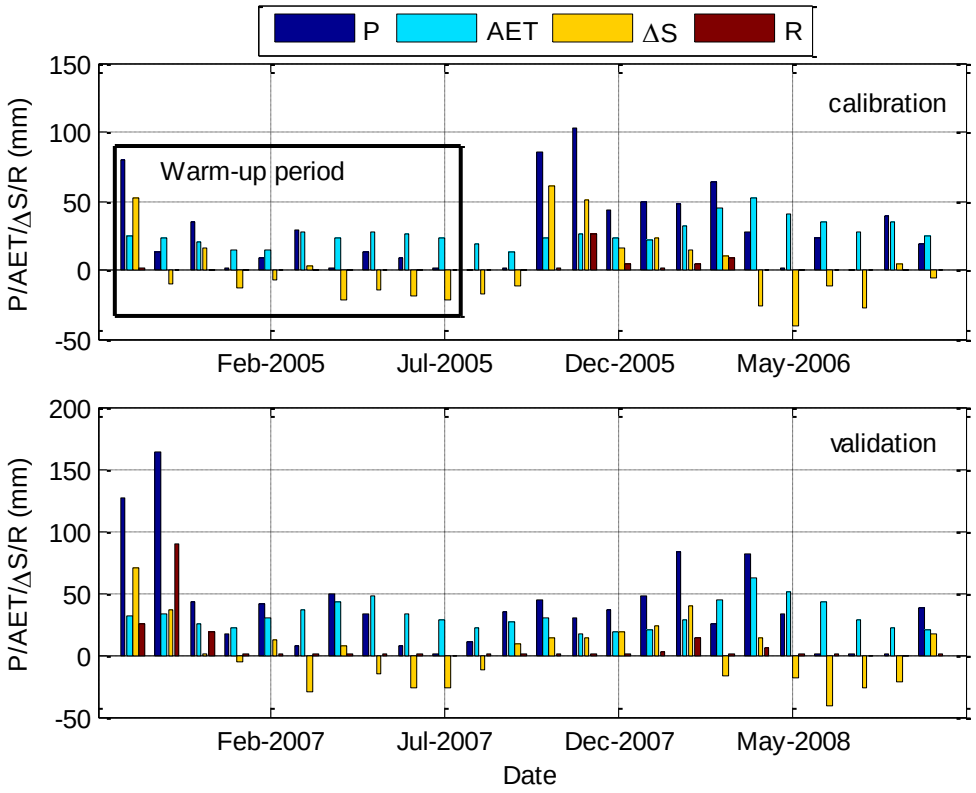

Fig. 5.4 Water balance analysis of MSCE calibration scenario IV for calibration and validation periods; P –precipitation, AET – actual evapotranspiration, ΔS – change of subsurface water storage, R – total runoff.

Figs 5.5a−d (page 40) are made to get a clear impression of SHETRAN's ability to reproduce the storm events No.1 and No.4 preceded by long periods of drought. Storms No.1 and No.4 are the largest storm events respectively during the calibration and validation periods. Figs 5.5a−b are respective comparisons of observed and simulated hydrographs for storms No.1 and No.4 at basin outlet; Figs 5.5c−d are comparisons of observed and simulated hydrographs for storm No.4 respectively at internal gauging stations Albernoa and Entradas. The NSE is 0.87 and 0.64 respectively for Storms No.1 and No.4 at basin outlet; it is 0.69 and 0.65 for Storms No.4 respectively at Albernoa and Entradas. It is shown that, for both storm events, SHETRAN model reproduced well the qualitative evolutions of the hydrographs at basin outlet, as well as at two internal gauging stations; however, it greatly underestimated the peak discharges and the simulated hydrographs are much less flashy than the observed ones.

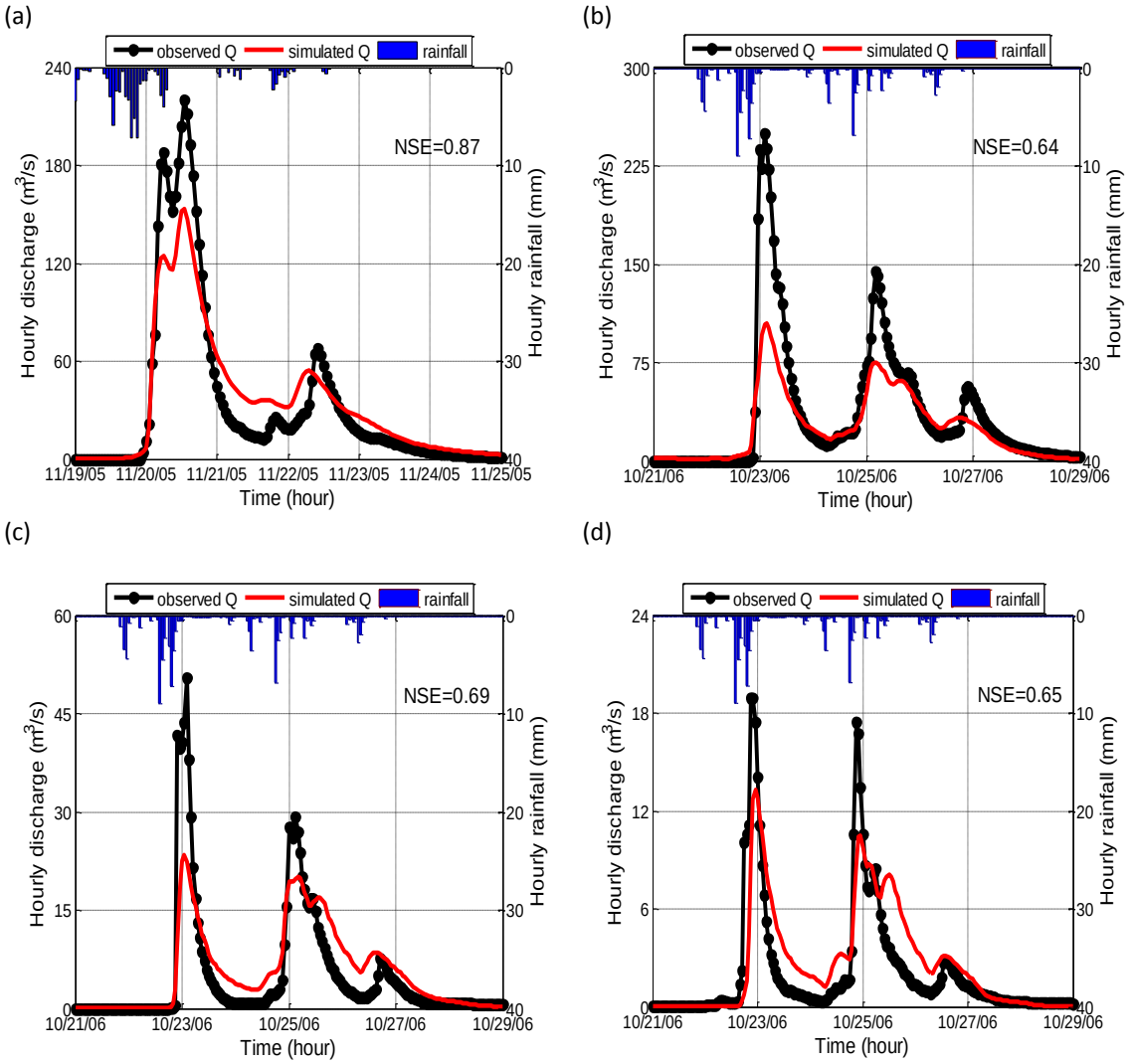

Fig. 5.5 Comparison of observed and simulated discharges from MSCE calibration scenario IV for the Cobres basin with spatial resolution of 2.0 km grid and temporal resolution of 1.0 hour: (a) Storm No.1 at basin outlet; (b) Storm No.4 at basin outlet; (c) Storm No.4 at internal gauging station Albernoa; (d) Storm No.4 at internal gauging station Entradas.

Comparison of Manual and MSCE Calibrations

To compare manual calibration with MSCE calibration, scenario I considers the most frequently used calibration parameters—Strickler overland flow resistance coefficients; based on scenario I, scenario II also considers the water balance controlling parameters—the AET/PET ratios at field capacity. As shown in Tables 5.2 and 5.3 (pages 31 and 36), manual calibration can achieve the same parameter setting and model performance as MSCE calibration for scenarios I and II. The success of manual calibration may be attributed to: (1) the rigorous and deliberate parameterization; (2) the narrow ranges of parameters set in this study; (3) the small number of calibration parameters involved. For these two scenarios, the MSCE calibrations do not distinctly

surpass manual calibrations in terms of model performances. It is shown that scenario IV considers 22 parameters obtaining satisfactory results in terms of calibration parameters and model performance. For scenario IV, we did not consider to carry out manual calibration due to its complexity and limitations. In summary, the advantages of MSCE calibration stem from it being capable of taking a large number of parameters into consideration, being objective, and excluding modeller's subjective interference, releasing them from monotonous laborious work.

Comparison of MSCE Calibrations

Scenarios I, II, III and IV involve respectively 2, 4, 10 and 22 calibration parameters; it is shown in Table 5.2 (page 31) that for the majority of calibration parameters, we get similar or even equal values, for all considered scenarios. This circumstance requires further investigation, which is beyond the scope of this work. Table 5.3 (page 36) displays that NSE is 0.81 and 0.60 respectively for calibration and validation of scenario I; NSE is around 0.85 and 0.65 respectively for calibration and validation of scenarios II and III; NSE is 0.86 and 0.74 respectively for calibration and validation of scenario IV. Model performance of scenario IV is better than for all the other three scenarios. By increasing number of considered key parameters, MSCE calibration does not always improve, unless all the key parameters are considered.

Conclusions

The MSCE optimization algorithm, introduced by Santos *et al*. (2003) based on the SCE-UA developed by Duan *et al*. (1992), is successfully applied to calibrate the SHETRAN model in the semi-arid Cobres basin with spatial resolution of 2.0 km and temporal resolution of 1 h. Twenty-two parameters are calibrated based on the two main types of land-use and the three main types of soil, and no initial parameter setting is selected. The calibrated parameters are within measured ranges of Cardoso (1965), well consistent with previous work of Bathurst *et al*. (1996) and well explained by physical reasoning. The results are very satisfactory. NSE is 0.86 for calibration and 0.74 for validation for basin outlet; it is respectively 0.65 and 0.82 for calibration, and 0.69 and 0.63 for validation of internal gauging stations Albernoa and Entradas; as for storm events, NSE is 0.87 and 0.64 respectively for Storms No.1 (during the calibration period) and No.4 (during the validation period) at basin outlet; it is 0.69 and 0.65 for Storm No.4 respectively at Albernoa and Entradas. As a confirmation to the study of Santos *et al*. (2003), the MSCE optimization algorithm is able to converge to the global optimal values.

For SHETRAN model, manual calibration can be successful if the rigorous and appropriate parameterization has been carried out and a few parameters are involved. MSCE is recommended due to the following advantages: being capable of taking a large number of parameters into consideration, being objective and excluding modellers' subjective interference and releasing them to other more important activities. To get the best model performance, all key parameters should be considered in MSCE calibration. Future studies should include other automatic calibration techniques, such as simulated annealing (Santos *et al*., 2012) and consider the influence of catchment discretization (Santos *et al*., 2011) especially when applying GIS and remote sensing techniques (Silva *et al*., 2012).

The study of Section 5.5 has been published as Zhang *et al*. (2013).

5.6 Multi-Objective Calibration of SHETRAN Model by NSGA-II

5.6.1 The NSGA-II Optimization Algorithm

The NSGA-II is an elitist MOEA developed by Deb *et al*. (2002) and has been successfully applied to multi-objective automatic calibration of semi physically based model SWAT (Bekele and Nicklow, 2007) and PBSD model WetSpa (Shafii and Smedt, 2009). The optimization is mainly based on a fast non-dominated sorting approach and an elitist evolution strategy. The non-dominated sorting approach is based on the concept of Pareto dominance and optimality. Solutions that are not dominated by other ones are put in the first front and assigned rank 1; then, solutions that are not dominated by other ones except those in the first front are put in the second front and assigned rank 2. In this way, all solutions are assigned to a specific front and rank number. Solutions with smaller rank numbers are preferable; and for those with the same rank number, NSGA-II uses crowding-distance to discriminate them and sets higher priority to those with larger values. The crowding-distance of a solution is defined as the sum of the absolute normalized differences in the objective function values of its two adjacent solutions; in particular, the solution with any objective function of smallest or largest values is assigned an infinite crowding-distance value.

The optimization starts with a parent population of size N (an even number), generated randomly by Latin hypercube sampling (LHS) technique, in the feasible parameter space and then followed by the listed steps: (1) performing non-dominated sorting and crowding-distance calculation to get the fitness values (rank number and crowding-distance) for each solution of the population; (2) extracting the first N

preferable solutions as the new parent population if the population is of size 2N, otherwise skipping this step. (3) using binary tournament selection to form a mating pool of size N/2 from the parent population; (4) using SBX (Deb and Agrawal, 1995) and PM (Deb 2001) operators to create an offspring population of size N from the mating pool; (5) combining parent and offspring populations to create a population of size 2N; (6) repeating steps 1 to 6 until the convergence criteria are satisfied.

According to Deb and Agrawal (1995), Deb (2001) and Deb *et al*. (2007), the crossover distribution index η_c influences the proximities between parent solutions and the resulting offspring solutions. A selection of η_c with large value may result in offspring solutions close to the parent solutions; contrarily, a selection of η_c with small value may give solutions far away from parents. Therefore, the spread of offspring solutions may be adjusted by the use of η_c with different magnitudes. According to Deb and Goyal (1996), the mutation distribution index η_m has a similar effect in directly controlling the spread of offspring solutions. As the automatic calibration of SHETRAN model is a non-linear problem involving high dimensionality, the evolution of optimization with larger spread of offspring solutions may lead to a quicker and thorough search through the full feasible parameter space. Consequently the use of smaller values of η_c and η_m may be preferable.

In this study, the NSGA-II parameters are selected based on literature and available computing resources. The matlab codes from Seshadri (2009) and Lin (2011) are adapted for this study and the “parfor” function is used to simultaneously perform 4 SHETRAN simulations. Considering the computational requirement, the population size is set to 50 and a maximum of 30 generations (also considered as a convergence criterion, around 16 hours required) is prescribed for each trial run; a total of 30 trial runs are performed (nearly 20 days required with the use of the available computer having Intel(R) Core(TM) i7-960 Processor 3.2 GHz) for each optimization to eliminate the random seed effects (Reed *et al*., 2013). The probabilities of crossover and mutation are set respectively as 0.9 and 0.1. The (η_c, η_m) is set as (0.5, 0.5), (2.0, 0.5) or (20.0, 20.0). The sets of η_c with values of 20.0 and 2.0 are respectively based on previous studies. Bekele and Nicklow (2007) applied NSGA-II for SWAT calibration with (η_c, η_m) of (20.0, 20.0) and Zhang *et al*. (2010) used (15, 20). Deb and Agrawal (1995) suggested η_c with values between 2.0 to 5.0 for real parameter optimization problems. Since η_c can be any positive value (Deb and Agrawal 1995), a value of 0.5 is further proposed. As for η_m, a value of 0.5 is proposed to create offspring solutions with larger spread.

5.6.2 Performance Metrics of NSGA-II Algorithm

Four performance metrics, namely hypervolume, additive Ɛ–indicator, generational distance and Opt-indicator, are used to compare the NSGA-II algorithm with different sets of (η_c, η_m). The first three metrics are based on Reed *et al*. (2013) and the last one is introduced in this study. The calculation of the metrics requires a reference Pareto set or the best known approximation to the Pareto optimal set. As the reference Pareto set is unknown in the study, the best known approximation set was generated by collecting all of the non-dominated solutions generated from the 90 trial runs (Tang *et al*., 2006). In addition, as the objective functions, namely RMSE, LOGE and 1-NSE, have different units and magnitudes, they were normalized for the calculation of performance metrics.

Hypervolume

Hypervolume measures the volume of objective space dominated by an approximation set. The hypervolume indicator is calculated as the ratio of hypervolume for the approximation set to that for the best known approximation set. It ranges from 0 to 1 (perfect) with larger value representing better performance.

Additive Ɛ-indicator

Additive Ɛ-indicator measures the worst case distance required to translate the approximation set solution to dominate its nearest neighbor in the best known approximation set. The distance of two solutions is defined as the maximum difference between objective values. To calculate Ɛ-indicator, distances between solutions in the best known approximation set and their closest solutions in the approximation set are calculated, and the maximum distance is considered as the additive Ɛ-indicator. It ranges from 0 (perfect) to +∞ with smaller values representing better performances.

Generational distance

Generational distance is defined by the average Euclidean distance of points in an approximation set to their nearest corresponding points in the best known approximation set. It ranges from 0 (perfect) to +∞ with smaller values representing better performances.

Opt-indicator

Similar to the additive Ɛ-indicator, the Opt-indicator measures the best case distance

required to translate the approximation set solution to dominate its nearest neighbor in the best known approximation set. It aims to distinguish the quality difference of the best optimized solutions for different optimization algorithms; and all solutions in the best known approximation set are considered as the best solutions. It ranges from 0 (perfect) to +∞ with smaller values representing better performances.

5.6.3 NSGA-II Calibration of SHETRAN Hydrological Parameters

There are 30 approximation sets for each generation of the optimization along the evolution process. So, the comparisons of the optimizations by the NSGA-II algorithm with (η_c, η_m) of (0.5, 0.5), (2.0, 0.5) and (20., 20.) were carried out in the following three aspects: (1) Comparison of the 30 approximation sets obtained from the last generation of each optimization; (2) Comparison of the means of performance metrics obtained from the 30 approximation sets of each optimization for all the generations; (3) Comparison of the 50^{th} and 95^{th} percentiles of performance metrics obtained from the 30 approximation sets of each optimization for all the generations. Moreover, the best known approximation sets derived from all the three optimizations were applied to the validation of SHETRAN simulations.

Comparison of the NSGA-II algorithm with (η_c, η_m) of (0.5, 0.5), (2.0, 0.5) and (20., 20.)

Figs 5.6a–d (page 46) show the ensemble of approximation sets obtained from the last (or 30^{th}) generation of the 90 trial runs of NSGA-II algorithm for SHETRAN calibration. The optimizations by the NSGA-II algorithm with (η_c, η_m) of (0.5, 0.5), (2.0, 0.5) and (20., 20.) are respectively shown in red, blue and light blue asterisks. Fig 5.6a is the 3-D, namely RMSE, LOGE and (1-NSE), display of the results and Figs 5.6b, c and d are projections respectively in the 2-Ds spaces of RMSE.vs.LOGE, (1-NSE).vs.LOGE and RMSE.vs.(1-NSE). It is clear from Figs 5.6a–d that (1) the results of the NSGA-II algorithm with (η_c, η_m) of (0.5, 0.5) are mostly better than that of (2.0, 0.5) and both of them are mostly better than that of (20., 20.), the three optimizations being clustered in distinct different objective spaces; (2) As pointed out previously, the “three-objective calibration” of SHETRAN model in this section is actually a “two-objective calibration”, because the (1-NSE) is linearly related with the squared RMSE with no intercept. Therefore, in the remaining of this section, comparisons of optimizations are based only on 2-D displays of objectives, e.g. RMSE.vs.LOGE.

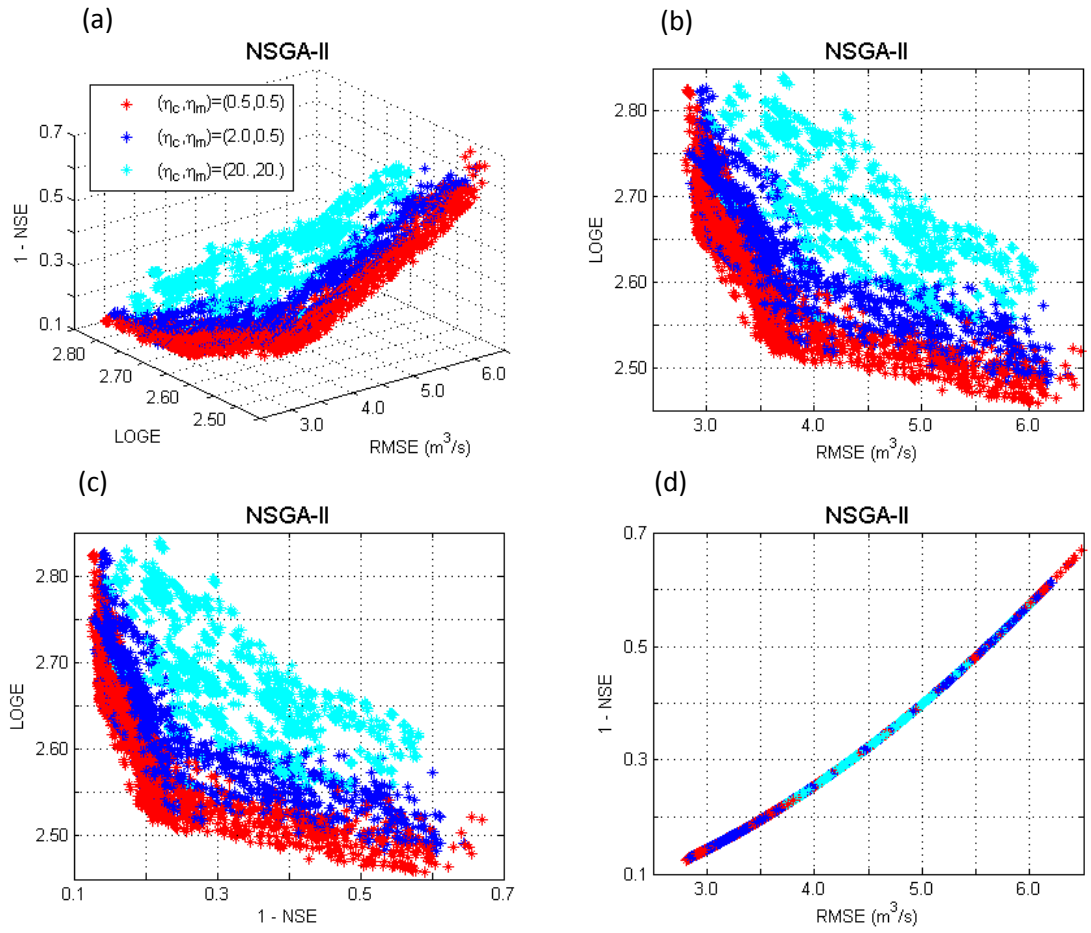

Fig. 5.6 (a) The ensemble of approximation sets obtained from the last generation of the 90 trial runs of NSGA-II algorithm for SHETRAN calibration where RMSE, LOGE and NSE are respectively root mean square errors, log-transformed errors and Nash-Sutcliffe Efficiency. The asterisks in red, blue and light blue colors respectively represent (η_c, η_m) with values (0.5, 0.5), (2.0, 0.5) and (20., 20.). Two-dimensional presentations of figure (a) are shown in (b), (c) and (d).

Figs 5.7a–b (page 47) display the best known approximation set derived from all the 90 trial runs, as well as the origins of these solutions. In Fig 5.7a, the best known approximation sets derived from the NSGA-II algorithm with (η_c, η_m) of (0.5, 0.5), (2.0, 0.5) and (20., 20.) are respectively shown in small black squares and circles filled in blue and purplish red colors; and the final one derived from all optimizations is shown in filled red circles. In Fig 5.7b, it is clear that most solutions of the final best known approximation set come from the optimization with (η_c, η_m) of (0.5, 0.5), shown in filled red circles, a few of them come from that of (2.0, 0.5), displayed in filled blue circles, and none of them come from that of (20., 20.). This is consistent with the conclusion, derived from Figs 5.6a–d, that the optimization by NSGA-II with (η_c, η_m) of (0.5, 0.5) produce better final results than that of (2.0, 0.5) and both of them produce better final results than that of (20., 20.). Fig 5.7b, on the other hand, also displays a typical false front in small black squares. As one may see in Figs 5.6a–d, the false fronts exist for

all the three optimizations, which have prevented them from reaching the best known front. This phenomenon has been recognized by Tang *et al*. (2006) for multi-objective calibration of the Leaf River SAC-SMA test by using the Ɛ-NSGA-II, SPEA2 and MOSCEM-UA algorithms; this study displays the variability of the three optimizations' performances of NSGA-II algorithm in Figs 5.8a–l (page 48) and Figs 5.9a–d (page 49).

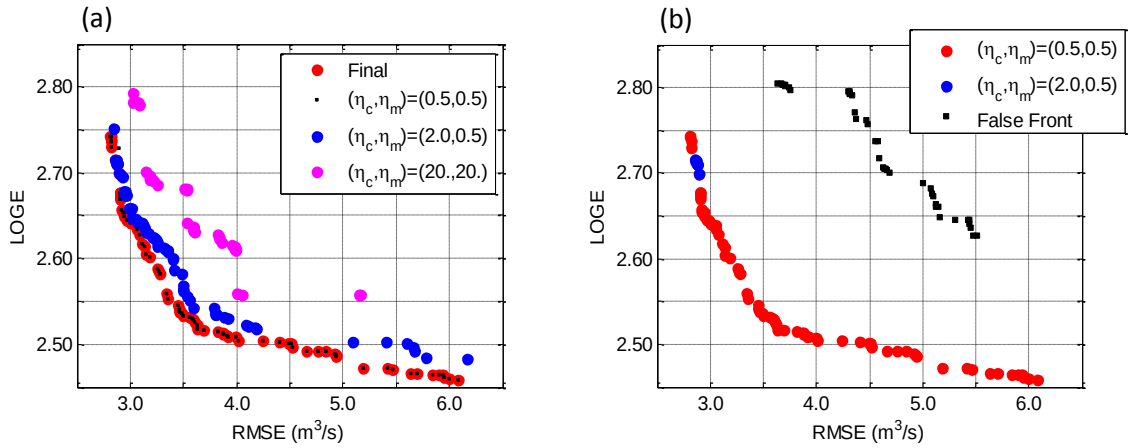

Fig. 5.7 (a) The best known approximation sets derived from 30 trial runs of NSGA-II algorithm with (η_c, η_m) of (0.5, 0.5), (2.0, 0.5) and (20., 20.) are respectively shown in small black squares, filled blue circles and filled purplish red circles. The final one derived from all trial runs is shown in filled red circles. (b) The final best known approximation set is made up of solutions from trial runs of NSGA-II algorithm with (η_c, η_m) of (0.5, 0.5) and (2.0, 0.5), respectively showing in filled red and blue circles. The false front, in small black squares, is an example of the approximation set derived from a trapped trial run of the NSGA-II algorithm.

Figs 5.8a–l (page 48) have shown the means and standard deviations of performance metrics of NSGA-II with (η_c, η_m) of (0.5, 0.5), (2.0, 0.5) and (20., 20.) respectively in the left, middle and right columns of plots; the means, standard deviations and variabilities in performance are respectively shown in solid line, dash line and shaded area. From the comparison of mean performances, it is clear that, for all the evolution processes, the optimization by NSGA-II with (η_c, η_m) of (0.5, 0.5) produce better results than that of (2.0, 0.5) and both of them lead to better final results than that of (20., 20.). To display the significance of differences, for performances obtained by optimizations, the Wilcoxon rank sum test was applied and the results show that performance metric scores for all the three optimizations, are all significantly different from each other at the 95% confidence level. From the comparison of the shaded areas, it is also shown that there is large variability in performance, during all the 30 generations' evolution processes, for all the three optimizations; and the variability for NSGA-II with (η_c, η_m) of (20., 20.) is always larger than the other two optimizations.

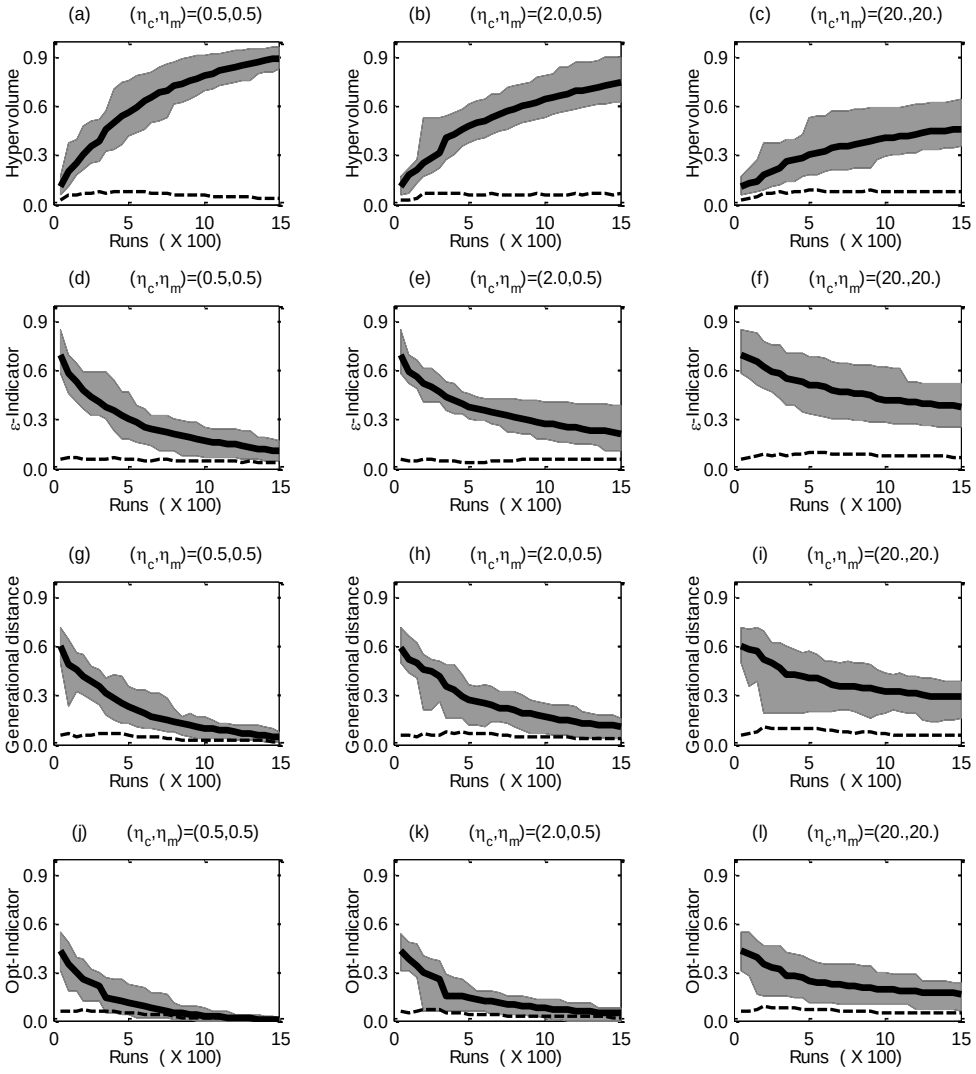

Fig. 5.8 Plots of dynamic performance results of NSGA-II algorithm, namely hypervolume (a, b and c), Ɛ-indicator (d, e and f), generational distance (g, h and i) and opt-indicator (j, k and l), versus total number of SHETRAN model runs. Mean performance is indicated by a solid line, the standard deviation by a dashed line, and the range of performance by the shaded region. The left, middle and right columns of plots were respectively generated from 30 trial runs of NSGA-II with (η_c, η_m) of (0.5, 0.5), (2.0, 0.5) and (20., 20.).

Figs5.9a–d (page 49) have shown the 50th and 95th percentiles of performance metrics of NSGA-II with (η_c, η_m) of (0.5, 0.5), (2.0, 0.5) and (20., 20.) respectively in red, blue and light blue colours; the 50th and 95th percentiles of performances are respectively shown in dashed and bold solid lines and Figs 5.9a–d compare performances respectively for hypervolume, Ɛ-indicator, generational distance and Opt-indicator. In agreement with results shown in Figs 5.6a–d (page 46) and Figs 5.8a–l, for both 50th and 95th percentiles of all four performance metrics and for nearly all the evolution processes, the optimization by NSGA-II with (η_c, η_m) of (0.5, 0.5) produces better

results than that of (2.0, 0.5) and both of them lead to better final results than that of (20., 20.). This supports our proposal of using NSGA-II algorithm with (η_c, η_m) of (0.5, 0.5) for multi-objective automatic calibration of SHETRAN model for Cobres basin.

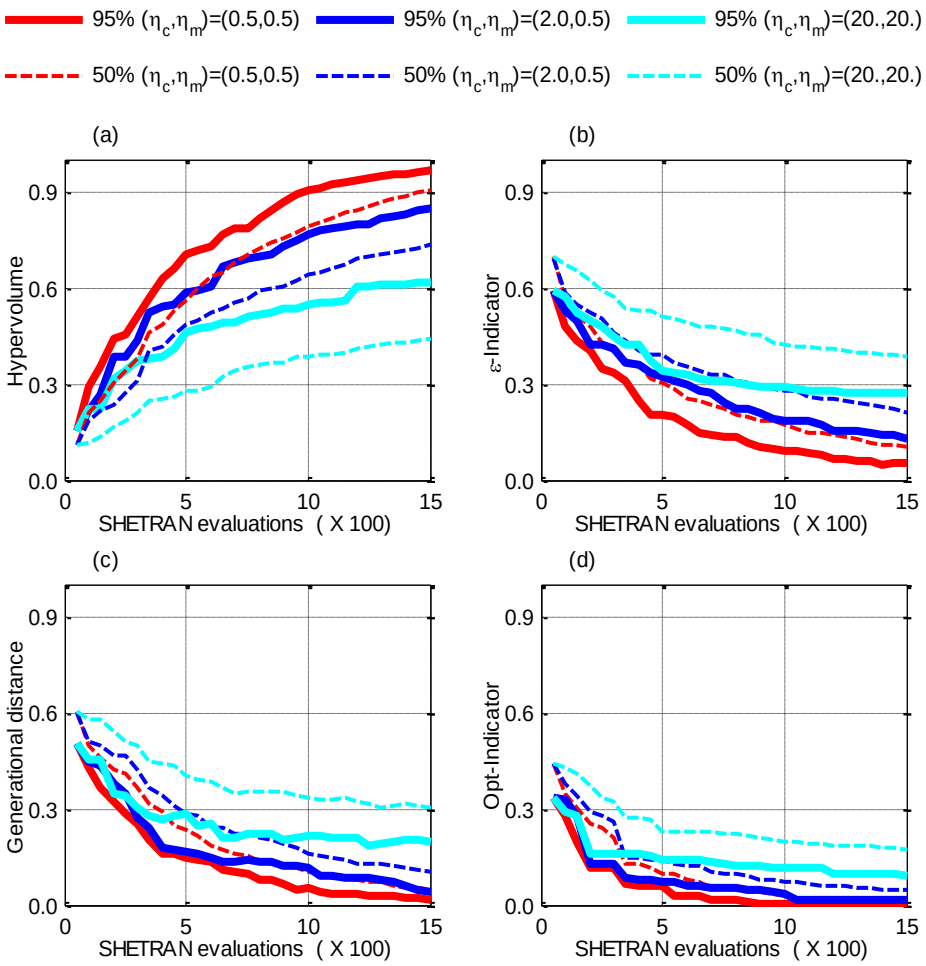

Fig. 5.9 Plots of dynamic performance results of NSGA-II algorithm, namely hypervolume (a), Ɛ-indicator (b), generational distance (c) and opt-indicator (d), versus total number of SHETRAN evaluations. The 50th and 95th percentiles of performance are respectively indicated in dash and bold solid lines. The red, blue and light blue lines were respectively generated from 30 trial runs of NSGA-II with (η_c, η_m) of (0.5, 0.5), (2.0, 0.5) and (20., 20.).

Validation of the best known approximation sets from the three optimizations

SHETRAN validation has been carried out for all the solutions of the best known approximation sets derived from NSGA-II with (η_c, η_m) of (0.5, 0.5), (2.0, 0.5) and (20., 20.). To make this a strong validation, results from the internal gauging stations Albernoa and Entradas have also been evaluated. Figs 5.10a–l (page 50) display SHETRAN model performance indicators, namely RMSE, LOGE and NSE, at basin outlet Monte da Ponte and internal gauging stations Albernoa and Entradas respectively in the left, middle and right columns of plots; results for the calibration

period are shown in the first two rows of plots and those for the validation period are shown in the last two rows of plots; the filled red triangles, blue squares and black circles respectively represent the solutions of the best known approximation sets derived from optimizations by NSGA-II with (η_c, η_m) of (0.5, 0.5), (2.0, 0.5) and (20., 20.).

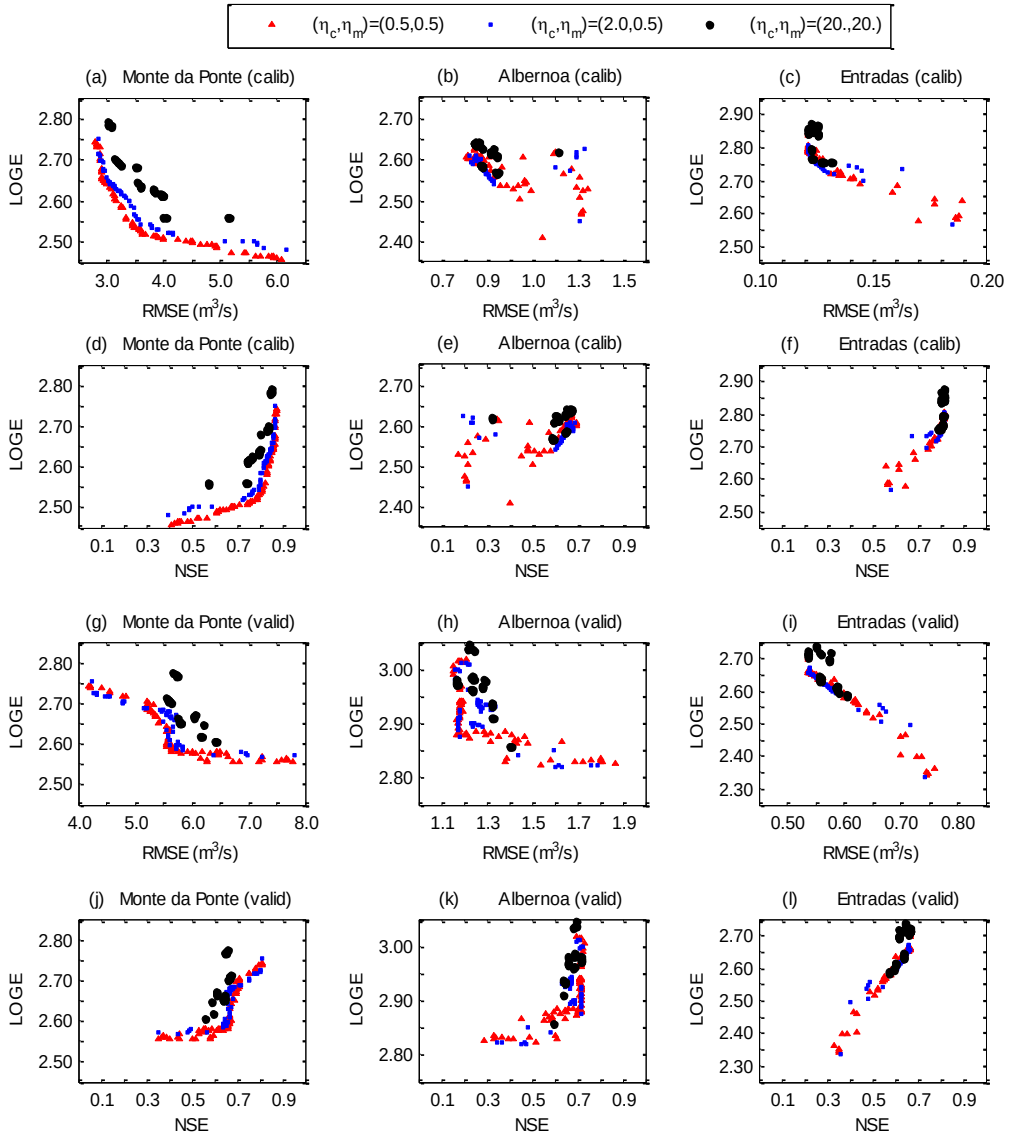

Fig. 5.10 Plots of SHETRAN model performance indicators, namely RMSE, LOGE and NSE, at basin outlet Monte da Ponte (a, d, g and j) and internal gauging stations Albernoa (b, e, h and k) and Entradas (c, f, i and l). The results for the calibration period are denoted by "(calib)" and those for the validation period by "(valid)". The filled red triangles, blue squares and black circles respectively represent the solutions of best known approximation sets derived from 30 trial runs of NSGA-II with (η_c, η_m) of (0.5, 0.5), (2.0, 0.5) and (20., 20.).

For both the calibration (Figs 5.10a–f) and validation (Figs 5.10g–l) periods, it is shown that the non-dominated solutions of the best known approximation set derived from NSGA-II with (η_c, η_m) of (0.5, 0.5) dominate those from NSGA-II with (η_c, η_m) of (2.0, 0.5) and (20., 20.) not only at basin outlet but also at internal gauging stations. The dominance of the results from the optimization with (η_c, η_m) of (0.5, 0.5) is small relative to those with (η_c, η_m) of (2.0, 0.5), as their non-dominated fronts overlap or locate near each other, especially for the validation period; however, the dominance of results from both optimizations with (η_c, η_m) of (0.5, 0.5) and (2.0, 0.5) are large compared to those from optimization with (η_c, η_m) of (20., 20.), especially at basin outlet for the validation period.

The results are very satisfactory in terms of NSE, as for the best simulation, the NSE, for basin outlet, is 0.87 for calibration and 0.81 for validation; the NSE, for internal gauging stations Albernoa and Entradas, is respectively 0.70 and 0.82 for calibration, and 0.72 and 0.66 for validation. The Section 5.5.2 has shown that the study period mainly consists of two main runoff generation periods, namely November 2005 and October to December 2008, which are respectively preceded by 12 and 6 months' droughts. Therefore, Figs 5.11a–d (page 52) have been made to display SHETRAN's capacity in reproducing storm events preceded by long periods of drought. Storms No.1 and No.4 are the largest storm events respectively during the calibration and validation periods. Figs 5.11a–b compare observed and simulated hydrographs for storms No.1 and No.4 at basin outlet; Figs 5.11c–d compare observed and simulated hydrographs for storm No.4 respectively at internal gauging stations Albernoa and Entradas. The observed discharges are denoted as "Q_{obs}" and shown in black line with dots. The simulated discharges, denoted as "Q_{sim1}", "Q_{sim2}", "Q_{sim3}" and "Q_{sim4}" and respectively shown in red, blue, purplish red, light blue lines, are from solutions with respective objective functions (RMSE, LOGE, NSE), for basin outlet, of (2.81, 2.74, 0.87), (3.81, 2.53, 0.77), (4.85, 2.49, 0.63) and (5.85, 2.46, 0.46) for the calibration period. The "Q_{sim1}" simulation is the best solution, in terms of NSE or RMSE, from the best known approximation set derived from the optimization by NSGA-II with (η_c, η_m) of (0.5, 0.5). The NSE of "Q_{sim1}", for basin outlet, is 0.89 and 0.75 respectively for Storm No.1 and No.4; for Albernoa and Entradas, they are respectively 0.74 and 0.66 for Storm No.4. It is shown that the "Q_{sim1}" reproduced very well the qualitative evolutions of hydrographs at basin outlet, especially for Storm No.1, as well as at the two internal gauging stations; however, it greatly underestimated the peak discharges, especially for Storm No.4, and the simulated hydrographs are much less flashy than the observed ones. As shown in Figs 5.11a–d, the other three simulations are solutions with larger

calibrated RMSEs (or smaller NSE), and their capacities of catching the storm peaks are much smaller than "Q_{sim1}". In a sense, Figs 5.11a–d give a graphical impression on the range of SHETRAN performances for storm events associated with the ranges of RMSE or NSE for model calibration.

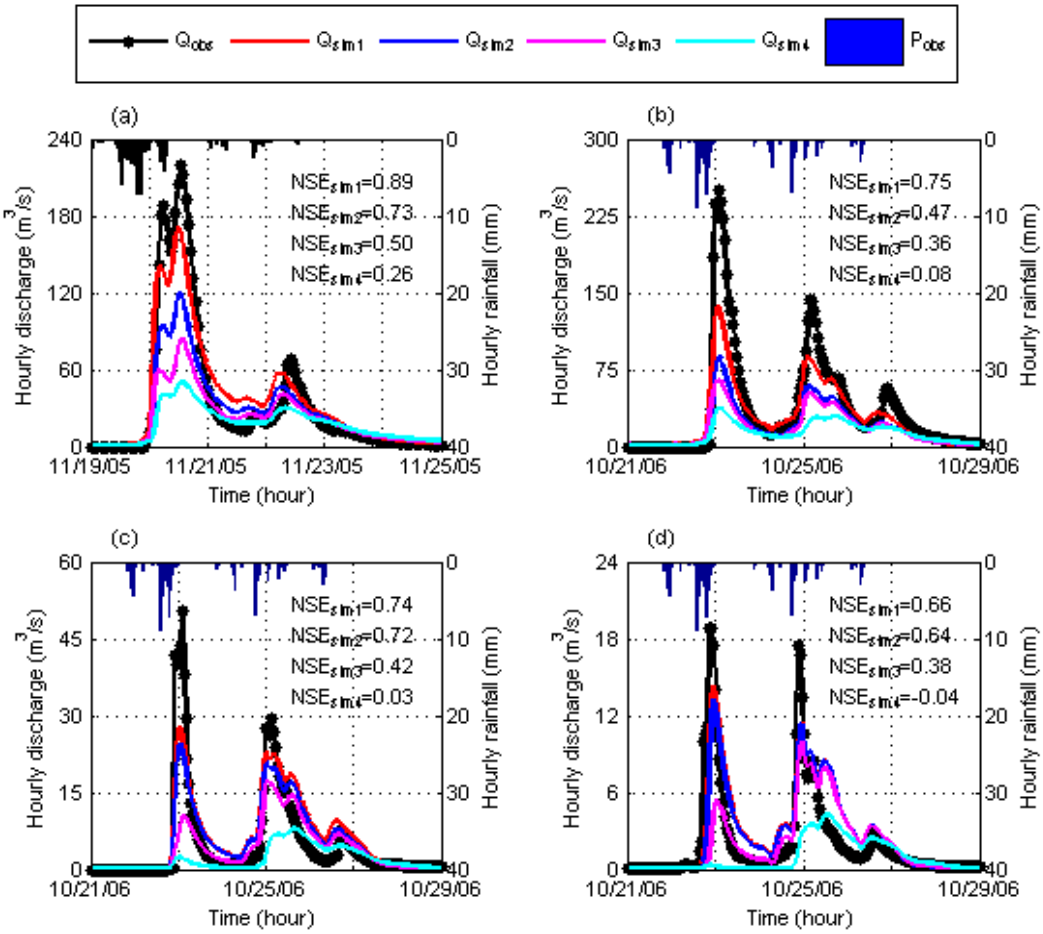

Fig. 5.11 Comparison between observed and simulated discharges from solutions obtained from automatic calibration of SHETRAN model by NSGA-II algorithm: (a) Storm No.1 at basin outlet; (b) Storm No.4 at basin outlet; (c) Storm No.4 at internal gauging station Albernoa; (d) Storm No.4 at internal gauging station Entradas. "Q_{sim1}", "Q_{sim2}", "Q_{sim3}" and "Q_{sim4}" are SHETRAN simulations, for the calibration period (2004-2006), with objective functions (RMSE, LOGE, NSE) at basin outlet of respective values (2.81, 2.74, 0.87), (3.81, 2.53, 0.77), (4.85, 2.49, 0.63) and (5.85, 2.46, 0.46).

Conclusions

Multi-objective calibration of SHETRAN model has been carried out successfully to the semi-arid Cobres basin with spatial resolution of 2.0 km and temporal resolution of 1 h by using the NSGA-II algorithm. The SBX and PM were used as GA operators and three optimizations were configured with (η_c, η_m) values of (0.5, 0.5), (2.0, 0.5) and (20., 20.). The optimizations intend to simultaneously minimizing RMSE, LOGE and (1-NSE). Each of them was repeated 30 times with initial parameter settings generated by the

LHS to eliminate the “random seed effects”. The results have shown that, as expected, the RMSE function evolves in the same direction as (1-NSE) with the change of proximity between observations and simulations. The calibration problem is actually a two-objective optimization. By comparing the three optimizations, it is shown that the one by NSGA-II with (η_c, η_m) of (0.5, 0.5) is the most efficient and achieved the best final non-dominated set, and the one by NSGA-II with (η_c, η_m) of (20., 20.) is the least efficient and achieved the worst final non-dominated set. This conclusion was made from the comparison of all results, the mean performance and the 50^{th} and 95^{th} percentile performances of the 30 trial runs among the three optimizations, as well as the SHETRAN performances at basin outlet and internal gauging stations Albernoa and Entradas, for solutions of the best known approximation sets, derived from the three optimizations during both calibration and validation periods. Based on this, we recommend values of the (η_c, η_m) of (0.5, 0.5), for NSGA-II in multi-objective calibration of SHETRAN model, in basins with similar characteristics of climate, soil, land use and topography. However, we cannot give a general conclusion on the use of smaller η_c and η_m for accelerating the NSGA-II in multi-objective calibration of hydrological models, as our study has used limited sets of η_c and η_m, our problem of optimization being a very specific case.

5.6.4 NSGA-II Calibration of SHETRAN Sediment Parameters

Set-up of SHETRAN sediment parameters

The sediment parameters’ set-up is based on the results of hydrological parameters calibration by using the MSCE scenario IV. It starts from the setting of vegetation parameters shown in Table 5.5 (page 54), based on Wicks (1988), Lukey *et al*. (2000) and a field survey of vegetation with similar climate condition. Then, soil particle size distributions are estimated. Since there is no measurement available, the method of Fooladmand and Sepaskhah (2006) is adopted to derive sediment particle-size distribution from soil textural data. There are nine types of soil identified in SHETRAN simulations with spatial resolution of 2.0 km for Cobres basin. Table 5.6 (page 54) has shown their soil textural data extracted from Cardoso (1965). As shown, each type of soil has one or two samples, and each sample has one to three horizons. Table 5.7 (page 55) has shown the sediment particle-size distribution, calculated by the method of Fooladmand and Sepaskhah (2006), for all horizons of the soil samples. For each soil type, the mass fraction of each sediment size group is an average, weighted by soil depth, of the corresponding mass fractions from all the soil horizons and the final results are displayed in Table 5.8 (page 55). Fooladmand and Sepaskhah (2006) have

indicated that their method is preferably applicable to soils with texture of silt content less than 60% and particles with diameter larger than 0.05 mm. As shown in Table 5.6, all soil types in Cobres basin are with texture of silt less than 60%. Since the particle diameters for which the mass fractions are calculated are all larger than 0.05 mm, the applicability of Fooladmand and Sepaskhah (2006) to our study is justified.

Table 5.5 Vegetation parameters for sediment transport simulations of Cobres basin

Parameter	Crop	Agroforestry	Forest	Bush
Percentage of canopy drainage falling as drips (%)	80	80	80	80
Drip diameter from canopy (mm)	5	5	5	5
Average drip fall height from canopy (m)	0.8	3.0	3.0	1.0
Percentage canopy cover (C_c) (%)	90	50	90	90
Percentage ground cover (C_g) (%)	90	50	90	90

Table 5.6 Soil textural data from Cardoso (1965) for soil types in Cobres basin

Soil type	Soil sample	Sample number	Horizon	Soil depth (m)	Sand (%)	Silt (%)	Clay (%)
V_x	V_x-459	9382	A_1	0.15	33.5	39.4	27.1
		9383	B_2	0.35	10.4	34.4	55.2
	V_x-460	9385	A_p	0.18	28.7	41.0	30.3
		9386	B_2	0.47	27.8	30.6	41.6
P_x	P_x-455	9369	A_p	0.20	61.6	22.1	16.3
		9370	B_2	0.20	54.9	20.2	24.9
	P_x-457	9375	A_1	0.15	47.3	36.0	16.7
		9376	B_2	0.20	35.9	37.6	26.5
E_x	E_x-140	8500	A_p	0.10	50.2	24.2	25.6
	E_x-144	8505	A_p	0.10	82.9	11.0	6.1
B_{vc}	B_{vc}-202	4687	A_p	0.25	23.9	22.2	53.9
		4688	B	0.15	21.3	20.1	58.6
	B_{vc}-204	5884	A_p	0.30	15.6	23.7	60.7
		5885	B	0.50	15.4	24.8	59.8
C_b	C_b-10	7420	A_p	0.20	70.2	10.2	19.6
		7421	A_3	0.20	68.0	10.2	21.8
		7422	B	0.20	65.5	10.3	24.2
	C_b-334	8372	A_p	0.32	58.9	12.5	28.6
		8373	B_2	0.28	45.0	12.1	42.9
		8374	B_3	0.18	51.8	16.6	31.6
P_{pm}	Consider it as the same as C_b soil						
S_r	Sr*-229	8188	A_p	0.25	66.6	15.7	17.7
		8189	A_3	0.28	59.7	16.0	24.3
		8190	B_2	0.22	53.4	11.0	35.6
	Sr*-4	9401	A_p	0.20	77.7	13.1	9.2
		9402	B	0.15	71.5	16.0	12.5
P_{pg}	P_{pg}-62	8318	A_p	0.20	74.8	13.1	12.1
		8319	B	0.30	71.6	14.2	14.2
E_p	E_p-148	8513	A_p	0.10	71.0	16.9	12.1

Table 5.7 Soil particle-size distribution for soil types in Cobres basin

Soil type	Soil sample	Sample number	Horizon	Mass fraction of sediment size groups (%)				
				0.10 (mm)	0.37 (mm)	0.89 (mm)	1.59 (mm)	2.00 (mm)
V_x	V_x-459	9382	A_1	78.9	17.2	3.4	0.5	0.0
		9383	B_2	94.3	4.8	0.8	0.1	0.0
	V_x-460	9385	A_p	82.5	14.4	2.7	0.4	0.0
		9386	B_2	82.0	14.4	3.2	0.4	0.0
P_x	P_x-455	9369	A_p	52.2	35.1	11.2	1.4	0.1
		9370	B_2	57.2	30.8	10.5	1.4	0.1
	P_x-457	9375	A_1	68.2	25.5	5.5	0.7	0.1
		9376	B_2	76.9	18.7	3.8	0.5	0.1
E_x	E_x-140	8500	A_p	62.6	28.0	8.2	1.1	0.1
	E_x-144	8505	A_p	27.0	45.8	24.1	2.9	0.2
B_{vc}	B_{vc}-202	4687	A_p	83.9	12.6	3.0	0.4	0.1
		4688	B	85.7	11.1	2.7	0.4	0.1
	B_{vc}-204	5884	A_p	90.4	7.8	1.6	0.2	0.0
		5885	B	90.6	7.6	1.6	0.2	0.0
C_b	C_b-10	7420	A_p	38.4	36.2	22.1	3.1	0.2
		7421	A_3	40.6	35.1	21.1	3.0	0.2
		7422	B	43.0	33.9	20.0	2.9	0.2
	C_b-334	8372	A_p	50.4	31.7	15.5	2.2	0.2
		8373	B_2	63.3	24.3	10.7	1.6	0.1
		8374	B_3	58.7	28.7	11.0	1.5	0.1
P_{pm}	Consider it as the same as C_b soil							
S_r	Sr*-229	8188	A_p	44.8	37.2	15.8	2.0	0.2
		8189	A_3	51.3	33.1	13.7	1.8	0.1
		8190	B_2	55.0	28.3	14.4	2.1	0.2
	Sr*-4	9401	A_p	33.2	43.4	20.7	2.5	0.2
		9402	B	40.5	40.5	16.7	2.1	0.2
P_{pg}	P_{pg}-62	8318	A_p	35.8	41.2	20.2	2.6	0.2
		8319	B	39.4	39.7	18.4	2.3	0.2
E_p	E_p-148	8513	A_p	41.4	40.5	15.9	2.0	0.2

Table 5.8 Mass fraction for sediment particle-size distribution of soil types in Cobres basin

Particle diameter (mm)		0.10	0.37	0.89	1.59	2.00
Mass Fraction (%)	V_x	85.4	11.8	2.4	0.3	0.1
	P_x	63.3	27.7	7.9	1.0	0.1
	E_x	44.8	36.9	16.1	2.0	0.2
	B_{vc}	88.5	9.2	2.0	0.3	0.0
	C_b	49.9	31.3	16.3	2.3	0.2
	P_{pm}	49.9	31.3	16.3	2.3	0.2
	S_r	45.8	35.9	16.0	2.1	0.2
	P_{pg}	37.9	40.3	19.1	2.5	0.2
	E_p	41.4	40.5	15.9	2.0	0.2

Then, the overland flow sediment transport capacity equation is selected, based on the results of simulations shown in Table 5.9 (page 57). Considering the possible variations of rainfall impact erodibility and overland flow erodibility, the simulated suspended sediment yield would be in the range of [0.029, 0.062] t/ha/year by using the Engelund-Hansen equation; and it would be in the range of [0.052, 14.732] t/ha/year by using the Yalin equation. The use of Yalin equation may provide a reasonable range of sediment yields, taking the basin size and the literature studies into consideration. According to Walling (1983), the observed sediment yields for catchments of around 1000 km^2 are in the range of [0.1, 10.0] t/ha/year. Bathurst *et al*. (1996) observed the sediment yields, for the 167-m^2 soil erosion plots at the Centro Experimental de Erosão de Vale Formoso, just to the east of the Cobres basin, in the ranges of [0.44, 2.0], [1.10, 1.34] and [0.24, 1.10] t/ha/year for the respective Wet (1977─1979), Dry (1980─1982) and Mean (1983─1985) periods. Since Cobres basin is of area 705 km^2, it is most probable that the sediment yield with values larger than 0.1 t/ha/year. Consequently, this excludes the eligibility of the Engelund-Hansen equation for the simulation of overland flow sediment transport capacity. As for the channel flow sediment transport capacity, three equations are available: the Engelund-Hansen equation, the Acker-White equation and the Ackers-White-Day equation. Experiments, not shown in thesis, have indicated that the sediment yield varies very little with the selection of different equation, so the Engelund-Hansen equation is used.

Table 5.9 Preliminary sediment simulations of Cobres basin for the period from October, 2004 to November, 2006

Model run[a]	k_r (J^{-1})	k_f (mg m^{-2} s^{-1})	k_b (mg m^{-2} s^{-1})	ISGSED	ISACKW	FPCRIT (%)	DLSMAX (mm)	DCBEDO (mm)	DLS (mm)	Fine sed yield t ha^{-1}·$year^{-1}$	Total sed yield t ha^{-1}·$year^{-1}$
No.1	**0.01**	**0.01**	**0.0**	**1**	**0**	**25**	**50**	**10**	**0.0**	**0.0286**	**0.0414**
No.2	**0.01**	**0.1**	**0.0**	**1**	**0**	**25**	**50**	**10**	**0.0**	**0.0594**	**0.0827**
No.3	**0.05**	**0.1**	**0.0**	**1**	**0**	**25**	**50**	**10**	**0.0**	**0.0596**	**0.0829**
No.4	**0.1**	**0.1**	**0.0**	**1**	**0**	**25**	**50**	**10**	**0.0**	**0.0597**	**0.0831**
No.5	**1.0**	**1.0**	**0.0**	**1**	**0**	**25**	**50**	**10**	**0.0**	**0.0619**	**0.0857**
No.7	**2.0**	**2.0**	**0.0**	**1**	**0**	**25**	**50**	**10**	**0.0**	**0.0619**	**0.0857**
No.6	**2.0**	**20.0**	**0.0**	**1**	**0**	**25**	**50**	**10**	**0.0**	**0.0619**	**0.0857**
No.8	**10.0**	**20.0**	**0.0**	**1**	**0**	**25**	**50**	**10**	**0.0**	**0.0619**	**0.0857**
No.9	**0.01**	**0.01**	**0.0**	**0**	**0**	**25**	**50**	**10**	**0.0**	**0.0517**	**0.0718**
No.10	**0.01**	**0.05**	**0.0**	**0**	**0**	**25**	**50**	**10**	**0.0**	**0.2476**	**0.3023**
No.11	**0.1**	**0.1**	**0.0**	**0**	**0**	**25**	**50**	**10**	**0.0**	**0.4934**	**0.5645**
No.12	**0.1**	**0.5**	**0.0**	**0**	**0**	**25**	**50**	**10**	**0.0**	**2.1693**	**2.2882**
No.13	**1.0**	**1.0**	**0.0**	**0**	**0**	**25**	**50**	**10**	**0.0**	**4.1138**	**4.2501**
No.14	**2.0**	**2.0**	**0.0**	**0**	**0**	**25**	**50**	**10**	**0.0**	**7.1873**	**7.3304**
No.15	**2.0**	**20.0**	**0.0**	**0**	**0**	**25**	**50**	**10**	**0.0**	**14.6856**	**14.8318**
No.16	**10.0**	**20.0**	**0.0**	**0**	**0**	**25**	**50**	**10**	**0.0**	**14.7323**	**14.8784**

Note:

[a] k_r and k_f are respectively raindrop impact erodibility and overland flow erodibility, k_b is bank flow erodibility. ISGSED with value of 1 (0) means the Engelund-Hansen (Yalin) equation is selected for calculation of overland flow sediment transport capacity. ISACKW with value of 0 means Engelund-Hansen equation is selected for calculation of channel flow sediment transport capacity. FPCRIT is user specified maximum sediment concentration that can be carried by flow, and 25 % is set to preliminary simulations which is equivalent to 662.5 g/l. DLSMAX with value of 50mm means that if the depth of loose sediment that builds up on the hillslope reaches 50 mm, the soil underneath is assumed to be protected and no further erosion take place. DCBEDO with value of 10mm means that the depth of active top bed layer is set to10 mm. Fine sediment is considered as sediment with diameter less than 0.1 mm.

Previous studies by Wicks *et al*. (1992), Wicks and Bathurst (1996), Adams and Elliott (2006), and Bathurst (2011) have indicated that the soil erodibility coefficients increase in value as the soil becomes easier to erode. The raindrop impact and overland flow erodibility coefficients are not directly measurable soil properties and are therefore required to be adjusted in calibration process according to model grid square scale, soil texture, soil conditions such as moisture content, animal effects such as compaction by grazing cattle, human effects such as tillage, and vegetation effects such as root binding. Bathurst *et al*. (1996) found the erodibility coefficients need to be varied between moderate rainfall events and extreme events. As for sediment transport simulations at Cobres basin, they used a 'normal' set (k_r = 0.13 J^{-1}, k_f = 1.3 mg/m^2/s) calibrated on all events other than the extreme event; and an 'extreme' set (k_r = 2.0 J^{-1}, k_f = 20.0 mg/m^2/s) calibrated on the largest erosion event in the calibration period. In this study, the simulation period is even drier than the dry period of Bathurst *et al*. (1996), as one may see in Table 5.10. Therefore, the erodibility coefficients may be smaller than the 'normal' set given by Bathurst *et al*. (1996), since in dry condition the surface soils are harder and less erodible than those in wetter conditions as explained in Adams and Elliott (2006). Preliminary simulations No.9 to No.13, shown in Table 5.9 (page 57), have indicated that simulated sediment yields could be in the range of [0.052, 4.114] t/ha/year, which is in agreement with those derived from the plot measurement of Bathurst *et al*. (1996), if the ranges of rainfall impact erodibility and overland flow erodibility coefficients are respectively set as [0.01, 1.0] J^{-1} and [0.01, 1.0] mg/m^2/s. Thus, for sediment parameter calibration, the range of raindrop impact erodibility and overland flow erodibility are respectively set as [0.01, 1.0] J^{-1} and [0.01, 1.0] mg/m^2/s. For baseline simulations, the raindrop impact erodibility is set as 0.1, 0.2 and 1.0 J^{-1} and the overland flow erodibility is set as 0.05, 0.1 and 0.5 mg/m^2/s respectively for clay, loam and Sandy loam.

Table 5.10 Statistics of annual rainfall and runoff at Cobres basin

Description	Year[a]	Rainfall (mm)	Runoff (mm)
Dry period in Bathurst *et al*. (1996)[b]	1980–1981	250	0
	1981–1982	483	86
Calibration simulation period in Rong *et al*. (2013)[c]	2004–2005	194	0
	2005–2006	502	55

Note:
[a]Years are defined October to September.
[b]Data is extracted from Bathurst *et al.* (1996).
[c]Data is extracted from Rong *et al.* (2013).

NSGA-II calibration of SHETRAN sediment parameters

The observed sediment discharge data for the period of Storm No.4, namely from October 23rd, 2006 05:00 to October 27th, 2006 23:00, is used in the automatic calibration of SHETRAN sediment parameters by NSGA-II algorithm with (η_c, η_m) of (0.5, 0.5). In the calibration of sediment parameters, the NSGA-II was preferred to MSCE since this last method is too time consuming. However, for the calibration of hydrological parameters, we used the previously computed set obtained from MSCE. Each SHETRAN simulation is carried out for the period from October 1st 2004 to November 4th 2006, using the hydrological parameters calibrated by MSCE as described in Section 5.5.2. The population size is set to 50; a maximum of 50 generations is prescribed for each trial run and only one trial run is performed. The optimization produced a non-dominated set of solutions in terms of RMSE and LOGE, from which the one with minimum RMSE was selected with the intention of getting better performance for sediment transport simulation during high flow processes. The calibrated (k_r, k_f), for the V_x, P_x and E_x soils, are respectively (0.01 J^{-1}, 0.01 mg/m^2/s), (0.01 J^{-1}, 0.01 mg/m^2/s) and (1.00 J^{-1}, 0.58 mg/m^2/s). The model performance indicators, namely RMSE, LOGE and NSE, for comparison between observed and simulated hourly sediment discharges are respectively 40.25 kg/s, 2.45 and 0.56. Fig 5.12 (page 60) compares observed and simulated hourly discharges and sediment discharges for Storm No.4. It can be seen that, for sediment discharge simulation, SHETRAN model greatly underestimated the first peak and overestimated all the recession process of the three peaks. After a long period of drought, the first peak of Storm No.4 transported a large amount of sediment due to the abundant sediment deposition, while the second and third peaks transported much less sediment than their precedent peaks probably due to the lack of deposited sediment as well as the smaller rainfall intensities as shown in Fig. 5.5b (page 40). And SHETRAN model did not represent well this process. For Storm No.4, the simulation overestimated the observed sediment yield (0.200 t/ha) by 78 %. Overall, the simulated sediment yield is 0.724 t/ha/year, which is in the range of [0.1, 10.0] t/ha/year, as suggested by Walling (1983). The calibration is satisfactory considering the nature and quantity of the observed sediment data.

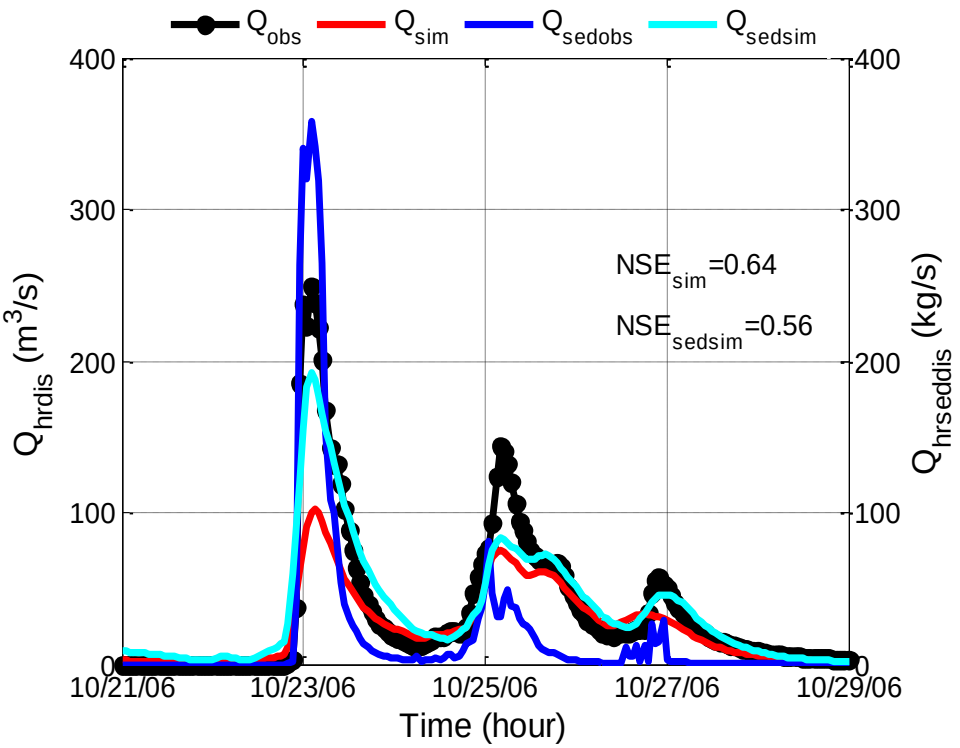

Fig. 5.12 Comparisons between observed and simulated hourly discharges and sediment discharges for the solution obtained from automatic calibration of sediment parameters by NSGA-II. "Q_{obs}", "Q_{sim}", "Q_{sedobs}" and "Q_{sedsim}" respectively represent observed discharge, simulated discharge, observed sediment discharge and simulated sediment discharge. Time is shown in the "MM/DD/YY" format.

5.7 Discussion

Automatic calibration is preferred because it provides an objective and extensive searching in the feasible parameter space. In this chapter, the applicability and efficiency of the MSCE and NSGA-II algorithms have been demonstrated for automatic calibration of SHETRAN model in the semi-arid Cobres basin with spatial resolution of 2.0 km and temporal resolution of 1 h. To simplify the process, we divided the calibration parameters into hydrological parameters and sediment parameters. The calibration started with the hydrological parameters and the results were used in following calibration of sediment parameters. The entire calibration process can be completed by either MSCE or NSGA-II independently. In this study, we calibrated the hydrological parameters of SHETRAN model by MSCE with the objective of minimizing RMSE; and then, using the obtained hydrological parameters, we calibrated the sediment parameters by NSGA-II with the objective of minimizing RMSE and LOGE; finally, the solution from the non-dominated set with minimum RMSE was selected.

For Cobres basin with spatial resolution of 2.0 km, twenty-two hydrological parameters were identified to be calibrated considering the key parameters of the two main types of

land-use and the three main types of soil; and six sediment parameters were identified for the main types of soil. The results are very satisfactory for both MSCE and NSGA-II calibrations of hydrological processes. As for the MSCE (the best solution from NSGA-II) calibration, NSE, for basin outlet, is 0.86 (0.87) for calibration and 0.74 (0.81) for validation; NSE, for internal gauging stations Albernoa and Entradas, is respectively 0.65 (0.70) and 0.82 (0.82) for calibration, 0.69 (0.72) and 0.63 (0.66) for validation; as for storm events, NSE, for basin outlet, is 0.87 (0.89) and 0.64 (0.75) respectively for Storms No.1 (during the calibration period) and No.4 (during the validation period); for Albernoa and Entradas, it is respectively 0.69 (0.74) and 0.65 (0.66) for Storm No.4. For the MSCE and NSGA-II calibrations, trial runs of optimizations were performed respectively once and ninety times, therefore no comparability exists between them. For NSGA-II, the SBX and PM were used as GA operators. Three optimizations were configured with (η_c, η_m) of respective values (0.5, 0.5), (2.0, 0.5) and (20., 20.); all of them were repeated 30 times with initial parameters randomly generated by the LHS. Comparisons have shown that the one with (η_c, η_m) of (0.5, 0.5) is the most efficient and provides best final solutions. Thus, NSGA-II algorithm with (η_c, η_m) of (0.5, 0.5) is recommended to multi-objective calibration of SHETRAN model in basins with similar characteristics of climate, soil, land use and topography.

The sediment parameters were calibrated for Storm No.4 by NSGA-II algorithm with (η_c, η_m) of (0.5, 0.5) and by using the hydrological parameters derived from the MSCE calibration. The result is satisfactory considering the low quality of the observed sediment data. For Storm No.4, the NSE, for basin outlet, is 0.56 for hourly sediment discharges and the simulation overestimated the sediment yield by 78%. The simulated sediment yield is 0.724 t/ha/year for the 25 months' simulation period, which is in the range, [0.1, 10.0] t/ha/year, given by Walling (1983). Therefore, the twenty-two hydrological parameters calibrated by MSCE and the six sediment parameters calibrated by NSGA-II are used in hydrological simulations of control and future climate scenarios, in Chapter 8.

6. Impacts of Spatial Scale on the SHETRAN Model

The impacts of spatial scale on SHETRAN hydrological simulations are described in this chapter. The objective of it is, based on the available data, to form a basis for the selection of proper spatial resolution for the SHETRAN hydrological simulations, and evaluating future climate change impacts. First, a concise introduction is presented; then the methods and data are described; next, the impacts of spatial scale on long-term runoff simulation and storm-runoff generation are respectively assessed; finally, a short discussion concludes this chapter.

6.1 Introduction

Similarly to other PBSD models, the application of the SHETRAN model requires the specification of spatial resolutions, both horizontally and vertically, for model simulations. Usually, the selection of a proper spatial resolution is a compromise among the availabilities of input data, such as DEM, maps of land-use and soil type, computational resources and the modelling purposes (Ewen *et al*., 1996; Henriksen *et al*., 2003). This is particularly true for basins with areas of middle to large sizes. The use of coarse spatial discretization can simplify the model set-up and reduce the work involved in data collecting and processing, as well as the execution time of model simulation; however, it may also cause the loss or inaccurate representation of information such as types of land-use and soil and drainage density, which would ultimately decrease the model performance. It is therefore desirable to investigate the effects of spatial resolution on model performance.

Previous studies about the effects of spatial discretization on model performance can be found in Refsgaard (1997) and Vázquez *et al*. (2002) for the MIKE-SHE model and Wildemeersch *et al*. (2014) for the HydroGeoSphere model. Their work leads to the conclusion that coarse grids may result in a poor simulation of discharges, due to the inadequate representation of the catchment river links. Although this conclusion was based on simulations with different grid sizes, the corresponding calibrations were either absent, or manual, or partially objective. In the present research, a fully objective global optimization method is used to compare the results from the simulations proposed for different horizontal spatial resolutions. The conclusion will be used, together with other information, in determining the final selection of an appropriate horizontal spatial resolution for SHETRAN simulations at Cobres basin, aiming to evaluate future climate change impacts, as described in Chapter 8.

6.2 Methods and Data

Three important aspects are essential for comparing the impacts of spatial discretization: (1) the possible model performances; (2) the final best model performances as well as their parameter settings; (3) the best model performances achieved by each step of the optimization process. They are designed to give an overall evaluation of the fitness of a spatial resolution to the model simulations. NSGA-II algorithm is a global optimization method which is capable of finding the non-dominated optimal solutions through searching of the whole possible parameter setting spaces (Deb *et al.*, 2002). Therefore, aspect (1) can be evaluated by comparison of ensembles of SHETRAN simulations from the whole set of optimization processes of different spatial resolutions. To be specific, the best solutions from each optimization step are included to form the ensemble of best solutions. Chapter 5 has demonstrated that the NSGA-II algorithm, together with the SBX and PM genetic algorithm operators and with (η_c, η_m) of (0.5, 0.5), is effective and efficient in SHETRAN model calibration. So, aspect (3) can be assessed by comparison of the best solutions for each evolved optimization step, and the selection of the final one, provides a conclusion for aspect (2).

Considering the availability of computational resources, we propose the comparison of spatial resolutions of 0.5, 1.0 and 2.0 km for the evaluation of spatial scale impacts on model performance; and each of the single SHETRAN simulation requires respectively around 45, 12 and 3 minutes. The NSGA-II parameters are set the same as described in Chapter 5. The SHETRAN calibrations are configured to evolve 30 generations with population size of 50 for minimizing the objective functions of RMSE, LOGE and (1-NSE), for each spatial resolution, by using the NSGA-II algorithm with (η_c, η_m) of (0.5, 0.5). By simultaneously performing 4 simulations, the model calibrations demand around 338, 64 and 16 hours to be completed respectively for spatial resolutions of 0.5, 1.0 and 2.0 km. Therefore, they will not be repeated to eliminate the random seed effects; instead, an initial parameter setting LHS1, sampled by the LHS technique, is used for the SHETRAN calibrations.

As in Chapter 5, the calibration period is set as from October 1st 2004 to September 30th 2006 and the objective functions are evaluated based on comparisons between observed and simulated hourly discharges at basin outlet, Monte da Ponte gauging station. For spatial resolution of 2.0 km, the SHETRAN model set-up and performance can be found in detail respectively in Sections 5.3 and 5.6.3. For the spatial resolutions of 0.5 and 1.0 km, the SHETRAN model is set up in the same way as described in

Section 5.3 and the twenty-two calibration parameters are constrained within the physically realistic ranges listed in Table 5.2 (page 31). Moreover, SHETRAN is also set up for the spatial resolution 1.5 km, but not calibrated due to computational limits; and its maps of land-use, soil types and river links will be displayed together with those from the other three spatial resolutions, to illustrate the effect of spatial resolutions on the model input.

The best solutions from model calibration are selected based on the criterion of NSE ≥ 0.85 and validated for the spatial resolutions of 1.0 and 2.0 km for possible future applications. For validation, the 0.5 km resolution was not considered, as explained in Section 6.4.1. According to Klemeš (1986), Bathurst *et al*. (2004) and Refsgaard *et al.* (2014), the SHETRAN model is validated from these four aspects: (1) Split-sample test; (2) Differential split-sample test; (3) Proxy-basin test and (4) Multi-site test, namely for internal and outlet responses. Based on SHETRAN simulations at Cobres basin, the validations (1) and (4) are carried out by comparing the observed and simulated hourly discharges at basin outlet and internal gauging stations Albernoa and Entradas for the period from October 1st 2006 to September 30th 2008; validation (2) is performed by comparisons of hourly discharges at basin outlet for the period from October 1st 1977 to September 29th 1979. Based on SHETRAN simulations at Albernoa basin, the validations (3) and (4) are assessed by comparing the observed hourly discharges with the simulations at basin outlet and internal gauging station Entradas for the periods from October 1st 2004 to September 30th 2006 and from October 1st 2006 to September 30th 2008. As the validations involve solutions with equally or nearly equally good model performances, the equifinality condition (Beven and Freer*,* 2001) can also be identified and tested. The rainfall, PET and discharge data were provided by Professor Bathurst, University of Newcastle, for the SHETRAN simulations at Cobres basin, for the period from October 1st 1977 to September 29th 1979.

The SHETRAN model calibrations and validations are evaluated in terms of long-term runoff and storm-runoff simulations. For long-term runoff simulation, the objective functions RMSE, LOGE and NSE are evaluated as well as graphics of model fit and monthly and annual mass balance errors. In order to validate the model's capability of reproducing extreme storm events, the events with peak discharges at Monte da Ponte gauging station with values larger than 200 m^3/s are selected for evaluation of storm-runoff simulation, by comparisons of objective functions such as NSE, mass balance error (MBE) and peak error (PKE), as well as, graphics of model fit. Definitions of MBE and PKE are shown in equations 6.1 and 6.2.

$$MBE = \frac{\sum_{i=1}^{n}(S_i - O_i)}{\sum_{i=1}^{n} O_i} \quad 6.1$$

$$PKE = \frac{Q_{sim}^{pk} - Q_{obs}^{pk}}{Q_{obs}^{pk}} \quad 6.2$$

Where O_i and S_i are respectively observed and simulated hourly discharges at i^{th} hour; n is the total number of hours; Q_{obs}^{pk} and Q_{sim}^{pk} are respectively observed and simulated peak discharges.

6.3 Impacts of Spatial Scale on the SHETRAN Model Input

Figs 6.1a–d (page 67), 6.2a–d (page 68) and 6.3a–d (page 69) respectively represent the impacts of spatial scale on the maps of land-use, soil type and river links. Table 6.1 (page 69) indicates the impact of spatial scale on drainage density of the Cobres basin. It is shown that the grid coarsening have caused (1) the loss of land-use and soil types, (2) reduction of the drainage density and (3) the misrepresentation of the land-use, soil type and river links. As shown in Figs 6.1a–d (page 67), the land-use type “urban” is identified in spatial resolutions of 0.5 and 1.0 km but not in the resolutions of 1.5 and 2.0 km; the “bush” is scattered in both south and northeast of the basin for spatial resolutions of 0.5 and 1.0 km, however, it is only concentrated in the south for the resolutions of 1.5 and 2.0 km. Similar situations can be found for the soil types “Cb”, “Ppm” and “Sr” in Figs 6.2a–d (page 68). Figs 6.3a–d (page 69) have demonstrated the better representations of river links in SHETRAN simulations, shown in red lines, by using the finer spatial resolutions. Notice that the “Cobres river INAG” was provided by SNIRH based on the map with scale of 1:100000. Table 6.1 (page 69) indicates that coarser resolution reduces the drainage density: the spatial resolution of 2.0 km reduces by around 18% the drainage density of 0.5 km resolution.

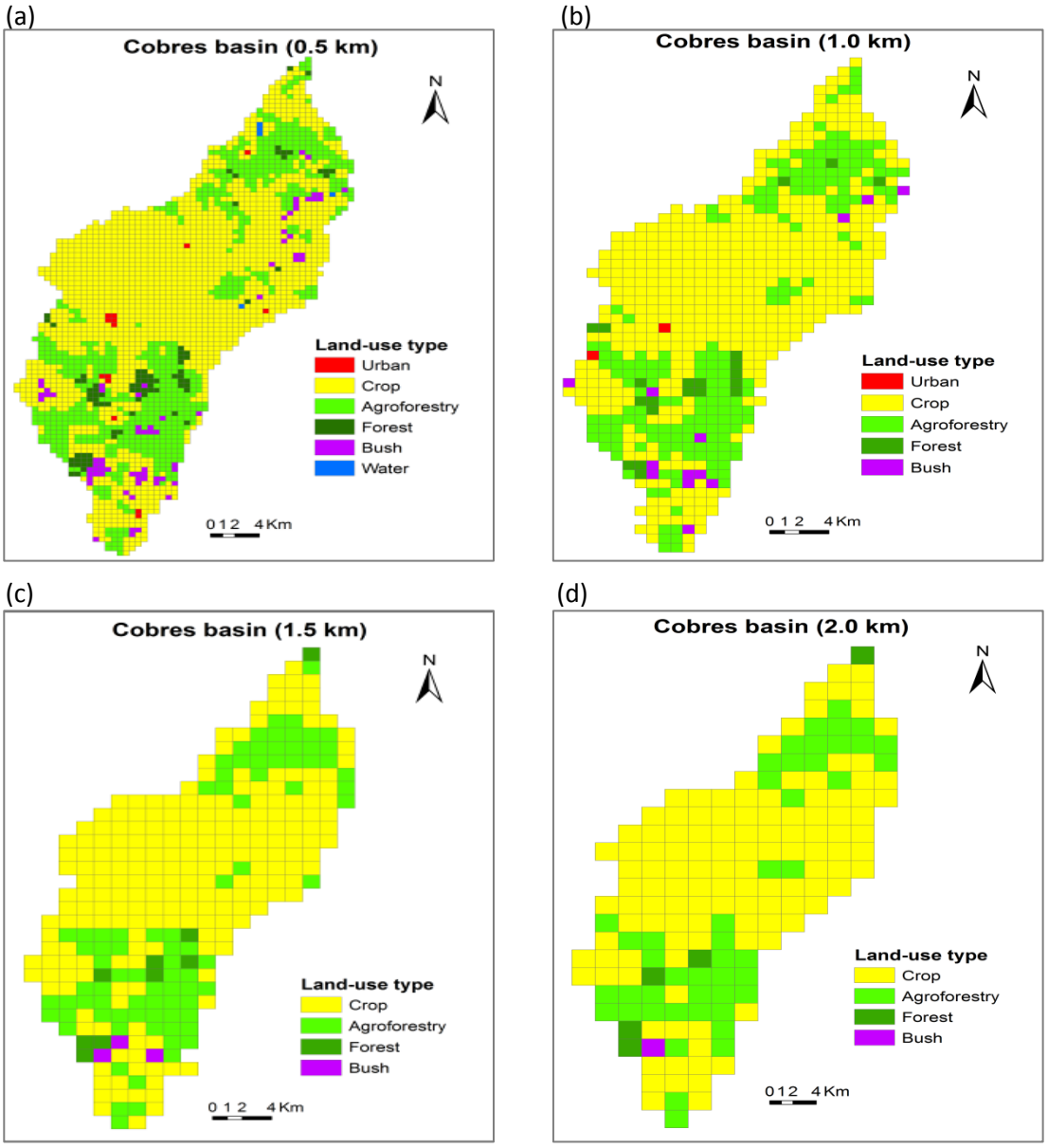

Fig. 6.1 Maps of land-use distribution for Cobres basin with respective spatial resolutions of 0.5, 1.0, 1.5 and 2.0 km.

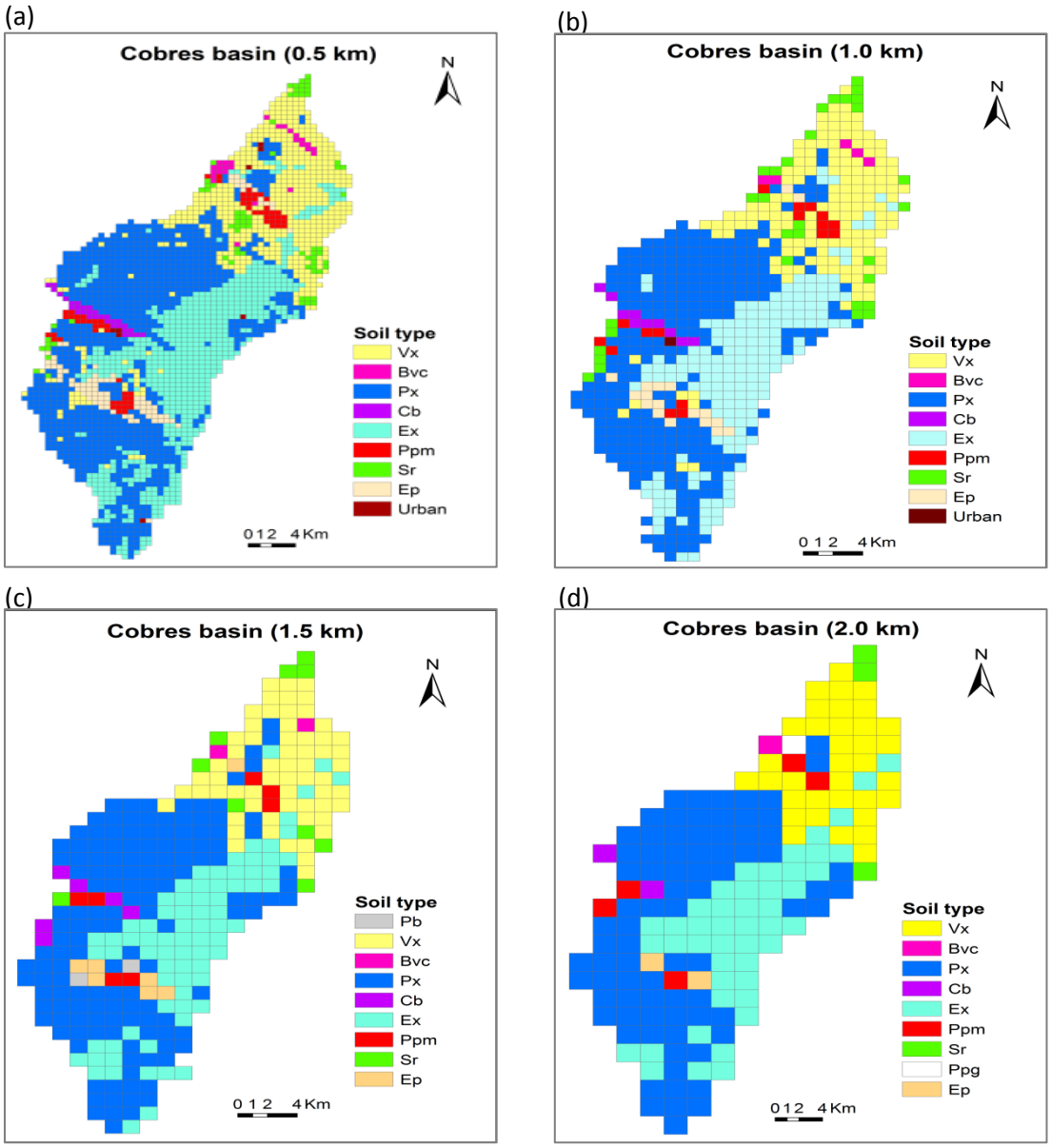

Fig. 6.2 Maps of soil type distribution for Cobres basin with respective spatial resolutions of 0.5, 1.0, 1.5 and 2.0 km.

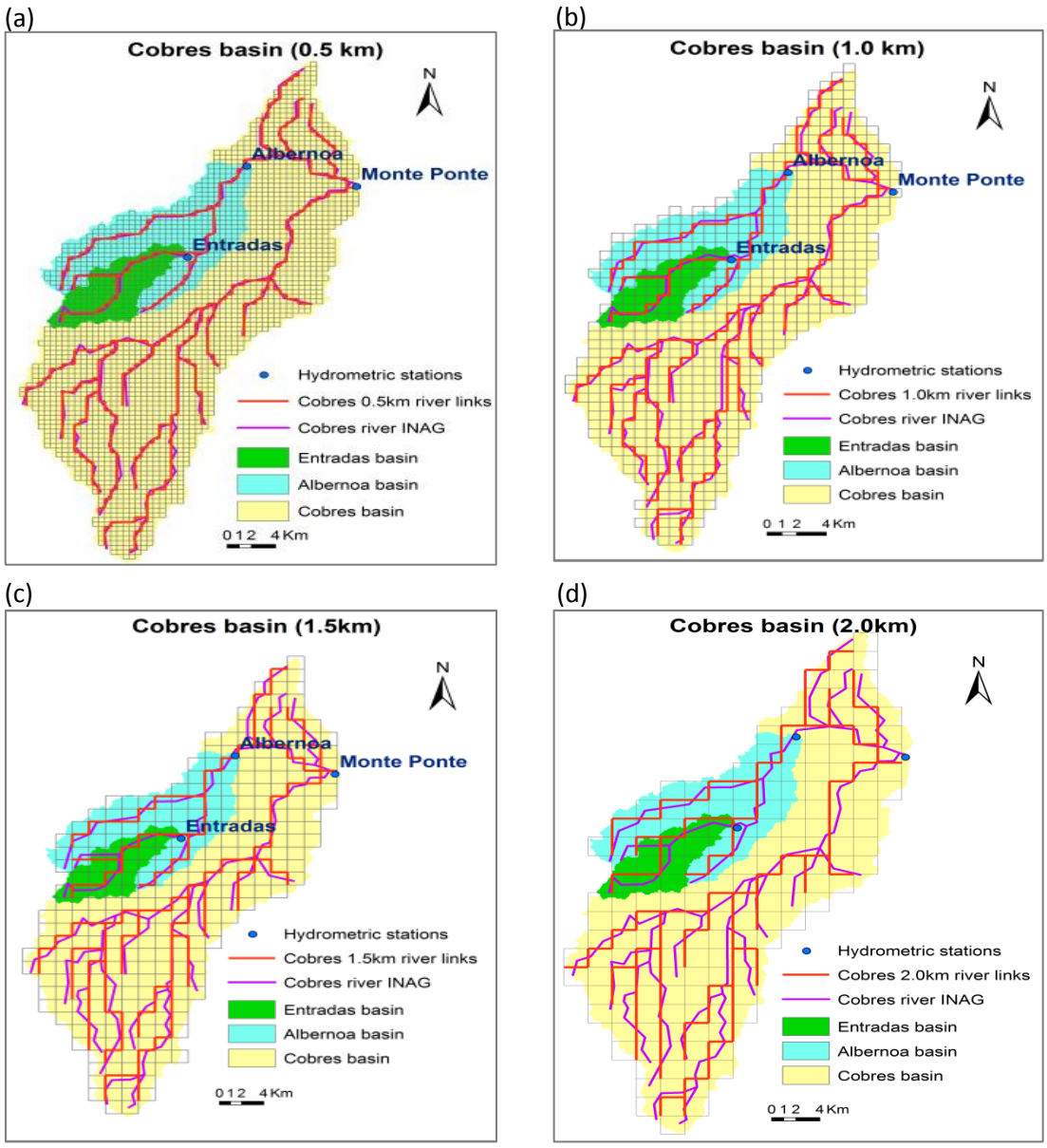

Fig. 6.3 Maps of river links distribution for Cobres basin with respective spatial resolutions of 0.5, 1.0, 1.5 and 2.0 km. The red lines represent river links, introduced by the non-standard set-up, developed in the thesis, in the SHETRAN simulations, and the purple ones indicate those provided by SNIRH.

Table 6.1 Area, total river length and drainage density of the Cobres basin

Spatial resolution	2.0 km	1.5 km	1.0 km	0.5 km	DEM (10 m)
Basin area (km^2)	700	713.25	705	664.5	705.3
Total river length (km)	262	274.5	294	304.5	694.7
Drainage density (km/km^2)	0.374	0.385	0.420	0.458	0.985

6.4 Impacts of Spatial Scale on the SHETRAN Model Performance

6.4.1 Introduction

This section presents the impacts of spatial scale on the SHETRAN model performance, in terms of long-term runoff simulation and storm-runoff generation, for both the calibration and validation periods. For calibration, the spatial resolutions of 0.5, 1.0 and 2.0 km were considered for the simulation at Cobres basin and comparisons were made for their model performances during the optimization processes (Figs 6.4–6.6, pages 71–73). Based on the criterion of NSE ≥ 0.85, the 8 and 25 best solutions, shown in Table 6.2 (pages 75–76), were respectively selected from the final results of the SHETRAN calibrations, with the spatial resolutions of 1.0 and 2.0 km for model validations, for possible future applications. For validation, the 0.5 km resolution was not considered, taking into account serious computational limitations, and the fact that validation was corroborated by higher than 0.85 Nash-Sutcliffe Efficiencies, for the two not so optimal spatial resolutions. For both calibration and validation periods, the selected best solutions were evaluated on long-term runoff simulation by using the split-sample test, differential split-sample test, proxy-basin test and multi-site test; and they were assessed on storm-runoff generation by considering the key factors important for sediment transport simulation such as peak discharge, storm runoff and storm hydrograph. The evaluations of long-term runoff simulations are shown in Figs 6.7a–l, 6.8a–b, 6.9a–h, 6.10a–h, 6.11a–c, 6.12a–c (pages 79–84) and Tables 6.3 and 6.4 (pages 81 and 83); the assessments of the storm-runoff generations are indicated in Figs 6.13, 6.14a–b, 6.15a–d, 6.16a–d and 6.17a–e (pages 85–89).

6.4.2 Impacts of Spatial Scale on Long-Term Runoff Simulation

- *Model performances during the optimization processes*

Figs 6.4a–c (page 71) compare model performances obtained from the entire optimization processes of the different spatial resolutions based on the same initial parameter setting LHS1.

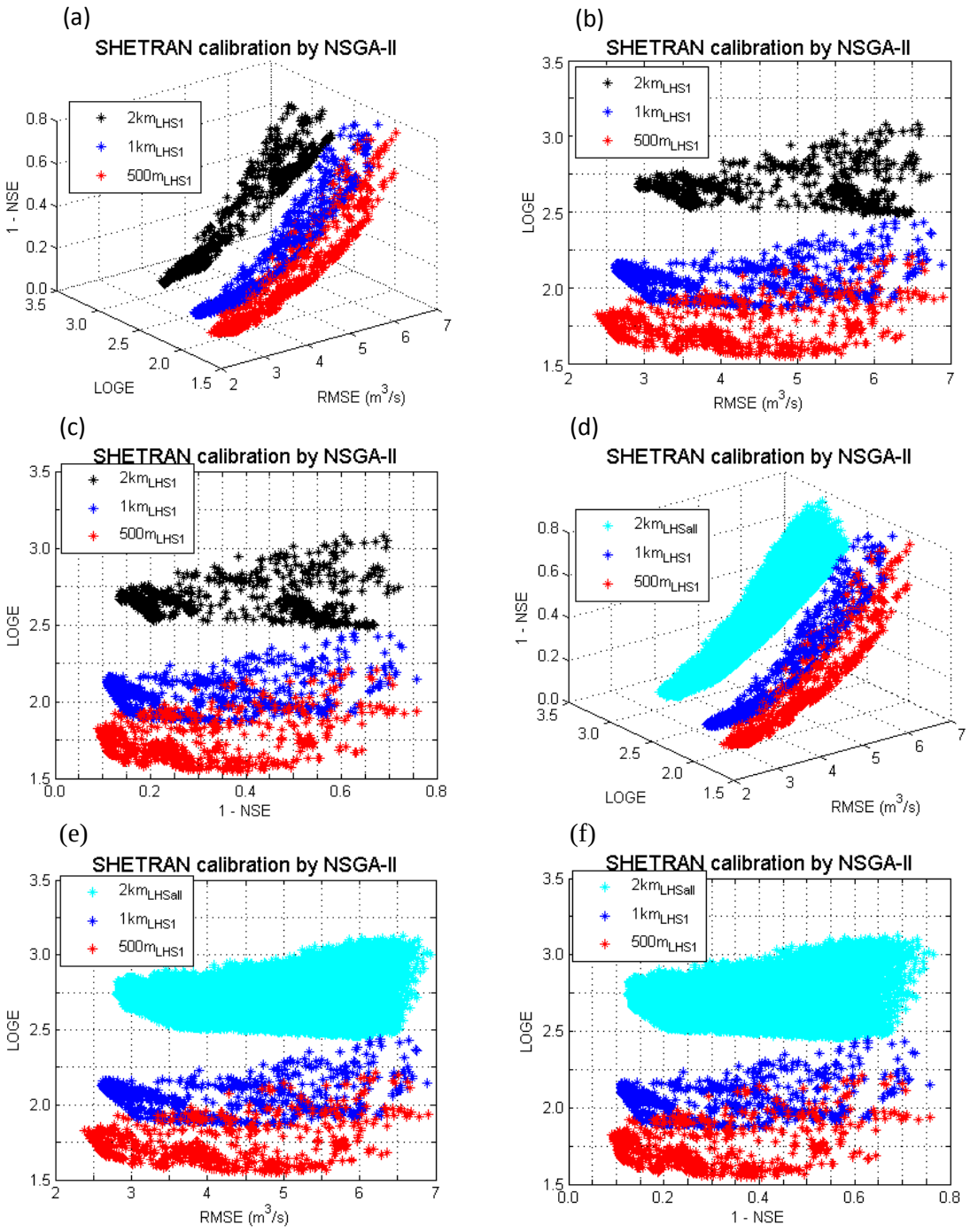

Fig. 6.4 Plots showing the comparisons of SHETRAN performances resulting from different spatial discretizations. The black (and light blue), blue and red asterisks represent the ensembles of elite solutions derived from the processes of SHETRAN calibration for Cobres basin with respective spatial resolutions of 2.0, 1.0 and 0.5 km. The subscripts LHS1 and LHSall respectively represent the 1st and all the 30 initial parameter settings generated by the LHS technique. The NSGA-II algorithm with (η_c, η_m) of (0.5, 0.5) was used for calibration.

Fig 6.4a displays the comparison of model performances with objectives RMSE, LOGE and (1-NSE), and Figs 6.4b–c indicate comparisons in projections on 2-D spaces RMSE.vs.LOGE and (1-NSE).vs.LOGE. It is clear that the model performances for

different spatial resolutions are located in distinctly different regions of the objective spaces. All in all, three conclusions can be taken: (1) all SHETRAN simulations for the 1.0 km resolution are better than those for the 2.0 km resolution and nearly all simulations for the 0.5 km resolution are better than those for the 1.0 km resolution; (2) Among all objectives, by using the finer spatial resolution, LOGE is improved to the maximum extent and the improvement is for all the possible simulations; however the RMSE and NSE are improved distinctly only for the best simulations. As indicated in Figs 6.4b–c, from the 2.0 to 1.0 km resolution, the ranges of model performances are shifted from [2.5, 3.1] to [1.8, 2.4] for LOGE, from [2.9, 6.7] to [2.6, 7.0] for RMSE and from [0.13, 0.73] to [0.10, 0.76] for (1-NSE); for the 0.5 km resolution the LOGE, RMSE and (1-NSE) are shifted respectively to [1.5, 2.2], [2.3, 7.0] and [0.09, 0.76]. (3) The model performances, for the finer spatial resolutions, are slightly more scattered in the objective space, particularly for the 0.5 km resolution. In Chapter 5, the SHETRAN calibration has been repeated 30 times, using different initial conditions, for Cobres basin, with spatial resolution of 2.0 km. The ensemble of model performances obtained from the entire optimization processes for all the 30 trial runs is included in Figs 6.4d–f. It is shown that the ranges of objective functions are not much shifted compared to those derived from the trial run LHS1. Therefore, the random seed effects may not change the conclusions derived from Figs 6.4a–c.

Fig 6.5 indicates the best known approximation sets obtained from the spatial resolutions of 0.5, 1.0 and 2.0 km.

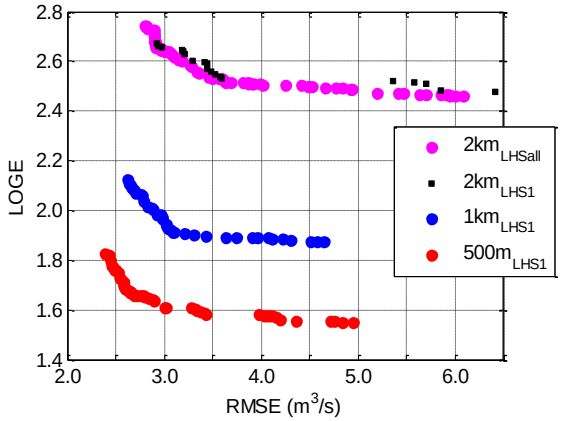

Fig. 6.5 The best known approximation sets shown in filled black squares (and filled purplish red circles), filled blue and red circles respectively for spatial discretization schemes of 2.0, 1.0 and 0.5 km. The subscripts LHS1 and LHSall respectively represent the 1st and all the 30 initial parameter settings generated by the LHS technique. The NSGA-II algorithm with (η_c, η_m) of (0.5, 0.5) was used for calibration.

It is shown that the finer spatial resolution can get better performances through model calibration. From Fig 6.5, two aspects are clear: (1) Based on the same initial

parameter setting LHS1, the finer the spatial resolution the distinctly better the final results obtained from SHETRAN calibrations are, and the separations for LOGE are much larger than those for RMSE; (2) Based on all the 30 trial runs, the final result from the 2.0 km resolution is far inferior to those from the 0.5 and 1.0 km based on the initial setting LHS1. The final approximation set from the spatial resolution of 0.5 km is the best known one for the considered SHETRAN calibration; it is therefore used to calculate the performance indicators, namely hypervolume, Ɛ-indicator, generational distance and Opt-indicator, as described in Section 5.6.2, for comparison of model performances for each optimization step of SHETRAN calibration, at Cobres basin, with the three spatial resolutions.

Figs 6.6a–d respectively compare the hypervolume, Ɛ-indicator, generational distance and Opt-indicator for each optimization step of the calibration processes.

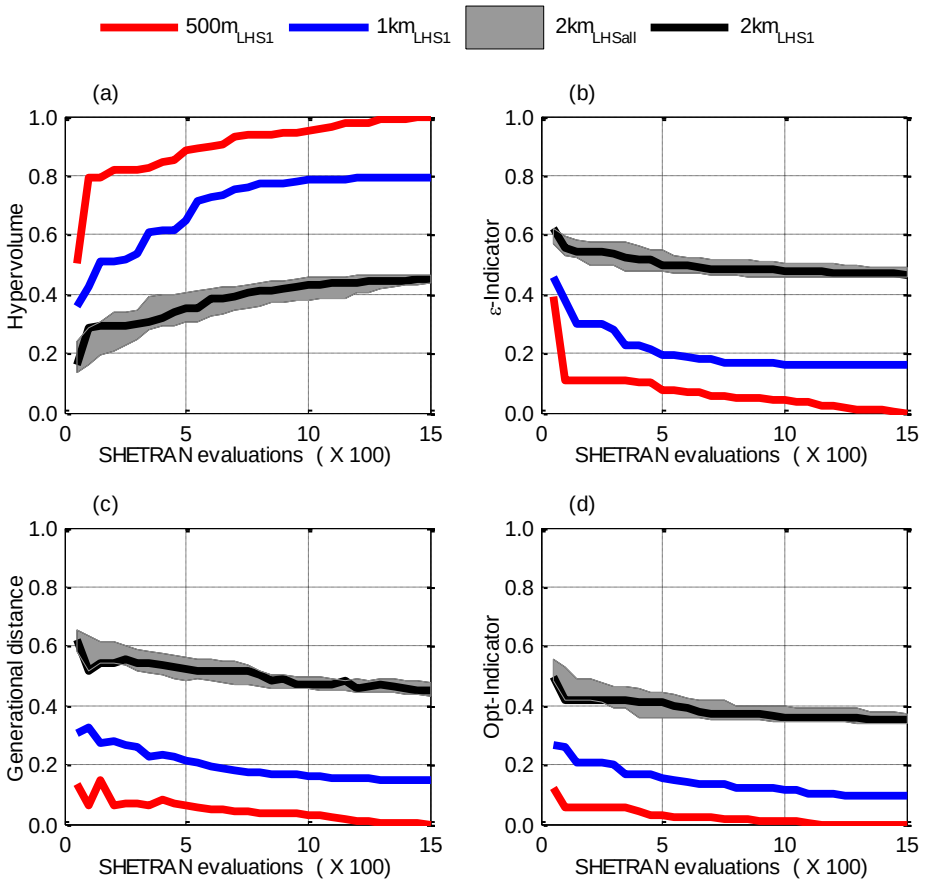

Fig. 6.6 Plots of dynamic performance results of NSGA-II algorithm, namely hypervolume (a), Ɛ-indicator (b), generational distance (c) and opt-indicator (d), versus total number of SHETRAN evaluations. The black (grey shadow area), blue and red solid lines refer to respective spatial discretization schemes of 2, 1.0 and 0.5 km. The subscripts LHS1 and LHSall respectively represent the 1st and all the 30 initial parameter settings generated by the LHS technique.

It is shown that, by using the same initial parameter setting LHS1, the 0.5 km resolution gets much better performances than those for the 1.0 km resolution, and both of them get much better performances than those for the 2.0 km resolution, in terms of all the four indicators and also all the involved optimization steps. Moreover, all of the 30 trial runs of the 2.0 km resolution get performances much inferior to those obtained from the calibration of 0.5 and 1.0 km resolutions based on the initial condition LHS1. In summary, the results from the Figs 6.4a–f (page 71), 6.5 (page 72) and 6.6a–d (page 73) are consistent, showing that the 0.5 km is the best horizontal spatial resolution, 1.0 km the second best and the 2.0 km the third or last, for the SHETRAN simulations at Cobres basin.

- *Model performances for the best solutions*

This section presents the SHETRAN model performances for the best solutions selected by the criterion of NSE ≥ 0.85, with calibration parameters shown in Table 6.2 (pages 75–76), for all the calibration and validation periods, namely 2004–2006, 2006–2008 and 1977–1979. For the sake of space economy, the results are displayed mostly in a single figure and table for all the three periods and for both basin's outlets and internal gauging stations; and, for the same type of results, they are indicated in consecutive figures and tables. However, all the results are described with the separate consideration of the split-sample test, differential split-sample test, proxy-basin test and multi-site test for long-term runoff simulation.

Split-sample test

The split-sample test was evaluated, for both 1.0 and 2.0 km resolutions, based on the model performances at basin outlet for SHETRAN calibrations (October 1st 2004 to September 30th 2006) and validations (October 1st 2006 to September 30th 2008) at Cobres basin. Figs 6.7a and 6.7d (Figs 6.7g and 6.7j) (page 79) display the objective functions RMSE, LOGE and NSE for SHETRAN calibrations (validations). Figs 6.10a–b (Figs 6.10c–d) (page 82) show graphs of observed and simulated hourly discharges at basin outlet for the main period of calibrations (validations). By using the best solution in terms of NSE for calibration, Fig 6.12a (Fig 6.12b) (page 84) compare monthly runoffs, between observations and simulations of SHETRAN calibrations (validations); Tables 6.3 (page 81) indicates the annual mass balance errors and the NSE indicators evaluated for the periods of calibration and validation. The results are consistent and demonstrate that the model performances for 1.0 km resolution are better than those for 2.0 km.

Table 6.2 The SHETRAN key hydrological parameters derived from calibrations at Cobres basin with spatial resolution of 1.0 km and 2.0 km

Parameters (unit)	1.0 km calibration by NSGA-II with (η_c, η_m) of (0.5, 0.5) and LHS1																
	I	II	III	IV	V	VI	VII	VIII	IX	X	XI	XII	XIII	XIV	XV	XVI	XVII
K_1 ($m^{1/3}s^{-1}$)	10.0	10.0	10.0	10.0	10.0	10.0	10.0	10.0	10.0	10.0	10.0	10.0	10.0	10.0	10.0	10.0	8.8
K_2 ($m^{1/3}s^{-1}$)	0.7	0.5	1.2	2.0	2.4	2.7	3.3	5.0	0.6	0.6	1.5	0.8	1.9	0.9	4.4	4.7	3.0
K_{s1} (m/day)	0.136	0.123	0.152	0.168	0.167	0.167	0.167	0.177	0.127	0.136	0.144	0.149	0.192	0.132	0.172	0.172	0.167
θ_{s1} (m^3/m^3)	0.516	0.516	0.516	0.514	0.514	0.514	0.513	0.514	0.516	0.516	0.515	0.516	0.517	0.515	0.517	0.517	0.513
θ_{r1} (m^3/m^3)	0.073	0.073	0.073	0.073	0.073	0.073	0.073	0.073	0.073	0.073	0.073	0.073	0.067	0.073	0.068	0.068	0.073
n_1 (-)	1.221	1.221	1.224	1.221	1.221	1.223	1.222	1.221	1.221	1.221	1.223	1.225	1.221	1.221	1.221	1.221	1.223
α_1 (cm^{-1})	0.0055	0.0055	0.0055	0.0055	0.0055	0.0055	0.0055	0.0076	0.0055	0.0055	0.0056	0.0055	0.0058	0.0058	0.0055	0.0055	0.0055
h_1 (m)	0.30	0.33	0.30	0.30	0.30	0.30	0.30	0.38	0.32	0.30	0.30	0.30	0.33	0.35	0.45	0.41	0.30
K_{s2} (m/day)	0.273	0.218	0.273	0.231	0.223	0.230	0.249	0.218	0.224	0.266	0.290	0.191	0.420	0.220	0.425	0.425	0.244
θ_{s2} (m^3/m^3)	0.418	0.418	0.420	0.419	0.419	0.419	0.419	0.419	0.418	0.418	0.418	0.419	0.418	0.418	0.419	0.419	0.419
θ_{r2} (m^3/m^3)	0.053	0.053	0.053	0.053	0.053	0.053	0.053	0.053	0.053	0.053	0.053	0.053	0.053	0.053	0.053	0.053	0.053
n_2 (-)	1.351	1.345	1.350	1.345	1.345	1.345	1.354	1.345	1.345	1.351	1.347	1.351	1.373	1.345	1.354	1.358	1.345
α_2 (cm^{-1})	0.0075	0.0075	0.0075	0.0075	0.0075	0.0075	0.0075	0.0075	0.0075	0.0075	0.0075	0.0075	0.0075	0.0075	0.0075	0.0075	0.0075
h_2 (m)	0.31	0.31	0.31	0.32	0.32	0.32	0.32	0.32	0.31	0.31	0.31	0.30	0.30	0.31	0.30	0.30	0.32
K_{s3} (m/day)	2.221	2.221	2.221	1.948	2.044	2.092	2.092	2.221	2.221	2.221	2.106	1.670	0.233	2.221	0.756	0.693	2.059
θ_{s3} (m^3/m^3)	0.448	0.457	0.455	0.457	0.457	0.457	0.457	0.456	0.457	0.448	0.456	0.455	0.449	0.457	0.446	0.448	0.457
θ_{r3} (m^3/m^3)	0.120	0.120	0.120	0.120	0.120	0.118	0.117	0.120	0.120	0.119	0.120	0.120	0.111	0.120	0.114	0.114	0.118
n_3 (-)	1.330	1.322	1.324	1.365	1.373	1.346	1.367	1.379	1.322	1.318	1.315	1.338	1.329	1.319	1.350	1.346	1.344
α_3 (cm^{-1})	0.0528	0.0527	0.0436	0.0354	0.0347	0.0347	0.0365	0.0366	0.0527	0.0528	0.0492	0.0404	0.0250	0.0465	0.0620	0.0606	0.0338
h_3 (m)	0.08	0.08	0.08	0.08	0.08	0.08	0.08	0.08	0.08	0.08	0.08	0.08	0.08	0.08	0.08	0.08	0.08
$AETPET_{FC1}$ (-)	0.502	0.501	0.503	0.505	0.505	0.504	0.506	0.500	0.501	0.500	0.502	0.504	0.500	0.501	0.500	0.500	0.505
$AETPET_{FC2}$ (-)	0.600	0.600	0.600	0.600	0.600	0.600	0.600	0.600	0.600	0.600	0.600	0.600	0.600	0.600	0.600	0.600	0.600

Table 6.2 Continued

Parameters (unit)	1.0 km calibration by NSGA-II with (η_c, η_m) of (0.5, 0.5) and LHS1								2.0 km calibration by NSGA-II with (η_c, η_m) of (0.5, 0.5) and LHS1							
	XVIII	XIX	XX	XXI	XXII	XXIII	XXIV	XXV	I	II	III	IV	V	VI	VII	VIII
K_1 ($m^{1/3}s^{-1}$)	10.0	10.0	10.0	10.0	10.0	10.0	9.5	10.0	10.0	9.4	10.0	10.0	10.0	9.1	10.0	10.0
K_2 ($m^{1/3}s^{-1}$)	3.2	3.2	0.9	1.3	2.0	0.8	2.5	1.1	5.0	5.0	5.0	5.0	5.0	5.0	5.0	4.9
K_{s1} (m/day)	0.168	0.169	0.145	0.145	0.192	0.153	0.168	0.148	0.190	0.192	0.192	0.192	0.192	0.192	0.188	0.192
θ_{s1} (m^3/m^3)	0.514	0.514	0.516	0.515	0.517	0.516	0.510	0.515	0.510	0.514	0.508	0.517	0.508	0.513	0.510	0.517
θ_{r1} (m^3/m^3)	0.073	0.073	0.073	0.073	0.068	0.073	0.073	0.073	0.068	0.065	0.069	0.068	0.067	0.068	0.068	0.068
n_1 (-)	1.221	1.221	1.221	1.223	1.221	1.223	1.221	1.222	1.260	1.264	1.301	1.261	1.332	1.274	1.280	1.268
α_1 (cm^{-1})	0.0055	0.0055	0.0055	0.0056	0.0058	0.0055	0.0055	0.0056	0.0055	0.0055	0.0055	0.0055	0.0055	0.0055	0.0055	0.0055
h_1 (m)	0.41	0.41	0.30	0.30	0.33	0.30	0.30	0.30	0.65	0.65	0.65	0.65	0.65	0.65	0.65	0.65
K_{s2} (m/day)	0.211	0.191	0.259	0.261	0.358	0.282	0.251	0.287	0.425	0.425	0.420	0.425	0.420	0.425	0.425	0.425
θ_{s2} (m^3/m^3)	0.420	0.420	0.419	0.418	0.418	0.420	0.419	0.418	0.418	0.418	0.418	0.418	0.418	0.418	0.418	0.418
θ_{r2} (m^3/m^3)	0.053	0.053	0.053	0.053	0.053	0.053	0.053	0.053	0.049	0.051	0.053	0.049	0.053	0.050	0.049	0.050
n_2 (-)	1.345	1.345	1.350	1.345	1.370	1.350	1.351	1.345	1.345	1.350	1.345	1.345	1.345	1.352	1.345	1.345
α_2 (cm^{-1})	0.0075	0.0075	0.0075	0.0075	0.0075	0.0075	0.0075	0.0075	0.0075	0.0075	0.0075	0.0075	0.0075	0.0075	0.0075	0.0075
h_2 (m)	0.32	0.32	0.31	0.31	0.30	0.31	0.32	0.31	0.30	0.30	0.30	0.30	0.30	0.30	0.30	0.30
K_{s3} (m/day)	2.221	2.221	2.221	2.221	0.988	2.221	1.960	2.221	1.640	1.992	1.911	1.777	1.779	1.814	1.696	1.812
θ_{s3} (m^3/m^3)	0.457	0.457	0.455	0.455	0.448	0.455	0.457	0.455	0.452	0.453	0.457	0.453	0.453	0.452	0.452	0.453
θ_{r3} (m^3/m^3)	0.113	0.120	0.119	0.120	0.104	0.120	0.120	0.120	0.055	0.051	0.051	0.051	0.051	0.051	0.056	0.051
n_3 (-)	1.382	1.378	1.331	1.313	1.331	1.325	1.351	1.329	1.311	1.311	1.311	1.319	1.324	1.311	1.311	1.318
α_3 (cm^{-1})	0.0386	0.0341	0.0577	0.0543	0.0349	0.0444	0.0348	0.0544	0.0263	0.0268	0.0250	0.0269	0.0250	0.0268	0.0268	0.0269
h_3 (m)	0.08	0.08	0.08	0.08	0.08	0.08	0.08	0.08	0.05	0.05	0.05	0.05	0.05	0.05	0.05	0.05
$AETPET_{FC1}$ (-)	0.501	0.501	0.503	0.502	0.500	0.503	0.507	0.502	0.500	0.500	0.502	0.500	0.502	0.500	0.500	0.500
$AETPET_{FC2}$ (-)	0.600	0.600	0.600	0.600	0.600	0.600	0.600	0.600	0.626	0.626	0.627	0.625	0.629	0.627	0.630	0.630

For SHETRAN calibrations, the results indicate that the use of 1.0 km resolution in SHETRAN simulation at Cobres basin improves LOGE to a great extent and RMSE, NSE (Figs 6.7a and 6.7d, page 79) and peak discharge error (Figs 6.10a–b, page 82) to a moderate extent, but do not lead to distinct differences in monthly (Fig 6.12a, page 84) and annual (Table 6.3, page 81) mass balance errors. The simulations with 1.0 km resolution have RMSE, LOGE and NSE in the ranges of [2.6, 3.0] m^3/s, [1.9, 2.1] and [0.85, 0.89], and those with 2.0 km have values around 3.0 m^3/s, 2.7 and 0.86. Figs 6.10a–b show that the use of 1.0 km resolution raises the simulated peak discharges, making the simulation closer to observations. Fig 6.11a (page 83) indicates that the calibration period is dry and runoff mainly occurred in November 2005; Fig 6.12a demonstrates that all the simulations represent well the monthly runoff for November 2005. Fig 6.12a and Table 6.3 show no distinct differences for the simulated monthly and annual runoffs between the 1.0 and 2.0 km resolutions.

For SHETRAN validations, the results indicate that the use of 1.0 km resolution greatly improves RMSE and NSE and slightly reduces LOGE (Figs 6.7g and 6.7j, page 79) and peak discharge errors (Figs 6.10c–d, page 82) as well as monthly (Fig 6.12b, page 84) and annual (Table 6.3) mass balance errors. The simulations with 1.0 km resolution have RMSE, LOGE and NSE in the ranges of [4.4, 4.9] m^3/s, [2.5, 2.6] and [0.74, 0.79], and those with 2.0 km have values around 5.4 m^3/s, 2.7 and 0.69. Figs 6.10c–d (page 82) indicate that the use of 1.0 km resolution raises the simulated peak discharges. Fig 6.11b (page 83) show that October 2006, November 2006 and December 2006 are months with distinct runoffs and from Fig 6.12b it can be concluded that the use of 1.0 km resolution distinctly increased the simulated monthly runoffs in these months. In Table 6.3, the best simulations underestimated the runoffs by 27% and 38% respectively for 1.0 and 2.0 km resolutions for the entire 2-year period.

Differential split-sample test

As shown in Figs 6.11a–c (page 83), the period from October 1st, 1977 to September 30th, 1979 is a very wet period (Bathurst *et al*., 1996), with a climate condition distinctly different from those prevailing in the periods used in the split-sample test. Therefore, validations for that period can provide a differential split-sample test of the SHETRAN model. Figs 6.8a–b (page 80), 6.10e–h (page 82), 6.12c (page 84) and Table 6.3 respectively show the objective functions RMSE, LOGE and NSE, graphics of model fit and monthly and annual mass balance errors for the differential split-sample test. The results are satisfactory for simulations with both 1.0 and 2.0 km resolutions; the use of 1.0 km resolution improves slightly model performances in terms of peak discharge and

monthly and annual mass balance errors. Figs 6.8a–b (page 80) indicate that the simulations with 1.0 km resolution have RMSE, LOGE and NSE around 14.0 m^3/s, 2.8 and [0.78, 0.79], and those with 2.0 km around 13.5 m^3/s, 3.1 and 0.80. Figs 6.10e–h (page 82) show that the use of 1.0 km resolution slightly improves the simulation of peak discharges. Fig 6.11c (page 83) shows that December 1977, March 1978, December 1978, January 1979 and February 1979 are months with runoffs larger than 50 mm; Fig 6.12c (page 84) demonstrates that the use of 1.0 km resolution has slightly increased the simulated monthly runoff in December 1978. In Table 6.3 (page 81) it can be seen that, the best simulations underestimated total runoff by 18% and 22%, respectively for 1.0 and 2.0 km resolutions, during the entire 2-year period.

Proxy-basin test

The results of the proxy-basin test are shown in Figs 6.9a–h (page 80) and Table 6.4 (page 83), respectively for the objective functions RMSE, LOGE and NSE and the annual mass balance errors, evaluated from the SHETRAN simulations at Albernoa basin. According to Moriasi *et al*. (2007), model simulations can be judged satisfactory if NSE > 0.50 and MBE ±25% for streamflow. The NSE (and the absolute value of MBE) are, for basin outlet and internal gauging station Entradas, respectively around 0.55 and 0.80 (less than 25% and 33%) for the validation period from October 1st 2004 to September 30th 2006; the NSE (and the absolute value of MBE) are, for both basin outlet and Entradas, around 0.60 (less than 25%) for the validation period from October 1st 2006 to September 30th 2008. The model performances for SHETRAN simulations at Albernoa basin are considered satisfactory. However, there are no clear improvements of model performances by using the parameters derived from calibrations at Cobres basin, with finer spatial resolution.

Multi-site test

The results for internal gauging stations are shown in Table 6.3 (page 81) and the second and third columns of Fig 6.7 (page 79), for SHETRAN simulations at Cobres basin from October 1st 2004 to September 30th 2008; they are displayed in Table 6.4 (page 83) and the second and fourth columns of Fig 6.9 (page 80) for SHETRAN simulations at Albernoa basin from October 1st 2004 to September 30th 2008. The NSE (MBE), for internal gauging stations Albernoa and Entradas, are at least around 0.70 (±30%) from the SHETRAN simulations at Cobres basin; the NSE (MBE) is, for internal gauging station Entradas, at least around 0.60 (±30%) from the SHETRAN simulations at Albernoa basin. Thus, the model performances for the multi-site test are considered

satisfactory. In addition, the improvements of model performance by using the finer spatial resolution are identified for some but not all cases.

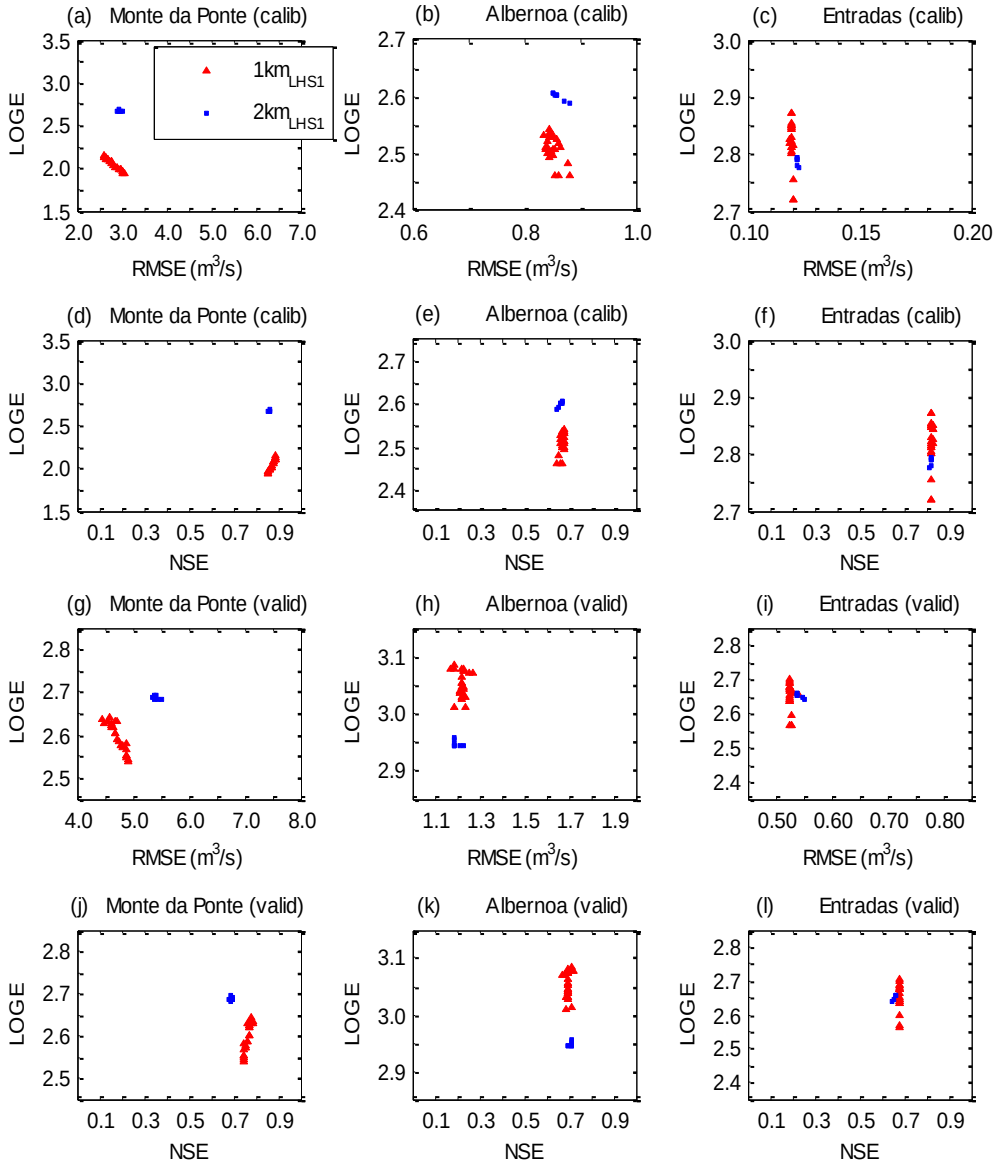

Fig. 6.7 Plots of SHETRAN model performance indicators, namely RMSE, LOGE and NSE, at basin outlet Monte da Ponte (a, d, g and j) and internal gauging stations Albernoa (b, e, h and k) and Entradas (c, f, i and l). The results for the calibration period (2004–2006) are denoted by "(calib)" and those for the validation period (2006–2008) by "(valid)". The filled red triangles and blue squares represent the solutions with NSE values higher or equal to 0.85, for calibration, derived respectively from the spatial discretization schemes of 1.0 and 2.0 km. The subscript LHS1 represents the 1st initial parameter setting generated by the LHS technique.

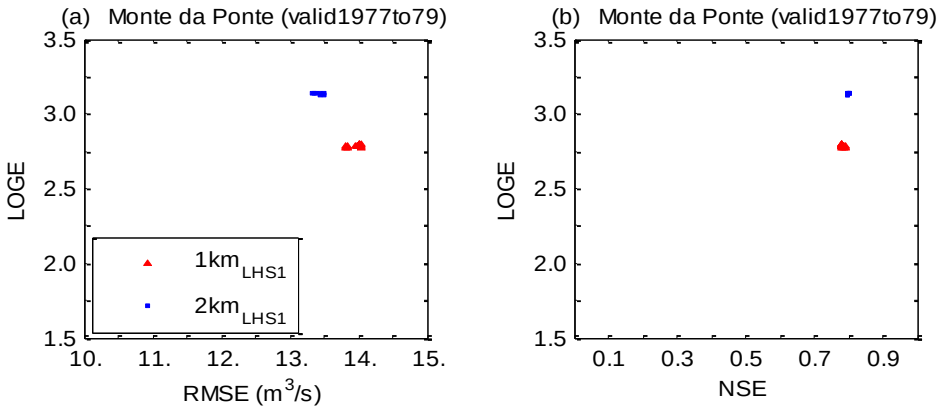

Fig. 6.8 Plots of SHETRAN model performance indicators, namely RMSE, LOGE and NSE, at basin outlet Monte da Ponte gauging station. The results are for the validation period 1977–1979. The filled red triangles and blue squares represent the solutions with NSE values higher or equal to 0.85, for calibration, derived respectively from the spatial discretization schemes of 1.0 and 2.0 km. The subscript LHS1 denotes the initial parameter setting used in model calibration.

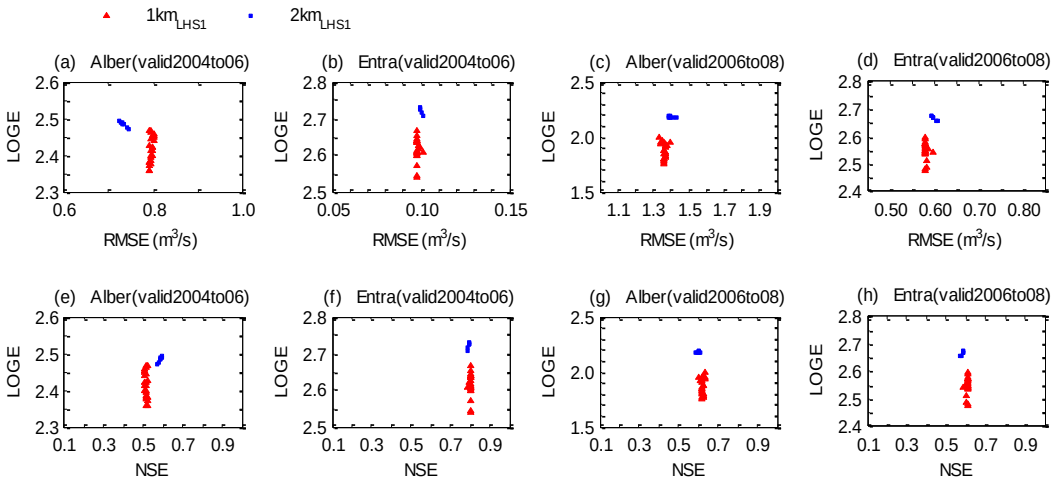

Fig. 6.9 Plots of SHETRAN model performance indicators, namely RMSE, LOGE and NSE, at basin outlet Albernoa (a, c, e and g) and internal gauging station Entradas (b, d, f and h). The results for the validation period (2004–2006) are denoted by "(valid2004to06)" and those for the validation period (2006–2008) by "(valid2006to08)". The filled red triangles and blue squares represent the solutions with NSE values higher or equal to 0.85, for SHETRAN calibration, at Cobres basin with respective spatial resolutions of 1.0 and 2.0 km. The subscript LHS1 denotes the initial parameter setting used in model calibration.

Table 6.3 Comparison of the model performances for the SHETRAN simulations at Cobres basin with spatial resolutions of 1.0 km and 2.0 km

Simulation[a]	Year	Rainfall (mm)	PET (mm)	Monte da Ponte (Basin outlet)					Albernoa (Internal gauging station)					Entradas (Internal gauging station)				
				R_{obs}	MBE (%)		NSE		R_{obs}	MBE (%)		NSE		R_{obs}	MBE (%)		NSE	
					1km	2km	1km	2km		1km	2km	1km	2km		1km	2km	1km	2km
Calibration[b]	2004-05[d]	1.8 (194.2)	358.2 (1475.7)	0.0 (11.6)	0	0	-	-	0.0 (0.1)	0	0	-	-	0.0 (0.0)	0	0	-	-
	2005-06	502.5	1345.8	55.1	-16	-16	-	-	50.5	-24	-28	-	-	44.8[f]	-35	-28	-	-
	2004-06[d]	504.3	1704.0	55.1	-16	-16	0.89	0.86	50.5	-24	-28	0.67	0.67	44.8[f]	-35	-28	0.82	0.82
Validation1[b]	2006-07[e]	447.2 (532.2)	1267.6 (1272.9)	104.5 (-)	-32	-41	-	-	79.6[g] (-)	-5	-16	-	-	130.1 (-)	-28	-17	-	-
	2007-08	421.4	1274.1	25.6	-7	-26	-	-	12.5	82	50	-	-	5.3	133	169	-	-
	2006-08[e]	868.7	2541.7	130.1	-27	-38	0.77	0.69	92.1[g]	7	-7	0.71	0.71	135.4	-22	-10	0.68	0.66
Validation2[c]	1977-78	648.0	1355.6	222.7	-20	-25	-	-	-	-	-	-	-	-	-	-	-	-
	1978-79	766.7	1417.9	385.8	-17	-20	-	-	-	-	-	-	-	-	-	-	-	-
	1977-79	1414.7	2773.5	608.5	-18	-22	0.79	0.80	-	-	-	-	-	-	-	-	-	-

[a]Years are defined from October to September; R_{obs} represent observed runoff.
[b]Basin mean rainfall based on six rain gauges indicated in Fig. 5.1 (page 26) (SNIRH); FAO Penman-Monteith PET from the meteorological station at Beja, provided by SAGRA/COTR.
[c]Rainfall, PET and discharge data, provided by Dr.Bathurst, which were used in Bathurst *et al*. (1996).
[d]Only August and September in 2005 are considered for calibration, and annual statistics of the year are presented in parenthesis.
[e]Data missing period, from November 4th 2006 23:00 to November 8th 2006 16:00, is not included, and annual statistics of the year are presented in parenthesis.
[f]Data missing, from November 19th 2005 09:00 to November 25th 2005 09:00, is not included.
[g]Data missing, from February 3rd 2007 17:00 to March 6th 2007 15:00, is not included.

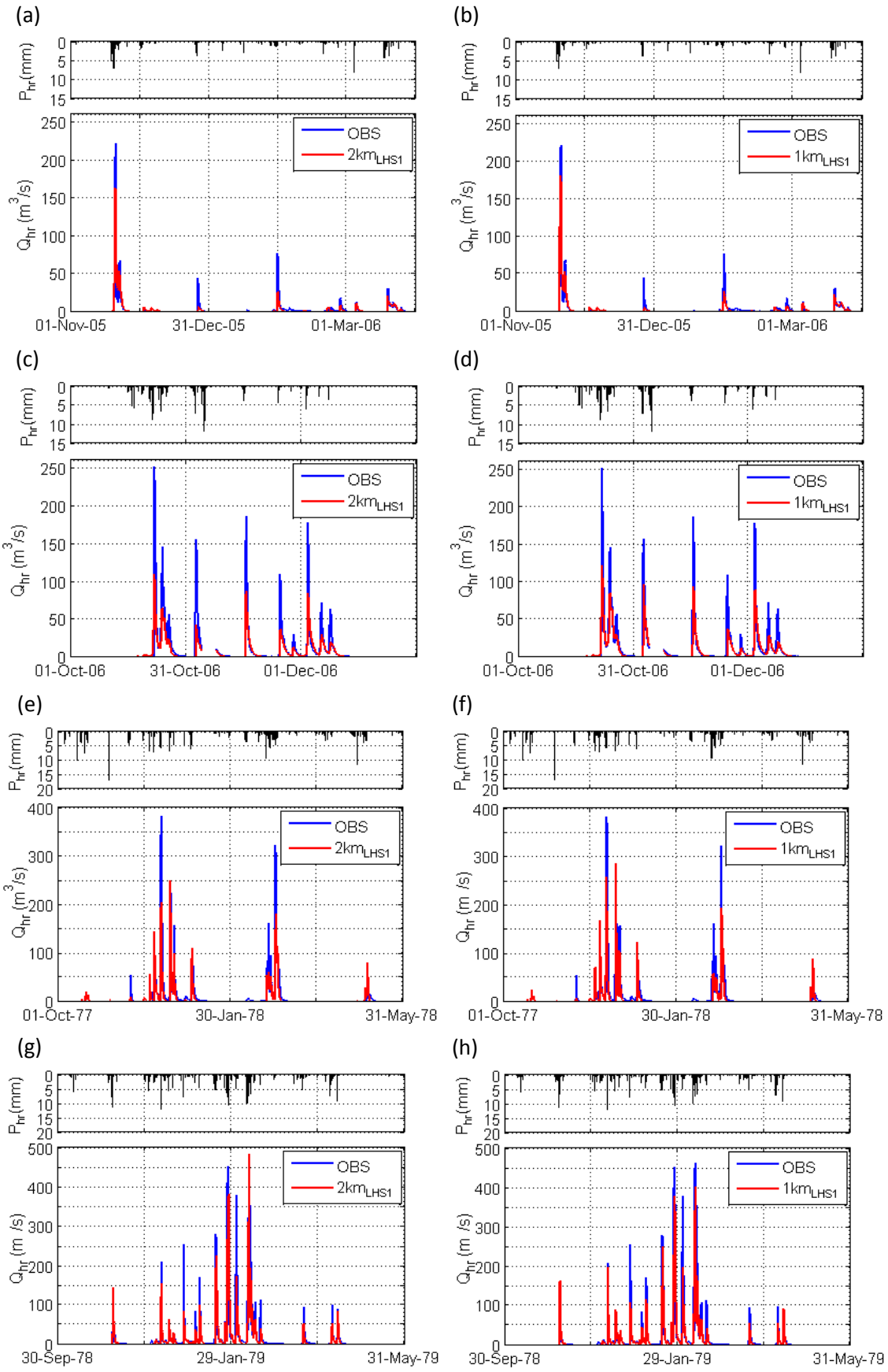

Fig. 6.10 Comparisons of observed and simulated hourly discharges from the SHETRAN calibrations for Cobres basin with respective spatial resolutions of 2.0 and 1.0 km during the main periods of simulations.

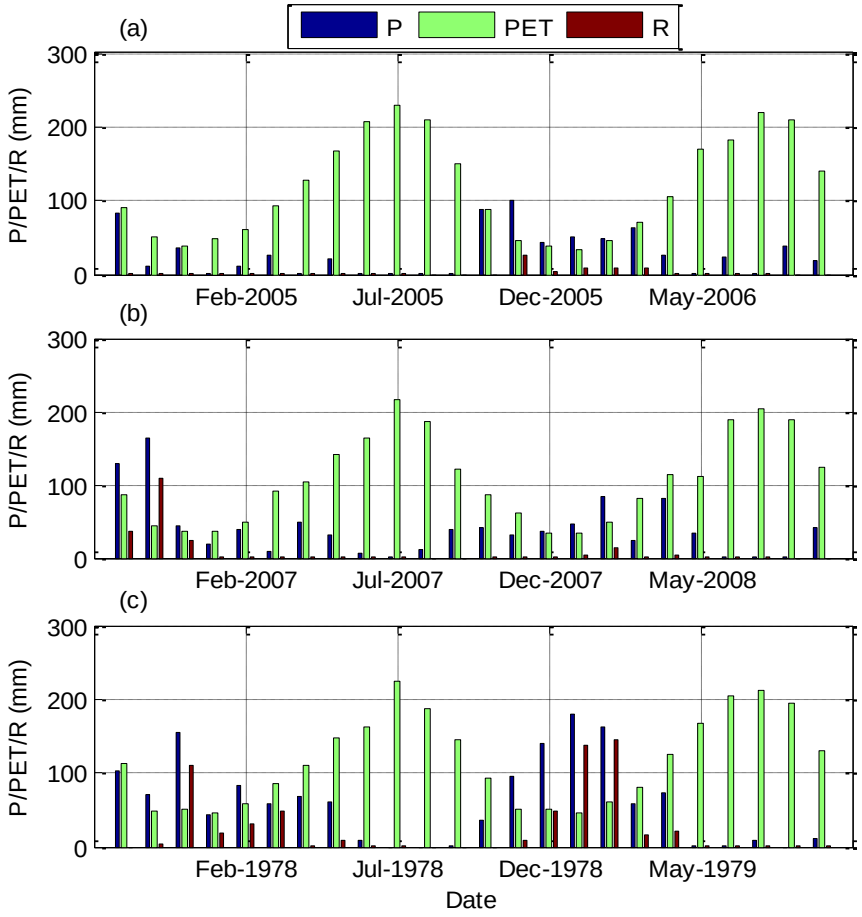

Fig. 6.11 Plots of monthly precipitation (P), potential evapotranspiration (PET) and runoff (R) for the calibration period 2004–2006 (a), the validation periods 2006–2008 (b) and 1977–1979 (c).

Table 6.4 Comparison of model performances for SHETRAN validation simulations at Albernoa basin with spatial resolutions of 1.0 km and 2.0 km

Simulation[a]	Year	Albernoa (Basin outlet)					Entradas (Internal gauging station)				
		R_{obs}	MBE (%)		NSE		R_{obs}	MBE (%)		NSE	
			1km	2km	1km	2km		1km	2km	1km	2km
Validation4	2004-05[b]	0.0	0	0	-	-	0.0	0	0	-	-
	2005-06	50.5	-11	2	-	-	44.8[d]	-33	-30	-	-
	2004-06[b]	50.5	-11	2	0.51	0.59	44.8[d]	-33	-30	0.80	0.80
Validation5	2006-07[c]	79.6[e]	18	3	-	-	130.1	-28	-20	-	-
	2007-08	12.5	13	-19	-	-	5.3	112	105	-	-
	2006-08[c]	92.1[e]	17	0	0.63	0.60	135.4	-23	-15	0.61	0.59

[a]Years are defined from October to September; R_{obs} represent observed runoff.
[b]Only August and September in 2005 are considered for calibration.
[c]Data missing period, from November 4th 2006 23:00 to November 8th 2006 16:00, is not included.
[d]Data missing, from November 19th 2005 09:00 to November 25th 2005 09:00, is not included.
[e]Data missing, from February 3rd 2007 17:00 to March 6th 2007 15:00, is not included.

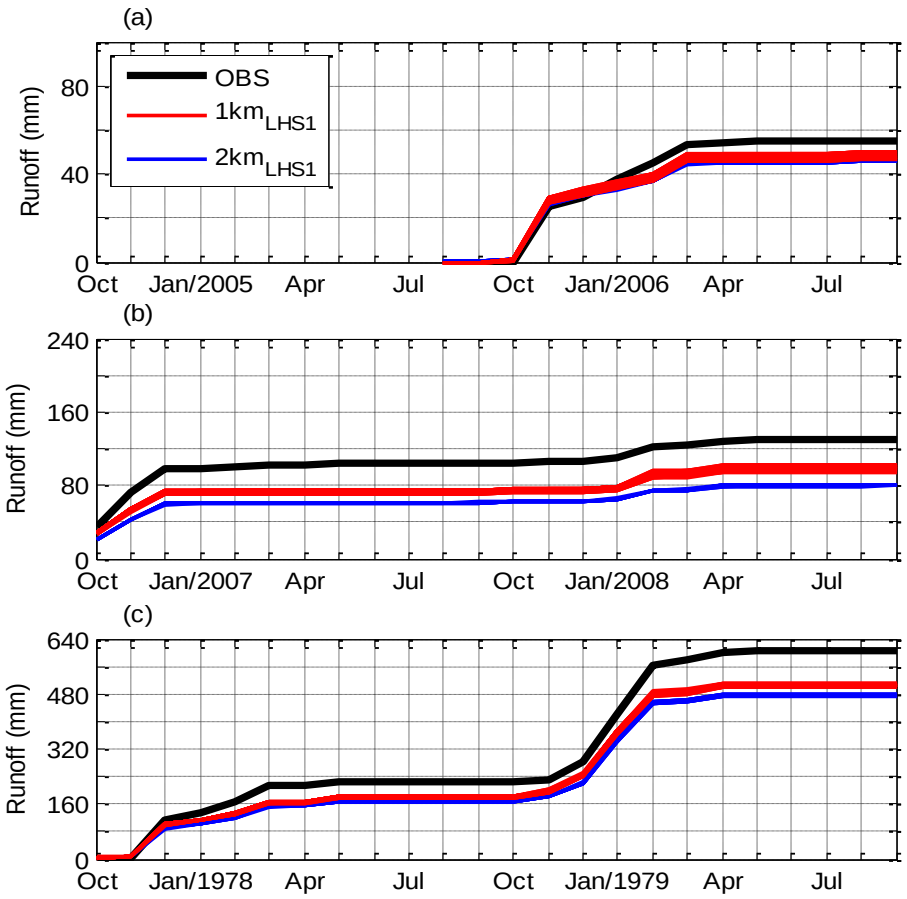

Fig. 6.12 Comparisons of accumulated monthly runoff at Monte da Ponte gauging station between observations (OBS) and the simulations by SHETRAN model, with respective spatial resolutions of 2.0 km (2kmLHS1) and 1.0 km (1kmLHS1), shown in thick black and normal red and blue lines. For the spatial discretization schemes of 1.0 and 2.0 km, the 8 and 25 solutions with values of NSE higher or equal to 0.85, for calibration, are displayed; for SHETRAN calibration, the NSGA-II algorithm with (η_c, η_m) of (0.5, 0.5) and initial parameter setting of LHS1 was used.

6.4.3 Impacts of Spatial Scale on Storm-Runoff Generation

Table 6.5 (page 85) has listed the observed characteristics of the 11 selected "large storm events" at Cobres basin. Storm No.1 is from the SHETRAN calibration period 2004–2006, storm No.4 is from the validation period 2006–2008 and storms No. I, II, III, IV, V, VI, VII, VIII and IX are from the validation period 1977–1979. Figs 6.13 (page 85) and 6.14a–b (page 86) display the performance indicators NSE, MBE and PKE for the selected large storm events; for storm No.4, performance indicators, evaluated at internal gauging stations Albernoa and Entradas, have also been displayed. The graphic comparisons of these events are shown in Figs 6.15a–d (page 87) for storms No.1 and 4, in Figs 6.16a–d (page 88) for storms No.I, II, III and IV and in Figs 6.17a–e (page 89) for storms No. V, VI, VII, VIII and XI.

Table 6.5 Observed characteristics of the 11 selected "large storm events" at Cobres basin

No.	Storm period	P (mm)	I_{mean} (mm/h)	I_{max} (mm/h)	R (mm)	C_R (%)	Q_b (m^3/s)	Q_p (m^3/s)
1	20–25 Nov, 2005	27.2	1.0	4.0	24.8	91.0	3.9	220.0
4	23–29 Oct, 2006	46.8	1.1	6.9	35.1	74.9	0.6	249.6
I	11–13 Dec, 1977	13.8	1.7	6.1	44.0	318.2	28.9	379.2
II	18–23 Dec, 1977	52.6	2.3	7.1	38.2	72.6	22.5	245.0
III	2–5 Mar, 1978	42.7	1.8	4.9	42.0	98.3	23.6	320.0
IV	11–13 Dec, 1978	11.1	3.7	9.1	11.9	106.4	2.9	208.6
V	27–29 Dec, 1978	19.3	3.2	8.0	13.6	70.6	6.0	253.5
VI	17–21 Jan, 1979	48.2	1.7	5.7	39.7	82.3	1.8	278.3
VII	26–29 Jan, 1979	60.8	3.0	10.7	58.0	95.4	14.1	450.6
VIII	1–4 Feb, 1979	29.2	1.3	5.3	37.0	126.6	7.8	377.5
IX	9–13 Feb, 1979	88.0	2.3	10.1	74.9	85.1	6.0	459.5

Note: P, rainfall; I_{mean}, mean rainfall intensity; I_{max}, maximum rainfall intensity; R, total runoff at basin outlet (area under curve of hydrograph); C_R, storm runoff coefficient (C_R = R/P); Q_b, baseflow (at the start of the flood); Q_p, peakflow (maximum peakflow for processes with multiple peaks).

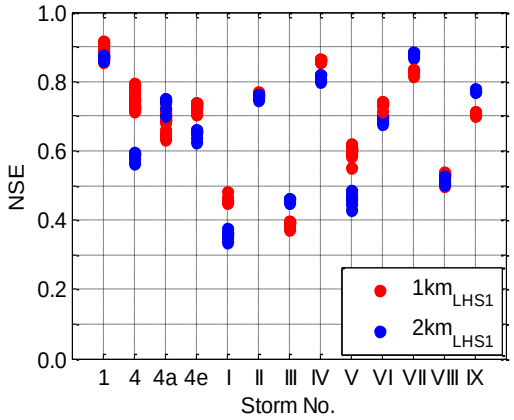

Fig. 6.13 NSE indicators for the SHETRAN simulations of the storms No.1, 4, I, II, III, IV, V, VI, VII, VIII and IX at Cobres basin with spatial resolutions of 1.0 and 2.0 km respectively shown in red and blue filled circles. The abscissa tick marks of 4, 4a and 4e are for storm No.4, showing results respectively evaluated at basin outlet and internal gauging stations Albernoa and Entradas; the others are for the respective storms evaluated at basin outlet. For the spatial discretization schemes of 1.0 and 2.0 km, the 8 and 25 solutions with values of NSE higher or equal to 0.85, for calibration, are displayed; for SHETRAN calibration, the NSGA-II algorithm with (η_c, η_m) of (0.5, 0.5) and initial parameter setting of LHS1 was used.

It can be seen that the results are very satisfactory for simulations of both 1.0 and 2.0 km resolutions; as a whole, the use of 1.0 km resolution has improved the simulations of storm-runoff generation in terms of NSE, MBE, PKE and model fit. According to Moriasi *et al*. (2007), the NSE with values in the ranges [-∞, 0.50], [0.50, 0.65], [0.65, 0.75] and [0.75, 1.00] are classified as unsatisfactory, satisfactory, good and very good. Accordingly, by using 1.0 km resolution, 5 storms (No.1, 4, II, IV and VII) are very well simulated, 2 storms (No.VI and IX) are well simulated, 2 storms (No.V and VIII) are

satisfactorily simulated and 2 storms (No.I and III) are unsatisfactorily simulated; by using 2.0 km resolution, 5 storms (No.1, II, IV, VII and IX) are very well simulated, 1 storm (No.VI) is well simulated, 2 storms (No.4 and VIII) are satisfactorily simulated and 3 storms (No.I, III and V) are unsatisfactorily simulated (Fig 6.13, page 85). In most cases, the simulations with 1.0 km resolution produce smaller mass balance and peak errors than those with 2.0 km resolution (Figs 6.14a–b). The use of 1.0 km (2.0 km) resolution has produced MBE with absolute values less than 25% for 8 (7) out of 11 storms; and the use of 1.0 km (2.0 km) resolution has produced PKE with absolute values less than 25% for 6 (6) out of 11 storms.

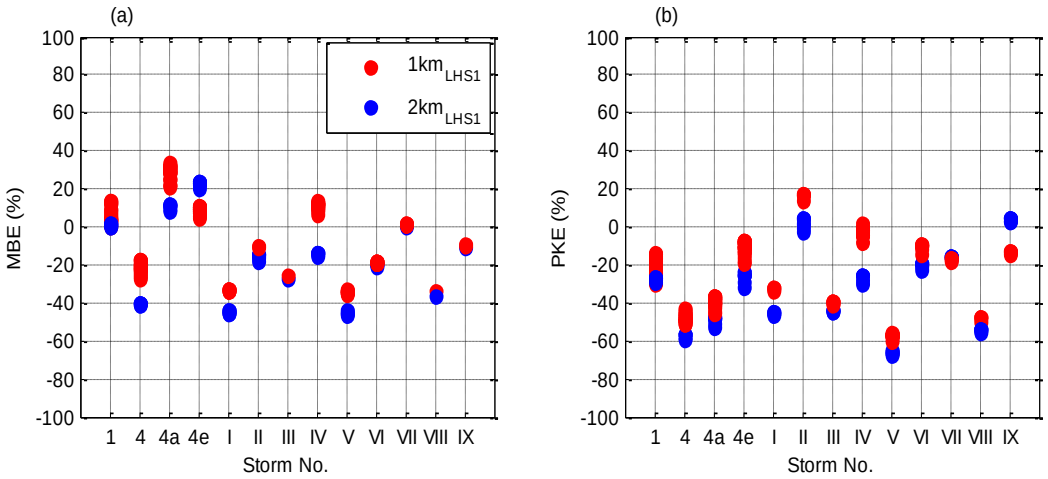

Fig. 6.14 MBE and PKE indicators for the SHETRAN simulations of the storms No.1, 4, I, II, III, IV, V, VI, VII, VIII and IX at Cobres basin with spatial resolutions of 1.0 and 2.0 km respectively shown in filled red and blue circles.

For the calibration period 2004–2006, storm No.1 was very well represented, in terms of NSE, MBE, PKE and model fit, by simulations with both 1.0 and 2.0 km resolutions; the use of 1.0 km resolution has improved the simulation of storm No.1 in terms of NSE, PKE and model fit. To be specific, for storm No.1, the NSE, MBE and PKE are in the ranges of [0.86, 0.92], [0%, 14%] and [-30%, -14%], and [0.86, 0.87], [0%, 2%] and [-30%, -27%], respectively for simulations with 1.0 and 2.0 km resolutions. For the validation period 2006–2008, storm No.4 was largely underestimated for basin outlet; the use of 1.0 km resolution has improved the simulation of storm No.4 in terms of NSE, MBE, PKE and model fit for basin outlet and the internal gauging station Entradas, as well as PKE for the internal gauging station Albernoa. For storm No.4, the NSE, MBE and PKE are in the ranges of [0.71, 0.79], [-28%, -17%] and [-51%, -43%], and [0.56, 0.59], [-41%, -40%] and [-59%, -56%], for basin outlet from simulations respectively with 1.0 and 2.0 km resolutions; the NSE, MBE and PKE are in the ranges of [0.63, 0.74], [21%, 33%] and [-46%, -37%], and [0.70, 0.75], [8%, 12%] and [-53%, -48%], for

Albernoa, from simulations respectively with 1.0 and 2.0 km resolutions; and the NSE, MBE and PKE are in the ranges of [0.71, 0.74], [5%, 11%] and [-19%, -7%], and [0.62, 0.66], [20%, 24%] and [-32%, -24%], for Entradas, from simulations respectively with 1.0 and 2.0 km resolutions.

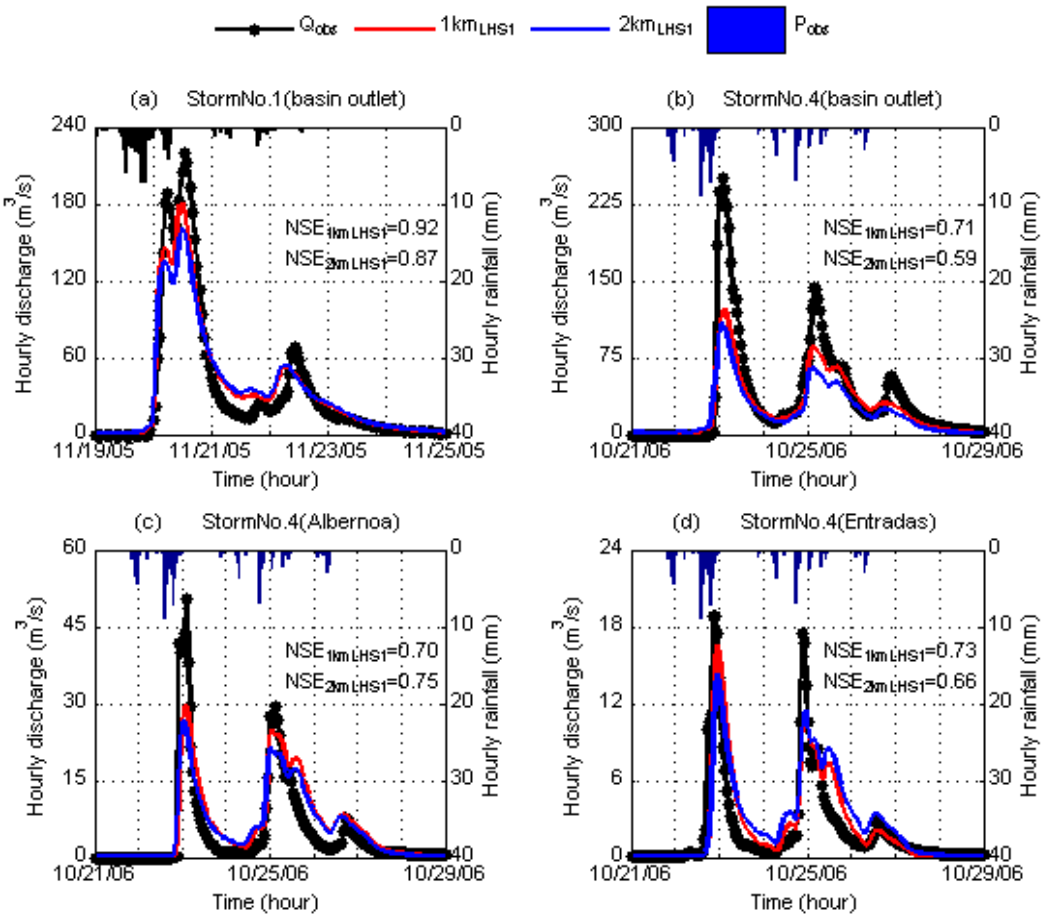

Fig. 6.15 Observed and simulated discharges from the SHETRAN calibrations by the NSGA-II algorithm with (η_c, η_m) of (0.5, 0.5) for the Cobres basin with spatial resolutions of 2.0 and 1.0 km: (a) Storm No.1 at basin outlet; (b) Storm No.4 at basin outlet; (c) Storm No.4 at internal gauging station Albernoa; (d) Storm No.4 at internal gauging station Entradas.

For the validation period 1977–1979, storms No.VII and IX are events with peak discharges around 450 m^3/s and total runoff volumes around or larger than 60 mm. They are the largest events considered in this study and have been well simulated with both 1.0 and 2.0 km resolutions. However, from Fig 6.13, 6.14a–b, 6.17c and 6.17e (pages 85, 86 and 89), the use of 1.0 km resolution does not seem to have improved the simulations for the two storms. For storm No.VII, the NSE, MBE and PKE are in the ranges of [0.81, 0.83], [1%, 2%], [-18%, -16%], and [0.87, 0.89], [0%, 1%], [-17%, -15%], respectively for simulations with 1.0 and 2.0 km resolutions; for storm No.IX, the NSE, MBE and PKE are in the ranges of [0.70, 0.71], [-10%, -9%], [-15%, -

13%], and [0.77, 0.78], -11%, [2%, 5%], respectively for simulations with 1.0 and 2.0 km resolutions. The storms No.I, III and VIII are events with peak discharges and total runoff volumes respectively in the ranges of [320, 380] m^3/s and [37, 44] mm. They are the events with second largest peak discharges and have been relatively poorly simulated with NSE values respectively around 0.40, 0.40 and 0.50. The SHETRAN simulations have largely underestimated the peak discharges and total runoff volumes. From Figs 6.13, 6.14a–b, 6.16a–c and 6.17d (pages 85, 86, 88 and 89), the use of 1.0 km resolution has improved the simulations for storm No.I but not for storms Nos.III and VIII. The storms Nos.II, IV, V and VI are events with peak discharges and total runoff volumes respectively in the ranges of [209, 278] m^3/s and [12, 40] mm. The simulations have represented well the storms Nos.II, IV and VI with NSE of values respectively around 0.75, 0.85 and 0.70 and relatively poorly the storm No.V with NSE around 0.5. From Figs 6.13, 6.14a–b, 6.16b–d and 6.17a–b, the use of 1.0 km resolution has distinctly improved the simulations for the storms IV and V in terms of NSE, MBE and PKE.

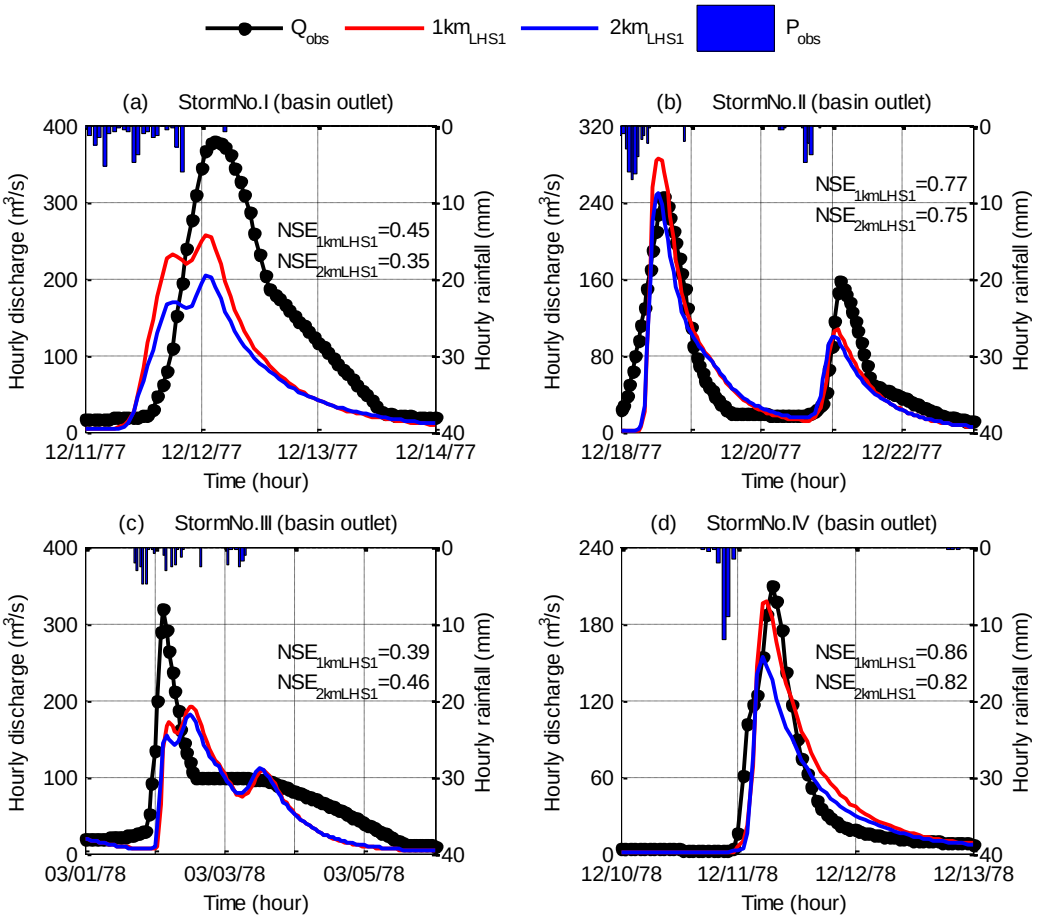

Fig. 6.16 Observed and simulated discharges at basin outlet from the SHETRAN calibrations by the NSGA-II algorithm with (η_c, η_m) of (0.5, 0.5) for the Cobres basin with spatial resolutions of 2.0 and 1.0 km: (a) Storm No.I; (b) Storm No.II; (c) Storm No.III and (d) Storm No.IV.

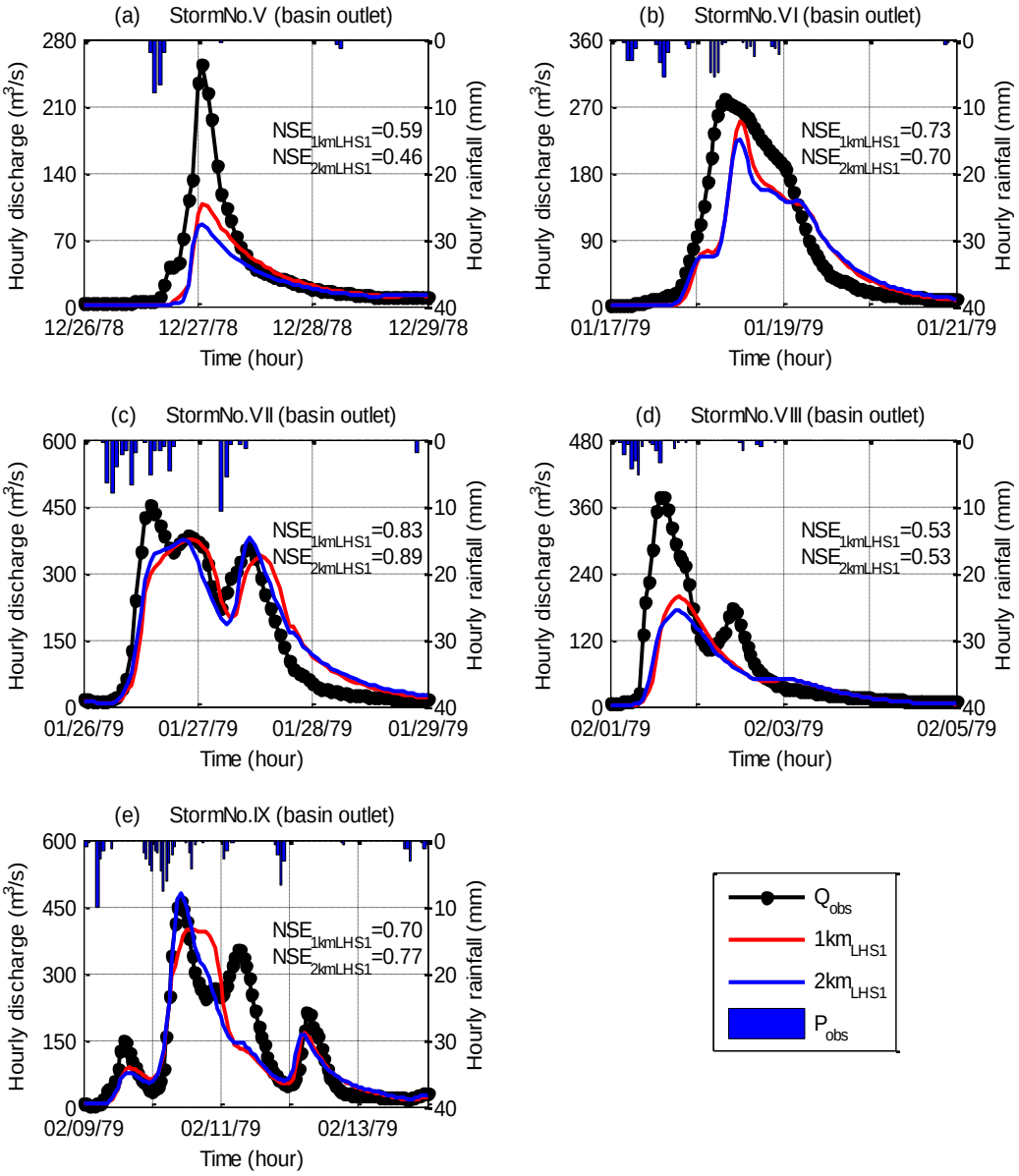

Fig. 6.17 Observed and simulated discharges at basin outlet from the SHETRAN calibrations by the NSGA-II algorithm with (η_c, η_m) of (0.5, 0.5) for the Cobres basin with spatial resolutions of 2.0 and 1.0 km: (a) Storm No.V; (b) Storm No.VI; (c) Storm No.VII; (d) Storm No.VIII and (e) Storm No.IX.

6.5 Discussion

The selection of an appropriate spatial resolution for SHETRAN hydrological simulation is important, due to the consideration of the computational requirements and model performances. This chapter aimed to investigate the impacts of horizontal spatial resolution on model performances of the SHETRAN hydrological simulations at Cobres basin. A fully objective global optimization method, NSGA-II algorithm, was used to compare the results from the simulations for the spatial resolutions 0.5, 1.0 and 2.0 km, in terms of the objective functions RMSE, LOGE and NSE. The results have shown

that, in descending order, from high to low, the fit of the spatial resolutions to the model simulations at Cobres basin is: 0.5, 1.0 and 2.0 km. The use of finer spatial resolution has improved LOGE to a substantial extent and RMSE and NSE to a moderate extent.

The SHETRAN calibrations were validated for simulations with spatial resolutions of 1.0 and 2.0 km for possible future applications. Based on the criterion of NSE ≥ 0.85, 8 and 25 best solutions were selected from the SHETRAN calibrations at Cobres basin with the spatial resolutions of respectively 1.0 and 2.0 km. The validation was successfully carried out for all the selected solutions, considering the four aspects: split-sample test, differential split-sample test, proxy-basin test and multi-site test. The good SHETRAN performances for both calibrations and validations, in terms of long-term runoff and storm-runoff evaluations, led to the fulfillment of the equifinality phenomenon (Beven and Freer 2001).

As a whole, the results are satisfactory for all simulations of the selected best solutions, in spite of the underestimation of peak discharges and annual runoffs; it can also be seen that the use of finer spatial resolution has improved LOGE to a substantial extent and RMSE, NSE, peak discharge error and monthly and annual mass balance errors to a moderate extent. The improvement in LOGE, RMSE and NSE, for the 1.0 km resolution can be explained by the better representation of land-use, soil types and river links as shown in Figs 6.1a–d, 6.2a–d and 6.3a–d (pages 67–69); and the substantial improvement of LOGE is related to the dominance of low flows in most of the simulation periods. According to Pallard *et al*. (2009), higher drainage densities lead to larger flood volumes and peaks. Therefore, a possible explanation of the association between higher resolution and flood peaks closer to the observed ones may be found in the fact that higher resolutions imply higher drainage densities as can be seen in Table 6.1 (page 69) and better agreement between the non-standard set-up, developed in the thesis, and that offered by SNIRH. It should however be pointed out that although 1.0 km resolution give better peak values and runoff volumes than the 2.0 km resolution, those values are still far from the observed ones. This may be explained by the fact that the drainage density configured in the 1.0 km resolution is, based on the river links from map with scale of 1:100000, only half of that from the map with scale of 1:25000 (Table 6.1, page 69). In addition, soil crust formation (Zhang *et al.,* 2013) represents another cause for the mismatch between simulated and observed peaks and flood volumes.

7. Downscaling of Climate Change Scenarios

In this chapter, the downscaling of climate change scenarios is carried out for Cobres basin. The multi-site stochastic rainfall model RainSim V3 combined with the rainfall conditioned weather generator ICAAM-WG have been used, with the change factor approach, to downscale projections of change derived from the 25 km resolution Regional Climate Model (RCM) HadRM3Q0, forced by boundary conditions from the Atmosphere-Ocean coupled General Circulation Model (AOGCM) HadCM3Q0, provided by the ENSEMBLES project for the A1B emission scenario for the period 2041–2070. At first, a short literature review is presented, followed by the detailed description of the methodology. Then, the results of control and future climate simulations are presented, including the evaluation of future climate change. Finally, a short discussion concludes this chapter.

7.1 Introduction

Southern Portugal is a semi-arid region (EEA 1996), the main climate characteristics being water scarcity and large variability of precipitation on both inter- and intra-annual scales (Mourato *et al.*, 2010). Studies based on observations have indicated that there are significant decreases of precipitation in February and March since 1960s (Matos *et al.*, 1994; Corte-Real *et al.*, 1998; Mourato *et al.*, 2010; Guerreiro *et al.*, 2014) and significant increase of temperature since 1940s (de Lima *et al.*, 2013). The region is becoming drier and warmer. This fact makes the evaluation of future climate change impacts on water resources and frequency of drought and flood events especially important. General Circulation Models (GCMs) can provide projections of future climate, but with resolutions too coarse, typically with a horizontal resolution of around 300 km, to match the requirements of hydrological impacts assessments. Therefore, downscaling is required for getting future climate scenarios at scales adequate to examine the impacts of climate change on hydrological systems. The downscaling methods are reviewed by Wilby and Wigley (1997), Prudhomme *et al.* (2002) and with a dedication to hydrological impacts studies by Fowler *et al.* (2007). These methods can be fundamentally classified into two categories: dynamic downscaling and statistical downscaling. Dynamic downscaling uses physically-based Regional Climate Models (RCMs) with boundary conditions provided by a GCM to produce higher resolution outputs. The resolutions are normally around 25–30 km, which is still too coarse for robust hydrological modelling (Fowler *et al.*, 2007). Therefore, additional statistical downscaling is required to translate the RCM output into a required resolution.

Fowler et al. (2007) suggested choosing the downscaling method most appropriate to climate variables that have the largest impact on the hydrological system. As for southern Portugal, water resources availability is the most important variable since fresh water sustains all the lives as well as agricultural and socioeconomic activities of the region. On the other hand, precipitation extremes, including either meteorological droughts or extremely large flood events, may have significant damaging impacts on the region, since most of its area is already susceptible to desertification under the mean climatic regime as evaluated by the Direcção-Geral do Ordenamento do Território e desenvolvimento Urbano (2007); and intense rainfall events, droughts and human activities such as excessive agriculture, deforestation and urbanization would bring about soil erosion and land degradation therefore accelerating the desertification process (Geeson *et al.*, 2002; Morgan 2005). In other words, we are also interested in assessing climate change impacts on the sediment transport. Since the majority of sediment is transported by large storm events (Lukey *et al.*, 2000), the downscaled climate variables should enable the hydrological model to reproduce well the storm-runoff generation processes. As indicated in Chapter 6, hourly rainfall and daily PET data can allow SHETRAN model to produce the reliable hydrological processes during large storm events, therefore our selected statistical downscaling methods should be able to provide these climate variables.

Stochastic weather generator models may be the right tools we are looking for, since they may be able to generate arbitrarily long weather variables, with spatial resolution relevant to hydrologists and temporal resolution down to daily or hourly level, based on the known statistics of the variables (Fowler *et al*., 2007). Kilsby and Jones *et al*. (2007) developed a daily weather generator that produces internally consistent series of meteorological variables including rainfall, temperature, humidity, wind, sunshine duration, as well as derivation of potential evapotranspiration (PET) for use in climate change studies. The model consists of two stochastic models of rainfall and weather. The rainfall model generates synthetic daily series which is then served as input for the weather model. The example application to Heathrow has demonstrated that their weather generator has capacity of reasonably reproducing mean daily rainfall and PET, as well as rainfall and temperature extremes. As an extension to their work, this study uses a more advanced version of stochastic rainfall model, RainSim V3 (Burton *et al.*, 2008), which is able to downscale rainfall onto multi-sites with temporal resolution of 1.0 hour; in addition, an improvement of the weather model has been made by considering the existence of the long dry spells and wet spells for southern Portugal.

As for uncertainties related to the climate impact assessments, previous studies have indicated that they are mainly originated from variability in internal parameterization of GCMs and RCMs, emission scenarios, downscaling methods, hydrological model structure and hydrological parameter setting etc. (Fowler *et al.*, 2007; Poulin *et al*., 2011; van Vliet *et al.*, 2012; Ouyang *et al.*, 2013). However, this study is not intended to consider any of these uncertainties due to the heavy computation requirements; instead we would like to present a systematic method of climate impact assessment by using the physically-based spatially-distributed (PBSD) hydrological model SHETRAN and weather variables downscaled for the control and future scenarios from the combination of dynamic and statistical downscaling methods. Respecting dynamic downscaling, the output of one Regional Climate Model (RCM) was considered (HadRM3Q0); regarding statistical downscaling, RainSim V3 was used for precipitation and ICAAM-WG, developed in this study, for temperature and other variables required for the computation of PET.

7.2 Methodology and Data

7.2.1 Data Preparation

- *Meteorological data*

Hourly and daily precipitation data respectively for the periods 2001–2010 and 1981–2010 were available at the Portuguese national water resources information system (SNIRH) for the 7 rain gauges at or near Cobres basin indicated in Fig 7.1 (page 95). Hourly precipitation data for the period 2001–2010 were also available at SNIRH for other 55 rain gauges located at the Guadiana basin (not shown in Fig 7.1), which has been used for derivation of the relationships between hourly and daily rainfall statistics. Daily weather data at the Beja climatological station were provided by the Portuguese Institute for the Ocean and Atmosphere (IPMA), among which precipitation, maximum and minimum 2-m air temperatures were available for the period 1981–2010 and sunshine duration, vapour pressure and wind speed for the period 1981–2004.

Table 7.1 (page 94) displays the characteristics of the 8 stations. It is indicated that mean annual precipitation, from the 7 rain gauges at or near Cobres basin, is around 469 mm (over the period 1981–2010), which ranges from 418 to 528 mm. The mean annual precipitation at Beja station is, around 556 mm, larger than those stations at or near Cobres basin by around 28 to 138 mm. Annual cycle variation of mean daily precipitation at Cobres basin, in Fig. 7.2 (page 96), has indicated that rainfall at Cobres basin mainly occurs during the period from October to April of the next year, less frequently in months May and September and very rarely in months June, July and

August. The relative less precipitation at March and, to a lesser extent, February, may be explained by the positive NAO indices of the two months in recent 50 years, as suggested by Matos *et al.* (1994), Corte-Real *et al*. (1998) and Guerreiro *et al.* (2014). The mean daily precipitation at Beja has the same annual cycle as that from all the stations at or near Cobres basin; and its value at each calendar month is close to the corresponding largest value at Cobres basin. Overall, precipitation at Beja is consistent and comparable with that from other stations at or near Cobres basin in spite of the differences in data source and natural rainfall variability.

Table 7.1 Characteristics of the stations located in the study area

Station ID	Station name (Abbreviation)	Latitude (ºN)	Longitude (ºW)	Altitude (m)	Annual mean precipitation (mm)	
					1981–2010	2041–2070
26J/04UG[a]	Albernoa (Alb)	37.86º	7.96	133	479	388
28I/01UG[a]	Almodôvar (Alm)	37.51	8.07	286	528	432
27I/01G[a]	Castro verde (Cas)	37.70	8.09	217	487	397
28J/03UG[a]	Santa Barbara de Padrões (Sbp)	37.64	7.98	239	448	364
27J/01UG[a]	São Marcos da Ataboeira (Sao)	37.70	7.94	182	418	340
26J/01UG[a]	Trindade (Tri)	37.89	7.89	172	452	368
27J/03C[a]	Vale de Camelos (Vdc)	37.81	7.87	142	470	384
562[b]	Beja (Bej)	38.04	-7.89	206	556	453

Note: [a]Data origin is SNIRH; [b]Data origin is IPMA

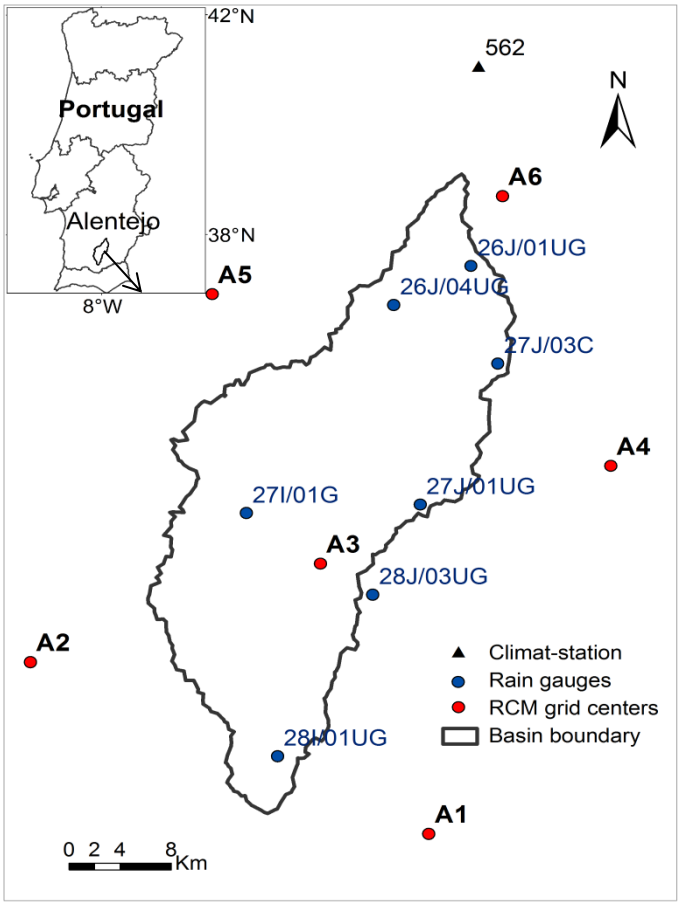

Fig. 7.1 Location map of the Cobres basin with climatological station (black triangle), rain gauges (blue dots) and the selected regional climate model grid cells' centers (red circles)

PET is estimated by the FAO Penman-Monteith method (Allen *et al.* 1998), using the daily series of 2-m air temperature (maxima and minima), sunshine duration, vapour pressure and wind speed at Beja for the period 1981–2004. The annual mean PET is estimated as 1222 mm. Annual cycle variations of mean daily PET, maximum and minimum 2-m air temperatures at Beja are shown in Fig 7.2. The annual cycle of PET, with highest values (around 6.5 mm/day) at July and lowest values (around 1.0 mm/day) at months January and December, is almost contrary to the corresponding cycle of mean daily precipitation.

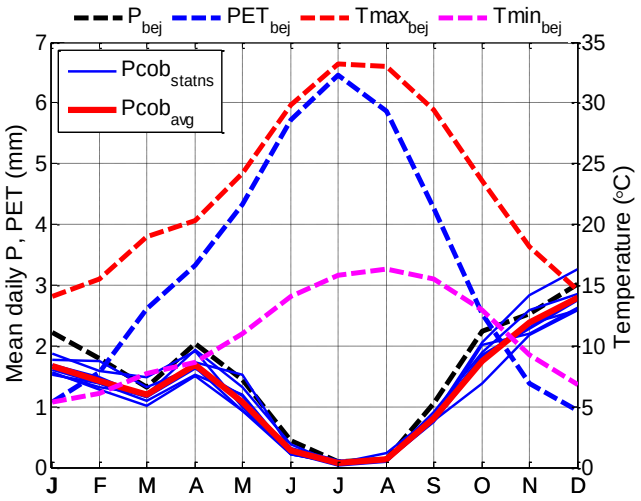

Fig. 7.2 Annual cycles of mean daily precipitation (P_{bej}), potential evapotranspiration (PET_{bej}), daily maximum ($Tmax_{bej}$) and daily minimum 2-m air temperature ($Tmin_{bej}$) for Beja station, mean daily precipitation for each station ($Pcob_{statns}$), and basin average precipitation ($Pcob_{avg}$) at Cobres basin. All are derived from the observations over the period from 1981–2010 except PET_{bej}, which is from 1981–2004.

- *Relationship between hourly and daily rainfall statistics*

The available 9 years hourly precipitation data for the 62 rain gauges at Guadiana basin are sufficient to establish the regional nonlinear downscaling regression relationships between hourly and daily statistics. As shown in Figs. 7.3a–3c (page 97), hourly variance (Var_{HP}), skewness ($Skew_{HP}$) and proportion dry hours (less than 0.1mm, $Pdry_{HP0.1}$) may be estimated respectively from the daily variance (Var_{DP}), skewness ($Skew_{DP}$) and proportion of dry days (less than 1.0 mm, $Pdry_{DP1.0}$), as indicated in equations (7.1), (7.2) and (7.3). The R^2 values for these relationships are respectively 0.974, 0.983 and 0.943. It is also indicated that the scatter points from Cobres basin exactly follow the relationships derived from the Guadiana basin.

$$Var_{HP} = (0.0159) Var_{DP}^{\ 0.87879} \tag{7.1}$$

$$\ln\left(\frac{Skew_{HP}}{\sqrt{Var_{HP}}}\right) = (3.4816) + (0.95326)\ln\left(\frac{Skew_{DP}}{\sqrt{Var_{DP}}}\right) \tag{7.2}$$

$$\ln\left(\frac{PDry_{HP0.1}}{1 - PDry_{HP0.1}}\right) = (0.94892) + (1.014)\ln\left(\frac{PDry_{DP1.0}}{1 - PDry_{DP1.0}}\right) \tag{7.3}$$

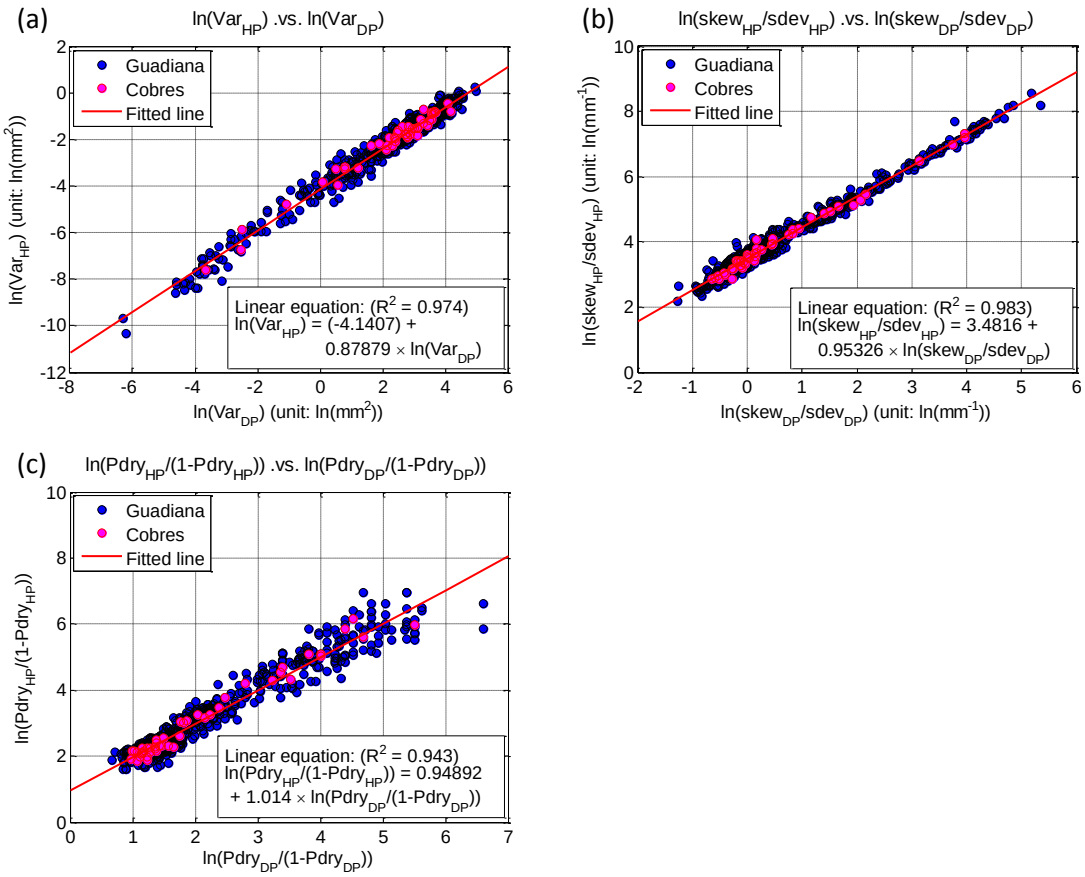

Fig. 7.3 Relationships between hourly and daily rainfall statistics, (a) variance, (b) skewness and (c) proportion dry, derived from pairs of the monthly statistics of the 62 stations located in the Guadiana basin (744 observed statistics). The 84 observed statistics, shown in red filled circles, are for the 7 stations of the Cobres basin located in the Guadiana basin

- *Climate model output*

Projections of future changes in climate over the Cobres basin are derived using Regional Climate Model (RCM) output from the European Union Sixth Framework Programme (FP6) ENSEMBLES project (van der Linden and Mitchell 2009). This project provides a series of high-resolution (from 50 to 25 km) transient RCM simulations (1951–2050 or 1951–2100) of European climate, primarily using the SRES A1B (medium, non-mitigation) emission scenario. In this study, the daily precipitation totals and daily maximum and minimum 2-m air temperatures from the 25 km resolution Regional Climate Model (RCM) HadRM3Q0 (Collins *et al.*, 2006), forced by boundary conditions from the Atmosphere-Ocean coupled General Circulation Model (AOGCM) HadCM3Q0, for the control (1981–2010) and future (2041–2070) periods are used (Table 7.2, page 98).

Table 7.2 The Regional Climate Model (RCM) experiment used from the RT3 ENSEMBLES

Ensembles acronym (Control/future)	RCM	Driving AOGCM	Emission scenario
METO-HC_HadRM3Q0	HadRM3Q0 (25 km)	HadCM3Q0 (1.25×1.875°)	A1B

7.2.2 Multi-Site Daily Precipitation Time Series: the RainSim V3 Model

The RainSim V3 model (Burton *et al.*, 2008), provided by Dr. Aidan Burton in the context of current collaboration between Newcastle University and University of Évora, is an advanced version of the Spatial-Temporal Neyman-Scott Rectangular Pulses (STNSRP) model developed by Cowpertwait (1995). It simulates rainfall as a continuous spatial-temporal process, which offers the possibility of providing rainfall time series at arbitrary spatial locations and with arbitrary time steps for distributed hydrological modelling applications. It is a stochastic rainfall model, which conceptualizes the occurrence of storm events as a temporal Poisson process and their rainfall intensities as a result of superimpositions of instantaneous intensities of all active raincells, generated by a stationary spatial Poisson process. The orographic effect is accounted for by a non-uniform scaling of the rainfall field with factors of the sampling sites proportional to their mean rainfalls, provided by observations or interpolations. The principal distinguishing features of the RainSim V3 model are: the integration of a robust and efficient optimization algorithm for model calibration, the exact fitting of mean rainfall statistics and the improved fitting of probability of dry hours and days. It also provides improved modelling of extremes by use of the third order moment (Cowpertwait 1998; Burton *et al.*, 2008). A most recent version of the STNSRP model, the nonhomogeneous spatial activation of raincells (NSAR) model (Burton *et al.*, 2010b), has considered the strong orographic effects on precipitation in mountainous catchments by generating raincells with a spatially nonhomogeneous Poisson process. However, since there is not much topographic variation in Cobres basin, the RainSim V3 model is used for generating synthetic rainfall series for rain gauges with available observed data. In other words, only the multi-site property of the model is used in this study.

In RainSim V3, storms give rise to a cluster of raincells with different time lags, spatial densities, radius, intensities and durations. Rainfall, for each raincell, occurs after a certain time, lagging the storm event, with a uniform density across its spatial extent and throughout its lifetime duration. The storm occurrence rate parameter λ, raincell occurrence rate parameter β, raincell centers' spatial density parameter ρ, raincell radius parameter γ, sampling sites' vector of scale factors Φ, rancell duration

parameter η and raincell intensity parameter ξ are all to be calibrated for each calendar month. As the simulated rainfall statistics exhibit high sample variability and so would need heavy computations to be determined with precision, expected rainfall statistics derived from analytical expressions are used for model calibration. Consequently, model calibration minimizes the objective function for comparison between expected statistics of the stochastic rainfall simulation process and a selected set of observed rainfall statistics. To generate synthetic rainfall series for a stationary climate, one must first calculate rainfall statistics that are most important for the application ("**Analysis**" mode in RainSim V3 if the rainfall series is available); then calibrate the model to get the parameters related to storm occurrence and raincells' activities ("**Fitting**" mode in RainSim V3); and finally simulate the synthetic rainfall series by using the calibrated parameters ("**Simulation**" mode in RainSim V3).

Considering the main objectives of our climate impact assessments, we selected the rainfall statistics, such as the daily mean (M_{DP}), variance (Var_{DP}), skewness ($Skew_{DP}$), proportion of dry days (less than 1.0 mm, $Pdry_{DP1.0}$), lag-1 autocorrelation ($L1AC_{DP}$) and spatial cross correlations between the rain gauges (XC_{DP}) and, hourly variance (Var_{HP}), skewness ($Skew_{HP}$), and proportion of dry hours (less than 0.1 mm, $Pdry_{HP0.1}$), for calibration and validation of the RainSim V3 model. The statistic M_{DP} is used to control the inter-annual variation and the total annual precipitation; the Var_{DP}, $Skew_{DP}$, Var_{HP} and $Skew_{HP}$ are designated to fit the modelling of extremes; $Pdry_{DP1.0}$ and $Pdry_{HP0.1}$ are considered for improving fitting the probability of dry days and hours; $L1AC_{DP}$ is chosen for obtaining better fitting of persistent events such as long dry spells.

7.2.3 Daily Temperature and Evapotranspiration Time Series: the Weather Generator (ICAAM-WG) Model

The weather generator developed by Kilsby and Jones *et al. (*2007) is an improved implementation of the Climatic Research Unit (CRU) daily weather generator (CRU-WG) (Watts *et al.*, 2004) that was originally developed by Jones and Salmon (1995). It consists of two components: the Neyman-Scott Rectangular Pulses (NSRP) model for daily rainfall simulation and the weather generator model based on first-order autoregressive process of weather variables such as daily maximum and minimum temperatures, sunshine duration, vapour pressure and wind speed. Kilsby and Jones *et al. (*2007) have demonstrated its capacity in reproducing inter-annual variability and extremes of the weather variables. As precipitation is the primary variable in a weather generator (Wilks and Wilby 1999), their improvement of weather variables' simulation might be largely contributed by the introduction of a more sophisticated rainfall model

capable of more accurately reproducing higher order rainfall statistics. Following their framework, this study integrates the RainSim V3 model, an advanced version of the NSRP model, and a modified weather model based on Kilsby and Jones *et al*. (2007) into a weather generator to get synthetic daily PET for the control and future periods. To differentiate it from others, we call it the ICAAM-Weather Generator (ICAAM-WG).

The sequence of weather variables' generation is: (1) Generating synthetic daily rainfall; (2) Deriving the autoregressive process of daily temperature from observed data; (3) Generating synthetic daily temperature by using synthetic daily rainfall and related autoregressive processes; (4) Deriving the autoregressive processes of daily sunshine duration, vapour pressure and wind speed from observed data; (5) Generating other synthetic daily weather variables by using synthetic daily rainfall, temperature and related autoregressive processes. By denoting a dry day (daily rainfall less than 0.1) as 0 and a wet day as 1, four possible combinations of previous day and current day are classified: 00, 11, 01 and 10. For two consecutive dry days (00) or wet days (11), Kilsby and Jones *et al. (*2007) considered the current day temperature to be linearly related to the previous day temperature; and for the two transition types (01 or 10), they considered the current day temperature to be linearly related to the previous day temperature and the wet day precipitation. As for Southern Portugal, there are frequently long dry spells in summer and wet spells in winter. From the available observed daily rainfall from Beja station, the percentages of the 4 types of day (00, 11, 01 and 10) are respectively: 64%, 16%, 10% and 10%, among which 88% of the 00 type is 000 and 62% of the 11 type is 111. Therefore, the second-order autoregressive process may be more appropriate for temperature, in case of these consecutive dry or wet spells (Personal communication with Professor Chris Kilsby from Newcastle University). Consequently, six types of day are considered in ICAAM-WG for autoregressive process of daily temperature: 000, 100, 011, 111, 01 and 10, among which the second-order (first-order) autoregressive process is proposed for the first four (last two) types of day. As for other weather variables such as daily sunshine duration, vapour pressure and wind velocity, the current day value is determined by the regression relationship with temperature, precipitation and its value on previous day, as proposed by Kilsby and Jones *et al*. (2007).

Instead of daily maximum and minimum temperature (T_{max} and T_{min}), daily mean temperature ($T = (T_{max} + T_{min})/2$) and the temperature range ($R = T_{max} – T_{min}$) are used in the weather model. Other weather variables generated by autoregressive processes with possible conditioning on precipitation are: vapour pressure (VP), wind speed (WS)

and sunshine duration (SS). Three steps are required for derivation of autoregressive processes: (1) Calculating standardized anomalies for all variables, in terms of 24 (12×2) half monthly periods, to remove their seasonal variations. This is carried out by subtracting the sample mean of the raw data and dividing by the corresponding sample standard deviation. (2) Deriving the autoregressive processes of temperature, by using the standard anomalies time series of T and R, for the above-mentioned six transition states; (3) Deriving the first-order autoregressive processes of VP, WS and SS, by using their standard anomalies time series, the standard anomaly time series of T and R and daily rainfall time series.

The proposed autoregressive models are shown in Appendix 2 and the final equations are determined by the regressive processes, from which only the independent variables with coefficients significant at the 5% level are kept. The autoregressive equations are assumed not to change with time. Therefore, they can be used, together with synthetic daily rainfall, to generate the standard anomalies of synthetic temperature, sunshine duration, vapour pressure and wind speed for any considered time-slices. The generated variables are then transformed back to absolute values using the appropriate means and standard deviations. PET is then calculated by using FAO Penman-Monteith method (Allen *et al.* 1998).

7.2.4 Change Factors Calculation for Future Time Slice 2041–2070

The change factor (CF) or 'perturbation' approach described in Kilsby and Jones *et al*. (2007) and Jones *et al*. (2009) is applied in this study. It assumes that the RCM model biases are consistent in control and future simulations. Therefore, the unbiased future statistics can be obtained by applying to the observed statistics the derived factors of change for various statistics from control to future scenarios. Comparing with the traditional CF approach (Diaz-Nieto and Wilby 2005; Prudhomme *et al.*, 2002), the present one offers the possibility of bias correction to the proportion of dry days and second or higher moments of statistics, which may greatly improve the representation of dry periods and high extremes in the future projection.

Simulated values of daily total precipitation and daily maximum and minimum 2-m air temperature for the 1981–2010 (control) and 2041–2070 (future) time-slices are extracted from the six RCM grid cells overlying the study area (Fig 7.1, page 95). For each grid cell, annual cycle of CFs for rainfall statistics such as daily mean (M_{DP}), variance (Var_{DP}), skewness ($Skew_{DP}$), proportion of dry days (less than 1.0 mm, $Pdry_{DP1.0}$) and lag-1 autocorrelation ($L1AC_{DP}$) are calculated. For air temperature, daily mean temperature and the temperature range are firstly derived from the daily

maximum and minimum temperatures; then, the annual cycle of CFs for temperature statistics such as mean (M_{DT}) and variance (Var_{DT}) of daily mean temperature and mean ($M_{\Delta DT}$) and variance ($Var_{\Delta DT}$) of the daily temperature range are evaluated. Sunshine duration is not perturbed, as maximum sunshine duration cannot increase; vapour pressure and wind speed are also not perturbed because their potential future changes are highly uncertain, differing largely among available RCM integrations.

CFs are derived using multiplicative factors for rainfall statistics and temperature variances, and additive ones for means of daily mean temperature and daily temperature range. For each calendar month *i*, CFs, $\alpha_{g,i}$, are calculated as the ratio of statistic *g*, for future (*Fut*) time-slice to it for control (*Con*) time-slice (equation 7.4) for rainfall statistics such as daily mean (M_{DP}), variance (Var_{DP}) and skewness ($Skew_{DP}$), and the variances of daily mean temperature (Var_{DT}) and daily temperature range ($Var_{\Delta DT}$). The calculated CFs are then applied, in equation (7.5), together with statistics observed during the control period (*Obs*), g_i^{Obs}, to get estimated future statistics g_i^{Est}. CFs of rainfall statistics $Pdry_{DP1.0}$ and $L1AC_{DP}$ cannot be directly evaluated from equation (7.4) (Burton *et al.*, 2010a). So, invertible transformations, namely equation (7.6) for $Pdry_{DP1.0}$ and the equation (7.7) for $L1AC_{DP}$, are required. The estimated future statistics are then derived from equations (7.4) and (7.5) by using the transformed variables instead of the original values. Respecting means of daily mean temperature (M_{DT}) and daily temperature range ($M_{\Delta DT}$), CFs are derived from RCM simulations by using equation (7.8) and then applied in equation (7.9), together with observed statistics, to get the future monthly statistics.

$$\alpha_{g,i} = \frac{g_i^{Fut}}{g_i^{Con}} \tag{7.4}$$

$$g_i^{Est} = \alpha_{g,i} g_i^{Obs} \tag{7.5}$$

$$X(Pdry) = \frac{Pdry}{1 - Pdry} \tag{7.6}$$

$$Y(L1AC) = \frac{1 + L1AC}{1 - L1AC} \tag{7.7}$$

$$\alpha_{T,i} = T_i^{Fut} - T_i^{Con} \tag{7.8}$$

$$T_i^{Est} = T_i^{Obs} + \alpha_{T,i} \tag{7.9}$$

Based on the output from the HadRM3Q0 model, annual cycles of nine CFs (five for precipitation, four for temperature) relative to the period 1981–2010 are shown in Figs 7.4a–4i (page 103) for all the six grid cells overlying Cobres basin. It is indicated that, for precipitation, in most cases the variations of CFs with different grid cells are small except for June, July and August; the large variations of M_{DP} in June and August,

Var_{DP} in June, $Skew_{DP}$ in July and $X(Pdry_{DP1.0})$ in August may probably be related to the small amount of precipitation in summer. For temperature, almost all the CFs from the six RCM grid cells are the same except some small discrepancies in late spring and summer months. As a whole, CFs for the six grid cells are spatially consistent indicating that a simple average of results from these grid cells is appropriate for use in this study. The CFs provide estimates of how rainfall and temperature statistics may vary between the control and future time-slice. From Fig 7.4a, daily mean precipitation is projected to increase in March and June (CF > 1), maintained in January (CF = 1) and decrease in other months (CF < 1). In Figs 7.4f and 7.4h, daily mean temperature is projected to increase 1.5–3.2 °C, with an average increase of around 2.4 °C and daily temperature range is also projected to increase around 0.5 °C except for January, March and October. More details of projected changes are discussed in Section 7.4 in the context of the downscaled climate change scenarios.

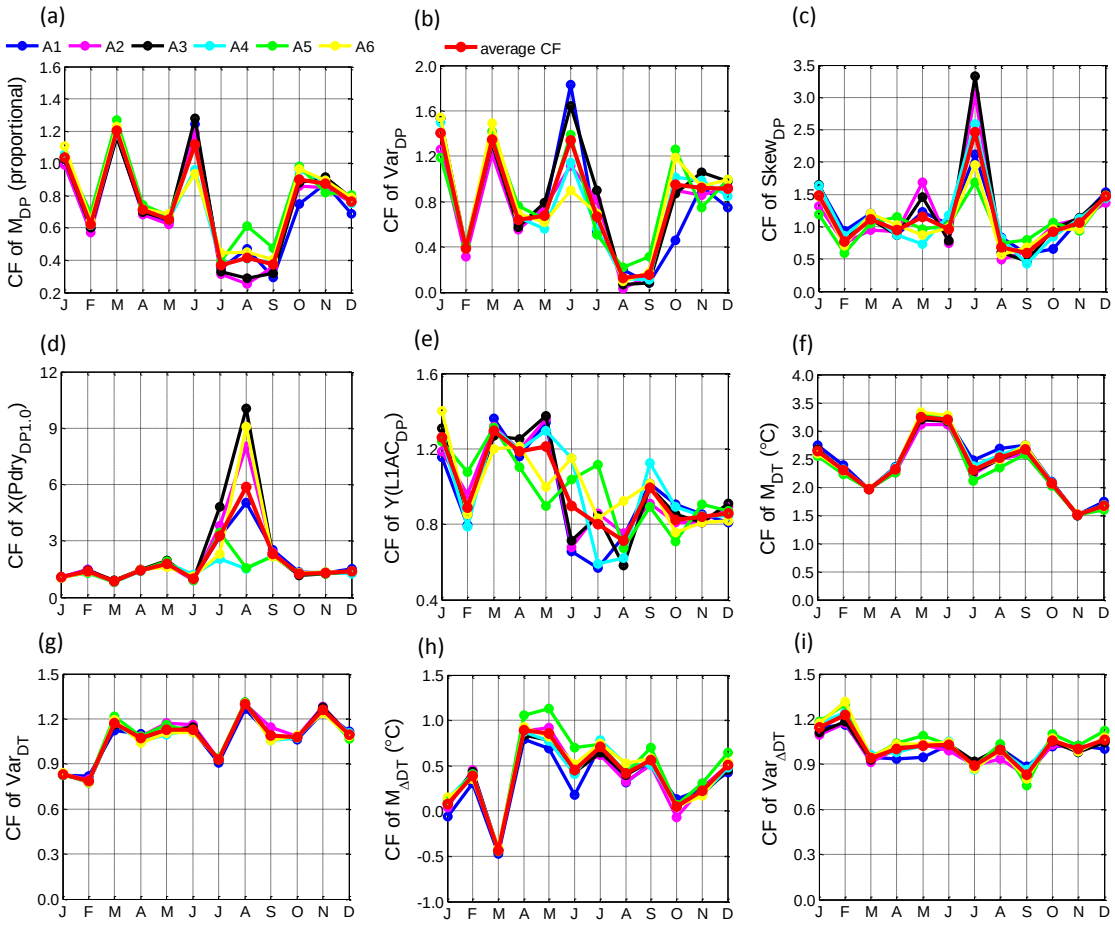

Fig. 7.4 Annual cycles of CFs for (a) mean M_{DP}, (b) variance Var_{DP}, (c) skewness $Skew_{DP}$, (d) transformed proportion of dry days $X(Pdry_{DP1.0})$ and (e) transformed lag-1 autocorrelation $Y(L1AC_{DP})$ of daily rainfall, (f) mean M_{DT} and (g) variance Var_{DT} of daily mean temperature and (h) mean $M_{\Delta T}$ and (i) variance $Var_{\Delta T}$ of daily temperature range, for the 6 RCM grid cells overlying Cobres basin; the average CF, shown in red colour, is the average of CFs from the 6 RCM grid cells.

7.2.5 Outline of the Climate Downscaling Method

Schematic summaries are presented in Appendix 3 to illustrate the steps of downscaling synthetic hourly rainfall and daily PET for Cobres basin respectively under control (1981–2010) and future (2041–2070) climate conditions. To downscale the climate change scenarios, statistics of rainfall, temperature, vapour pressure, wind speed and sunshine duration are not directly calculated from the RCM model output. Instead, factors of change for these statistics are derived from the control to future scenarios. By using the RainSim V3 and ICAAM-WG models, the control climate is validated for the observed annual cycles of these statistics; the future climate scenario is projected based on estimated values of these statistics for future climate obtained by applying CFs to the observed statistics.

The downscaling of 1000-year stationary hourly rainfall for the control period at Beja and 7 Cobres rain gauges, described in A3.1, is performed to validate the RainSim V3 model. The downscaled rainfall series at Beja is then converted into daily series, to condition the autoregressive equations of temperature, sunshine duration, vapour pressure and wind speed for getting 1000-year PET for the control period at Cobres basin, as indicated in A3.3, to validate the ICAAM-WG model. Three 1000-year replicates are generated for validation. Then, with the projected future rainfall and temperature statistics, derived from the change factor approach, procedures shown in A3.2 and A3.4 are carried out successively to downscale the three 1000-year synthetic hourly rainfall and daily PET at Cobres basin for the future time-slice. Finally, future climate changes are evaluated from the comparison between the downscaled control and future scenarios.

7.3 Results of Control Climate Simulations

7.3.1 Validation of the RainSim V3 Model

The daily rainfall observations for the control period, 1981–2010, for Beja and the 7 rain gauges at Cobres basin (Fig 7.1, page 95) are used to calibrate the RainSim V3 model. The calibrated model is then used to generate three 1000-year climatically stationary simulations for the control period at the rain gauges' locations. The steps, indicated in A3.1, for validation of the RainSim V3 model can be categorized as: preparation of rainfall statistics (steps 1 to 4); calibration of RainSim V3 (step 5); generation (step 6) and analysis (step 7) of synthetic rainfall and comparison of observed, fitted and simulated rainfall statistics (step 8). The model's three modes, namely "analysis" (steps 1, 3 and 7), "fitting" (step 5) and "simulation" (step 6), are used throughout the

validation process. To calibrate the RainSim V3 model, monthly rainfall statistics, such as M_{DP}, Var_{DP}, $Skew_{DP}$, $Pdry_{DP1.0}$, $L1AC_{DP}$, spatial cross correlation between the rain gauges (XC_{DP}), Var_{HP}, $Skew_{HP}$ and $Pdry_{HP0.1}$, are required. A total of 1104 statistics (12 calendar months × [8 × 5 single-site daily statistics + 28 cross-correlation daily statistics + 8 × 3 single-site hourly statistics]) are evaluated from the observations. Daily statistics (M_{DP}, Var_{DP}, $Skew_{DP}$, $Pdry_{DP1.0}$, $L1AC_{DP}$ and XC_{DP}) are evaluated directly from available daily rainfall series of control period. Hourly statistics (Var_{HP}, $Skew_{HP}$ and $Pdry_{HP0.1}$) are not calculated directly from available hourly rainfall series due to their short length of record. Instead, they are obtained by applying the regional nonlinear relationships between hourly and daily rainfall statistics, which are equations (7.1), (7.2) and (7.3) derived from Guadiana basin data, to the evaluated daily statistics (Var_{DP}, $Skew_{DP}$ and $Pdry_{DP1.0}$). During calibration, a set of storm parameters, corresponding to the control climate condition, and the analytically expected rainfall statistics are obtained through the embedded optimization algorithm. The storm parameters are then used to generate a 1000-year simulation, sampled in hourly time steps, at Beja and the 7 rain gauges at Cobres basin. Steps 6–8 are repeated to get three replicates.

As indicated in Figs 7.5a_1–h_3 (pages 106–107) and 7.6a_1–b_3 (page 108) (Santa Barbara de Padrões is not shown due to the space limit), the 3 replicates of 1000-year synthetic hourly rainfall at Beja and 7 rain gauges at Cobres basin, represent well the spatial and temporal variation of observed rainfall statistics for the control period (1981–2010). The simulated rainfall statistics greatly match their respective expected statistics with small discrepancies arising from the stochastic nature of the simulations. The simulated annual cycles of M_{DP} (Figs 7.5a_1–a_3), $Skew_{DP}$ (Figs 7.5c_1–c_3), $Pdry_{DP1.0}$ (Figs 7.5d_1–d_3), $L1AC_{DP}$ (Figs 7.5e_1–e_3) and $Skew_{HP}$ (Figs 7.5f_1–f_3) were excellently reproduced by the RainSim V3 model for all the 3 replicates. The STNSRP process fitted and simulated monthly M_{DP} exactly for each of the 8 rain gauges indicating the model's capability of capturing the nonhomogeneous rainfall amounts process by the use of intensity scaling field (Burton *et al.*, 2008; Burton *et al.*, 2010b). The fitted and simulated $Skew_{DP}$, $Pdry_{DP1.0}$, $L1AC_{DP}$ and $Skew_{HP}$ are spatially uniform, namely each month's fit and simulation for these statistics is the same for all rain gauges. However, the variations of these statistics across the basin are relatively much smaller than their inter-annual differences, as shown by the annual cycles of observed values. Since the STNSRP process reproduced well the inter-annual variability of these statistics, the spatially uniform simulation is sufficient to make them comparable to the observed statistics. The 3 replicates of the two spatial cross-correlation plots (Figs 7.6a_1–a_3 and Figs 7.6b_1–b_3) indicate rainfall is less (more) correlated in summer (winter) for close

rain gauges, which may probably be explained by the dominant convective (frontal) activities. The tendency of the pattern was well fitted and simulated by the model, although the observed correlations show more stochastic variations than the fitted and simulated ones.

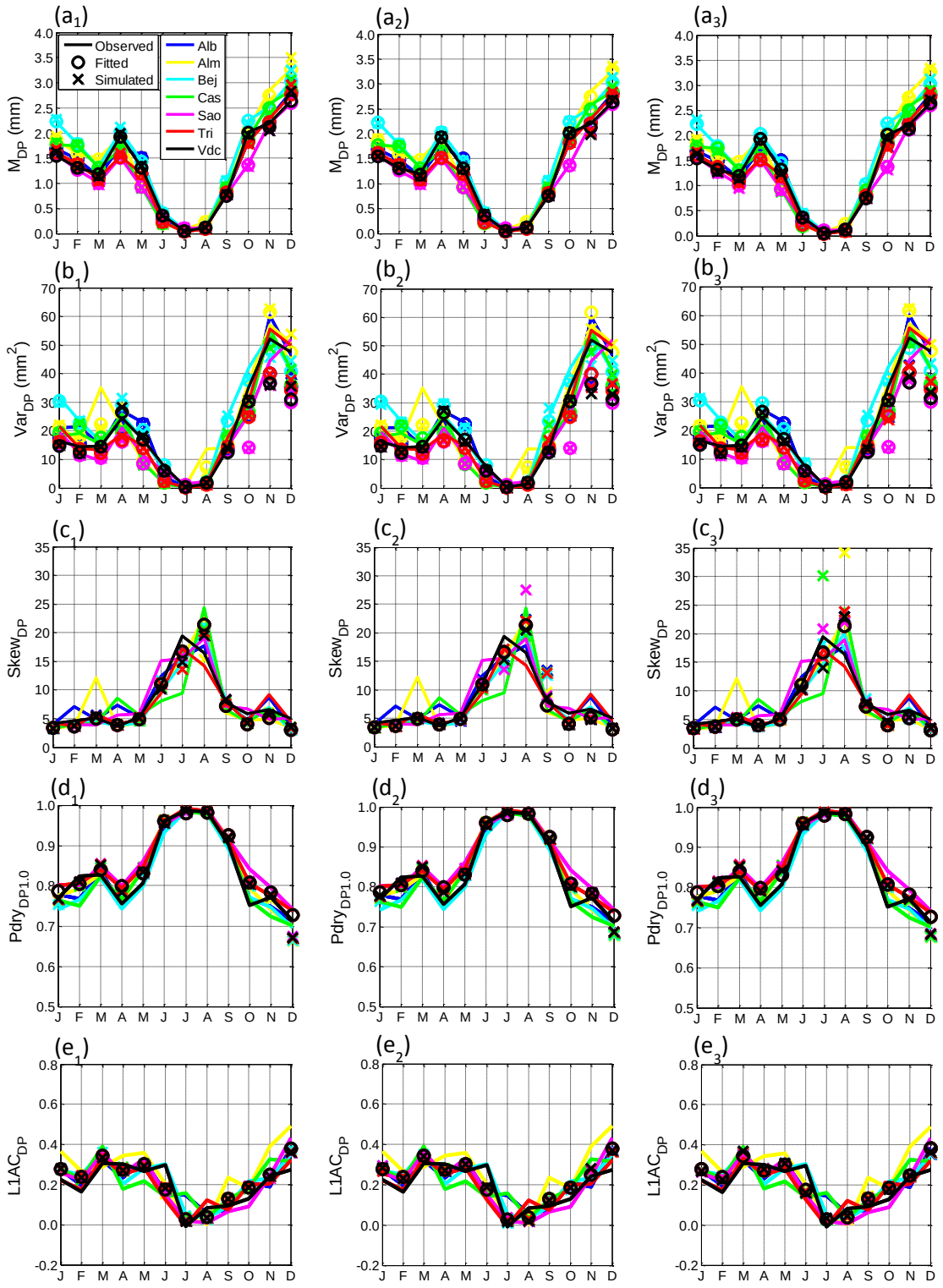

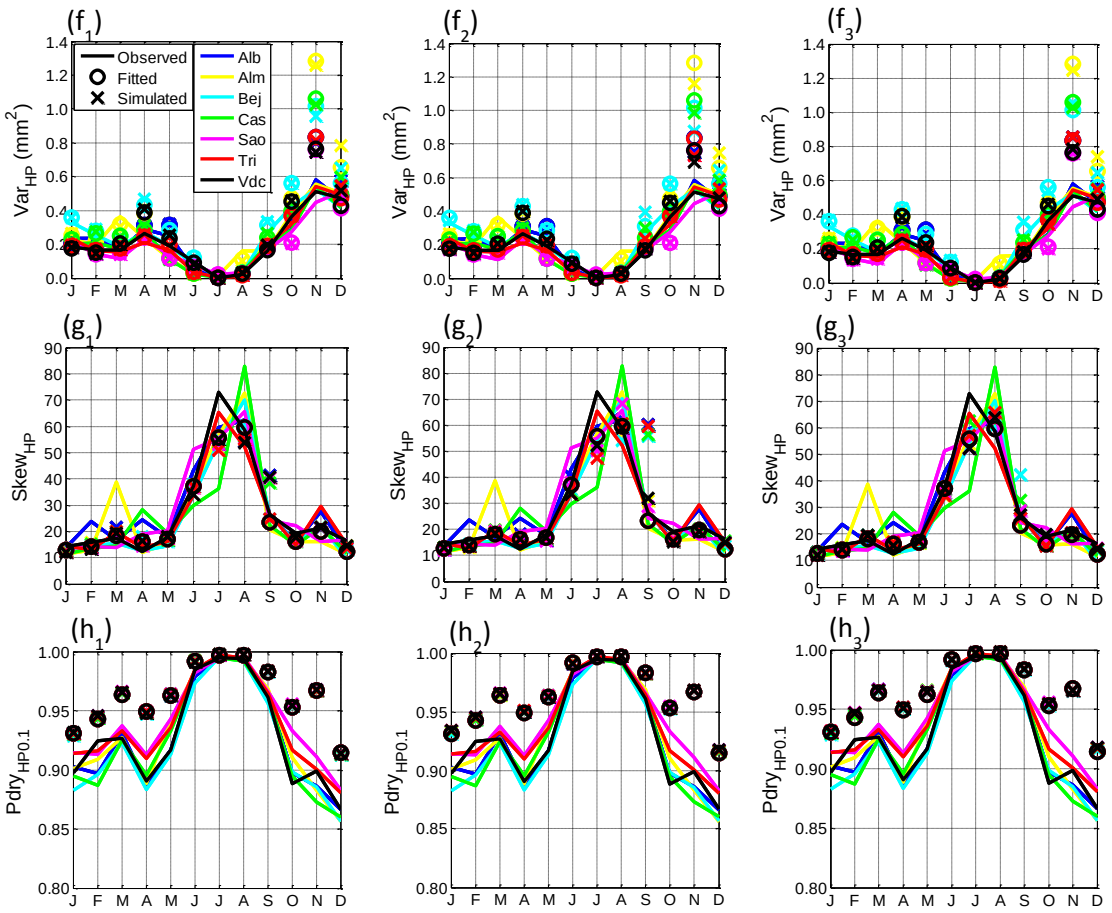

Fig. 7.5 Comparison of the annual cycles of observed (solid lines), fitted (circles) and simulated (crosses) daily (a_1, a_2 and a_3) mean, (b_1, b_2 and b_3) variance, (c_1, c_2 and c_3) skewness, (d_1, d_2 and d_3) proportion of dry days and (e_1, e_2 and e_3) lag-1 autocorrelation and hourly (f_1, f_2 and f_3) variance, (g_1, g_2 and g_3) skewness and (h_1, h_2 and h_3) proportion dry hours during the control period (1981−2010) for the 7 rain gauges at the Cobres basin with each colour representing one site. The first (Figs. a_1, b_1, c_1, d_1, e_1, f_1, g_1 and h_1), second (Figs. a_2, b_2, c_2, d_2, e_2, f_2, g_2 and h_2) and third (Figs. a_3, b_3, c_3, d_3, e_3, f_3, g_3 and h_3) column of figures respectively represents results from the 1st, 2nd and 3rd 1000-year synthetic hourly rainfall.

For the three replicates, the hourly dry probability $Pdry_{HP0.1}$ was well fitted and simulated in summer months but slightly overestimated in other months (around 5% to 7%). The fitted and simulated $Pdry_{HP0.1}$ are spatially uniform originated from the homogeneous rainfall occurrence assumed in the RainSim V3 model (Burton *et al.*, 2010b). The annual cycle of Var_{DP} (Figs 7.5b_1–b_3) and Var_{HP} (Figs 7.5f_1–f_3) were mostly well reproduced for all the 3 replicates with discrepancies noticeable mainly in October, November and December. The use of the intensity scaling field in the STNSRP process implicitly assumes that dimensional statistics vary in proportion to an appropriate power of the mean (e.g., that the daily coefficient of variation [CV] is spatially uniform) (Burton *et al.*, 2010b). This underestimates (overestimates) the variance at stations with higher (lower) observed CV but lower (higher) M_{DP}, which may

explain underestimated Var_{DP} of 'Sao' at October and 'Alb', 'Sao', 'Tri' and 'Vdc' at November and December (the overestimated Var_{HP} of 'Alm' at November).

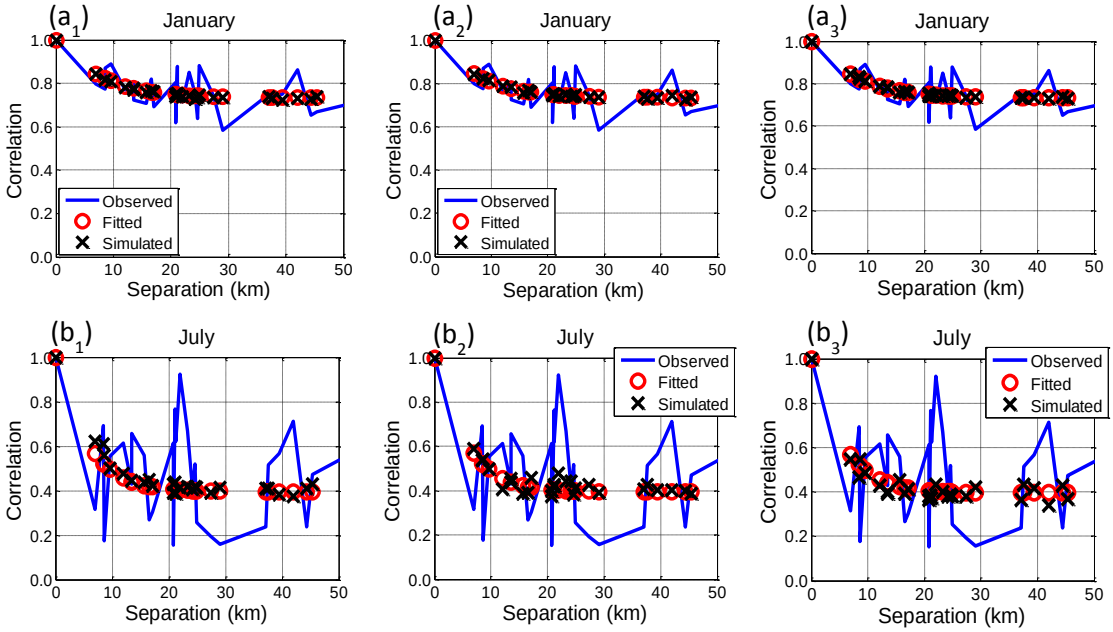

Fig. 7.6 Observed (solid blue lines), fitted (red circles) and simulated (black crosses) cross-correlations against separation for January (a_1, a_2 and a_3) and July (b_1, b_2 and b_3). The first (Figs. a_1 and b_1), second (Figs. a_2 and b_2) and third (Figs. a_3 and b_3) columns respectively represent results from the 1st, 2nd and 3rd series of 1000-year synthetic hourly rainfall.

In Figs 7.10a–d (page 119), the ability of the RainSim V3 model in reproducing the realistic rainfall extremes is also assessed for stations with long records of daily rainfall series. To get extreme value plot for observed data, annual maximum daily rainfall time series were extracted for Beja for the period 1961 –2010 from IPMA and for Castro verde, Almodôvar and Trindade for the period 1931–2010 from SNIRH, discarding years containing missing data. Numbers of 40, 71, 72 and 75 observed maxima were identified respectively for Beja, Castro verde, Almodôvar and Trindade stations. The maxima were then ranked and plotted in Figs 7.10a–d as black dots. Then, the three replicates of 1000-year synthetic rainfall were partitioned into fifty 60-year series, and annual maxima were extracted and ranked for each 60-year series. Consequently, there were 50 possible values for each rank. The 5th, 50th and 95th percentiles were evaluated for each rank and plotted in Figs 7.10a–d as blue solid lines. Figs 7.10a–c have indicated that the observed annual maxima at Beja, Castro verde and Almodôvar stations are completely in agreement with the ranges provided by the synthetic data, indicating an excellent extreme simulation provided by the RainSim V3. Fig 7.10d has shown that the maxima with return periods between 5 and 30 years were slightly underestimated for Trindade station, which may be explained by the underestimation of

daily rainfall variance displayed in Figs 7.5b_1–b_3 (page 106). As this test was not used in model calibration, it has strongly confirmed the RainSim V3's high performance in estimating extreme values.

7.3.2 Validation of the ICAAM-WG Model

According to Kilsby and Jones *et al. (*2007) and Jones *et al*. (2009), a single-site application of the ICAAM-WG model is appropriate for basins up to approximately 1000 km^2. This has justified our use of weather data at Beja to develop the ICAAM-WG model for the entire Cobres basin (705 km^2). The processes for generation of 1000-year synthetic weather variables are summarized in the schematic chart A3.3 as: derivation of autoregressive processes for daily T and R (steps 1 to 3); generation of synthetic series of daily T_{max} and T_{min} (steps 4 to 6); derivation of autoregressive processes of daily VP, WS and SS (steps 7 to 8); generation of synthetic series of daily VP, WS and SS (steps 9 to 10) and calculation of synthetic PET series (step 11). From observed daily T_{max}, T_{min} and DP for the 1980–2010, the final autoregressive equations of daily T and R are:

Very dry periods (**000**: the day before previous day dry, previous day dry, current day dry):

$$T_i = 0.93923 \times T_{i-1} - 0.21561 \times T_{i-2} + 0.04692 + e_i \quad (7.10)$$

$e_i \sim (0, \sigma_e^2)$, $\sigma_e = 0.6223$

$$R_i = 0.53332 \times R_{i-1} + 0.16670 + e_i \quad (7.11)$$

$e_i \sim (0, \sigma_e^2)$, $\sigma_e = 0.7454$

Moderate dry periods (**100**: the day before previous day wet, previous day dry, current day dry):

$$T_i = 0.88940 \times T_{i-1} - 0.09909 \times T_{i-2} + 0.16225 + e_i \quad (7.12)$$

$e_i \sim (0, \sigma_e^2)$, $\sigma_e = 0.5669$

$$R_i = 0.50874 \times R_{i-1} + 0.11274 + e_i \quad (7.13)$$

$e_i \sim (0, \sigma_e^2)$, $\sigma_e = 0.6856$

Moderate wet periods (**011**: the day before previous day dry, previous day wet, current day wet):

$$T_i = 0.78874 \times T_{i-1} - 0.10167 \times T_{i-2} - 0.21771 + e_i \quad (7.14)$$

$e_i \sim (0, \sigma_e^2)$, $\sigma_e = 0.7534$

$$R_i = 0.18686 \times R_{i-1} - 0.026662 \times P_i - 0.49154 + e_i \quad (7.15)$$

$e_i \sim (0, \sigma_e^2)$, $\sigma_e = 0.8436$

Very wet periods (**111**: the day before previous day wet, previous day wet, current day wet):

$$T_i = 0.75319 \times T_{i-1} + 0.00457 \times P_i - 0.11674 + e_i \quad (7.16)$$

$e_i \sim (0, \sigma_e^2)$, $\sigma_e = 0.6086$

$$R_i = 0.24934 \times R_{i-1} - 0.01669 \times P_i - 0.55743 + e_i \quad (7.17)$$

$e_i \sim (0, \sigma_e^2)$, $\sigma_e = 0.7239$

Dry wet transition (**01**: previous day dry, current day wet):

$$T_i = 0.69150 \times T_{i-1} - 0.05977 + e_i \quad (7.18)$$

$e_i \sim (0, \sigma_e^2)$, $\sigma_e = 0.6443$

$$R_i = 0.34515 \times R_{i-1} - 0.01599 \times P_i - 0.55633 + e_i \quad (7.19)$$

$e_i \sim (0, \sigma_e^2)$, $\sigma_e = 0.8338$

Wet dry transition (**10**: previous day wet, current day dry):

$$T_i = 0.70959 \times T_{i-1} - 0.14613 + e_i \quad (7.20)$$

$e_i \sim (0, \sigma_e^2)$, $\sigma_e = 0.6299$

$$R_i = 0.40933 \times R_{i-1} + 0.08359 + e_i \quad (7.21)$$

$e_i \sim (0, \sigma_e^2)$, $\sigma_e = 0.7090$

As indicated in equations (7.10)–(7.21), the autoregressive process of temperature for days of type 000 is different from that for days of type 100, and similarly differences can be identified between days of types 011 and 111. This may confirm the necessity of the six transition states' classification. The magnitudes of coefficients of the mean temperature for the day before previous day have implicated the possible existence of second-order autoregressive process of temperature for the days of types 000, 100 and 011. The magnitudes of coefficients of current day rainfall for days of types 011 and 111 are comparable with that for days of type 01, which signifies the importance of including the influence of current day rainfall on the current day temperature. Nevertheless, the validation of the weather generator simulations for the control period will demonstrate the final effects.

The 1000-year synthetic series of T_{max} and T_{min} for control period are then generated by applying the 1000-year synthetic DP at Beja into the equations (7.10) to (7.21) and putting back the seasonal variation of daily T and R. From observed daily T, R, VP, WS, SS and DP for 1981–2004, the final autoregressive equations are obtained:

Vapour pressure:

$$VP_i = 0.34725 \times T_i - 0.30440 \times R_i + 0.01151 \times P_i + 0.50615 \times VP_{i-1} - 0.01865 + e_i \quad (7.22)$$

$e_i \sim (0, \sigma_e^2)$, $\sigma_e = 0.6016$

Wind speed:

$$WS_i = -0.11254 \times T_i - 0.13132 \times R_i + 0.02809 \times P_i + 0.45741 \times WS_{i-1} - 0.04873 + e_i \quad (7.23)$$

$e_i \sim (0, \sigma_e^2)$, $\sigma_e = 0.8047$

Sunshine duration:

$$SS_i = -0.03586 \times T_i + 0.54979 \times R_i + 0.12942 \times SS_{i-1} + e_i \quad (7.24)$$

$e_i \sim (0, \sigma_e^2)$, $\sigma_e = 0.7698$

The 1000-year synthetic series of daily VP, WS and SS for the control period are then generated by applying standard anomalies of synthetic daily T and R, the 1000-year

synthetic DP into the equations (7.22) to (7.24) and putting back their respective seasonal variations. Finally, the 1000-year synthetic daily PETs are computed from FAO Penman-Monteith equation. To generate three replicates, steps 4 to 6 and 9 to 11 of A3.3 are required to be repeated three times.

To validate the ICAAM-WG model, the 3000-year synthetic weather variables are divided into 100 30-year series. The 3 replicates of 1000-year simulation can be treated as 100 30-year simulations. For each 30-year series, average daily T_{max}, T_{min}, VP, WS, SS and PET are evaluated for all the 24 half monthly periods. The performance of the ICAAM-WG in reproducing the mean climatology at Beja is assessed in Figs 7.7a–f (page 112), by comparing the observed averages of the weather variables (blue circles) with the range (red error bar with two standard deviation range) estimated from the 100 simulations. It is shown that the annual cycles of average daily T_{max}, T_{min}, VP, WS and SS are all well represented throughout the year although slight overestimation of T_{max} and SS and underestimation of WS in summer are identified. Consequently, the annual cycle of PET is skillfully reproduced with a little overestimation in summer. Overall, the synthetic weather variables are in good agreement with the observed values.

7.4 Results of Future Climate Simulations

7.4.1 Simulation of Future Precipitation

The projected monthly rainfall statistics M_{DP}, Var_{DP}, $Skew_{DP}$, $Pdry_{DP1.0}$ and $L1AC_{DP}$ for the future time-slice, 2041–2070, for Beja and the 7 rain gauges at Cobres basin (Fig 7.1, page 95) are estimated by using the CF approach described in Section 7.2.4. The projected annual cycles of hourly rainfall statistics such as Vap_{HP}, $Skew_{HP}$ and $Pdry_{HP0.1}$ are evaluated based on the projected daily rainfall statistics Var_{DP}, $Skew_{DP}$, $Pdry_{DP1.0}$ and equations (7.1)–(7.3). The spatial cross correlation between the rain gauges (XC_{DP}) are assumed to be constant along time. These statistics are then used to calibrate the RainSim V3 model and generate three 1000-year climatically stationary simulations for the future period. Steps, displayed in schematic chart A3.2, for simulation of future projected multi-site precipitation can be outlined as: preparation of future rainfall statistics (steps 1 to 3); calibration of RainSim V3 (step 4); generation (step 5) and analysis (step 6) of synthetic rainfall and comparison of projected, fitted and simulated statistics for the future period with the corresponding observed, fitted and simulated statistics for control period (step 7).

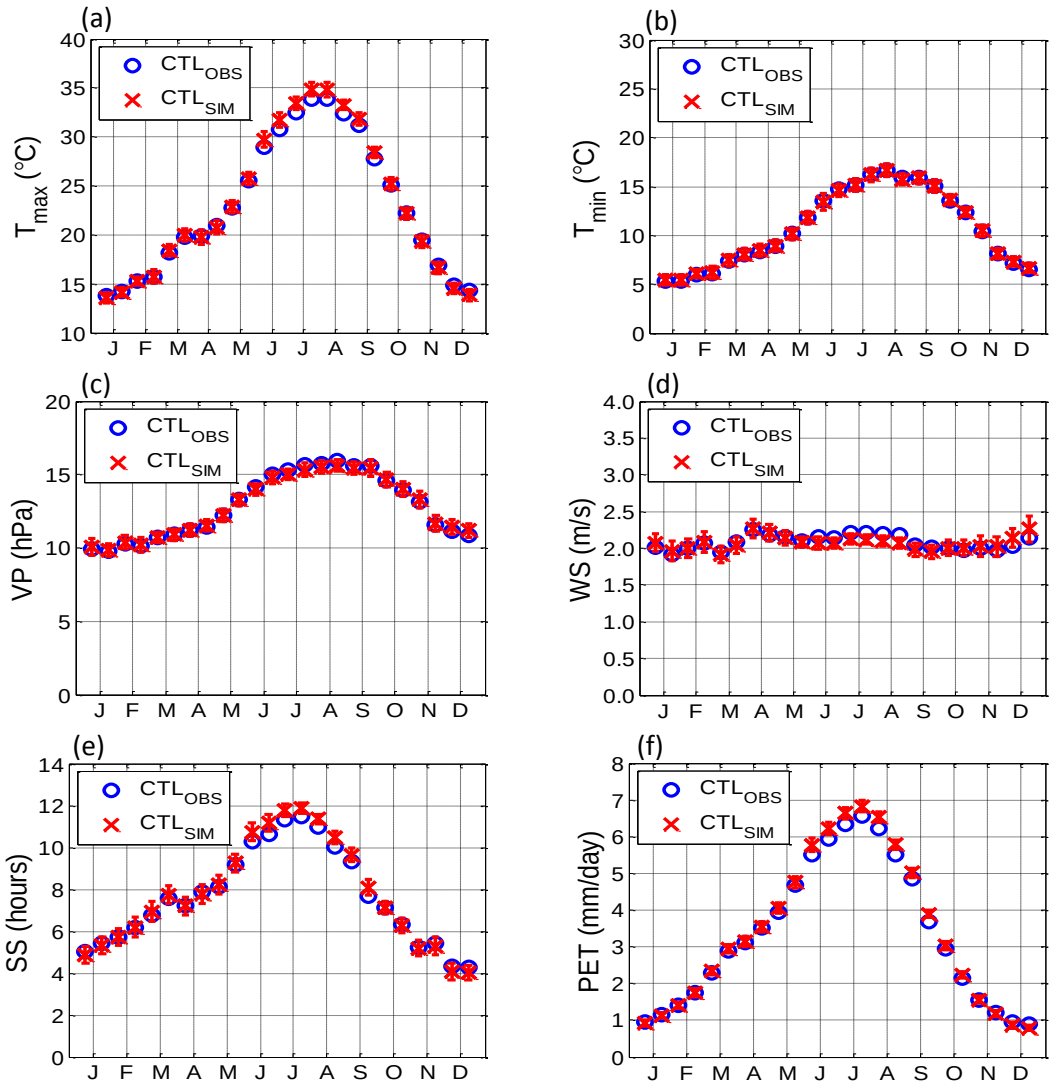

Fig. 7.7 Validation of weather generator (ICAAM-WG) for simulated daily (a) maximum temperature (T_{max}), (b) minimum temperature (T_{min})), (c) vapour pressure (VP), (d) wind speed (WS), (e) sunshine duration and (f) potential evapotranspiration (PET) at Beja station during the control period (1981–2010); the circles indicate the observed weather statistics, the crosses represent the simulated means of corresponding values and the error bars represent variability denoted by two standard deviations of the simulated 100 annual means.

The downscaled synthetic rainfall series have projected change of statistics consistent with the CFs calculated in Section 7.2.4: (1) Monthly M_{DP}, Var_{DP}, (1 – $Pdry_{DP1.0}$) (daily rainfall occurrence) are projected to decrease in the non-summer months except January and March; (2) Frontal activities are projected less frequently in autumn and December but more frequently in January and spring. Figs 7.8 (pages 113–114), 7.9 (pages 115–116) and schematic charts A4.1 and A4.2 illustrate the comparison of monthly statistics between future and control periods respectively for Beja, Castro verde, Almodôvar and Trindade stations.

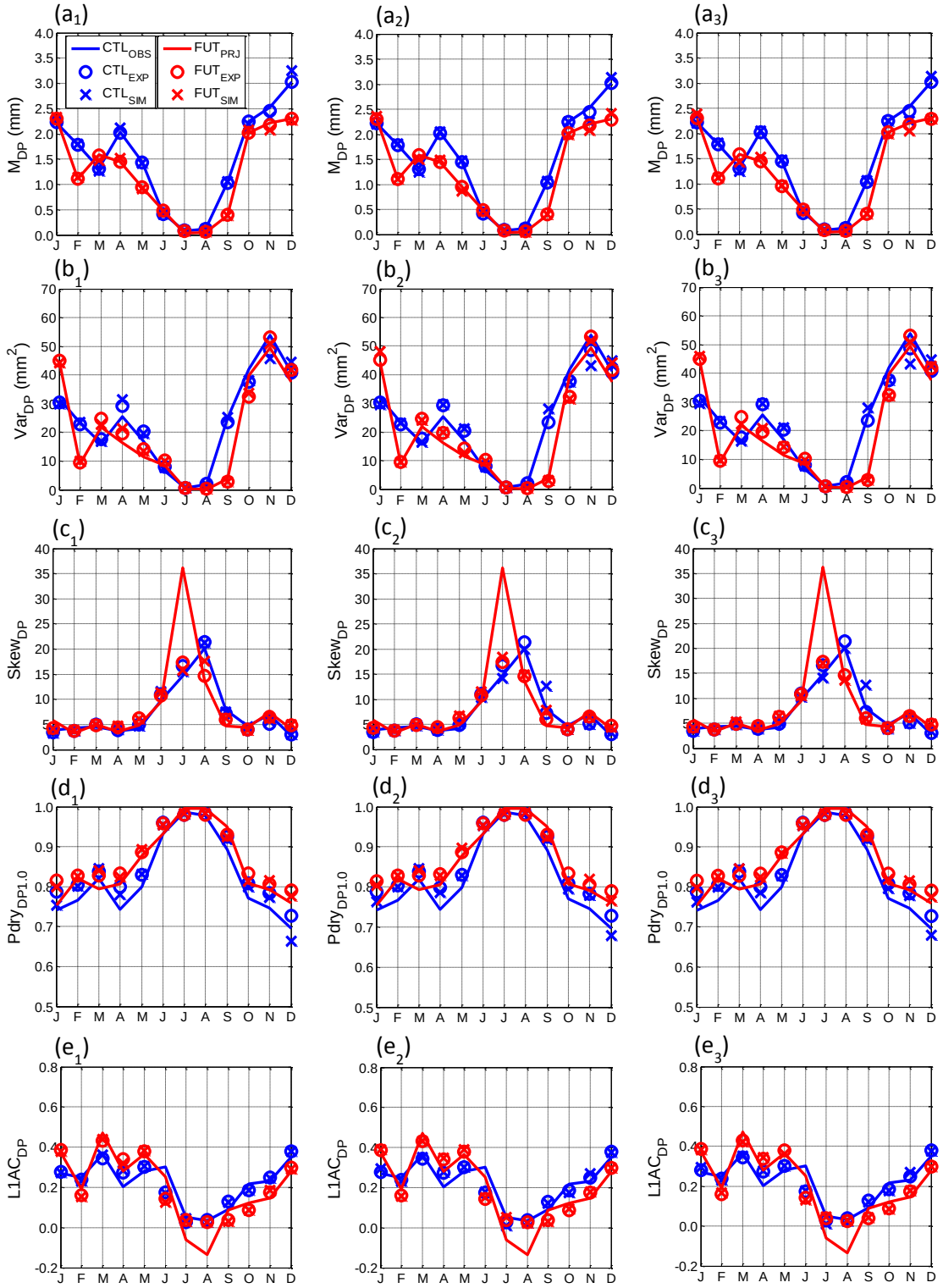
(a1)
(a2)
(a3)
CTLOBS
CTLEXP
CTLSIM
FUTPRJ
FUTEXP
FUTSIM
MDP (mm)
(b1)
(b2)
(b3)
VarDP (mm2)
(c1)
(c2)
(c3)
SkewDP
(d1)
(d2)
(d3)
PdryDP1.0
(e1)
(e2)
(e3)
L1ACDP
J F M A M J J A S O N D

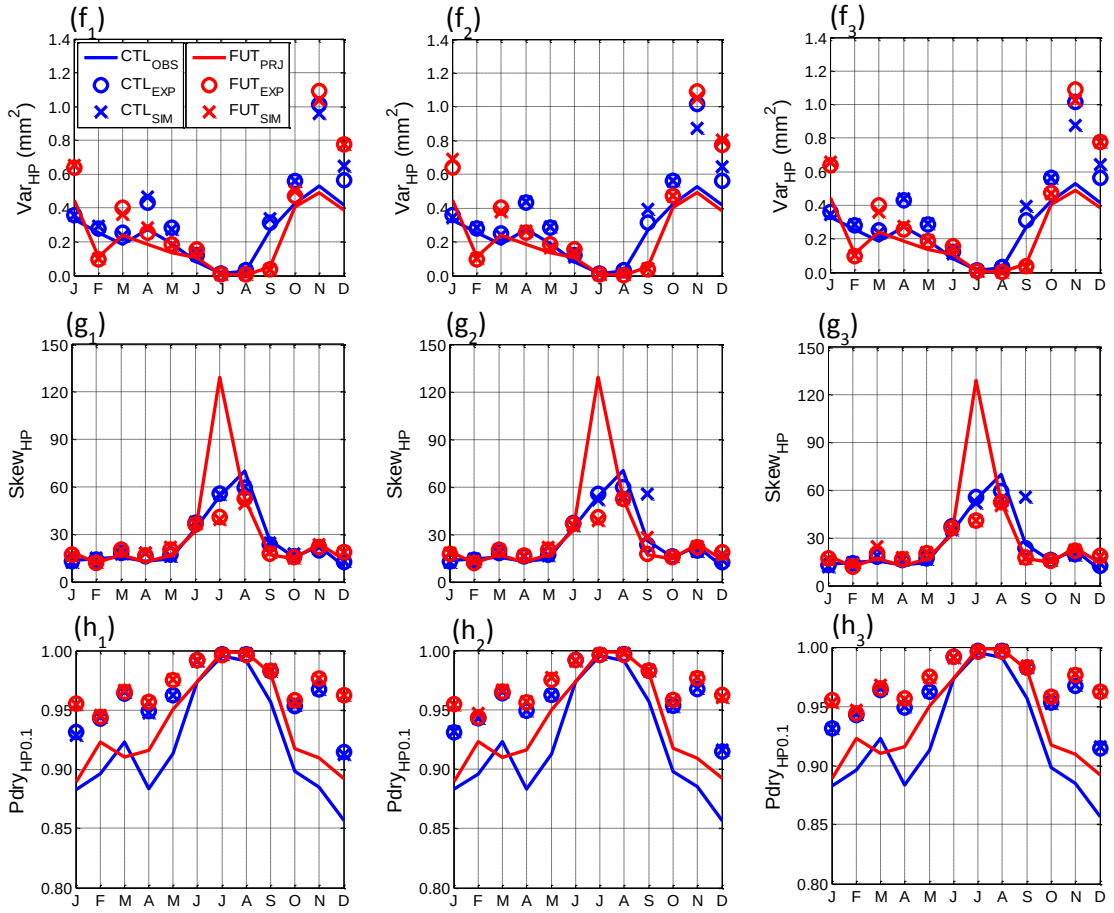

Fig. 7.8 Annual cycles of daily (a_1, a_2 and a_3) mean, (b_1, b_2 and b_3) variance, (c_1, c_2 and c_3) skewness, (d_1, d_2 and d_3) proportion of dry days and (e_1, e_2 and e_3) lag-1 autocorrelation and hourly (f_1, f_2 and f_3) variance, (g_1, g_2 and g_3) skewness and (h_1, h_2 and h_3) proportion dry hours for precipitation at the Beja station from the three 1000-year simulations of the future period (2041–2070) compared to the control period (1981–2010). The observed (OBS) or projected (PRJ), fitted (EXP) and simulated (SIM) statistics are respectively shown in solid lines, circles and crosses and in respective colors of blue and red for the control (CTL) and future (FUT) periods.

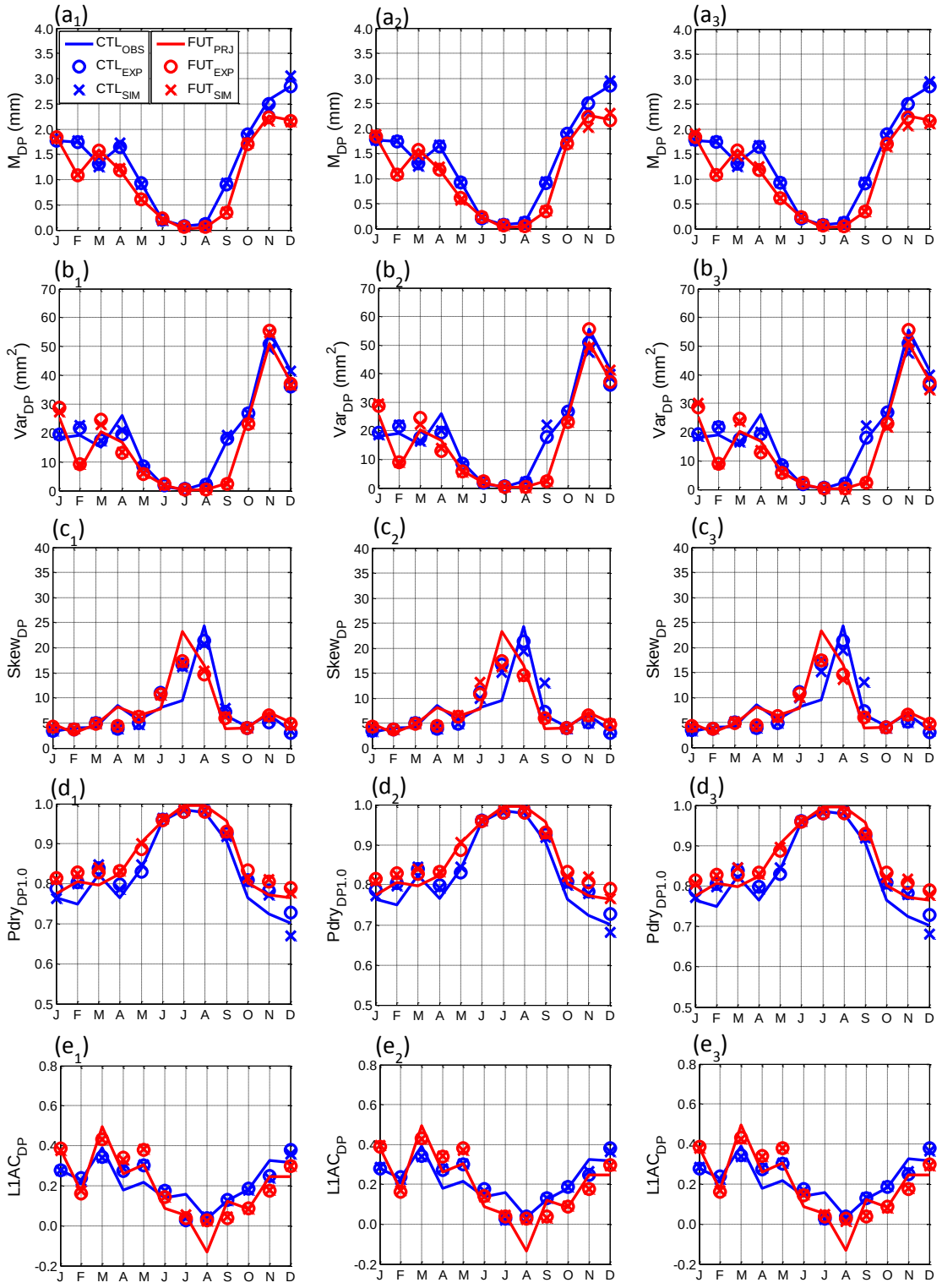
(a1)
(a2)
(a3)
(b1)
(b2)
(b3)
(c1)
(c2)
(c3)
(d1)
(d2)
(d3)
(e1)
(e2)
(e3)
CTLOBS
CTLEXP
CTLSIM
FUTPRJ
FUTEXP
FUTSIM
MDP (mm)
VarDP (mm2)
SkewDP
PdryDP1.0
L1ACDP
J F M A M J J A S O N D

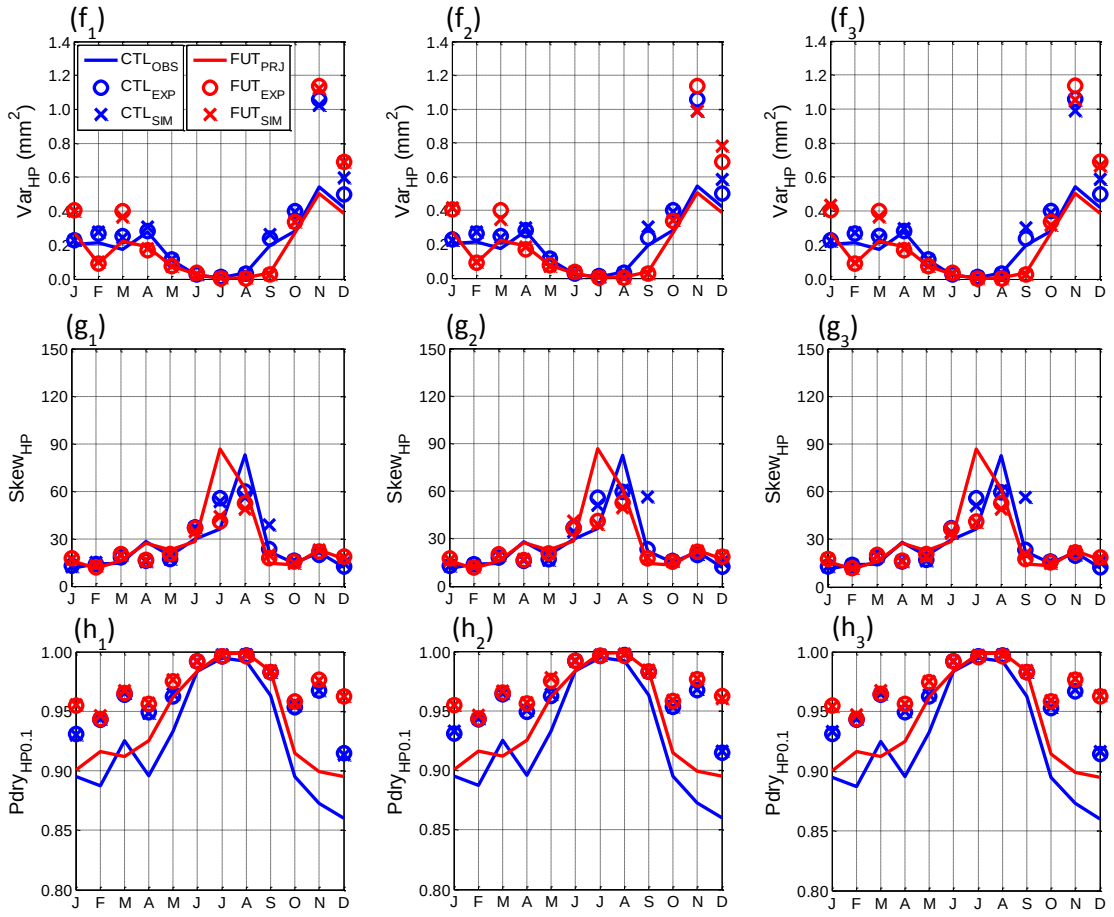

Fig. 7.9 Annual cycles of daily (a_1, a_2 and a_3) mean, (b_1, b_2 and b_3) variance, (c_1, c_2 and c_3) skewness, (d_1, d_2 and d_3) proportion of dry days and (e_1, e_2 and e_3) lag-1 autocorrelation and hourly (f_1, f_2 and f_3) variance, (g_1, g_2 and g_3) skewness and (h_1, h_2 and h_3) proportion dry hours for precipitation at the Castro verde station from the three 1000-year simulations of the future period (2041–2070) compared to the control period (1981–2010). The observed (OBS) or projected (PRJ), fitted (EXP) and simulated (SIM) statistics are respectively shown in solid lines, circles and crosses and in respective blue and red colors for the control (CTL) and future (FUT) periods.

As indicated in these figures, the fitted (red circles) and simulated (red crosses) monthly rainfall statistics for the future period excellently match their corresponding projected (in red solid lines) rainfall statistics except for $Skew_{DP}$ and $Skew_{HP}$ in July, $L1AC_{DP}$ in July and August, Var_{HP} in January, March, November and December and $Pdry_{HP0.1}$ in months except July, August and September. For $Skew_{DP}$ and $Skew_{HP}$ in July, the fitted and simulated values are much smaller than the projected ones indicating that the RainSim V3 model smoothed the extreme rainfall in that month; for $L1AC_{DP}$ in July and August, the fitted and simulated values are nearly 0 which is a result from the correction of unrealistic negative values projected by the CF approach. As explained in Section 7.3.1, the overestimations of fitted and simulated Var_{HP} are due to the use of intensity scaling field in the STNSRP process, and the overestimations of $Pdry_{HP0.1}$ are related to the homogeneous rainfall occurrence assumption adopted in the RainSim V3 model. Overall, the fitted and simulated monthly statistics correspond well with the projected values indicating a successful validation of the RainSim V3 model for the future climate scenario.

As shown in Figs 7.8 (pages 113–114), 7.9 (pages 115–116) and schematic charts A4.1 and A4.2, the comparisons of rainfall statistics for future time slice 2041–2070 with those for present time-slice 1981–2010 have displayed an evaluation of climate change: (1) Future non-summer months excepting January and March will be drier, especially for December, February, April, May and September (projected M_{DP} is decreased respectively around 1 and 0.5 mm/day for December and the other four months), with nearly the same rainfall skewness but lower intensity, variance and occurrence than those observed or generated for the control period. (2) Future January and March are different from other wet months, as indicated by CFs in Figs 7.4a–e (page 103). Future January will be wet with the same rainfall intensity and skewness but higher variance and lower occurrence than those observed or simulated for the control period; future March will be wetter, with the same rainfall occurrence and skewness but slightly higher rainfall intensity (projected M_{DP} is decreased around 0.2 mm/day) and variance, than in the control period. (3) Future summer months will be dry with the same low rainfall intensity, variance and occurrence, high skewness and dominated by convective activities as for control climate.

To evaluate climate change impacts on extreme events, Figs 7.10a–d (page 119) and Tables 7.3a–d (pages 119–120) are presented. Figs 7.10a–d are comparisons of extreme plots between future and control periods respectively for Beja, Castro verde, Almodôvar and Trindade stations. It is indicated, in Figs 7.10a–d, that the future high and medium frequencies extreme events, namely those with return period less than 10

years, have nearly the same magnitudes as the observed or simulated ones for the control period; however, future low frequency extreme events have distinctly higher magnitudes than those for the control period. The annual maximum daily rainfall is around 15% or 10 mm (10% or 5 mm) larger for future extreme events, with a return period between 20 and 50 years (between 10 and 20 years), than those under the control climate. Tables 7.3a–d have assessed the climate change impacts on precipitation extreme indices characterizing both wet and dry conditions. These indices were used in Costa and Soares (2009) in the context of combating desertification processes in Southern Portugal. SDII is average wet day precipitation (DP >= 1.0 mm); R5D is highest consecutive 5-day precipitation total; R30 is number of days with daily precipitation totals above or equal to 30 mm; CDD is maximum number of consecutive dry days (DP < 1.0 mm); FDD is number of dry spells (consecutive period with at least 8 dry days, DP < 1.0 mm); AII is average dry day precipitation (DP < 10 mm). The results, in Tables 7.3a–d, have shown that in the future: (1) high frequency rainfall events and droughts are slightly drier or remain the same; (2) extreme rainfall events and droughts are more intense and severe. In Tables 7.3a–b, respectively at 5^{th} and 50^{th} percentiles of the future climate, the SDII decreases around 6% and 1% (or 0.5 and 0.1 mm); the R5D decreases around 6% (or 2.4 mm) and increases 2% (or 1.6 mm); the R30 remains unchanged; the CDD increases around 10% and 5% (or 4 days); the FDD decreases 13% and 9% (or 1) and the AII decreases 17% and 20% (or 0.1 mm). In Tables 7.3c–d, for future climate respectively at 95^{th} and 98^{th} percentiles, the SDII decreases around 3% and 4% (or 0.3 and 0.5 mm); the R5D increases around 8% and 7% (or 9.5 and 9.3 mm); the R30 remains the same; the CDD increases around 13% and 14% (or 17 and 19 days); the FDD decreases 0 and 1; the AII decreases around 0.1 mm. Considering the large values of R5D and CDD at 95^{th} and 98^{th} percentiles, their distinct increases under future climate make the extreme rainfall events and droughts more intense and severe.

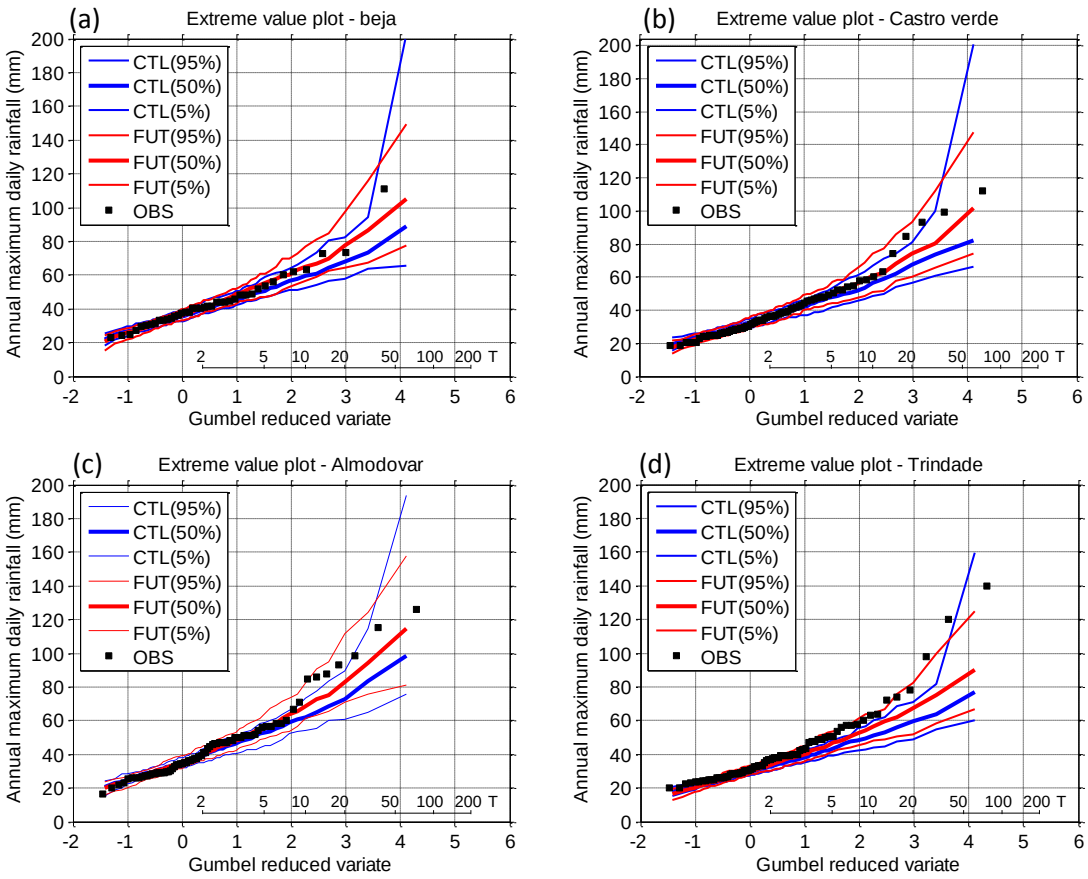

Fig. 7.10 Gumbel plots comparing observed and simulated extreme daily rainfall for (a) Beja, (b) Castro verde, (c) Almodôvar and (d) Trindade. The observed rainfall, shown in black solid squares, is for 1961–2010 at Beja station provided by IPMA and for 1931−2011 at stations Castro Verde, Almodôvar and Trindade provided by SNIRH; the simulated rainfall was generated by the RainSim V3 model, shown in respective blue and red solid lines for the control (1981−2010) and future (2041−2070) periods.

Table 7.3a Climate change impacts on moderate precipitation extreme indices (5th percentile)

Statistics[a]	CTL: 1981–2010 ($q_{0.05}$)				FUT: 2041–2070 ($q_{0.05}$)			
	Bej	Cas	Alm	Tri	Bej	Cas	Alm	Tri
SDII (mm)	7.7	6.8	7.3	6.4	7.2	6.4	6.8	6.0
R5D (mm)	46.6	41.7	45.8	38.0	44.9	38.4	42.3	36.9
R30 (days)	0.0	0.0	0.0	0.0	0.0	0.0	0.0	0.0
CDD (days)	42.0	43.0	42.0	44.0	46.0	47.0	46.0	48.4
FDD (freq.)	8.0	8.0	8.0	8.0	7.0	7.0	7.0	7.0
AII (mm)	0.3	0.3	0.3	0.3	0.2	0.3	0.3	0.2

Note: [a]The definitions of the statistics are introduced in section 7.4.1.

Table 7.3b Climate change impacts on moderate precipitation extreme indices (50th percentile)

Statistics[a]	CTL: 1981–2010 ($q_{0.50}$)				FUT: 2041–2070 ($q_{0.50}$)			
	Bej	Cas	Alm	Tri	Bej	Cas	Alm	Tri
SDII (mm)	9.4	8.4	9.0	7.9	9.3	8.2	8.9	7.8
R5D (mm)	72.2	66.3	74.0	61.5	75.8	67.0	75.0	62.5
R30 (days)	2.0	1.0	2.0	1.0	2.0	1.0	2.0	1.0
CDD (days)	74.0	75.0	75.0	80.0	78.0	79.0	78.0	84.0
FDD (freq.)	11.0	11.0	11.0	11.0	10.0	10.0	10.0	10.0
AII (mm)	0.5	0.5	0.5	0.5	0.4	0.4	0.4	0.4

Table 7.3c Climate change impacts on moderate precipitation extreme indices (95th percentile)

Statistics[a]	CTL: 1981–2010 ($q_{0.95}$)				FUT: 2041–2070 ($q_{0.95}$)			
	Bej	Cas	Alm	Tri	Bej	Cas	Alm	Tri
SDII (mm)	11.6	10.4	11.2	9.8	11.8	10.7	11.6	10.1
R5D (mm)	117.5	115.0	128.6	104.7	131.4	122.1	139.1	111.0
R30 (days)	5.0	4.0	4.0	3.0	5.0	3.0	4.0	3.0
CDD (days)	125.0	128.0	126.0	128.0	142.0	142.0	143.0	147.7
FDD (freq.)	14.0	14.0	14.0	14.0	14.0	14.0	14.0	13.0
AII (mm)	0.7	0.7	0.7	0.7	0.6	0.6	0.6	0.6

Table 7.3d Climate change impacts on moderate precipitation extreme indices (98th percentile)

Statistics[a]	CTL: 1981–2010 ($q_{0.98}$)				FUT: 2041–2070 ($q_{0.98}$)			
	Bej	Cas	Alm	Tri	Bej	Cas	Alm	Tri
SDII (mm)	12.2	11.0	11.9	10.3	12.6	11.4	12.4	10.8
R5D (mm)	136.6	133.5	152.8	120.8	150.5	142.8	160.2	127.2
R30 (days)	6.0	5.0	5.0	4.0	5.0	4.0	5.0	4.0
CDD (days)	140.0	141.0	140.6	142.6	161.0	160.0	160.0	160.6
FDD (freq.)	15.0	15.0	15.0	15.0	14.0	14.0	14.0	14.0
AII (mm)	0.8	0.8	0.8	0.8	0.7	0.7	0.7	0.7

7.4.2 Simulation of Future PET

The three 1000-year climatically stationary synthetic rainfall series, generated in Section 7.4.1, for future time-slice 2041–2070 at Beja is used to condition the ICAAM-WG model to generate three 1000-year climatically stationary time series of weather variables to compute future PET for Cobres basin. The projected annual cycles of mean and variance of daily T and R for future period are estimated based on the CF approach introduced in Section 7.2.4. The future 24 half months mean and variance of daily VP, WS and SS are assumed to be the same as observed, because the prediction of daily VP and WS is highly uncertain and maximum SS cannot increase. Following schematic chart A3.4, steps for getting future synthetic daily PET at Beja are: preparation of future temperature statistics (steps 1 to 3); generation of synthetic series of future daily T_{max} and T_{min} (steps 4 to 6); generation of synthetic series of future daily VP, WS and SS (steps 7 to 8) and calculation of synthetic future PET series (step 9). Steps 4–9 are repeated three times to get three replicates of 1000-year synthetic future PET.

Figs 7.11a–e (page 122) show that the 24 half monthly means of simulated future synthetic daily T_{max}, T_{min}, VP, WS and SS correspond well with the expected values except for some slight overestimation of T_{max} and SS and underestimation of WS in summer. This has validated the ICAAM-WG model in reproducing the projected future mean climatology at Beja. It is shown, in Fig 7.11a–b, that the projected future T_{max} and T_{min} increases respectively around 2–4 and 1.5–3 °C throughout the year, which displays good agreement with the CFs evaluated in Section 7.2.4. Finally, the projected future synthetic daily PET, Fig 7.11f, increases substantially in May and summer (around 1.0 mm/day) and relatively less in other months (around 0.4 mm/day).

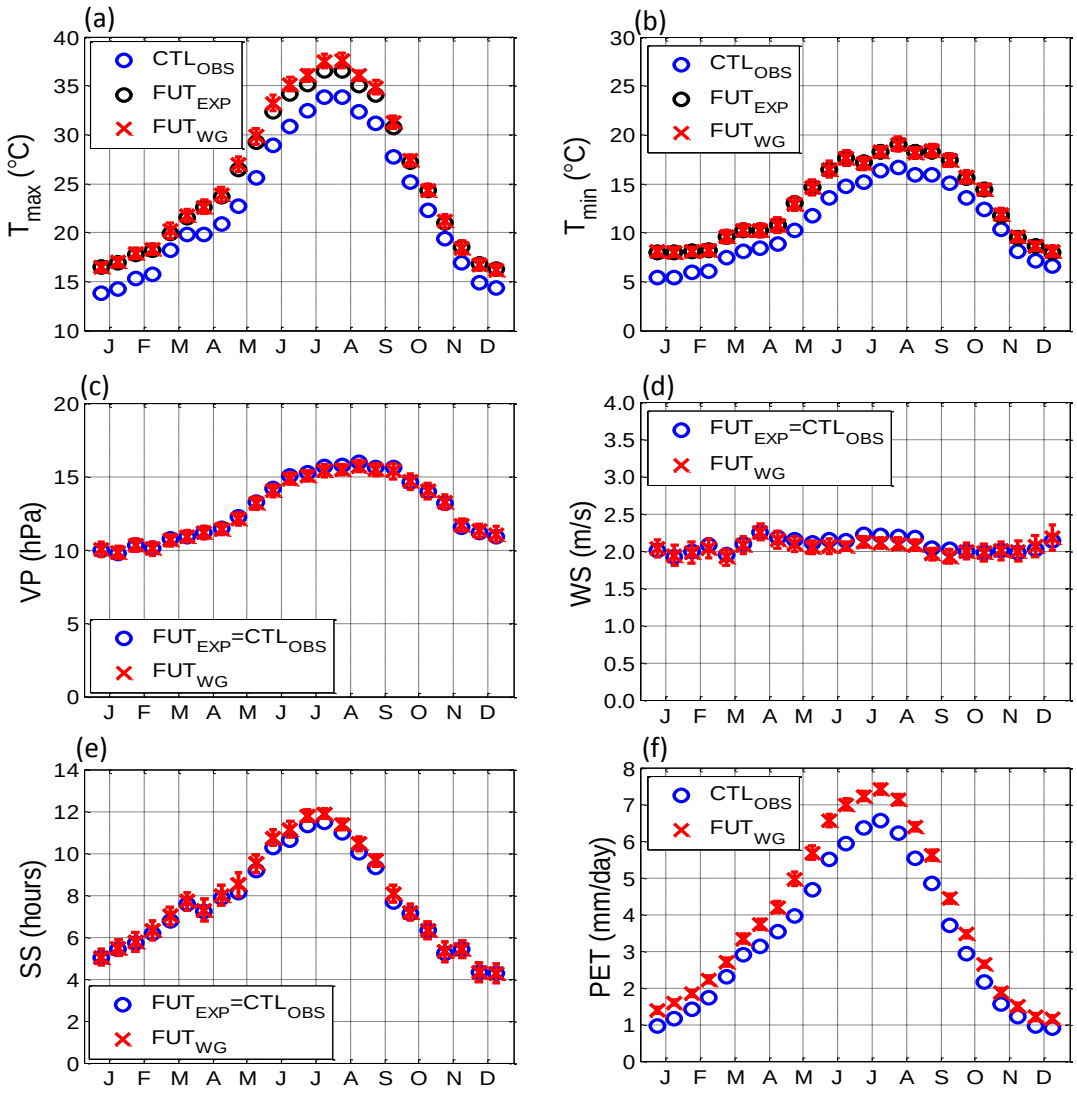

Fig. 7.11 Comparison of the annual cycless of observed (1981–2010: blue circles) and future (1981–2010: red crosses, black circles) daily (a) maximum temperature (T_{max}) and (b) minimum temperature (T_{min}), (c) vapour pressure (VP), (d) wind speed (WS), (e) sunshine duration (SS) and (f) potential evapotranspiration (PET) at Beja station; the circles indicate the observed or expected future weather statistics, the crosses represent the simulated means of corresponding values and the error bars represent variability denoted by two standard deviations of the simulated 100 annual means.

7.5 Discussion

The three 1000-year climatically stationary synthetic hourly rainfall series were generated by the RainSim V3 model, for Beja and the other 7 rainfall stations at Cobres basin, based on the observed statistics and projections of climate derived from the CF approach (Kilsby and Jones *et al.*, 2007) and RCM model METO-HC_HadRM3Q0 output provided by the ENSEMBLES project for the A1B emission scenario, respectively for the control (1981–2010) and future (2041–2070) time-slices. The ICAAM-WG model was developed at Beja station based on Kilsby and Jones *et al*.

(2007) with the inclusion of weather types for considering the existence of the long dry spells and wet spells for southern Portugal. The three 1000-year climatically stationary synthetic series of daily T_{max}, T_{min}, VP, WS, SS and FAO Penman-Monteith PET were then generated, by the ICAAM-WG, respectively for the control and future periods, with the condition of synthetic daily rainfall at Beja station. The objective of downscaling the projection of changes derived from the RCM model was achieved in this chapter. The generated synthetic hourly rainfall and daily PET, for the control and future periods, serve as input of SHETRAN model (Chapter 8), for the assessment of future climate change impacts on hydrological and sediment transport processes.

According to our objective of climate downscaling, the evaluation of model performance should answer whether or not the synthetic series can reproduce well: (1) the spatial and temporal (inter- and intra-annual) variations of water resources; (2) the magnitude and occurrence of extremes and persistence for climate scenarios. For synthetic hourly rainfall series, point (1) was considered in calibration and validation of the RainSim V3 model by evaluation of annual cycle variations of rainfall mean, variance and cross correlation among stations. Skewness is a third order moment property, very important for simulation of extreme rainfall events (Cowpertwait, 1998; Burton *et al.*, 2008) and lag-1 autocorrelation coefficient is crucial for simulation of persistent events such as long dry spells (Jones *et al.*, 2009). Therefore, point (2) was considered in model calibration and validation by assessment of annual cycles of rainfall skewness, occurrence (or 1–dry probability) and lag-1 autocorrelation. In addition, extreme value plots, not included in calibration but in validation, were evaluated for consideration of point (2). As for the synthetic daily PET series, since it was conditioned by synthetic daily precipitation and mainly influences point (1), the validation of the ICAAM-WG model was concluded from evaluation of 24 half monthly means of daily PET and its determinant factors such as T_{max}, T_{min}, VP, WS and SS.

The rainfall and PET simulations for control climate scenario are very satisfactory. The RainSim V3 model accurately reproduced monthly M_{DP}, mostly well represented monthly Var_{DP} and Var_{HP} and reasonably simulated the seasonality of rainfall cross-correlation properties. The annual cycles of $Skew_{DP}$, $Pdry_{DP1.0}$, $L1AC_{DP}$ and $Skew_{HP}$ were well reproduced in spite of the spatially uniformity assumed in the RainSim V3 model (Burton *et al.*, 2008). The annual cycles of $Pdry_{HP0.1}$ were well reproduced in summer but slightly overestimated in other months (around 5% to 7%) due to the homogeneity of rainfall occurrence assumed in the model (Burton *et al.*, 2010b). The ability of the RainSim V3 model in reproducing the realistic rainfall extremes was also demonstrated for stations with long records of daily rainfall series. The ICAAM-WG

model represented well the 24 half months means of T_{max}, T_{min}, VP, WS, SS and PET, with slight overestimations of T_{max}, SS and PET and underestimation of WS in summer. Overall, the RainSim V3 and ICAAM-WG models have the capacity of reproducing synthetic hourly rainfall and daily PET series in conformity to our objectives.

The future climate simulations have shown that the future rainfall is projected to decrease (around 0.2–0.9 mm/day) in non-summer months especially in December (around 0.9 mm/day) and in February, April, May and September (around 0.5 mm/day), increase slightly (around 0.2 mm/day) in March and not change in January and summer months. Future high frequency events are projected to almost not change, but future low frequency events such as extreme rainfall events and droughts are projected to be more intense and severe, around 10%–15% larger than those from the control period. In summary, future climate is projected to decrease in mean and increase in extremes. This is consistent with Rajczak *et al*. (2013), concerning the projected change of precipitation climate between time-slices 1970–1999 and 2070–2099 for southern Europe from 10 RCMs provided by the ENSEMBLES project. Future PET is projected to increase in May and summer around 1 mm/day and in other months around 0.4 mm/day. The projected decrease in mean daily precipitation and large increase in PET is expected to deteriorate summer drought, lower the water resources availability throughout the year and probably accelerate desertification process in southern Portugal. Therefore, the downscaled climate scenarios are used in Chapter 8 to evaluate the potential impact of climate change on hydrological processes and sediment transportation at Cobres basin.

8. Assessment of Future Climate Change Impacts

Assessment of future climate change impacts are carried out for Cobres basin in this chapter based on SHETRAN simulations under control (1981–2010) and future (2041–2070) climates by using the three 1000-year hourly rainfall and daily PET generated in Chapter 7 and the calibrated SHETRAN parameters derived in Chapter 5. This chapter begins with a short introduction, and then the methodology is presented. The evaluations of climate change impacts are carried out in terms of hydrological processes and sediment transport, with the aim of answering the following three issues: (1) How much impact would future climate change have on the available water resources at Cobres basin? (2) How much impact would if have for extreme events? (3) How much impact would if have for basin sediment yield? Finally, a short discussion is given in reply to the questions.

8.1 Introduction

In the last decade, the average temperature over continental Europe that is 1.3 °C warmer than the preindustrial level marked the highest record since preindustrial era (EEA 2012); and the precipitation has decreased in southern Europe with consequent decreases in river flows and increases in the frequency and intensity of droughts (EEA 2012). The decreasing water availability has been observed (EEA 2012) and Seneviratne *et al.* (2012) concluded with medium confidence that since the 1950s southern Europe has experienced a trend to more intense and longer droughts. Regional climate models from the PRUDENCE (Christensen *et al*. 2007) and ENSEMBLES (van der Linden and Mitchell 2009) projects have also projected an exacerbated water stress in southern Europe for future (Blenkinsop and Fowler 2007; Heinrich and Gobiet 2012; Majone *et al.*, 2012; Forzieri *et al.*, 2013; Fraga *et al.*, 2013; Hagemann *et al.*, 2013; Rajczak *et al.*, 2013). Climate change impacts are required to be assessed with better confidence to provide stakeholders with more suitable adaptation measures, because the increase of temperature and decrease of water availability would bring about catastrophic economic losses mainly due to the increase in energy demand for cooling and the reduction in hydropower generation and agricultural production (EEA 2012). For example, the considerable reductions in river flow during the 2004–2005 drought (Santos *et al.*, 2007) across the Iberian Peninsula caused a total estimate of EUR 883 million, equivalent to 0.6% of GDP (Demuth 2009; EEA 2012).

Studies of climate change impacts on southern Europe have not reached consensus conclusion about the extreme events (EEA 2012; Seneviratne *et al.,* 2012). Future precipitation extremes may increase in Iberia Peninsula (Rajczak *et al.*, 2013), but fluvial flood extremes may decrease or increase depending on the domain, climate model and greenhouse gas emission scenario (Feyen *et al.*, 2012; Rojas *et al.*, 2012). These studies are all based on direct use of simple bias-correction of RCM model data and the conclusions were derived from extreme value analysis of 30 data points; therefore their results should be interpreted with caution. As climate in Iberia Peninsula is highly variable in space and time, research of climate change impacts on extreme events should be evaluated on catchment scale and bias-correction of RCM data should consider high-order rainfall statistics that are related to the extreme events.

This study mainly concerns future climate change impacts on southern Portugal where annual rainfall is around 400–900 mm (Ramos and Reis 2002) and with large intra- and inter-annual variability (Corte-Real *et al.*, 1998; Mourato *et al.*, 2010). Climate studies in this region are mainly focused on water scarcity and drought-related aspects, which does not exclude the importance of future climate change impacts on extreme events, not only because of their contribution in sediment transport but also in terms of their consequences in catastrophic losses. In the 1876 extreme event, the Guadiana river branch in Mértola raised 25 meters on December 14th, 1876 and the extreme discharge lasted 3 days and took away everything in its way (Varino 2011); this would bring about enormous monetary and life losses, if it had happened now and no appropriate adaptation measures had been planned and implemented.

The objective of this chapter is to assess future climate change impacts on two aspects: (1) water availability and sediment yield; (2) extreme discharge and sediment discharges. The future climate change impacts on available water resources and sediment yield are evaluated based on the analysis of annual and monthly water balance components and annual and seasonal flow duration curves. The future climate change impacts on annual maximum daily discharge and sediment discharge are assessed by comparing the empirical cumulative probability plots (CDFs), extreme value plots and fitted theoretical distributions during control and future conditions.

8.2 Methodology

8.2.1 SHETRAN Model Simulation

Climate change impacts on hydrological process and sediment transport are evaluated using the SHETRAN hydrological model. In Chapter 5, we set up the SHETRAN model

based on land-use map from CORINE land cover 2006 (Caetano *et al.*, 2009) and soil type map from IHERA. Based on model structure and previous study, we configured 28 parameters (22 hydrological parameters and 6 sediment parameters), related with the two main types of land-use and three main types of soil, to be calibrated. The automatic calibrations of SHETRAN model by MSCE and NSGA-II have produced different settings of calibration parameters, all allowing well reproduction of hydrological processes for both calibration and validation periods. This phenomenon has been well known as equifinality problem (Beven and Freer 2001). The parameter uncertainty may result in differences in future climate change impacts. On the other hand, from Chapter 6, we have concluded that SHETRAN model simulations with spatial resolution of 1.0 km grid and temporal resolutions of 1.0 hour rainfall and 1.0 day PET would give better representation of storm-runoff processes at Cobres basin than those with 2.0 km. However, due to the limited computing resources, we do not consider the parameter uncertainty and the 0.5 km and 1.0 km grid resolutions for assessment of future climate impacts. Instead, we chose 2.0 km grid and selected the set of calibration parameters derived from Sections 5.5.2 and 5.6.4 and considered them valid for both control and future climate conditions. In Chapter 7, we have obtained three 1000–year synthetic hourly rainfall and daily PET respectively under control and future conditions. In this chapter, the future climate change impacts are evaluated by comparison of the hydrological and sediment transport processes derived from SHETRAN simulations driven by those 2 series of 3000–year synthetic rainfall and PET data.

8.2.2 Statistical Methods

- *Descriptive statistical measures*

To evaluate future climate impacts on water resources availability and annual sediment yield, we extracted the descriptive statistical measures, such as mean, standard deviation (STD), coefficient of variation (CV), 5^{th}, 50^{th}, 95^{th}, 98^{th} and 99^{th} percentiles ($q_{0.05}$, $q_{0.50}$, $q_{0.95}$, $q_{0.98}$ and $q_{0.99}$), from the empirical frequency distributions of annual variables like rainfall, PET, AET, subsurface storage (ΔS), runoff and sediment yield under control and future conditions. To avoid compensation effects by averaging over the year, we compare the annual cycle variations of these variables by using boxplots (Wilks 2006). Furthermore, to get future climate impacts on the hydrological regime of Cobres basin, we plotted the flow duration curves, for the whole year and the four individual seasons, under control and future climate scenarios, using the same methodologies as described in Davie (2008).

- *Extreme value analysis*

We describe extreme events as a collection of annual maxima or block maxima (largest in a block of around 365 values). In this study, we analyze annual maximum daily discharge and sediment discharge at Monte da Ponte (outlet) station, under control and future conditions, to assess whether the frequency and magnitude of extreme storm events are likely to increase as a result of climate change and quantify the possible changes. The parametric distribution is a compact representation of the empirical distribution, which facilitates derivation of probabilities for extreme values outside of the provided data sets, calculation of quantiles for specified probabilities and comparisons among given extreme distributions. The annual maxima of daily discharge and sediment discharge are generally heavy tailed and may be described by the generalized extreme value (GEV) distribution (Stedinger *et al.*, 1993; Katz *et al.*, 2002; Wilks 2006). In this study, the distribution of extreme events is fitted by the trial-and-error method, and two steps are required: (1) a GEV distribution is fitted to the data, and then the probability plot and goodness-of-fit tests decide whether the fit is appropriate as described by Stedinger *et al.* (1993); (2) the L-moment diagram is used to confirm the goodness-of-fit or further investigate the possible distributions consistent with the available data set. If GEV distribution appears inconsistent with the data, alternative distributions, suggested by the L-moment diagram, are fitted to the data and probability plots and goodness-of-fit tests distinguish the most appropriate distribution from the others. The cumulative distribution functions (CDFs) of GEV, gamma and three-parameter lognormal distributions are shown in Appendix 5.

The fitting of data to specified distributions can be carried out by using either the maximum likelihood method (Wilks 2006) or the L-moment method (Hosking 1990; Hosking and Wallis 1997). We use the matlab functions in statistic toolbox (version R2013a) developed by the MathWorks Company to fit the data by the former method and the R functions in the lmom package (version 2.1) developed by Hosking to do the fitting by the latter method. Then, we select the better one by comparison of the derived probability plots. Two goodness-of-fit tests, namely the Lilliefors test and the Filliben test, described in Wilks (2006) are applied. In the Lilliefors test, the test statistic is set as D_n the largest absolute difference between empirical and fitted cumulative probabilities (equation 8.1). The null hypothesis is that the data were drawn from the distribution being tested, and a sufficiently large discrepancy will result in the null hypothesis being rejected. Statistical simulation is used to derive the critical value of D_n. We generate 1000 samples, with the length of tested data, from the tested distribution, by using corresponding matlab functions and calculate D_n for each of 1000 samples.

The α-level critical value is then approximated as the (1- α) quantile of the 1000 synthetic D_n.

$$D_n = \max_x |F_n(x) - F(x)| \quad (8.1)$$

Where $F_n(x)$ is the empirical cumulative probability, estimated as $F_n(x(i)) = i/n$ for the i^{th} smallest data value; and $F(x)$ is the theoretical cumulative distribution function evaluated at x.

The test statistic of the Filliben test is the correlation between the empirical quantiles x(i) and the quantiles from the function of tested distribution $\Phi^{-1}(p_i)$, with p_i estimated using equation 8.2 which approximate the cumulative probability for the i^{th} order statistic. The null hypothesis is that the data were drawn from the tested distribution, and if the correlation is smaller than the appropriate critical value the null hypothesis is rejected. We generate 1000 samples, with the length of tested data, from the tested distribution and calculate correlation between empirical and theoretical quantiles for each of the 1000 samples. The α-level critical value of correlation is approximated as the $\alpha \times 100\%$ quantile of the 1000 synthetic correlations.

$$p\left(x_{(i)}\right) = \frac{i-a}{n+1-2a}, \quad a = 0.3175 \quad (8.2)$$

The L-moment diagram is generated by using functions “lmrd” and “lmrdpoints” in the lmom package (version 2.1) developed by Hosking.

8.3 Assessment of Future Climate Change Impacts

Future climate change impacts are assessed in terms of hydrological and sediment transport processes. To indicate the future climate impacts on water resources availability and sediment yield, Table 8.1 (page 130) and Figs 8.1a–f (page 131) show the water balance components and sediment yield respectively at annual and monthly scales; Figs 8.2a–e (page 134) compare flow duration curves for the whole year, autumn, winter and spring between control and future conditions. To display the future climate impacts on extreme events, Figs 8.3a–b (page 135) and Figs 8.4a–d (page 137) compare, in different ways, the extreme value plots of annual maximum daily discharge and sediment discharge between control and future scenarios; Figs 8.5a–d (page 138) display the theoretical fit of the four empirical extreme value distributions; Fig 8.6 (page 139), Tables 8.2a–b (page 141) and Tables 8.3a–b (page 141) indicate the results of goodness-of-fit tests for the proposed distribution fits; and finally Figs 8.7a–b (page 140) show histograms and parameters of the best distribution fits.

8.3.1 Future Climate Change Impacts on Water Availability and Sediment Yield

- *Annual water balance components and sediment yield*

Table 8.1 shows the statistics for evaluation of climate change impacts on catchment average changes in mean, standard deviation, coefficient of variation, 5th, 50th, 95th 98th and 99th percentiles of the annual rainfall, PET, AET, subsurface storage, runoff and sediment yield. It is indicated that future (2041–2070) basin average annual rainfalls are decreased around 80–90 mm or 10%–30% for high, medium and low frequency extremes. Together with the 200 mm or 15% increase of annual PETs, the future annual runoffs are projected to decrease around 8–88 mm or 30%–80%, with 30%, 60% and 80% respectively for extremely wet, medium wet and extremely dry years; consequently, the future annual sediment yields are projected to decrease around 0.26–2.13 t ha^{-1} year^{-1} or 30%–87%, with 30%, 55% and 87% respectively for extremely wet, medium wet and extremely dry years. Future annual PETs increase around 200 mm for all probability levels; however, the future annual AETs decrease around 20–60 mm or 5%–20% with larger decrease associated with less annual rainfall. AET is determined by PET, crop characteristics and soil water stress condition (Allen *et al.* 1998). Because we considered the same land-use types for control and future conditions, the decrease of AETs reflects the existence of water shortage for future crops, forests and other plants.

Table 8.1 Statistics for evaluation of climate change impacts on catchment: average changes in mean, standard deviation (STD), coefficient of variation (CV), 5th, 50th, 95th 98th and 99th percentiles ($q_{0.05}$, $q_{0.50}$, $q_{0.95}$, $q_{0.98}$ and $q_{0.99}$) for annual rainfall (P), PET, AET, subsurface storage (ΔS), runoff (R) and sediment yield (SY)

Annual statistics	CTL period: 1981–2010 (**FUT** period: 2041–2070)					
	P(mm)	PET(mm)	AET(mm)	ΔS(mm)	R(mm)	SY(t ha^{-1} year^{-1})
Mean	474 (**386**)	1257 (**1453**)	376 (**335**)	2 (**2**)	96 (**48**)	2.35 (**1.29**)
STD	104 (**102**)	27 (**27**)	40 (**50**)	24 (**22**)	68 (**49**)	1.68 (**1.26**)
CV	0.22 (**0.27**)	0.02 (**0.02**)	0.11 (**0.15**)	13.0 (**9.82**)	0.70 (**1.01**)	0.71 (**0.98**)
$q_{0.05}$	315 (**228**)	1213 (**1408**)	309 (**251**)	-37 (**-36**)	10 (**2**)	0.30 (**0.04**)
$q_{0.50}$	467 (**382**)	1257 (**1452**)	377 (**334**)	2 (**2**)	85 (**33**)	2.04 (**0.91**)
$q_{0.95}$	654 (**561**)	1301 (**1497**)	440 (**416**)	42 (**38**)	227 (**144**)	5.57 (**3.72**)
$q_{0.98}$	708 (**613**)	1312 (**1509**)	454 (**435**)	53 (**46**)	270 (**182**)	6.78 (**4.94**)
$q_{0.99}$	738 (**661**)	1322 (**1521**)	463 (**445**)	60 (**53**)	295 (**212**)	7.63 (**5.50**)

- *Monthly water balance components and sediment yield*

Figs 8.1a–f display the boxplots for annual cycles of monthly rainfall, PET, subsurface storage change, AET, runoff and sediment yield under control and future scenarios.

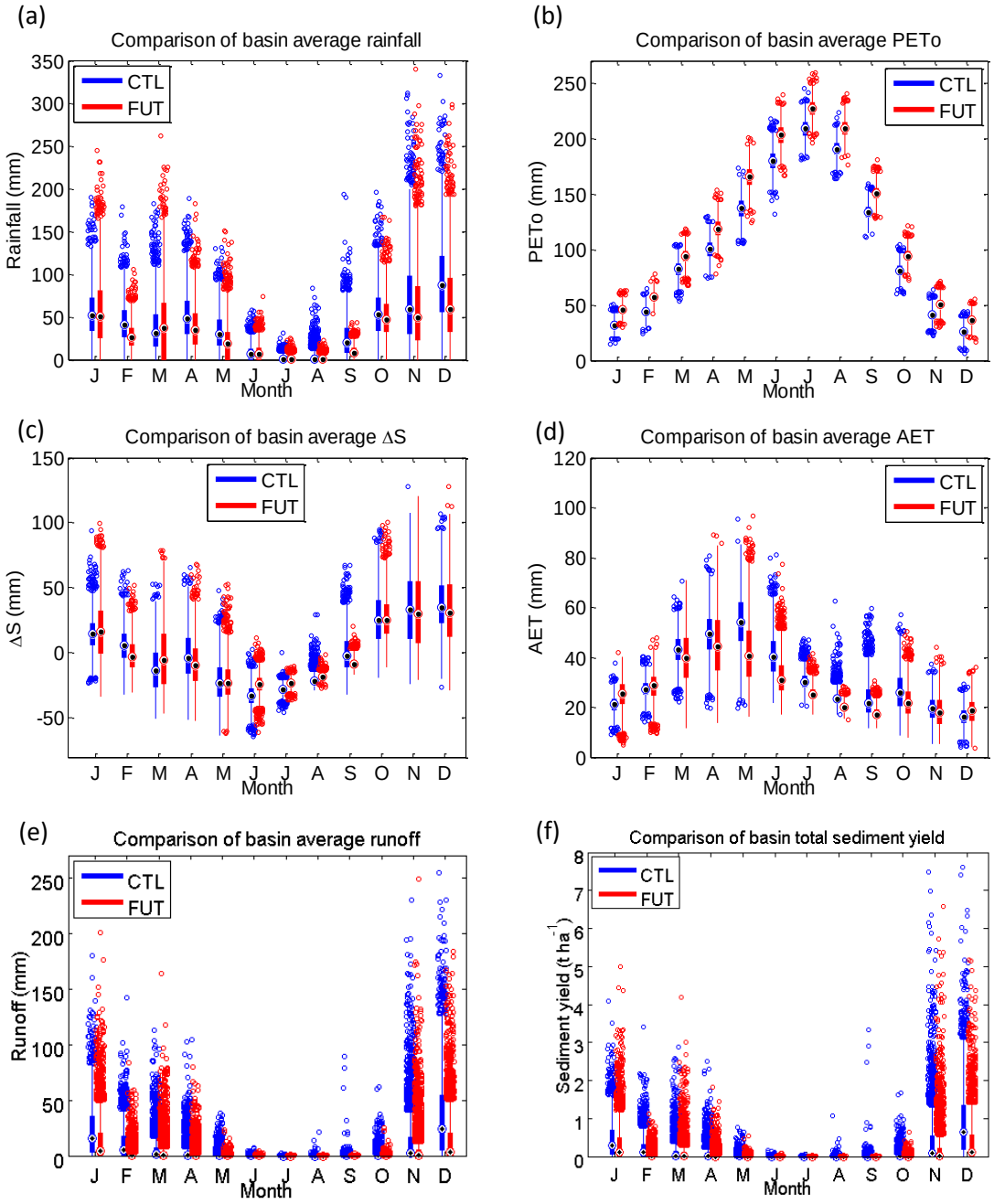

Fig. 8.1 Boxplots showing the annual cycles of monthly rainfall (a), PET (b), change of subsurface storage (ΔS) (c), AET (d), runoff (e) and sediment yield (f) under control (blue) and future (red) climate conditions. The small circles embedded with black dots represent the median value for each month, the lower (upper) limits of the compacted boxes represent the first quartile $_{q0.25}$ (third quartile q0.75), the lower (upper) limits of the whiskers represent the "$q_{0.25} - 1.5 \times (q_{0.75} - q_{0.25})$" ("$q_{0.75} + 1.5 \times (q_{0.75} - q_{0.25})$") and the circles below the lower whiskers (above the upper whiskers) represent outliers.

The boxplots in Figs 8.1a–f are plots of five sample quantiles: the lower limit of the lower whisker, $q_{0.25}-1.5\times(q_{0.75}-q_{0.25})$, the lower limit of the compacted solid box, $q_{0.25}$, the median, $q_{0.5}$, the upper limit of the compacted solid box, $q_{0.75}$, and the upper limit of the upper whisker, $q_{0.25}+1.5\times(q_{0.75}-q_{0.25})$. The compacted solid boxes indicate the Interquartile Ranges (IQRs) or the central 50% of the data and, the locations of the median, display the measures of symmetry of the data. Outliers are shown in empty circles that stay above or below the whiskers. We can see from Fig 8.1a that: (1) monthly rainfalls under both control and future conditions are all right-skewed due to the existence of large extreme values; (2) future monthly rainfalls decrease in non-summer months, except for January and March, and the decreases are identified for all the probability levels which are especially pronounced in September, December, February, April and May; (3) future January and March are with larger IQRs and extreme rainfall amounts, although the median value keeps the same in January and increases slightly in March; (4) future summer months continue with little rainfall and the extreme rainfall amounts in August decrease distinctly. From Fig 8.1b, we know that (1) the probability distributions of monthly PETs under both control and future conditions are symmetric; (2) future monthly PETs increase for all the probability levels and the increases are larger in May and summer months.

Figs 8.1e–f have shown that monthly runoff and sediment yield at Cobres basin are highly right-skewed for present and future climates. Under control condition, runoff and sediment erosion mainly occur in November and winter months, although under extreme circumstances substantial quantities may be identified in October and spring, especially in March and April. December and January are the only two months that may always have runoff generation and sediment yield and with large IQRs and extreme amounts; November and February may have no runoff and sediment yield at a probability level of 50% but with unneglectable IQRs and considerable extreme values. Under future condition, the monthly runoff and sediment yield are much more right-skewed with all median values of 0, meaning no runoff and sediment yields would occur all over the year at a probability level of 50%. December and January are the only two months with non-ignorable amounts of runoff and sediment yield in the future at a probability level of 50%. Under extreme circumstances, November, December and January in the future may have destructive amounts of runoff and sediment yield and future February, March and April may have considerable quantities. As for summer and September, no runoff and sediment yield is identified for future, even under extreme conditions; the possible extreme values in August and September under control condition decrease to zero in the future.

Fig 8.1d displays future monthly decrease of AET except for winter months, indicating future vegetation and crop growths are more water-limited than under control climate. Fig 8.1c depicts monthly subsurface water increase or decrease under control and future conditions, which, together with monthly rainfall (Fig 8.1a) and AET (Fig 8.1d), explains future climate change on monthly runoff (Fig 8.1e) and sediment yield (Fig 8.1f). Spring is the season with considerable rainfall but nearly no runoff, and consequently no sediment yield, at Cobres basin for both control and future conditions; because the rainfall amounts (around 20─50 mm in median) are not sufficient to supply AETs (around 40─55 mm in median) which leads to subsurface water deficits (around 3─23 mm in median). Summer is a completely dry season with no rainfall but high subsurface water deficits (around 18─32 mm in median) which well explains the complete absence of runoff and sediment yield. Under control condition, September is the first month with considerable rainfall after the summer drought, however, this rainfall amount (around 18 mm in median) is completely used in AET dispense (around 22 mm in median), therefore no runoff and consequently no sediment yield is produced; future September is even drier with only a little rainfall (around 8 mm in median) quite insufficient for supplying AET (around 17 mm in median) and produce runoff and sediment yield. October is the first month with abundant rainfall (around 50 mm in median) sufficient to provide AET (around 25 mm in median) and refresh subsurface water storage (around 25 mm in median) under both control and future conditions; however, no runoff is generated in this month, consequently no sediment yield is produced. November and winter are the only months with the wettest soil moisture conditions and the lowest PETs in the year. Under the control condition, there is 50% probability that runoff, and consequent sediment yield may be generated in November and February; however as a consequence of precipitation decrease, nearly no runoff and sediment yield are produced in the future. December is the month with most runoff and sediment yield, under either control (around 54 mm runoff and 1.4 t ha^{-1} sediment yield in 75^{th} percentile) or future (around 20 mm and 0.6 t ha^{-1} in 75^{th} percentile) conditions, due to the largest rainfall amounts and smallest AET dispense; similarly, January is the month with second largest runoff generation and sediment yield. Under future condition, precipitation decreases in December and AET increases in both December and January, which leads to a probability level of 50% for runoff generation and sediment yield in these two months. Nevertheless, extreme runoff and sediment yield may occur mainly in November, December and January, probably with largest magnitude, or secondarily in February, March and April, probably with moderate magnitude. The future extreme values, shown in Figs 8.1e─f, seem to be much smaller than the control ones, for which further investigations are shown in the next section.

- *Annual and seasonal flow duration curves*

Fig 8.2a and Fig 8.2b indicate annual and seasonal flow duration curves under respective control and future conditions; comparisons between control and future are respectively shown in Fig 8.2c, Fig 8.2d, Fig 8.2e and Fig 8.2f for the whole year, autumn, winter and spring.

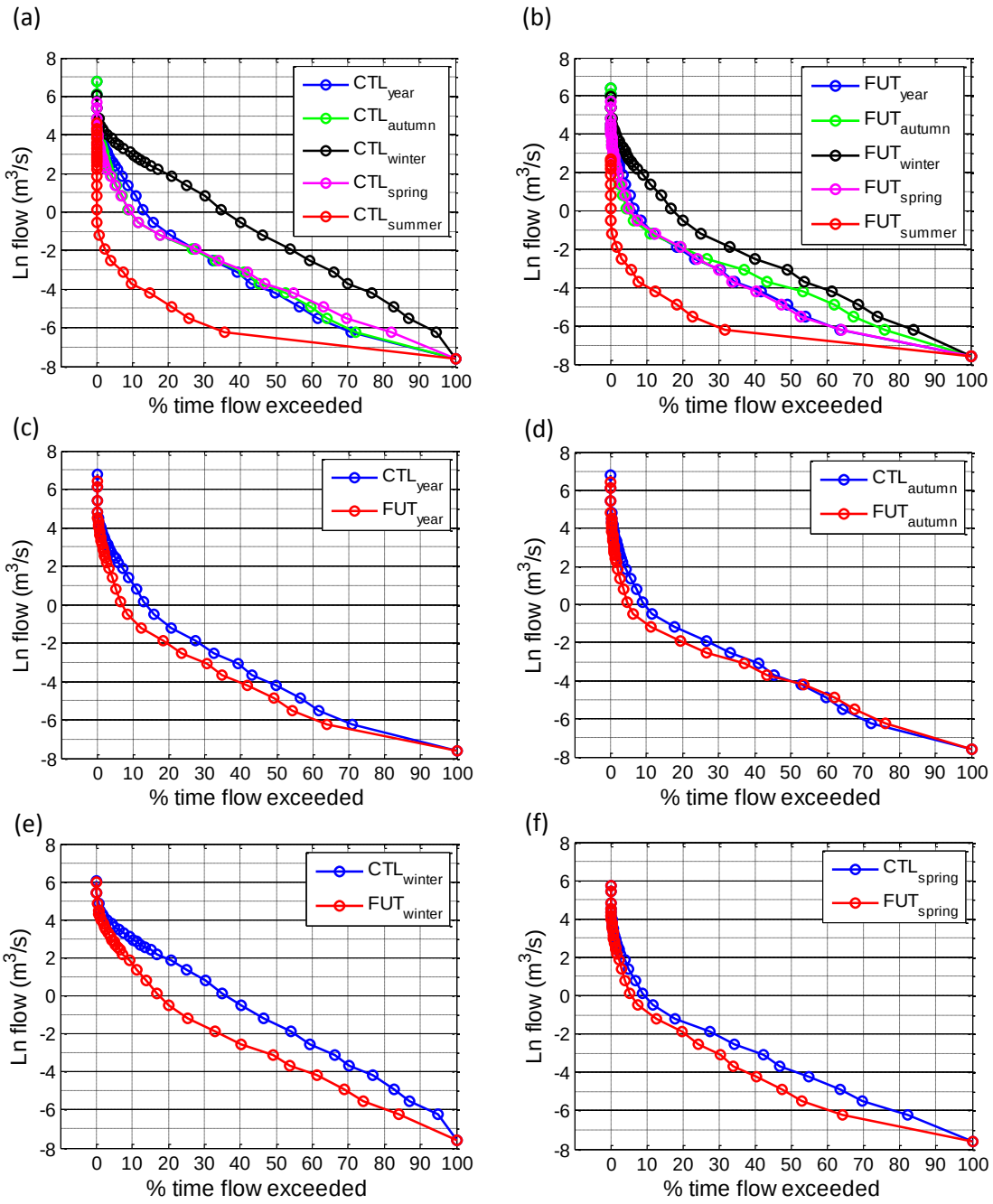

Fig. 8.2 Flow duration curves derived from the three 1000-year SHETRAN hydrological simulations under the (a) control and (b) future conditions, which are shown in blue, green, black, purplish-red and red colors respectively for the whole year, autumn, winter, spring and summer. Comparisons are shown in (c), (d), (e) and (f), with blue representing control and red for future, respectively for the whole year, autumn, winter and spring. The abscissa shows the percentage of flow exceeded and the ordinate indicates flows at outlet of the Cobres basin in a natural log-scale.

Flow duration curve reflects how representative is the water flowing down a river, or simply a curve of discharge values versus its exceedance probabilities. In this study, we used daily mean discharge at Monte da Ponte station (basin outlet) to plot these curves. Under control condition (Fig 8.2a), winter is the wettest season of a year with discharges higher than 1 m^3/s for around 1 month and 20 m^3/s for nearly 9 days; summer is a completely dry season and normally no water is available; spring and autumn, with nearly the same flow duration curves, are seasons with no flow for most (~85%) of the time and with discharges larger than 1 m^3/s for only around 9 days; finally, the whole year at Cobres basin is mostly (~80% of time) dry with discharges larger than 1 m^3/s for around 50 days and 2.7 m^3/s for around 36 days. Under future condition (Fig 8.2b), winter is still the wettest season of the year, although much drier than under control condition (Fig 8.2e), with discharges higher than 1 m^3/s for around 15 days and 20 m^3/s for nearly 3 days; summer is also completely dry with no discharge; spring and autumn, drier than under control condition (Fig 8.2d and 8.2f), with no flow for around 90% of the time and with discharges larger than 1 m^3/s for only around 4–5 days; the whole year, drier than the present climate (Fig 8.2c), is with no flow for around 90% of the time and with discharges larger than 1 m^3/s for only around 25 days and 2.7 m^3/s for around 16 days.

8.3.2 Future Climate Change Impacts on Extreme Events

- *Future climate change impacts on extreme events*

Future climate change impacts on extreme events are shown in Figs 8.3a–b and 8.4a–d.

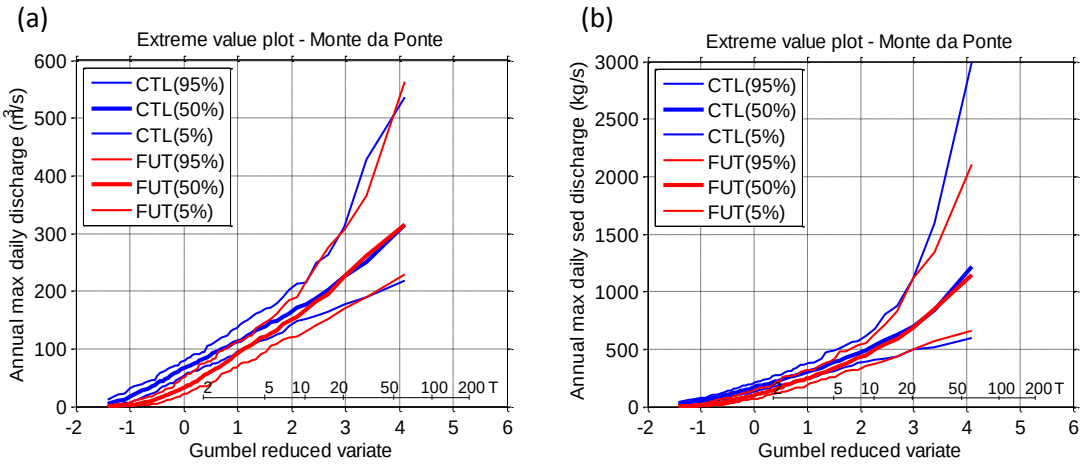

Fig. 8.3 Gumbel plots comparing annual maximum daily (a) discharge and (b) sediment discharge for Monte da Ponte gauging station (basin outlet) in blue and red colors respectively under control (1981−2010) and future (2041−2070) conditions. 5%, 50% and 95% represent the 5th, 50th and 95th percentile of the extremes.

Figs 8.3a–b were plotted by dividing the 3000-year simulated annual maxima series into 50 60-year series as described in Section 7.4.1 and displayed in Figs 7.10a–d (page 119), which were designed to provide information about how the future extreme runoffs would be changed under future extreme rainfalls. Figs 8.4a–d (page 137) are derived directly from the 3000-year simulated annual maxima series. Fig 8.4a and Fig 8.4c are cumulative probability plots respectively used to distinctly compare discharges and sediment discharges for high frequency events under control and future conditions; Fig 8.4b and Fig 8.4d are used to carry out the comparisons more clearly for medium and low frequency events. We categorize extreme events by their return periods (T) or non-exceedance probabilities (P) as five types, namely: high ($T \leq 2$ years or $P \leq 0.5$), medium ($2 < T \leq 10$ years or $0.5 < P \leq 0.9$), low ($10 < T \leq 20$ years or $0.9 < P \leq 0.95$), very low ($20 < T \leq 50$ years or $0.95 < P \leq 0.98$) and extremely low ($T > 50$ years or $P > 0.98$) frequency events. It is indicated, in Fig 8.3a and Figs 8.4a–b, that (1) future high, medium and low frequency flows are respectively decreased around 35%–80% (or 20–35 m^3/s), 5%–35% (or 10–30 m^3/s) and 3%–5% (or 5–10 m^3/s); (2) future very low and extremely low frequency flows are nearly the same or slightly decreased compared to their values under control conditions; (3) for extremes in discharge, values smaller than 200 m^3/s, the non-exceedance probabilities are larger in future climate than in present climate, for those with values larger than 200 m^3/s, their probabilities in future climate are nearly the same as those in present climate. In other words, the future extremes have discharges of magnitude smaller or similar to those under control climate and the increases of future rainfall maxima, indicated in Figs 7.10a–d, do not result in corresponding increases of runoff. Similarly, from Fig 8.3b and Fig 8.4c–d, (1) future high, medium and low frequency sediment discharges are respectively decreased around 30%–60% (or 50–70 kg/s), 10%–25% (or 40–60 kg/s) and 1%–5% (or 6–30 kg/s); (2) future very low and extremely low frequency sediment discharges are nearly the same or slightly decreased compared to their values under control conditions; (3) for extremes in sediment discharges, values smaller than 600 kg/s, the non-exceedance probabilities are larger in future climate than in present climate, for those with values larger than 600 kg/s, their probabilities in future climate are nearly the same as those in present climate.

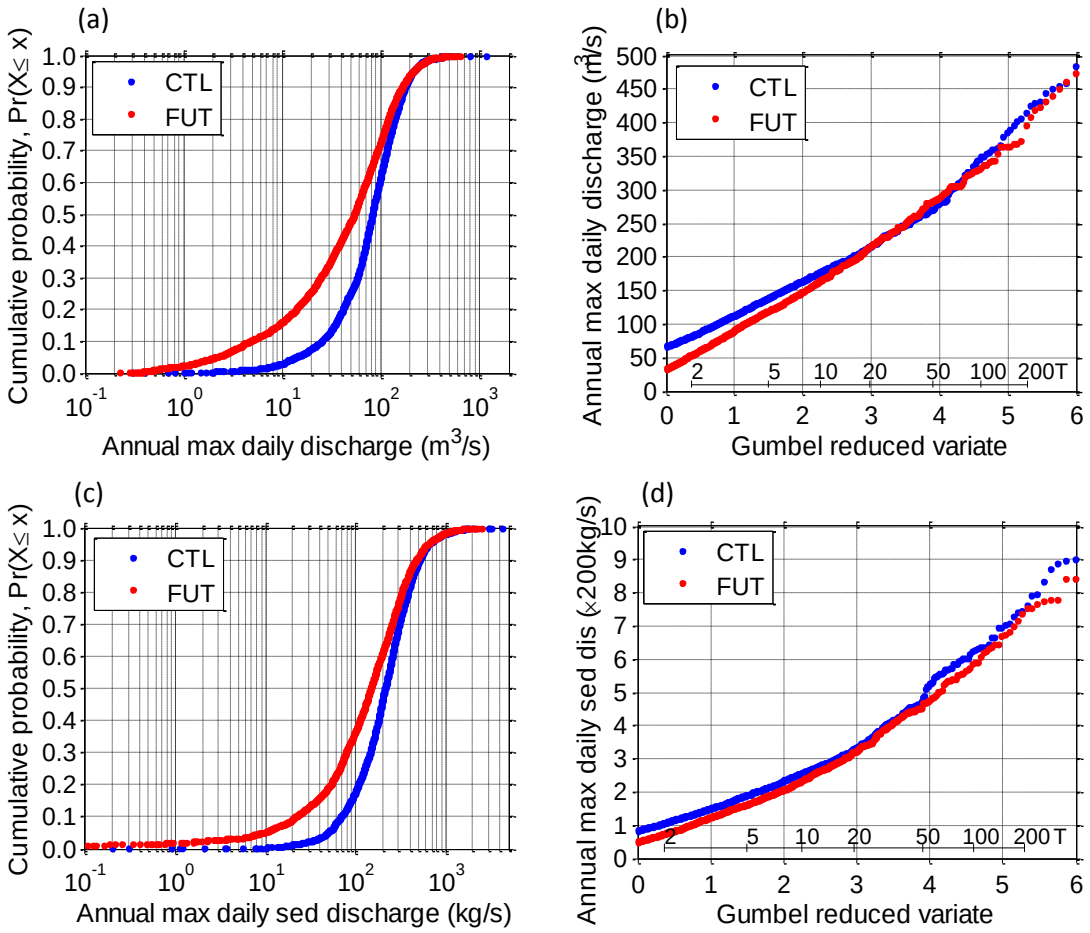

Fig. 8.4 Empirical cumulative frequency distribution functions for (a) the annual maximum daily discharge and (c) the annual maximum daily sediment discharge under control (CTL) and future (FUT) conditions. Empirical extreme plots for comparison of (b) annual maximum daily discharge and (d) annual maximum daily sediment discharge under control and future conditions. The 3000-year synthetic daily discharge and sediment discharge series were used to derive the plots.

- *Theoretical fit of empirical extreme value distributions*

GEV distributions have been fitted, by using the maximum likelihood and L-moment methods, to the 3000-year simulated series of annual maximum daily discharge and sediment discharge under control and future conditions. The results have shown that L-moment method gave better fits for all of the four cases than the maximum likelihood; therefore it is adopted and the results are shown in Figs 8.5a–d (page 138) with Figs 8.5a and 8.5c referring to control condition and Figs 8.5b and 8.5d to future condition.

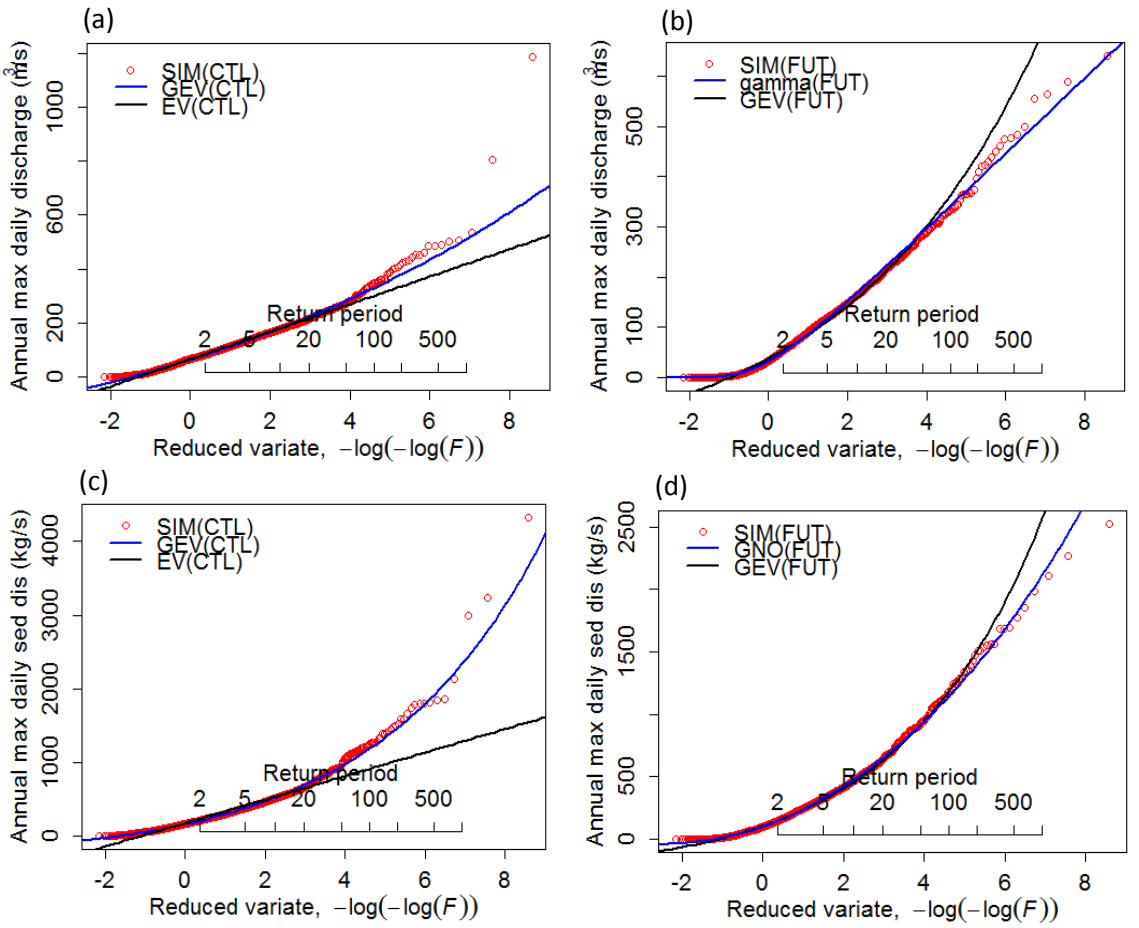

Fig. 8.5 Probability distributions of annual maximum daily discharge under (a) control and (b) future conditions and annual maximum daily sediment discharge under (c) control and (d) future conditions. The red circles are derived from SHETRAN model simulations; the blue and black lines are fitted, by using the R functions of the lmom package (version 2.1), based on postulated distributions, namely generalized extreme value (GEV), Gumbel or extreme value (EV), gamma and three-parameter lognormal (ln3) distributions. The blue lines are corresponding best fits.

From visual comparison, we find that GEV distribution fits well the 3000-year simulated annual maxima series under control condition for all the data ranges and for future condition it fits well the annual maximum discharges and sediment discharges with return periods respectively in the ranges of [2, 50] and [2, 200] years.

In order to check the goodness-of-fit and explore possible candidate distributions for better fit, we plotted the L-moment diagram (Fig 8.6, page 139) for the four annual maxima series.

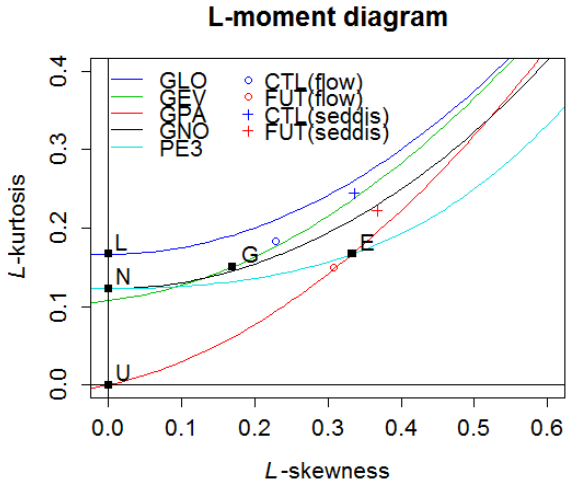

Fig. 8.6 L-moment diagram indicating relationships among L-skewness and L-Kurtosis for the generalized logistic (GLO), generalized extreme value (GEV), generalized Pareto (GPA), generalized normal (GNO), Pearson type III (PE3), exponential (E), Gumbel (G), logistic (L), normal (N) and uniform (U) and the distribution of the 3000-year annual maximum daily discharge under control (blue circle) and future (red circle) conditions and the 3000-year annual maximum daily sediment discharge under control (blue cross) and future (red cross) conditions.

As shown in Fig 8.6, the annual maxima series of simulated flow and sediment discharge under control condition, indicated in blue circles and crosses, may be well fitted by the GEV distribution; for future condition, the annual maxima series of simulated flow, displayed in red circles, may be well fitted by the Pearson type III (or gamma), generalized Pareto or exponential distributions and the annual maxima series of sediment discharge, shown in red crosses, may be well fitted by the generalized normal distribution. Therefore, Fig 8.6 has confirmed the goodness-of-fit of GEV distribution for annual maxima series under control condition; for future condition, it has indicated the lack-of-fit of GEV distribution and suggested better options. We visually tested the goodness-of-fit of the candidate distributions for future condition by making probability plots and we found that gamma and the three-parameter lognormal distributions respectively fit well the annual maxima series of simulated discharge and sediment discharge for all the data ranges, as shown in Figs 8.5b and 8.5d.

The Lilliefors test and the Filliben test have been applied to further test the goodness-of-fit of proposed distributions shown in Figs 8.5a–d. We applied the two goodness-of-fit tests to both the whole 3000-year samples and the original three splitted 1000-year samples. From Lilliefors tests indicated in Table 8.2a (page 141), under control condition the annual maximum daily discharge series match the GEV distribution at a significance level of 5%; and under future condition it does not match the GEV distribution but matches the gamma distribution at a significance level of 5%. According to Filliben tests shown in Table 8.2b (page 141), under control condition the annual

maximum daily discharge series does not match the GEV distribution at a significance level of 5%; and under future condition it matches neither the GEV distribution nor the gamma distribution at a significance level of 5%. Similarly, for the annual maximum daily sediment discharge series, the Lilliefors tests displayed in Table 8.3a (page 141) shows that under control condition it matches the GEV distribution at a significance level of 5%, and under future condition it does not match the GEV distribution but instead match the three-parameter lognormal distribution at a significance level of 5%; the Filliben tests displayed in Table 8.3b (page 141) show that under control condition it matches the GEV distribution at a significance level of 5%, and under future condition it matches both the GEV distribution and the three-parameter lognormal distribution at a significance level of 5%. It is indicated that the results of the Lilliefors tests are all consistent with visual fit of goodness-of-fit test for the distributions proposed in Figs 8.5a–d (page 138), which demonstrates the feasibility of representing the empirical distributions by the proposed theoretical distributions. The results of the Filliben tests are not always consistent with the visual fits, which may be explained by the non-resistance property of the Pearson correlation coefficient (Wilks 2006).

Finally, we compared the histograms of fitted distributions in Figs 8.7a–b.

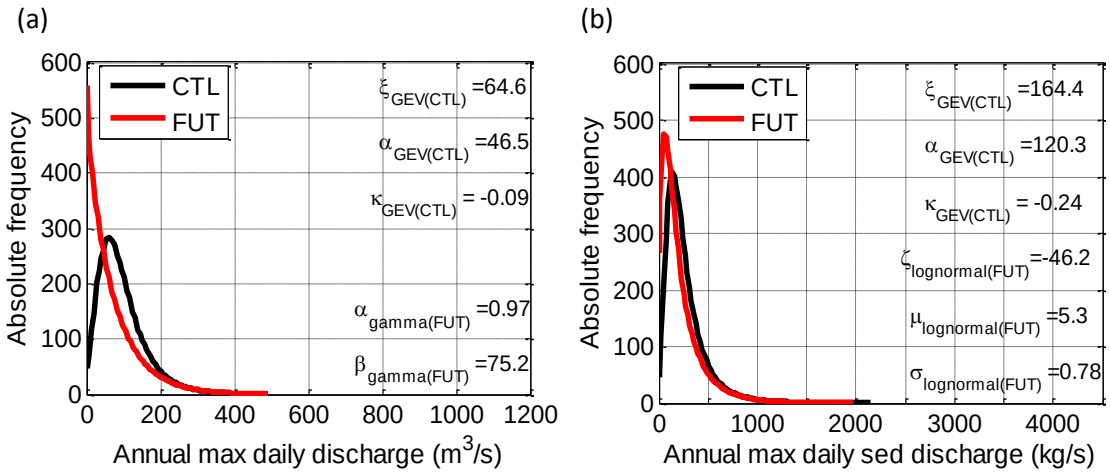

Fig. 8.7 Histograms of fitted distributions for (a) annual maximum daily discharge and (b) annual maximum daily sediment discharge under control (CTL) and future (FUT) conditions.

It is found that: (1) The probability density function (PDF) of the future annual maximum discharge is much more right-skewed with its highest probability density located at 0 m^3/s; non-exceedance probabilities of future annual maximum discharges with values in the range of [0, 200] m^3/s are higher and are especially higher for those in the range of [0, 60] m^3/s. (2) The PDF of the future annual maximum sediment discharge is more right-skewed with its highest probability density located nearer to 0 kg/s; non-

exceedance probability of future annual maximum discharges with values in the range of [0, 500] kg/s is higher and it is especially higher for values in the range of [0, 50] kg/s.

Table 8.2a Lilliefors test for annual maximum daily discharge under CTL and FUT conditions

Test	Null distribution	D_{nmax} ($Crit_{0.05}$)			
		1st 1000 year	2nd 1000 year	3rd 1000 year	3000 year
CTL	GEV	0.025 (0.043)	0.025 (0.043)	0.020 (0.043)	0.020 (0.024)
FUT	GEV	0.073 (0.042)	0.064 (0.042)	0.065 (0.042)	0.069 (0.024)
FUT	gamma	0.028 (0.042)	0.051 (0.044)	0.032 (0.043)	0.035 (0.024)

Table 8.2b Filliben test for annual maximum daily discharge under CTL and FUT conditions

Test	Null distribution	R ($Crit_{0.05}$)			
		1st 1000 year	2nd 1000 year	3rd 1000 year	3000 year
CTL	GEV	0.884 (0.991)	0.912 (0.991)	0.917 (0.988)	0.987 (0.996)
FUT	GEV	0.912 (0.970)	0.920 (0.976)	0.922 (0.961)	0.991 (0.981)
FUT	gamma	0.878 (0.907)	0.885 (0.910)	0.870 (0.899)	0.929 (0.912)

Table 8.3a Lilliefors test for annual max daily sediment discharge under CTL and FUT conditions

Test	Null distribution	D_{nmax} ($Crit_{0.05}$)			
		1st 1000 year	2nd 1000 year	3rd 1000 year	3000 year
CTL	GEV	0.019 (0.041)	0.026 (0.041)	0.021 (0.042)	0.014 (0.025)
FUT	GEV	0.039 (0.042)	0.044 (0.042)	0.048 (0.042)	0.046 (0.025)
FUT	lognormal	0.025 (0.042)	0.034 (0.043)	0.036 (0.043)	0.033 (0.025)

Table 8.3b Filliben test for annual max daily sediment discharge under CTL and FUT conditions

Test	Null distribution	R ($Crit_{0.05}$)			
		1st 1000 year	2nd 1000 year	3rd 1000 year	3000 year
CTL	GEV	0.963 (0.956)	0.988 (0.959)	0.988 (0.952)	0.996 (0.974)
FUT	GEV	0.989 (0.927)	0.987 (0.940)	0.986 (0.926)	0.990 (0.944)
FUT	lognormal	0.999 (0.973)	0.994 (0.944)	0.980 (0.948)	0.999 (0.987)

8.4 Discussion

Future climate change impacts on water resources availability, annual sediment yield and annual maximum discharge and sediment discharge were evaluated for Cobres basin based on SHETRAN hydrological and sediment transport simulations driven by the downscaled scenarios obtained in Chapter 7 for control (1981–2010) and future (2041–2070) climates. In the study, we did not consider the possible changes of land-use in the future; therefore we used the best parameter setting of SHETRAN model, which is optimized from the available data for the period 2004–2008 by using MSCE

and NSGA-II methods, for both climate scenarios. With the aim of assessing future climate change impacts on available water resources and basin sediment yield, we compared future annual runoff and sediment yield at high, medium and low frequency levels with those under control conditions and analyzed the changes by comparing the annual and monthly water balance components under both climate conditions. In order to get future climate change impacts on extreme events, we extracted annual maximum discharge and sediment discharge for both scenarios, carried out the extreme value analysis by comparison of the empirical distributions and theoretical fits.

Future mean climate is drier with decreased rainfall, increased PET and consequently decreased runoff and sediment yield. Under future climate, annual rainfall is projected to decrease around 80–90 mm (or 10%–30%) and annual PET is projected to increase around 200 mm (or 15%); annual runoffs and sediment yields are projected to decrease respectively around 8–88 mm (or 30%–80%) and 0.26–2.13 t ha^{-1} $year^{-1}$ (or 30%–87%). Annual AET is projected to decrease in the future around 20–60 mm (or 5%–20%) with larger decrease associated with less annual rainfall. The monthly AET is projected to decrease all over the year except for winter, indicating vegetation and crop growths are more water-limited in future climate. Spring, summer and early autumn months are periods with no runoff, and consequently no sediment yield, for both control and future scenarios, due to the lack of rainfall (in summer months) or the insufficient rainfall to compensate the water loss from AET and subsurface storage change. November and winter months are periods with runoff and sediment yield under control climate; December and January are months with runoff and sediment yield with occurrence at a probability level of 50% under future climate.

Future wet extremes are more right-skewed with their highest probability density located near 0. Future annual maximum discharge and sediment discharge are projected to decrease, respectively around 3%–80% and 1%–60%, for return periods less than 20 years and the decreases are larger, respectively around 35%–80% and 30%–60, for return periods less than 2 years; annual maxima have the same or slightly less intensities, for those with return periods larger than 20 years. In other words, for extremes with discharge (sediment discharge) values smaller than 200 m^3/s (600 kg/s), the non-exceedance probabilities are larger in future climate than in present climate; for those with values larger than 200 m^3/s (600 kg/s), their probabilities in future climate are nearly the same as those in present climate. Moreover, the series of annual maximum discharge (sediment discharge), under control condition, follows the GEV distribution with location parameter of 64.6 m^3/s (164.4 kg/s), scale parameter of 46.5 m^3/s (120.3 kg/s) and shape parameter of -0.09 (-0.24); under future condition, the

series of annual maximum discharge follows the gamma distribution with scale parameter of 75.2 m^3/s and shape parameter of 0.97 and the series of annual maximum sediment discharge follows the three-parameter lognormal distribution with location parameter of -46.2 kg/s, mean of 5.3 kg/s and standard deviation of 0.78 kg/s.

In summary, future droughts should be put in the top list of climate adaptation measures for water supply and desertification combating problems in southern Portugal; and future wet extremes should not be ignored, but well anticipated as the larger extremes maintain similar magnitude to those under control conditions. This has confirmed the increasingly concerns of water scarcity and drought problems for future (EEA 2012; Seneviratne *et al.*, 2012), and provided a comprehensive evaluation of future climate change impacts on extreme events in southern Portugal. However, considering the limitation of this work, further studies are expected to evaluate uncertainties involved in assessment of future climate change impacts on hydrological process and sediment transport, which result from the variability in internal parameterization of GCMs and RCMs, greenhouse gas emission scenarios, downscaling methods, hydrological model structure and hydrological parameter setting.

9. Conclusions and Expectations

9.1 Summary

In this study, SHETRAN hydrological model has been successfully calibrated by using two global optimization methods MSCE and NSGA-II. It is demonstrated that the fitness, in descending order from high to low, of the spatial resolutions to the SHETRAN hydrological simulations at Cobres basin is: 0.5, 1.0 and 2.0 km. The best solutions from SHETRAN calibrations with NSE of values larger or equal to 0.85 and spatial resolutions of 1.0 and 2.0 km have been successfully validated, for possible future applications, by considering the tests of split-sample, differential split-sample, proxy-basin and multi-site. Due to the limits of computational resources, 2.0 km was selected as the spatial resolution and the best solution from the MSCE calibration was applied to the simulations of hydrological scenarios for both control (1981–2010) and future (2041–2070) climates. In summary, the following aspects can be concluded:

- Future projections have presented relatively to the reference period a drier mean climate, with mean annual rainfall decreased by ~88 mm (19%), mean annual PET increased ~196 mm (16%) and consequent mean annual runoff and sediment yield decreased respectively ~48 mm (50%) and ~1.06 t/ha/year (45%). The future mean annual AET is projected to decrease ~41 mm (11%), which occurs mainly in spring, indicating a more water-limited future climate for vegetation and crop growth. Under reference conditions, November to February is the period in which runoff and sediment yield occur frequently; however, in future, it is reduced to December and January, with changes in the occurrence rate of ~50%.
- Future projections point to increases in the meteorological drought (scarcity of precipitation, Tables 7.3a–d, pages 119–120), agricultural drought (reduction in soil moisture, Figs 8.1a, b and d, page 131) and hydrological drought (reduction in runoff, Figs 8.1e, page 131, and 8.2c–f, page 134). Moreover, the extreme droughts are projected to be more intense and severe (Tables 7.3c–d, page 120; Figs 8.1a, b and d, page 131; 8.2c–f, page 134 and Fig 8.4a, page 137). These impacts demand policymakers to adopt and execute efficient adaptation measures to avoid the socioeconomic drought. Effect of climate change, particularly of the increase in temperature, is to reduce productivity, refered in a paper that used projections done in this thesis (Carvalho *et al.,* 2013).

- ❖ Future projections have displayed a level of around 15% increases in precipitation extremes with return periods in the range of [20, 50] years but either slight increase or no change in those with return periods respectively in the ranges of [10, 20] and [2, 10] years. The increases of precipitation extremes are in accordance with the results obtained by other authors, e.g. Rajczak *et al.* (2013).
- ❖ Future projections have shown no changes or slight decreases in annual maximum discharge and sediment discharge for extremes with return periods larger than 20 years; and both quantities present decreases for extremes with return periods less than 20 years and the decreases are especially greater for those less than 2 years. The annual maximum discharge (sediment discharge) series, under control climate, are projected to follow the GEV distribution with location parameter of 64.6 m^3/s (164.4 kg/s), scale parameter of 46.5 m^3/s (120.3 kg/s) and shape parameter of 0.09 (-0.24); under future climate, the annual maximum discharge series are projected to follow the gamma distribution with scale parameter of 75.2 m^3/s and shape parameter of 0.97 and the annual maximum sediment discharge series follows the three-parameter lognormal distribution with location parameter of -46.2 kg/s, mean of 5.3 kg/s and standard deviation of 0.78 kg/s.

9.2 Main Achievements

All in all, the main achievements can be identified as follows:

- An integrated modelling method has been developed for evaluation of climate change impacts on water resources, sediment yield and extreme events at a catchment scale, which can be easily applied to any other catchments.
- A quantified evaluation of climate change impacts on an agricultural dominated basin in southern Portugal has been provided in terms of water resources, sediment yield and wet and dry extreme events.
- The rainfall conditioned weather generator—ICAAM-WG has been developed in this study based on the modified Climate Research Unit daily Weather Generator (CRU-WG) (Kilsby and Jones *et al.,* 2007). The development of ICAAM-WG has considered the climate characteristic of southern Portugal, namely long dry and wet spells.
- For the first time, SHETRAN hydrological model has been successfully calibrated by using two objective global optimization methods, namely the MSCE and NSGA-II algorithms.

- For the first time, the effects of spatial resolution on SHETRAN model performances have been investigated with the aid of a global optimization algorithm, which provides objective conclusions.
- The capability of SHETRAN hydrological model in simulating water resources and extreme events under different climate conditions are successfully demonstrated by the strong validations such as the split-sample test, differential split-sample test, proxy-basin test and multi-site test.

9.3 Main Limitations of the Work

The main limitations of the work are as follows:

- The uncertainties resulting from GCMs, RCMs, GHGs, statistical downscaling methods and hydrological models were not considered in the future climate projections.
- The uncertainties resulting from the SHETRAN hydrological model, such as model structure uncertainty and parameter uncertainty, were not considered.
- The application of 2.0 km, not the best spatial resolution for Cobres basin, to the SHETRAN hydrological simulations of climate scenarios may have caused some levels of underestimations in runoff volumes and peak discharges.
- The bad quality of the observed sediment discharge data may have introduced substantial errors in the calibration of sediment parameters and consequently in sediment transport simulations for the climate scenarios.

9.4 Further Research

Further research should be carried out including the following aspects:

- The considerations of ensembles of GCMs, RCMs, GHGs, statistical downscaling methods and hydrological models in future climate projections.
- The applications of the state-of-the-art global optimization methods to automatic calibration of SHETRAN model.
- The improvement in sediment measurements.

10. References

Abbott, M. B., Bathurst, J. C., Cunge, J. A., O'Connel, P. E. and Rasmussen, J. 1986a: An introduction to the European hydrological system—systeme Hydrologique Europeen, "SHE", 1: history and philosophy of a physically-based distributed modelling system. *J. Hydrol.*, **87**, 45–59.

Abbott, M. B., Bathurst, J. C., Cunge, J. A., O'Connel, P. E. and Rasmussen, J. 1986b: An introduction to the European hydrological system—systeme Hydrologique Europeen, "SHE", 2: structure of a physically-based distributed modelling system. *J. Hydrol.*, **87**, 61–77.

Ackers, P. and White, W. R., 1973: Sediment transport: new approach and analysis. *J. Hydraul. Div., Am. Soc. Civ. Engrs., 99(HY11)*, 2041–2060.

Adams, R. and Elliott, S., 2006: Physically based modelling of sediment generation and transport under a large rainfall simulator. *Hydrol. Process.*, **20**(11), 2253–2270.

Allen, R. G., Pereira, L. S., Raes, D. and Smith, M., 1998: Crop evapotranspiration: Guidelines for computing crop water requirements. *FAO irrigation and drainage paper* **56**, Rome, Italy.

Ariathurai, R. and Arulanandan, K., 1978: Erosion rates of cohesive soils, *J. Hydraul. Div., Am. Soc. Agric. Engrs., 104(HY2)*, 279–283.

Baartman, J. E. M., van Lynden, G. W. J., Reed, M. S., Ritsema, C. J. and Hessel, R., 2007: Desertification and land degradation: origins, processes and solutions—a literature review. Scientific Report 20, *DESIRE Report Series*, Wageningen.

Bathurst, J. C., 1986: Sensitivity analysis of the Systeme Hydrologique Europeen for an upland catchment. *J. Hydrol.*, **87**: 103–123.

Bathurst, J. C. and O'connell, P. E., 1992: Future of distributed modelling: the Système Hydrologique Européen. *Hydrol. Process.*, **6**(3), 265–277.

Bathurst, J. C., Wicks, J. M. and O'Connell, P. E., 1995: The SHE/ SHESED basin scale water flow and sediment transport modelling system. In: Singh, V.P. (ed). *Computer Models of Watershed Hydrology*, Water Resources Publications, Highlands Ranch, CO, 563–594.

Bathurst, J. C., Kilsby, C. and White, S., 1996: Modelling the impacts of climate and land-use change on basin hydrology and soil erosion in Mediterranean Europe. In: Brandt, C. J., Thornes, J. B. (eds) *Mediterranean Desertification and Land Use*. John Wiley & Sons Ltd, Chichester, UK, pp 355–387.

Bathurst, J. C., Lukey, B., Sheffield, J. and Hiley, R. A., 1998: Modelling badlands erosion with SHETRAN at Draix, southeast France. In *Modelling Soil Erosion, Sediment Transport and Closely Related Hydrological Processes*, International Association of Hydrological Sciences Publ. No. 249, Wallingford, Oxon, UK, 129–136.

Bathurst, J. C., Sheffield, J., Vicente, C., White, S. M. and Romano, N., 2002: Modelling large basin hydrology and sediment yield with sparse data: the Agri basin, southern Italy. In: Geeson, N. A., Brandt, C. J. & Thornes, J. B. (eds) *Mediterranean Desertification: A Mosaic of Processes and Responses*. John Wiley & Sons Ltd, Chichester, UK, pp 397–415.

Bathurst, J. C. and Bovolo, C. I., 2004: Development of Guidelines for Sustainable Land Management in the Agri and Cobres Target Basins, Deliverable 28 of the EU funded MEDACTION project, 37pp. Available from: http://www.ncl.ac.uk/medaction.

Bathurst, J. C., Ewen, J., Parkin, G., O'Connell, P. E. and Cooper, J. D., 2004: Validation of catchment models for predicting land-use and climate change impacts. 3. Blind validation for internal and outlet responses. *J. Hydrol.*, **287**: 74–94.

Bathurst, J. C., Moretti, G., El-Hames, A., Beguería, S. and García-Ruiz, J. M., 2007: Modelling the impact of forest loss on shallow landslide sediment yield, Ijuez river catchment, Spanish Pyrenees. *Hydrol. Earth Syst. Sci.*, **11**(3), 569–583.

Bathurst, J. C., 2011: Predicting Impacts of Land Use and Climate Change on Erosion and Sediment Yield in River Basins Using SHETRAN, in: Morgan, R. P. C. & Nearing, M. A. (eds) *Handbook of Erosion Modelling*, Blackwell Publishing Ltd, pp 263–288.

Bathurst, J. C., Birkinshaw, S. J., Cisneros, F., Fallas, J., Iroumé, A., Iturraspe, R., Novillo, M. G., Urciuolo, A., Alvarado, A., Coello, C., Huber, A., Miranda, M., Ramirez, M. and Sarandón, R., 2011: Forest impact on floods due to extreme rainfall and snowmelt in four Latin American environments 2: Model analysis. *J. Hydrol.*, **400**: 292–304.

Bekele, E. G. and Nicklow, J. W., 2007: Multi-objective automatic calibration of SWAT using NSGA-II. *J. Hydrol.*, **341**, 165-176, doi:10.1016/j.jhydrol.2007.05.014.

Bennett, J. P., 1974: Concepts of mathematical modelling of sediment yield, *Water Resour. Res.*, **10**(3), 485–492.

Benito, G., Díez-Herrero, A. and Fernández de Villalta, M., 2004: Flood response to solar activity in the Tagus basin (Central Spain) over the last millennium. *Clim. Chang.*, **66**(1), 27–28.

Beven, K., Warren, R. and Zaoui, J., 1980: SHE: towards a methodology for physically-based distributed forecasting in hydrology. *IAHS-AISH Publ*, **129**, 133–137.

Beven, K. J. and O'Connell, P. E., 1982: On the role of physically-based distributed modelling in hydrology. *Report No.81*, Institute of hydrology.

Beven, K., 1989: Changing ideas in hydrology—the case of physically-based models. *J. hydrol.*, **105**(1), 157–172.

Beven, K. and Binley, A., 1992: The future of distributed models: model calibration and uncertainty prediction. *Hydrol. Process.*, **6**(3), 279–298.

Beven, K. and Freer, J., 2001: Equifinality, data assimilation, and uncertainty estimation in mechanistic modelling of complex environmental systems using the GLUE methodology. *J. Hydrol.*, **249**, 11–29.

Birkinshaw, S. J., James, P. and Ewen, J., 2010: Graphical User Interface for Rapid Set-up of SHETRAN Physically-Based River Catchment Model. *Environ. Model. & Softw.*, **25**, 609–610.

Birkinshaw, S. J., Bathurst, J. C., Iroumé, A. and Palacios, H., 2011: The effect of forest cover on peak flow and sediment discharge – an integrated field and modelling study in central-southern Chile. *Hydrol. Process*, **25**(8): 1284–1297.

Blasone, R. S., Madsen, H. and Rosbjerg, D., 2007: Parameter estimation in distributed hydrological modelling: comparison of global and local optimisation techniques. *Nord. Hydrol.*, **38**(4-5), 451-476, doi: 10.2166/nh.2007.024.

Blenkinsop, S. and Fowler, H. J., 2007: Changes in European drought characteristics projected by the PRUDENCE regional climate models. *Int. J. Climatol.,* 27, 1595–1610.

Brath, A., Montanari, A. and Toth, E., 2004: Analysis of the effects of different scenarios of historical data availability on the calibration of a spatially-distributed hydrological model. *J. Hydrol.*, **291**, 232-253, doi:10.1016/j.jhydrol.2003.12.044.

Brunner, P. and Simmons, C. T., 2012: HydroGeoSphere: A fully integrated, physically based hydrological model. *Groundw.*, **50**(2), 170–176.

Burton, A., Kilsby, C. G., Fowler, H. J., Cowpertwait, P. S. P. and O'Connell, P. E., 2008: RainSim: A spatial–temporal stochastic rainfall modelling system. *Environ. Model. Softw.*, **23**, 1356–1369. doi:10.1016/j.envsoft.2008.04.003.

Burton, A., Fowler, H. J., Blenkinsop, S. and Kilsby, C. G., 2010a: Downscaling transient climate change using a Neyman–Scott Rectangular Pulses stochastic rainfall model. *J. Hydrol.*, **381**(1–2), 18–32. doi:10.1016/j.jhydrol.2009.10.031

Burton, A., Fowler, H. J., Kilsby, C. G. and O'Connell, P. E., 2010b: A stochastic model for the spatial-temporal simulation of nonhomogeneous rainfall occurrence and amounts. *Water Resour. Res.*, **46**, W11501, doi:10.1029/2009WR008884.

Caetano, M., Nunes, V. and Nunes, A., 2009: CORINE land cover 2006 for continental Portugal. Instituto Geográfico Português. Technical Report.

Cardoso, C., 1965: Solos de Portugal: sua classificação, caracterização e génese 1 – a sul do rio tejo. Lisbon, Portugal.

Carvalho, M., Serralheiro, R., Corte-Real, J. and Valverde, P., 2013: Implications of climate variability and future trends on wheat production and crop technology adaptations in Southern regions of Portugal. 8th International Conference of EWRA "Water Resources Management in an Interdisciplinary and Changing Context" Porto, Portugal, June 26th-29th,2013.

Chen, H., Xu, C. Y. and Guo, S., 2012: Comparison and evaluation of multiple GCMs, statistical downscaling and hydrological models in the study of climate change impacts on runoff. *J. Hydrol.,* 434, 36–45.

Chien, H., Yeh, P. J. F. and Knouft, J. H., 2013: Modeling the potential impacts of climate change on streamflow in agricultural watersheds of the Midwestern United States. *J. Hydrol.*, **491**, 73–88.

Chow, V. T., 1959: Open-channel hydraulics. International Student Edition, McGraw-Hill, Tokyo.

Christensen, J. H., Carter, T. R., Rummukainen, M. and Amanatidis, G., 2007: Evaluating the performance and utility of regional climate models: the PRUDENCE project. *Clim. Chang.*, **81**(1), 1–6.

Collins, M., Booth, B. B. B., Harris, G. R., Murphy, J. M., Sexton, D. M. H. and Webb, M. J., 2006: Towards quantifying uncertainty in transient climate change. *Clim. Dyn.*, **27**(2-3), 127–147. doi:10.1007/s00382-006-0121-0.

Corte-Real, J., Zhang, X., and Wang, X., 1995a: Large-scale circulation regimes and surface climate anomalies in the Mediterranean, *Int. J. Climatol*., **15**, 1135–1150.

Corte-Real, J., Zhang, X., and Wang, X., 1995b: Downscaling GCM information to regional scales: A non-parametric multivariate regression approach, *Clim. Dyn.,* **11**, 413–424.

Corte-Real J., Qian, B. and Xu, H., 1998: Regional climate change in Portugal: precipitation variability associated with large-scale atmospheric circulation. *Int. J. Climatol.*, **18**, 619–635.

Corte-Real, J., Qian, B. and Xu, H., 1999a: Circulation patterns, daily precipitation in Portugal and implications for climate change simulated by the second Hadley Centre GCM. *Clim. Dyn.*, **15**(12), 921–935.

Corte-Real, J., Hu, H. and Qian, B., 1999b: A weather generator for obtaining daily precipitation scenarios based on circulation patterncors. *Clim. Res.*, **13**(1), 61–75.

Costa, A. C. and Soares, A. (2009): Trends in extreme precipitation indices derived from a daily rainfall database for the South of Portugal. *Int. J. Climatol.*, **29**, 1956–1975.

Costa, A. C., Santos, J. A. and Pinto, J. G., 2012: Climate change scenarios for precipitation extremes in Portugal. *Theor. Appl. Climatol.,* **108**(1–2), 217–234.

Cowpertwait, P. S. P., 1995: A generalized spatial–temporal model of rainfall based on a clustered point process. *Proc. R. Soc. Lond.*, **450**, 163–175.

Cowpertwait, P. S. P., 1998: A Poisson-cluster model of rainfall: high-order moments and extreme values. *Proc. R. Soc. Lond.*, **454**, 885–898.

Davie, 2008: Fundamentals of Hydrology, 2nd edition. Routledge, Taylor & Francis Group, London and New York, 200 pp.

Day, T. J., 1980: A study of the transport of graded sediments. Hydraulics Research Station, Wallingford, *Rep. no. IT 190*.

Das, T., Maurer, E. P., Pierce, D. W., Dettinger, M. D. and Cayan, D. R., 2013: Increases in flood magnitudes in California under warming climates. *J. Hydrol.*, **501**, 101–110.

Demaria, E. M. C., Maurer, E. P., Thrasher, B., Vicuña, S. and Meza, F. J., 2013: Climate change impacts on an alpine watershed in Chile: Do new model projections change the story? *J. Hydrol.*, **502**, 128–138.

de Lima, M. I. P., Santo, F. E., Ramos, A. M. and de Lima, J. L. M. P., 2013: Recent changes in daily precipitation and surface air temperature extremes in mainland Portugal , in the period 1941 – 2007. *Atmos. Res.*, **127**, 195–209. doi:10.1016/j.atmosres.2012.10.001.

Deb, K., 2001: Multi-objective optimization using evolutionary algorithms, Wiley, Chichester, UK.

Deb, K. and Agrawal, R. B., 1995: Simulated binary crossover for continuous search space, *Complex Syst.*, **9**, 115–148.

Deb, K. and Goyal, M., 1996: A combined genetic adaptive search (GeneAS) for engineering design. *Comput. Sci. Inform.*, **26**, 30–45.

Deb, K., Pratap, A., Agarwal, S. and Meyarivan, T., 2002: A fast and elitist multiobjective genetic algorithm: NSGA-II. *IEEE Trans. Evol. Computation.,* **6**(2), 182–197.

Deb, K., Karthik, S. and Okabe, T., 2007: Self-adaptive simulated binary crossover for real-parameter optimization, in: *Proc. Genet. Evol. Comput. Conf.* (GECCO-2007), London, UK, 7-11 July, 2007, 1187–1194.

Demuth, S., 2009: Learning to live with drought in Europe. *World Sci.* (*Nat. Sci. Q. Newsl.*), **7**(3), 18–20.

Diaz-Nieto, J. and Wilby, R. L., 2005: A comparison of statistical downscaling and climate change factor methods: impacts on low flows in the River Thames, United Kingdom. *Clim. Chang.,* **69**(2-3), 245–268.

Direcção-Geral do Ordenamento do Território e Desenvolvimento Urbano, 2007: Combate à Desertificação : Orientações para os Planos Regionais de Ordenamento do Território, Ficha Técnica.

Duan, Q., Sorooshian, S. and Gupta, V. 1992: Effective and efficient global optimization for conceptual rainfall-runoff models. *Water Resour. Res.*, **28**(4), 1015–1031.

Dumedah, G., Berg, A. A., Wineberg, M. and Collier, R., 2010: Selecting model parameter sets from a trade-off surface generated from the non-dominated sorting genetic algorithm-II. *Water Resour. Manag.,* **24**, 4469-4489, doi: 10.1007/s11269-010-9668-y.

Durão, R., Pereira, M. J., Costa, A. C., Côrte-Real, J. M., and Soares, A., 2009: Indices of precipitation extremes in Southern Portugal-a geostatistical approach. *Nat. Hazard. Earth Syst. Sci.*, **9**(1), 241–250.

Eckhardt, K. and Arnold, J. G., 2001: Automatic calibration of a distributed catchment model. *J. Hydrol.*, **251**, 103–109.

Elliott, A. H., Oehler, F., Schmidt, J. and Ekanayake, J. C., 2012: Sediment modelling with fine temporal and spatial resolution for a hilly catchment. *Hydrol. Process.*, **26**: 3645–3660.

Engelund, F. and Hansen, E., 1967: A monograph on sediment transport in alluvial streams, *Teknisk Forlag*, Copenhagen, 65pp.

Engman, E. T., 1986: Roughness coefficients for routing surface runoff. Proc. Am. Soc. Civ. Engrs., *J. Irrig. Drain. Eng.*, **112**, 39–53.

Environment Canada, 2001: Threats to sources of drinking water and aquatic ecosystems health in Canada. National Water Research Report No.1. National Water Resources Research Institute, Burlington, Ontario, 72 pp.

European Environment Agency, 1996: Water resources problems in Southern Europe. Topic report No 15/1996, Copenhagen, Denmark.

European Environment Agency, 2012: Climate change, impacts and vulnerability in Europe 2012. Topic report No 12/2012, Copenhagen, Denmark.

European Space Agency, 2012: DesertWATCH extension final report, 47pp.

Ewen, J. and Parkin, G., 1996: Validation of catchment models for predicting land-use and climate change impacts. 1. Method. *J. Hydrol.*, **175**: 583–594.

Ewen, J., Parkin, G. and O'Connell, P. E., 2000: SHETRAN: distributed river basin flow and transport modeling system. *J. Hydrol. Eng.*, **5**(3), 250–258.

Ewen, J., O'Donnell, G., Burton, A. and O'Connell, E., 2006: Errors and uncertainty in physically-based rainfall-runoff modelling of catchment change effects. *J. hydrol.,* **330**(3), 641–650.

Feddes, R. A., Kowalik, P., Neuman, S. P. and Bresler, E., 1976: Finite difference and finite element simulation of field water uptake by plants. *Hydrol. Sci. Bull.*, **21**, 81–98.

Feyen, L., Dankers, R., Bódis, K., Salamon, P. and Barredo, J. I., 2012: Fluvial flood risk in Europe in present and future climates. *Clim. Chang.,* **112**: 47─62.

Fooladmand, H. R. and Sepaskhah, A. R., 2006: Improved estimation of the soil particle-size distribution from textural data. *Biosyst. Eng.*, **94**(1), 133─138.

Forzieri, G., Feyen, L., Rojas, R., Flörke, M., Wimmer, F. and Bianchi, A. 2014: Ensemble projections of future streamflow droughts in Europe. *Hydrol. Earth Syst. Sci.,* **18**(1), 85─108. doi: 10.5194/hess-18-85-2014.

Fowler, H. J., Blenkinsop, S. and Tebaldi, C., 2007: Linking climate change modelling to impacts studies : recent advances in downscaling techniques for hydrological modelling. *Int. J. Climatol.*, **27**, 1547–1578. doi:10.1002/joc.1556.

Francés, F., Vélez, J. I. and Vélez, J. J., 2007: Split-parameter structure for the automatic calibration of distributed hydrological models. *J. Hydrol.*, **332**, 226-240.

Fraga, H., Malheiro, A. C., Moutinho-Pereira, J. and Santos, J. A., 2013: Future scenarios for viticultural zoning in Europe: ensemble projections and uncertainties. *Int. J. Biometeorol.,* **57**, 909─925. doi: 10.1007/s00484-012-0617-8.

Geeson, N. A., Brandt C. J. and Thornes, J. B., 2002: Mediterranean Desertification: A Mosaic of Processes and Responses. John Wiley & Sons Ltd, Chichester, UK, 444pp.

Giorgi, F., Jones, C. and Asrar, G. R., 2009: Addressing climate information needs at the regional level: the CORDEX framework. *World Meteorol. Organ. (WMO) Bull.*, **58**(3), 175.

Goderniaux, P., Brouyère, S., Fowler, H. J., Blenkinsop, S., Therrien, R., Orban, P. and Dassargues, A., 2009: Large scale surface–subsurface hydrological model to assess climate change impacts on groundwater reserves. *J. Hydrol.*, **373**(1), 122–138.

Goderniaux, P., Brouyere, S., Blenkinsop, S., Burton, A., Fowler, H. J., Orban, P. and Dassargues, A., 2011: Modeling climate change impacts on groundwater resources using transient stochastic climatic scenarios. *Water Resour. Res.,* 47(12), W12516.

Guerreiro, S. B., Kilsby, C. G. and Serinaldi, F., 2014: Analysis of time variation of rainfall in transnational basins in Iberia: abrupt changes or trends? *Int. J. Climatol.,* **34**(1), 114–133.

Haddeland, I., Clark, D. B., Franssen, W., Ludwig, F. and Vo, F. *et al.*, 2011: Multimodel Estimate of the Global Terrestrial Water Balance: Setup and First Results. *J. Hydrometeorol.*, **12**(5), 869–884, doi:10.1175/2011JHM1324.1.

Hagemann, S., Chen, C., Clark, D. B., Folwell, S., Gosling, S. N., Haddeland, I., Hanasaki, N., Heinke, J., Ludwig, F., Voss, F. and Wiltshire, A. J., 2013: Climate change impact on available water resources obtained using multiple global climate and hydrology models. *Earth Syst. Dynam.,* 4, 129─144. doi: 10.5194/esd-4-129-2013.

Hall, G., D'Souza, R. and Kirk, M., 2002: Foodborne disease in the new millennium: out of the frying pan and into the fire? *Med. J. Aust.*, **177**, 614–618.

Haylock, M. R., Cawley, G. C., Harpham, C., Wilby, R. L. and Goodess, C. M., 2006: Downscaling heavy precipitation over the United Kingdom: a comparison of dynamical and statistical methods and their future scenarios. *International J. Climatol.*, **26**(10), 1397–1415.

Heinrich, G. and Gobiet, A., 2012: The future of dry and wet spells in Europe: A comprehensive study based on the ENSEMBLES regional climate models. *Int. J. Climatol.,* **32**(13), 1951–1970. doi: 10.1002/joc.2421.

Henderson, F.M., 1966: Open Channel Flow. The MacMillan Company, New York, USA.

Henriksen, H. J., Troldborg, L., Nyegaard, P., Sonnenborg, T. O., Refsgaard, J. C. and Madsen, B., 2003: Methodology for construction, calibration and validation of a national hydrological model for Denmark. *J. Hydrol*., **280**(1–4), 52–71.

Hosking, J. R. M., 1990: Analysis and Estimation of Distributions Using Linear Combinations of Order Statistics. *J. R. Stat. Soc. Ser. B (Methodol.)*, **52**(1), 105–124.

Hosking, J. R. M. and Wallis, J. R., 1997: Regional frequency analysis: an approach based on L-moments. Cambridge University Press.

Huntington, T.G., 2006: Evidence for intensification of the global water cycle: review and synthesis. *J. Hydrol*., **319**, 83–95.

IPCC, 2007: Climate Change 2007: The Physical Science Basis. Contribution of Working Group I to the Fourth Assessment Report of the Intergovernmental Panel on Climate Change, In: Solomon, S., Qin, D., Manning, M., Chen, Z., Marquis, M., Averyt, K. B., Tignor, M. and Miller, H. L. (eds), Cambridge University Press, Cambridge, United Kingdom and New York, NY, USA, 996 pp.

IPCC, 2012: Managing the Risks of Extreme Events and Disasters to Advance Climate Change Adaptation. A Special Report of Working Groups I and II of the Intergovernmental Panel on Climate Change. In: Field, C.B., Barros, V., Stocker, T. F., Qin, D., Dokken, D. J., Ebi, K. L., Mastrandrea, M. D., Mach, K. J., Plattner, G. -K., Allen, S. K., Tignor, M. and Midgley, P.M. (eds) Cambridge University Press, Cambridge, UK, and New York, NY, USA, 582 pp.

IPCC, 2013: Climate Change 2013: The Physical Science Basis. Contribution of Working Group I to the Fifth Assessment Report of the Intergovernmental Panel on Climate Change, In: Stocker, T. F., Qin, D., Plattner, G. K., Tignor, M., Allen, S. K., Boschung, J., Nauels, A., Xia, Y., Bex, V. and Midgley, P. M. (eds), Cambridge University Press, Cambridge, United Kingdom and New York, NY, USA, 1535 pp.

Jones, P. D. and Salmon, M., 1995: Development and integration of a stochastic weather generator into a crop growth model for European agriculture. MARS project, final report to Institute of Remote Sensing Applications, Agricultural Information Systems (ISPRA), UK.

Jones, P. D., Kilsby, C. G., Harpham, C., Glenis, V. and Burton, A., 2009: UK Climate Projections science report: projections of future daily climate for the UK from the Weather Generator. University Of Newcastle, UK, p48. ISBN 978-1-906360-06-1.

Julien, P. Y. and Simons, D. B., 1985: Sediment transport capacity of overland flow, *Trans. Am. Soc. Agric. Engrs*., **28**(3), 755–762.

Katz, R. W., Parlange, M. B. and Naveau, P., 2002: Statistics of extremes in hydrology. *Adv. Water Resour.*, 25, 1287–1304.

Kharin, V., V. and Zwiers, F., W., 2004: Estimating extremes in transient climate change simulations. *J. Clim.*, **18**, 1156–1173.

Kilsby, C. G., Jones, P. D., Burton, A., Ford, A. C., Fowler, H. J., Harpham, C., James, P., Smith, A. and Wilby, R. L., 2007: A daily weather generator for use in climate change studies. *Environ. Model. Softw.*, **22**, 1705–1719. doi:10.1016/j.envsoft.2007.02.005.

Kilsby, C. G., Tellier, S. S., Fowler, H. J. and Howels, T. R., 2007: Hydrological impacts of climate change on the Tejo and Guadiana Rivers. *Hydrol. Earth Syst. Sci.*, **11**(3), 1175–1189.

Klemeš, V., 1986: Operational testing of hydrological simulation models. *Hydrol. Sci. J.,* **31**(1), 13–24.

Koutroulis, A. G., Tsanis, I. K., Daliakopoulos, I. N. and Jacob, D., 2013: Impact of climate change on water resources status: A case study for Crete Island, Greece. *J. Hydrol.*, **479**, 146–158.

Kundzewicz, Z. W., Mata, L. J., Arnell, N. W., Döll, P., Kabat, P., Jiménez, B., Miller, K. A., Oki, T., Sen, Z. and Shiklomanov, I. A., 2007: Freshwater resources and their management. Climate Change 2007: Impacts, Adaptation and Vulnerability. Contribution of Working Group II to the Fourth Assessment Report of the Intergovernmental Panel on Climate Change, Parry, M. L., Canziani, O. F., Palutikof, J. P., van der Linden, P. J. and Hanson, C. E., Eds., Cambridge University Press, Cambridge, UK, 173–210.

Leavesley, G. H., 1994: Modeling the effects of climate change on water resources-a review. *Clim. Chang.*, **28**(1-2), 159–177.

Li, F., Zhang, Y., Xu, Z., Teng, J. and Liu, C. *et al.*, 2013: The impact of climate change on runoff in the southeastern Tibetan Plateau. *J. Hydrol.*, **505**, 188–201.

Lin, S., 2011: NGPM–A NSGA-II Program in Matlab v1.4, in: File Exchange at MATLAB CENTRAL, http://www.mathworks.com/matlabcentral/fileexchange/31166, last access: 14 August 2012.

Lukey, B. T., Bathurst, J. C. Hiley, R. A. and Ewen, J., 1995: SHETRAN sediment transport component: equations and algorithms. WRSRU/TR/9510/60.0, University of Newcastle upon Tyne, UK.

Lukey, B. T., Sheffield, J., Bathurst, J. C., Hiley, R. A. and Mathys, N., 2000: Test of the SHETRAN technology for modelling the impact of reforestation on badlands runoff and sediment yield at Draix. *J. Hydrol.*, **235**, 44–62.

Lutz, S. R., van Meerveld, H. J., Waterloo, M. J., Broers, H. P. and van Breukelen, B. M., 2013: A model-based assessment of the potential use of compound specific stable isotope analysis in river monitoring of diffuse pesticide pollution. *Hydrol. Earth Syst. Sci.*, **17**, 4505–4524. doi: 10.5194/hess-17-4505-2013.

Madsen, H. 2000: Automatic calibration of a conceptual rainfall-runoff model using multiple objectives. *J. Hydrol.*, **235**, 276–288.

Madsen, H., 2003: Parameter estimation in distributed hydrological catchment modelling using automatic calibration with multiple objectives. *Adv. Water Resour.*, **26**, 205-216.

Majone. B, Bovolo, C. I., Bellin, A., Blenkinsop, S. and Fowler, H. J., 2012: Modeling the impacts of future climate change on water resources for the Gállego river basin (Spain). *Water Resour. Res.*, **48**, W01512, doi:10.1029/2011WR010985.

Maraun, D., Wetterhall, F., Ireson, A. M., Chandler, R. E. and Kendon, E. J. *et al*., 2010: Precipitation downscaling under climate change: Recent developments to bridge the gap between dynamical models and the end user. *Rev. Geophys.*, **48**(3), RG3003.

Matos, R. M. A., Corte-Real, J. A. M. and Zhang, X., 1994: 'Relationship between climate variation and fresh water snails in Alentejo', Proceeding of the 4th National Conference on Environmental Quality, Vol. III, Lisbon, April 1994, 227–232 (in Portuguese).

Moriasi, D. N., Arnold, J. G., Van Liew, M. W., Bingner, R. L., Harmel, R. D. and Veith, T. L., 2007: Model evaluation guidelines for systematic quantification of accuracy in watershed simulations. *Trans. ASABE*, **50**(3), 885–900.

Monteith, J. L., 1965: Evaporation and environment. In: The State and Movement of Water in Livin Organisms, Proc. 15th Symposium Society for Experimental Biology, Swansea. Cambridge University Press, London, 205-234.

Mourato, S., 2010: Modelação do impacte das alterações climáticas e do uso do solo nas bacias hidrográficas do Alentejo. PhD thesis, University of Évora, Portugal.

Mourato, S., Moreira, M. and Corte-real, J., 2010: Interannual variability of precipitation distribution patterns in Southern Portugal. *Int. J. Climatol.,* **30**, 1784–1794.

Morgan, R. P. C., 2005: Soil erosion and conservation. Blackwell Science Ltd, UK, 304 pp.

Moss, R. H., Edmonds, J. A., Hibbard, K. A., Manning, M. R., Rose, S. K. and Van Vuuren, D. P. *et al*., 2010: The next generation of scenarios for climate change research and assessment. *Nat.*, **463**(7282), 747–756.

Nakicenovic, N. and Swart, R. (eds), 2000: Special report on emissions scenarios. *A special report of working group III of the intergovernmental panel on climate change*. Cambridge University Press: Cambridge, UK, 570pp.

Nash, J. E. and Sutcliffe, J. V., 1970: River flow forecasting through conceptual models part I - a discussion of principles. *J. Hydrol.*, **10**, 282–290.

Nasr, A., Bruen, M., Jordan, P., Moles, R., Kiely, G. and Byrne, P., 2007: A comparison of SWAT, HSPF and SHETRAN/GOPC for modelling phosphorus export from three catchments in Ireland. *Water res.*, **41**(5), 1065–1073.

Nelder, J. A. and Mead, R. 1965: A simplex method for function minimization. *Comput. J.*, **7**, 308–313.

Newcastle University: SHETRAN water flow component, equations and algorithms. Available at: http://research.ncl.ac.uk/shetran/water%20flow%20equations.pdf.

Nunes, J., 2007: Vulnerability of Mediterranean watersheds to climate change: the desertification context. PhD thesis, New University of Lisbon, Portugal.

Ortega, J. A. and Garzón, G., 2004: Influencia de la oscilación del Atlántico norte en las inundaciones del Río Guadiana. In Benito, G. and Herrero, A. D. (eds), *Riesgos naturales y antrópicos en Geomorfología*. (Madrid: CSIC), 117–126.

Osman, A. M. and Thorne, C. R., 1988: Riverbank stability analysis, I: theory, *J. Hydraul. Engrg., Am. Soc. Civ. Engrs.*, **114**(2), 134–150.

Ouyang, F., Lu, H., Zhu, Y., Zhang, J., Yu, Z., Chen, X. and Li, M., 2013: Uncertainty analysis of downscaling methods in assessing the influence of climate change on hydrology. *Stoch Environ Res Risk Assess*, doi:10.1007/s00477-013-0796-9.

Pallard, B., Castellarin, A. and Montanari, A., 2009: A look at the links between drainage density and flood statistics. *Hydrol. Earth Syst. Sci*., **13**(7), 1019–1029.

Palma, P., Ledo, L., Soares, S., Barbosa, I. R. and Alvarenga, P., 2014: Spatial and temporal variability of the water and sediments quality in the Alqueva reservoir (Guadiana Basin; southern Portugal). *Sci. Total Environ.*, **470**, 780–790.

Park, S. W., Mitchell, J. K. and Scarborough, J. N., 1982: Soil erosion simulation on small watersheds: a modified ANSWERS model. *Trans. Am. Solc. Agric. Engrs.*, **25**, 1581–1588.

Parkin, G., 1996: A three-dimensional variably-saturated subsurface modelling system for river basins. PhD thesis, University of Newcastle upon Tyne, UK.

Parkin, G., O'Donnell, G., Ewen, J., Bathurst, J. C., O'Connell, P. E. and Lavabre, J., 1996: Validation of catchment models for predicting land-use and climate change impacts. 2. Case study for a Mediterranean catchment. *J. Hydrol.*, **175**: 595–613.

Pereira, L. S., Louro, V., do Rosário, L. and Almeida, A., 2006: Desertification, territory and people, a holistic approach in the Portuguese context. In Kepner, W., Rubio, J. L., Mouat D. A. and Pedrazzini, F. (eds) *Desertification in the Mediterranean: a security issue*. Springer: Dordrecht; 269–289.

Pires, R. O., Reis, J. L., Santos, F. L. and Castanheira, N. L., 2007: Polyacrylamide application in center pivot irrigation systems for erosion and runoff control. *Rev. de Ciências Agrárias*, **30**(1), 172–178.

Poulin, A., Brissette, F., Leconte, R., Arsenault, R. and Malo, J., 2011: Uncertainty of hydrological modelling in climate change impact studies in a Canadian, snow-dominated river basin. *J. Hydrol.*, **409**, 626–636. doi:10.1016/j.jhydrol.2011.08.057.

Prudhomme, C., Reynard, N. and Crooks, S., 2002: Downscaling of global climate models for flood frequency analysis: Where are we now? *Hydrol. Process.*, **16**, 1137–1150.

Qian, B., Corte-Real, J. and Xu, H., 2000: Is the North Atlantic Oscillation the most important atmospheric pattern for precipitation in Europe? *J. Geophys. Res.: Atmos.* (1984–2012), **105**(D9), 11901–11910.

Rajczak, J., Pall, P. and Schär, C., 2013: Projections of extreme precipitation events in regional climate simulations for Europe and the Alpine Region, *J. Geophys. Res.: Atmos.*, **118**, 3610–3626. doi:10.1002/jgrd.50297.

Ramos, C. and Reis, E., 2002: Floods in southern Portugal: their physical and human causes, impacts and human response. *Mitig. Adapt. Strateg. Glob. Chang.,* **7**, 267–284.

Ramos, A. F. and Santos, F. L., 2009: Water use, transpiration, and crop coefficients for olives (cv. Cordovil), grown in orchards in southern Portugal. *Biosyst. Eng.*, **102**, 321–333.

Rasmussen, P. P., Gray, J. R., Glysson, G. D. and Ziegler, A. C., 2009: Guidelines and procedures for computing time-series suspended-sediment concentrations and loads from in-stream turbidity-sensor and streamflow data. *US Geological Survey Techniques and Methods*, book 3, chapter4, 51pp.

Reed, P. M., Hadka, D., Herman, J. D., Kasprzyk, J. R. and Kollat, J. B., 2013: Evolutionary multiobjective optimization in water resources: The past, present, and future, *Adv. Water Resour.*, 51, 438–456. doi:10.1016/j.advwatres.2012.01.005.

Refsgaard, J. C., 1997: Parameterisation, calibration and validation of distributed hydrological models. *J. Hydrol.*, **198**: 69–97.

Refsgaard, J. C., Storm, B. and Clausen, T., 2010: Système Hydrologique Europeén (SHE): review and perspectives after 30 years development in distributed physically-based hydrological modelling. *Hydrol. Res.,* 41(5), 355–377. doi: 10.2166/nh.2010.009.

Refsgaard, J. C., Madsen, H., Andréassian, V., Arnbjerg-Nielsen, K. and Davidson, T. A. *et al*., 2014: A framework for testing the ability of models to project climate change and its impacts. *Clim. Chang.,* **122**(1-2), 271–282.

Robarts, R., Kumagai, M. and Magadza, C.H., 2005: Climate change impacts on lakes: technical report of the session 'Ecosystem Approach to Water Monitoring and Management' organized at the World Water Forum II in Kyoto. Climatic Change Ecosystem Approach to Water Monitoring and Management, UNEP Publication, Nairobi.

Rodgers, J. L. and Nicewander, W. A., 1988: Thirteen ways to look at the correlation coefficient. *Am. Stat.*, **42**, 59–66.

Rodrigo, F. S. and Trigo, R. M., 2007: Trends in daily rainfall in the Iberian Peninsula from 1951 to 2002. *Int. J. Climatol.*, **27**(4), 513–529.

Rojas, R., Feyen, L., Bianchi, A. and Dosio, A., 2012: Assessment of future flood hazard in Europe using a large ensemble of bias-corrected regional climate simulations. *J. Geophys. Res.*, **117**, D17109. doi: 10.1029/2012JD017461.

Rojas, R., Feyen, L. and Watkiss, P., 2013: Climate change and river floods in the European Union: Socio-economic consequences and the costs and benefits of adaptation. *Glob. Environ. Chang.,* **23**, 1737–1751. doi: 10.1016/j.gloenvcha.2013.08.006.

Rubio, J. L. and Recatalà, L., 2006: The relevance and consequences of Mediterranean desertification including security aspects. In Kepner, W., Rubio, J. L., Mouat D. A. and Pedrazzini, F. (eds) *Desertification in the Mediterranean: a security issue*. Springer: Dordrecht; 113–165.

Rutter, A. J., Kershaw, K. A., Robins, P. C. and Morton, A. J., 1971–72: A predictive model of rainfall interception in forests, 1. Derivation of the model from observations in a plantation of Corsican pine. *Agric. Meteorol.*, **9**, 367–384.

Rutter, A. J., Morton, A. J. and Robins, P. C., 1975: A predictive model of rainfall interception in forests, 2. Generalisation of the model and comparison with observations in some coniferous and hardwood stands. *J. Appl. Ecol.*, **12**, 367–380.

Salgueiro, A. R., Machado, M. J., Barriendos, M., Pereira, H. G. and Benito, G., 2013: Flood magnitudes in the Tagus River (Iberian Peninsula) and its stochastic relationship with daily North Atlantic Oscillation since mid-19th Century. *J. Hydrol.,* **502**, 191–201.

Santo, F. E., Ramos, A. M., de Lima, M. I. P. and Trigo, R. M., 2013: Seasonal changes in daily precipitation extremes in mainland Portugal from 1941 to 2007. *Reg. Environ. Chang.*, 1–24.

Santos, C. A. G., Srinivasan, V. S., Suzuki, K. and Watanabe, M., 2003: Application of an optimization technique to a physically based erosion model. *Hydrol. Process.*, **17**(5): 989–1003.

Santos, C. A. G., Freire, P. K. M. M., Silva, R. M., Arruda, P. M. and Mishra, S. K., 2011: Influence of the catchment discretization on the optimization of runoff-erosion modelling. *J. Urban Environ. Eng.*, **5**(2), 91–102.

Santos, C. A. G., Freire, P. K. M. M. and Arruda, P. M. 2012: Application of a simulated annealing optimization to a physically based erosion model. *Water Sci. Technol.*, **66**(10), 2099–2108.

Santos, J., Corte-Real, J. and Leite, S., 2007: Atmospheric large-scale dynamics during the 2004/2005 winter drought in Portugal. *Int. J. Climatol.,* **27**, 571–586. doi: 10.1002/joc.1425.

Santos, J. F., Pulido-Calvo, I. and Portela, M. M., 2010: Spatial and temporal variability of droughts in Portugal. *Water Resour. Res.*, **46**(3), W03503, doi:10.1029/2009WR008071.

Saxton, K. E. and Rawls, W. J., 2006: Soil water characteristic estimates by texture and organic matter for hydrologic solutions. *Soil Sci. Soc. Am. J.*, **70**, 1569–1578.

Schneider, C., Laizé, C. L. R., Acreman, M. C. and Florke, M., 2013: How will climate change modify river flow regimes in Europe? *Hydrol. Earth Syst. Sci.,* **17**(1), 325–339.

Schoof, J. T., 2013: Statistical downscaling in climatology. *Geogr. Compass*, **7**(4), 249–265.

Schwefel, H. P., 1995: Evolution and Optimum Seeking, Wiley, NewYork, USA.

Searcy, J. K. and Hardison, C. H., 1960: Double-mass curves. In: Manual of Hydrology: Part I, General Surface Water Techniques, U.S. Geol. Surv., Water-Supply Pap., 1541-B: Washington, D.C., 31–59.

Seneviratne, S. I., and Nicholls, N., et al., 2012: Changes in climate extremes and their impacts on the natural physical environment, in Managing the Risks of Extreme Events and Disasters to Advance Climate Change Adaptation: A Special Report of Working Groups I and II of the Intergovernmental Panel on Climate Change (IPCC), pp. 109–230, Cambridge Univ. Press, Cambridge, U. K.

Seshadri, A., 2009: Multi-Objective Optimizaion using Evolutionary Algorithm, in: File Exchange at MATLAB CENTRAL, http://www.mathworks.com/matlabcentral/fileexchange/10351, last access: 14 August 2013.

Shafii, M. and Smedt, F. D., 2009: Multi-objective calibration of a distributed hydrological model (WetSpa) using a genetic algorithm. *Hydrol. Earth Syst. Sci.*, **13**, 2137-2149, 10.5194/hess-13-2137-2009.

Silva, L. L., 2006: The effect of spray head sprinklers with different deflector plates on irrigation uniformity, runoff and sediment yield in a Mediterranean soil. *Agr. Water Manage.*, **85**(3), 243–252.

Silva, R. M., Montenegro, S. M. G. L. and Santos, C. A. G. 2012: Integration of GIS and remote sensing for estimation of soil loss and prioritization of critical sub-catchments: a case study of Tapacurá catchment. *Nat. Hazards*, **62**(3), 953–970.

Srikanthan, R. and McMahon, T. A., 1980: Stochastic generation of monthly flows for ephemeral streams. *J. Hydrol.,* **47**(1), 19–40.

Solomon, S., Plattner, G. K., Knutti, R. and Friedlingstein, P., 2009: Irreversible climate change due to carbon dioxide emissions. *Proc. Natl. Acad. Sci.*, **106**(6), 1704–1709.

Stedinger, J. R., Vogel, R. M. and Foufoula-Georgiou, E., 1993: Frequency analysis of extreme events, in *Handbook of Hydrology*, edited by Maidment, D. A., pp 18.1–18.66, McGraw-Hill, New York.

Sun, H., Cornish, P. S. and Daniell, T. M., 2001: Turbidity-based erosion estimation in a catchment in South Australia. *J. Hydrol.,* **253**(1), 227–238.

Tang, Y., Reed, P. and Wagener, T., 2006: How effective and efficient are multiobjective evolutionary algorithms at hydrologic model calibration? *Hydrol. Earth Syst. Sci.*, **10**, 289–307.

Therrien, R., McLaren, R., Sudicky, E. A. and Panday, S., 2006: HydroGeo-Sphere, a Three-Dimensional Numerical Model Describing Fully- Integrated Subsurface and Surface Flow and Solute Transport. Groundwater Simulation Group, Waterloo, Ont., Canada.

Trenberth, K. E., Dai, A. G., Rasmussen, R. M. and Parsons, D.B., 2003: The changing character of precipitation. *Bull. Am. Meteorol. Soc*., **84**, 1205–1217.

Thornes, J. B., 1998: Mediterranean Desertification. In: Mairota, P., Thornes, J. B. and Geeson, N. (eds) *Atlas of Mediterranean Environments in Europe*. John Wiley & Sons Ltd, Chichester, UK, pp2–4.

UNCCD, 2004: Preserving our common ground. UNCCD 10 years on. United Nations Convention to Combat Desertification. Bonn, Germany.

van der Linden, P. and Mitchell, J. F. B. (eds.) 2009: ENSEMBLES: Climate Change and its Impacts: Summary of research and results from the ENSEMBLES project. Met Office Hadley Centre, FitzRoy Road, Exeter EX1 3PB, UK. 160pp.

van Genuchten, M. Th., Leij, F. J. and Yates, S. R., 1991: The RETC code for quantifying the hydraulic functions of unsaturated soils, Report No: EPA/600/2-91/065. Robert S. Kerr Environmental Research Laboratory, U.S. Environmental Protection Agency, Ada, Oklahoma.

van Vliet, M. T. H., Blenkinsop, S., Burton, A., Harpham, C., Broers, H. P. and Fowler, H. J., 2012: A multi-model ensemble of downscaled spatial climate change scenarios for the Dommel catchment , Western Europe. *Clim. Chang.*, **111**, 249–277.

Vanmaercke, M., Poesen, J., Maetens, W., de Vente, J. and Verstraeten, G., 2011: Sediment yield as a desertification risk indicator. *Sci. Total Environ*., **409**(9), 1715–1725.

Vaquero, J. M., 2004: Solar signal in the number of floods recorded for the Tagus river basin over the last millennium. *Clim. Chang.*, **66**, 23–26.

Varino, F. C. M., 2011: Reassessing the impacts and atmospheric circulation of large storms over Portugal. MSc thesis, University of Lisbon, Portugal.

Vázquez, R. F., Feyen, L., Feyen, J. and Refsgaard, J. C., 2002: Effect of grid size on effective parameters and model performance of the MIKE-SHE code. *Hydrol. Process.,* **16**(2), 355–372.

Vicente-Serrano, S. M., Lopez-Moreno, J. I., Beguería, S., Lorenzo-Lacruz, J. and Sanchez-Lorenzo, A. *et al*., 2014: Evidence of increasing drought severity caused by temperature rise in southern Europe. *Environ. Res. Lett.,* **9**(4), 044001(9pp).

Walling, D. E., 1983: The sediment delivery problem. *J. Hydrol.*, **65**, 209–237.

Wang, D., Hagen, S. C. and Alizad, K., 2013: Climate change impact and uncertainty analysis of extreme rainfall events in the Apalachicola River basin, Florida. *J. Hydrol.*, **480**, 125–135.

Watts, M., Goodess, C. M. and Jones, P., D., 2004: The CRU daily weather generator. BETWIXT Technical Briefing Note 1, Version 2, February 2004.

Wicks, J. M., 1988: Physically-based mathematical modelling of catchment sediment yield. PhD thesis, Univ. of Newcastle upon Tyne, Newcastle upon Tyne, England.

Wicks, J. M., Bathurst, J. C. and Johnson, C. W., 1992: Calibrating SHE soil-erosion model for different land covers. Proc. Am. Soc. Civ. Eng., *J. Irrig. Drain. Eng.*, **118**(5), 708–723.

Wicks, J. M. and Bathurst, J. C., 1996: SHESED: a physically-based, distributed erosion and sediment yield component for the SHE hydrological modelling system. *J. Hydrol.*, 175(1–4), 213–238.

Wilby, R. L. and Wigley, T. M. L., 1997: Downscaling general circulation model output: a review of methods and limitations. *Prog. Phys. Geogr.*, **21**, 530–548.

Wildemeersch, S., Goderniaux, P., Orban, P., Brouyère, S. and Dassargues, A., 2014: Assessing the effects of spatial discretization on large-scale flow model performance and prediction uncertainty. *J. Hydrol.,* **510**, 10–25.

Wilks, D. S. and Wilby, R. L., 1999: The weather generation game: a review of stochastic weather models. *Prog. Phys. Geogr.*, **23**, 329–357.

Wilks, D. S., 2006: Statistical Methods in the Atmospheric Sciences. Academic Press, San Diego, 648 pp.

Willmott, C. J., 1981: On the validation of models. *Phys. Geogr.*, **2**, 184–194.

Xu, Y., Zhang, X., Ran, Q. and Tian, Y., 2013: Impact of climate change on hydrology of upper reaches of Qiantang River Basin, East China, *J. Hydrol.*, **483**, 51–60.

Yalin, M. S., 1963: An expression for bed-load transportation. *J. Hydraul. Div., Am. Soc. Civ. Engrs., 89(HY3),* 221–250.

Zhang, X., Srinivasan, R., Zhao, K. and Liew, M. V., 2008: Evaluation of global optimization algorithms for parameter calibration of a computationally intensive hydrologic model. *Hydrol. Process.*, **23**(3), 430-441, doi: 10.1002/hyp.7152.

Zhang, X., Srinivasan, R. and Liew, M. V., 2010: On the use of multi-algorithm, genetically adaptive multi-objective method for multi-site calibration of the SWAT model. *Hydrol. Process.*, **24**(8), 955-969, doi: 10.1002/hyp.7528.

Zhang, R., Santos, C. A. G., Moreira, M., Freire, P. K. M. M. and Corte-Real, J., 2013: Automatic Calibration of the SHETRAN Hydrological Modelling System Using MSCE. *Water Resour. Manage.*, **27**(11), 4053–4068.

Zhang, X., Wang, X. L., and Corte-Real, J., 1997: On the relationships between daily circulation patterns and precipitation in Portugal. *J. Geophys. Res.: Atmos.* (1984–2012), **102**(D12), 13495–13507.

Appendices

Appendix 1: Sensitivity Analysis for the SHETRAN Simulation at Cobres Basin with Spatial Resolution of 2.0 Km and Temporal Resolution of 1.0 Km

The sensitivity analysis was carried out to find parameters most sensitive to the mass balance error (MBE) and the Nash-Sutcliffe Efficiency (NSE). As shown in Tables A.1─A.2, this objective was achieved by the 8 scenarios, which are all based on the baseline simulation with only one or two types of parameters altered. Specifically, in scenario 1, the decreases of the AET/PET ratios for the two main types of land-use distinctly improved the MBE and NSE, which was therefore kept in other scenarios. In scenarios 2─8, only one parameter from the main type of soil or land-use type was changed based on scenario 1, and the changes were setting the parameter to its limit value. Consequently, the sensitivity of the AET/PET ratio is shown by comparison of MBE and NSE from scenario 1 with the baseline simulation; and the sensitivity of other parameters is shown from the comparison of their respective scenario with scenario 1. It is clear that, by setting the parameter to its limit value, the changes of MBE and NSE are largest for van Genuchten α, large for parameters such as AET/PET ratio, Strickler overland flow resistance coefficient, top soil depth, van Genuchten n, saturated water content and residual water content, and very small for saturated hydraulic conductivity. In conclusion, the MBE and NSE of SHETRAN simulations are most sensitive to van Genuchten α, sensitive to AET/PET ratio, Strickler overland flow resistance coefficient, top soil depth, van Genuchten n, saturated water content and residual water content, and not so much sensitive to saturated hydraulic conductivity.

Table A1.1 Description of SHETRAN key hydrological parameters for the simulations of the baseline and scenarios for sensitivity analysis

Parameters (unit)	Description	Baseline	Scenarios for Sensitivity Analysis							
			1	2	3	4	5	6	7	8
K_1 ($m^{1/3}/s$)	Strickler overland flow resistance coefficient for crops	5.0	5.0	5.0	5.0	5.0	5.0	5.0	5.0	**10.0**
K_2 ($m^{1/3}/s$)	Strickler overland flow resistance coefficient for agroforestry	2.0	2.0	2.0	2.0	2.0	2.0	2.0	2.0	2.0
K_{s1} (m/day)	Saturated hydraulic conductivity of V_x soil	0.160	0.160	0.160	0.160	0.160	0.160	0.160	0.160	0.160
θ_{s1} (m^3/m^3)	Saturated water content of V_x soil	0.513	0.513	0.513	0.513	0.513	0.513	0.513	0.513	0.513
θ_{r1} (m^3/m^3)	Residual water content of V_x soil	0.073	0.073	0.073	0.073	0.073	0.073	0.073	0.073	0.073
n_1 (-)	van Genuchten n of V_x soil	1.324	1.324	1.324	1.324	1.324	1.324	1.324	1.324	1.324
α_1 (cm^{-1})	van Genuchten α of V_x soil	0.0140	0.0140	0.0140	0.0140	0.0140	0.0140	0.0140	0.0140	0.0140
h_1 (m)	Top soil depth of V_x soil	0.40	0.40	0.40	0.40	0.40	0.40	0.40	0.40	0.40
K_{s2} (m/day)	Saturated hydraulic conductivity of P_x soil	0.200	0.200	**0.425**	0.200	0.200	0.200	0.200	0.200	0.200
θ_{s2} (m^3/m^3)	Saturated water content of P_x soil	0.418	0.418	0.418	0.418	0.418	**0.519**	0.418	0.418	0.418
θ_{r2} (m^3/m^3)	Residual water content of P_x soil	0.053	0.053	0.053	0.053	0.053	0.053	**0.041**	0.053	0.053
n_2 (-)	van Genuchten n of P_x soil	1.345	1.345	1.345	1.345	**1.422**	1.345	1.345	1.345	1.345
α_2 (cm^{-1})	van Genuchten α of P_x soil	0.0075	0.0075	0.0075	**0.0225**	0.0075	0.0075	0.0075	0.0075	0.0075
h_2 (m)	Top soil depth of P_x soil	0.30	0.30	0.30	0.30	0.30	0.30	0.30	**0.40**	0.30
K_{s3} (m/day)	Saturated hydraulic conductivity of E_x soil	1.227	1.227	0.613	0.613	1.227	1.227	1.227	1.227	1.227
θ_{s3} (m^3/m^3)	Saturated water content of E_x soil	0.446	0.446	0.446	0.446	0.446	0.446	0.446	0.446	0.446
θ_{r3} (m^3/m^3)	Residual water content of E_x soil	0.120	0.120	0.120	0.120	0.120	0.120	0.120	0.120	0.120
n_3 (-)	van Genuchten n of E_x soil	1.311	1.311	1.311	1.311	1.311	1.311	1.311	1.311	1.311
α_3 (cm^{-1})	van Genuchten α of E_x soil	0.0250	0.0250	0.0250	0.0250	0.0250	0.0250	0.0250	0.0250	0.0250
h_3 (m)	Top soil depth of E_x soil	0.10	0.10	0.10	0.10	0.10	0.10	0.10	0.10	0.10
$AETPET_{FC1}$ (-)	The AET/PET ratio at field capacity for crop	0.60	**0.50**	**0.50**	**0.50**	**0.50**	**0.50**	**0.50**	**0.50**	**0.50**
$AETPET_{FC2}$ (-)	The AET/PET ratio at field capacity for agroforestry	0.70	**0.60**	**0.60**	**0.60**	**0.60**	**0.60**	**0.60**	**0.60**	**0.60**

Note: [a]The SHETRAN simulations are configured with spatial resolution of 2.0 km and temporal resolution of 1.0 hour

Table A1.2 Comparison of model performances from the SHETRAN simulations of the baseline and scenarios, with key parameters indicated in the Table A1.1

Indicator (unit)[a]	Baseline	Scenarios for Sensitivity Analysis							
		1	2	3	4	5	6	7	8
MBE (%)[b]	**-35.6**	**-22.0**	**-21.9**	**-38.7**	**-26.2**	**-32.4**	**-23.2**	**-35.8**	**-18.0**
RMSE[c]	4.59	4.10	4.10	5.18	4.47	4.90	4.19	5.07	3.31
LOGE[c]	2.07	1.95	1.93	1.99	1.95	1.97	1.95	1.97	1.98
NSE[c]	**0.66**	**0.73**	**0.73**	**0.57**	**0.68**	**0.62**	**0.72**	**0.59**	**0.83**
PMCC[c]	0.87	0.89	0.89	0.86	0.88	0.87	0.89	0.87	0.93
IOA[c]	0.86	0.90	0.90	0.79	0.86	0.82	0.89	0.80	0.94

Note:
[a]The SHETRAN simulations are evaluated by comparing the observed and simulated hourly discharge at Cobres basin outlet, Monte da Ponte gauging station; and the bold words and figures are the names and values of the indicators that are used for sensitivity analysis.
[b]MBE is mass balance error, which is defined in equation 6.1 of Section 6.2;
[c]RMSE, LOGE, NSE, PMCC and IOA are root mean square error, log transformed error, Nash-Sutcliffe efficiency, coefficient of determination and index of agreement, which are defined in equations 5.1−5.5 of Section 5.4.

Appendix 2: The Proposed Autoregressive Processes in the ICAAM-WG Model

The proposed autoregressive models of temperature are:

Very dry periods (**000**: the day before previous day dry, previous day dry, current day dry):

$$T_i = a_1 \times T_{i-1} + a_2 \times T_{i-2} + b_1 + e_i \quad \text{(A2.1)}$$

$$R_i = a_3 \times R_{i-1} + a_4 \times R_{i-2} + b_2 + e_i \quad \text{(A2.2)}$$

Moderate dry periods (**100**: the day before previous day wet, previous day dry, current day dry):

$$T_i = a_5 \times T_{i-1} + a_6 \times T_{i-2} + a_7 \times P_{i-2} + b_3 + e_i \quad \text{(A2.3)}$$

$$R_i = a_8 \times R_{i-1} + a_9 \times R_{i-2} + a_{10} \times P_{i-2} + b_4 + e_i \quad \text{(A2.4)}$$

Moderate wet periods (**011**: the day before previous day dry, previous day wet, current day wet):

$$T_i = a_{11} \times T_{i-1} + a_{12} \times T_{i-2} + a_{13} \times P_i + a_{14} \times P_{i-1} + b_5 + e_i \quad \text{(A2.5)}$$

$$R_i = a_{15} \times R_{i-1} + a_{16} \times R_{i-2} + a_{17} \times P_i + a_{18} \times P_{i-1} + b_6 + e_i \quad \text{(A2.6)}$$

Very wet periods (**111**: the day before previous day wet, previous day wet, current day wet):

$$T_i = a_{19} \times T_{i-1} + a_{20} \times T_{i-2} + a_{21} \times P_i + a_{22} \times P_{i-1} + a_{23} \times P_{i-2} + b_7 + e_i \quad \text{(A2.7)}$$

$$R_i = a_{24} \times R_{i-1} + a_{25} \times R_{i-2} + a_{26} \times P_i + a_{27} \times P_{i-1} + a_{28} \times P_{i-2} + b_8 + e_i \quad \text{(A2.8)}$$

Dry wet transition (**01**: previous day dry, current day wet):

$$T_i = a_{29} \times T_{i-1} + a_{30} \times P_i + b_9 + e_i \quad \text{(A2.9)}$$

$$R_i = a_{31} \times R_{i-1} + a_{32} \times P_i + b_{10} + e_i \quad \text{(A2.10)}$$

Wet dry transition (**10**: previous day wet, current day dry):

$$T_i = a_{33} \times T_{i-1} + a_{34} \times P_{i-1} + b_{11} + e_i \quad \text{(A2.11)}$$

$$R_i = a_{35} \times R_{i-1} + a_{36} \times P_{i-1} + b_{12} + e_i \quad \text{(A2.12)}$$

The proposed autoregressive models of vapour pressure, wind speed and sunshine duration are:

Vapour pressure:

$$VP_i = c_1 \times T_i + d_1 \times R_i + f_1 \times P_i + g_1 \times VP_{i-1} + h_1 + e_i \quad \text{(A2.14)}$$

Wind speed:

$$WS_i = c_2 \times T_i + d_2 \times R_i + f_2 \times P_i + g_2 \times WS_{i-1} + h_2 + e_i \quad \text{(A2.15)}$$

Sunshine duration:

$$SS_i = c_3 \times T_i + d_3 \times R_i + f_3 \times P_i + g_3 \times SS_{i-1} + h_3 + e_i \quad \text{(A2.13)}$$

Where a_1 to a_{36}, b_1 to b_{12}, c_1 to c_3, d_1 to d_3, f_1 to f_3, g_1 to g_3 and h_1 to h_3 are regression weights; T_i, R_i, P_i, VP_i, WS_i and SS_i are respectively mean temperature, temperature range, precipitation, vapour pressure, wind speed and sunshine duration on day i, and those with suffix $i-1$ and $i-2$ are respectively values for previous day and the day before previous day. e_i is white noise on day i, which is independent of the one on any other day and has a Gaussian distribution with zero mean and variance σ_e^2. The correlations among VP_i, WS_i and SS_i will arise naturally through the common dependences on T_i, R_i and P_i.

Appendix 3: Schematic Summary of the Procedure to Downscale the Climate Change Scenarios.

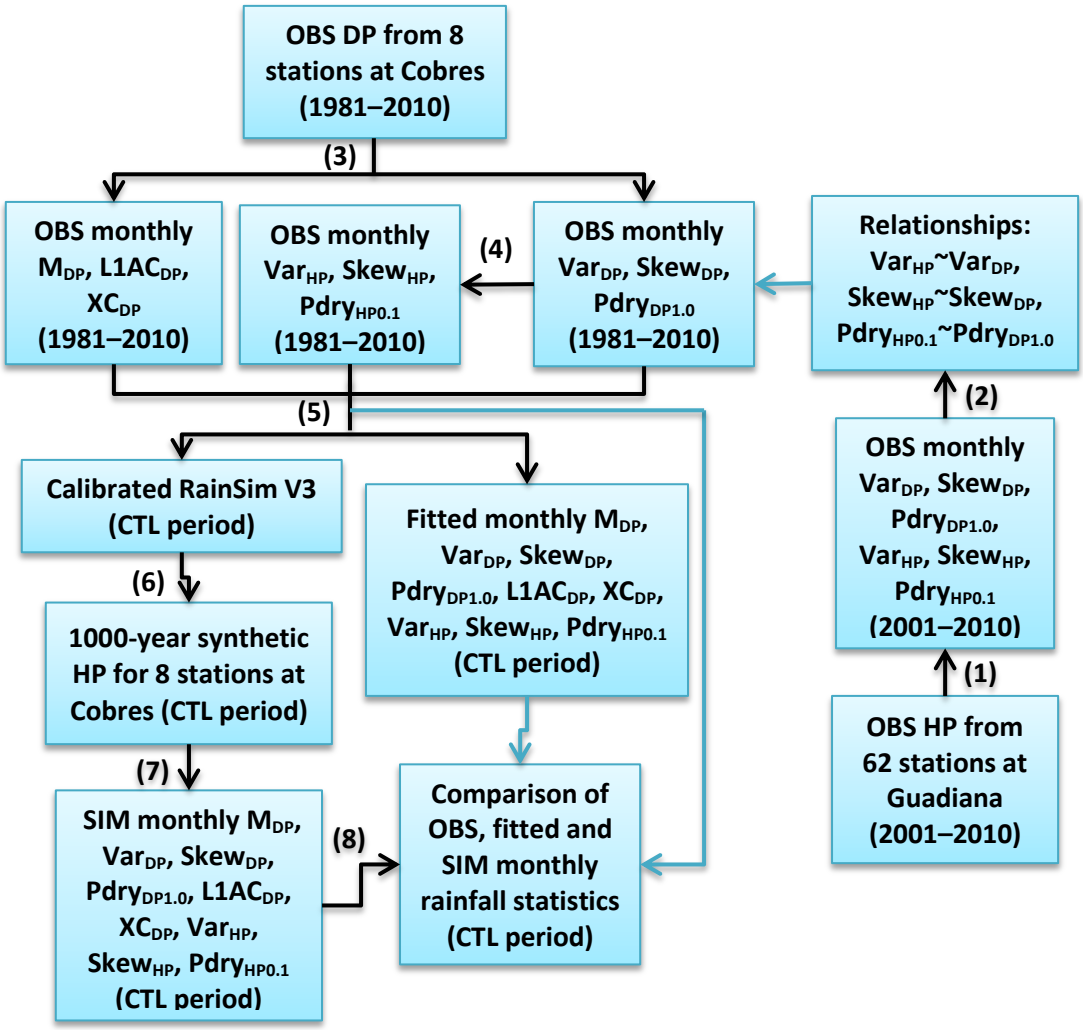

Fig. A3.1 Schematic chart of validation of the RainSim V3 model with numbering corresponding to the steps directed in black arrows.

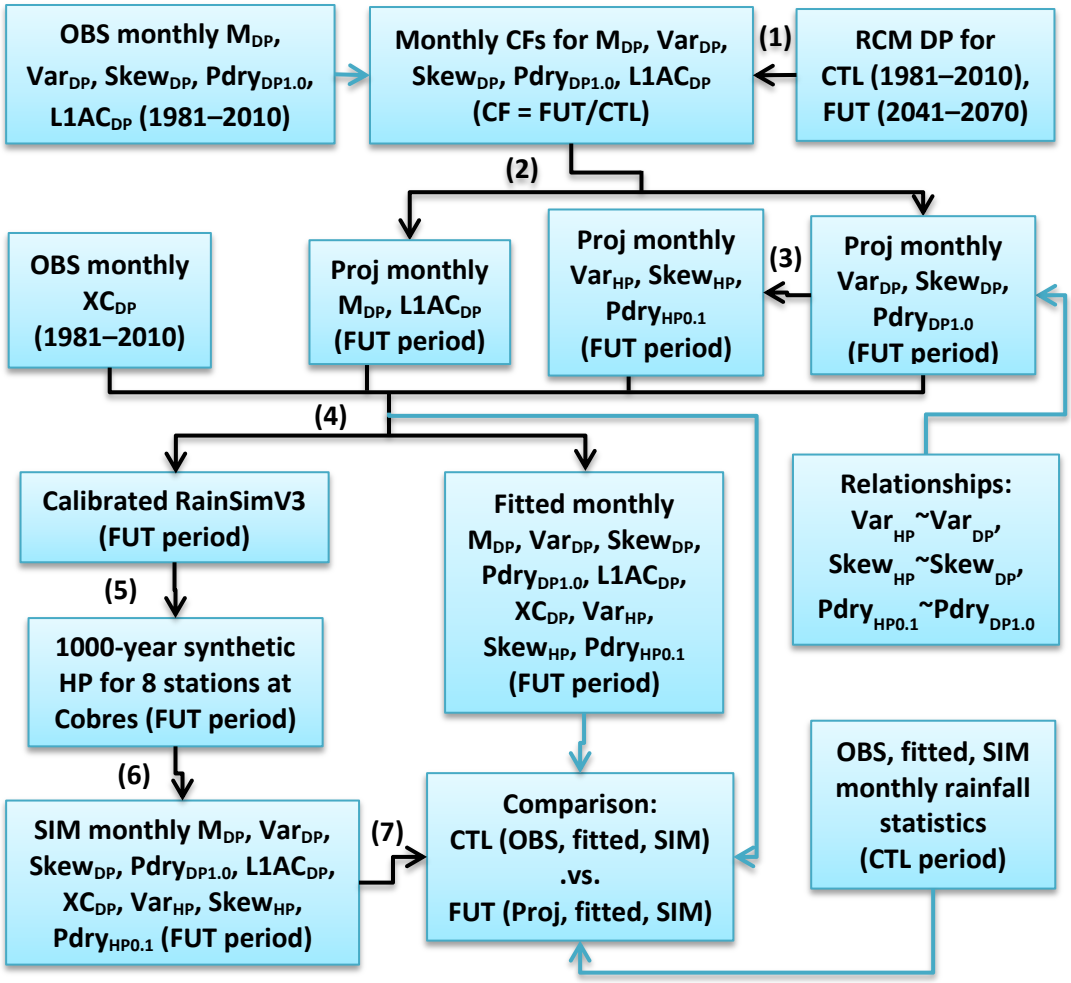

Fig. A3.2 Schematic chart of future rainfall simulation by using the RainSim V3 model with numbering corresponding to the steps directed in black arrows.

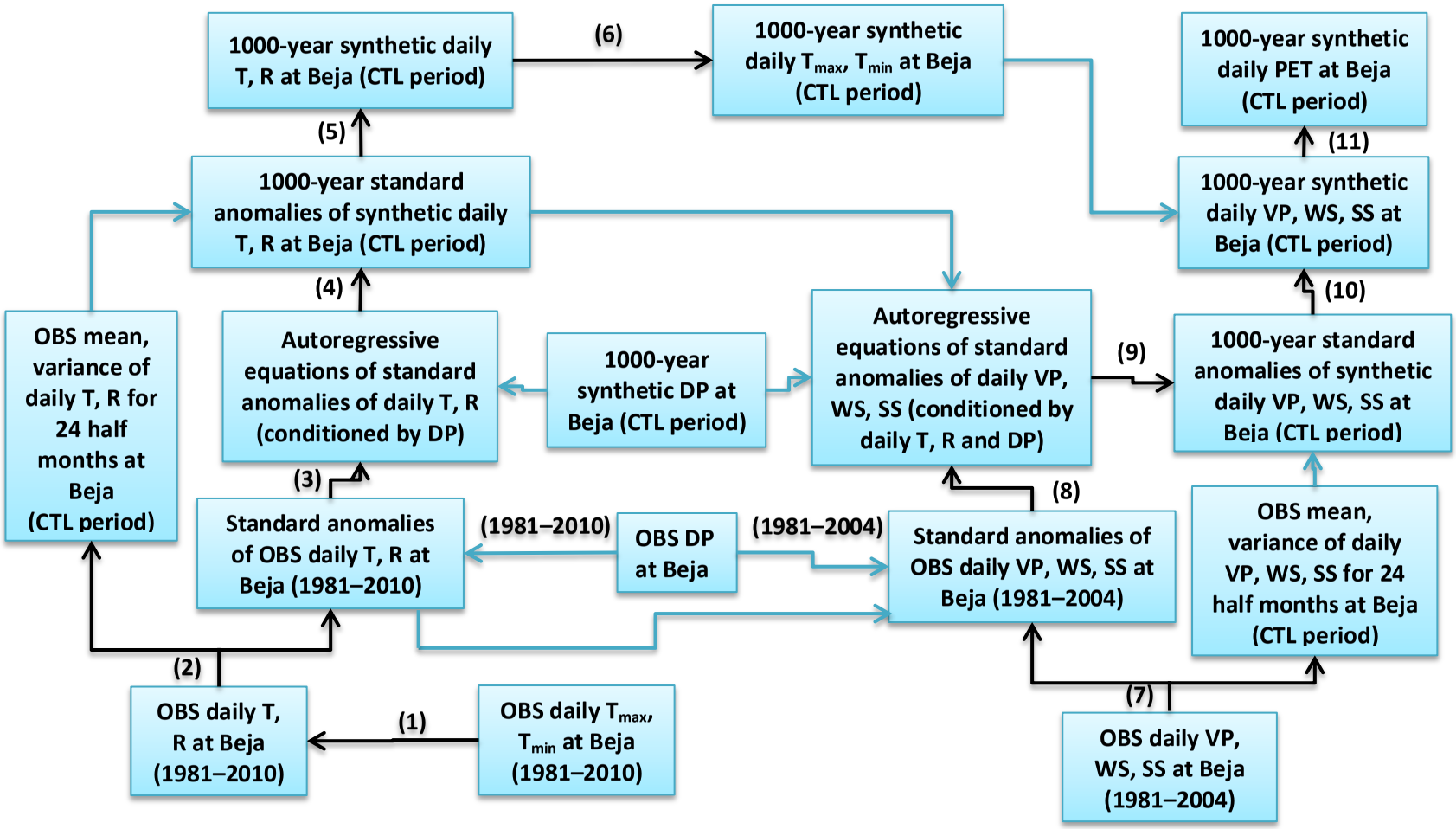

Fig. A3.3 Schematic chart of validation of the ICAAM-WG model with numbering corresponding to the steps directed in black arrows.

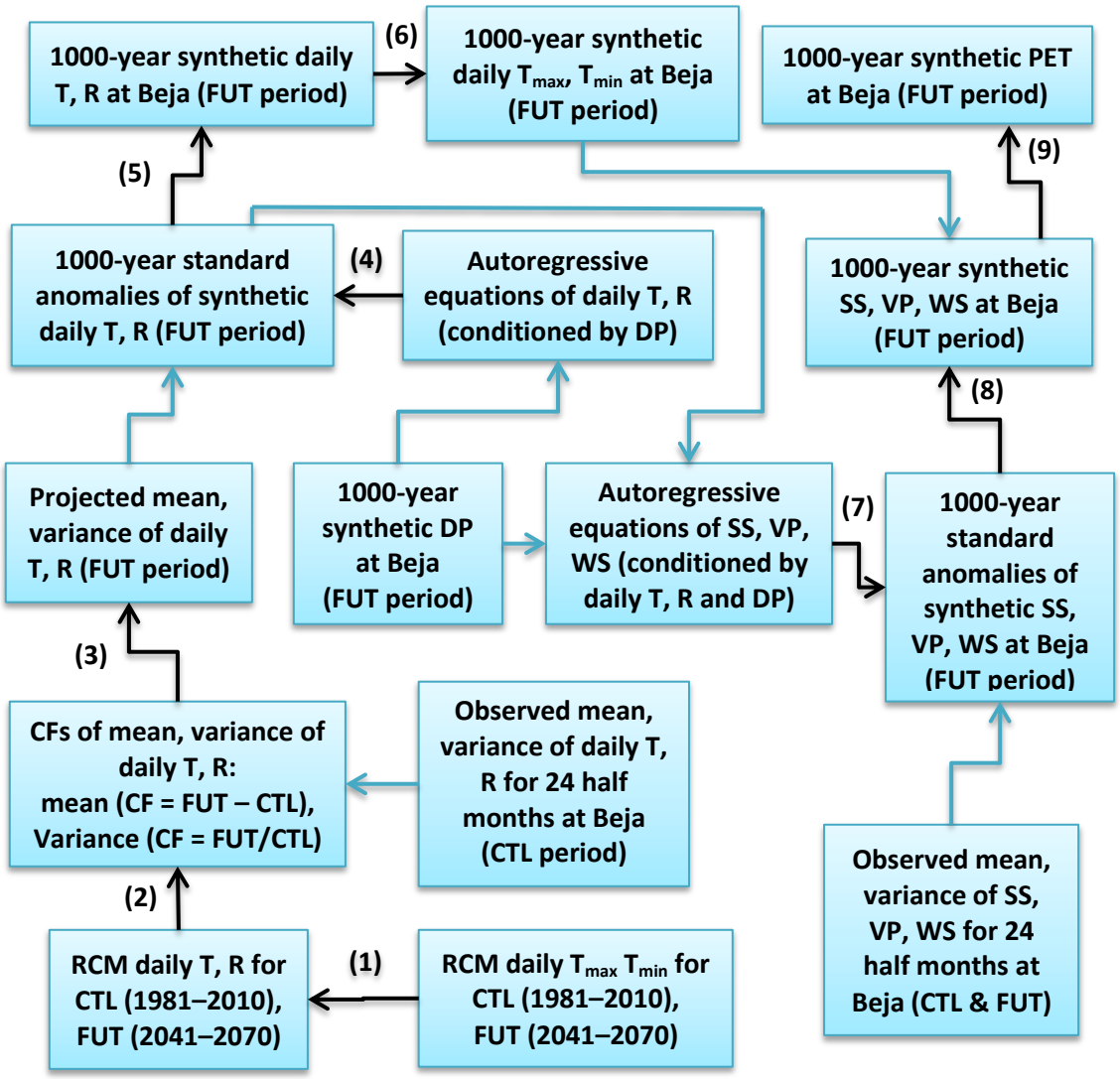

Fig. A3.4 Schematic chart of future PET simulation by using the ICAAM-WG model with numbering corresponding to the steps directed in black arrows.

Appendix 4: Plots for Control and Future Rainfall Simulations

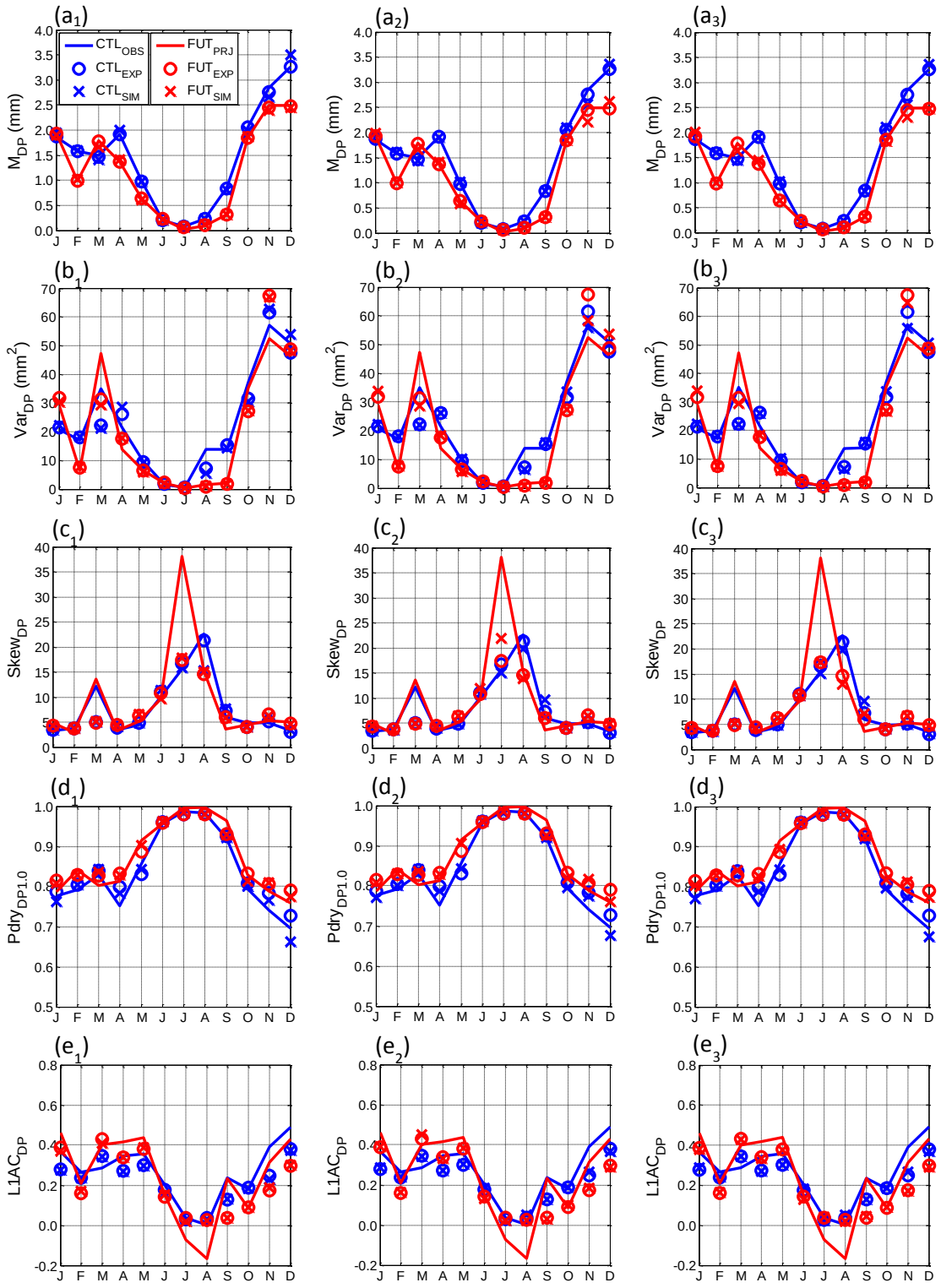

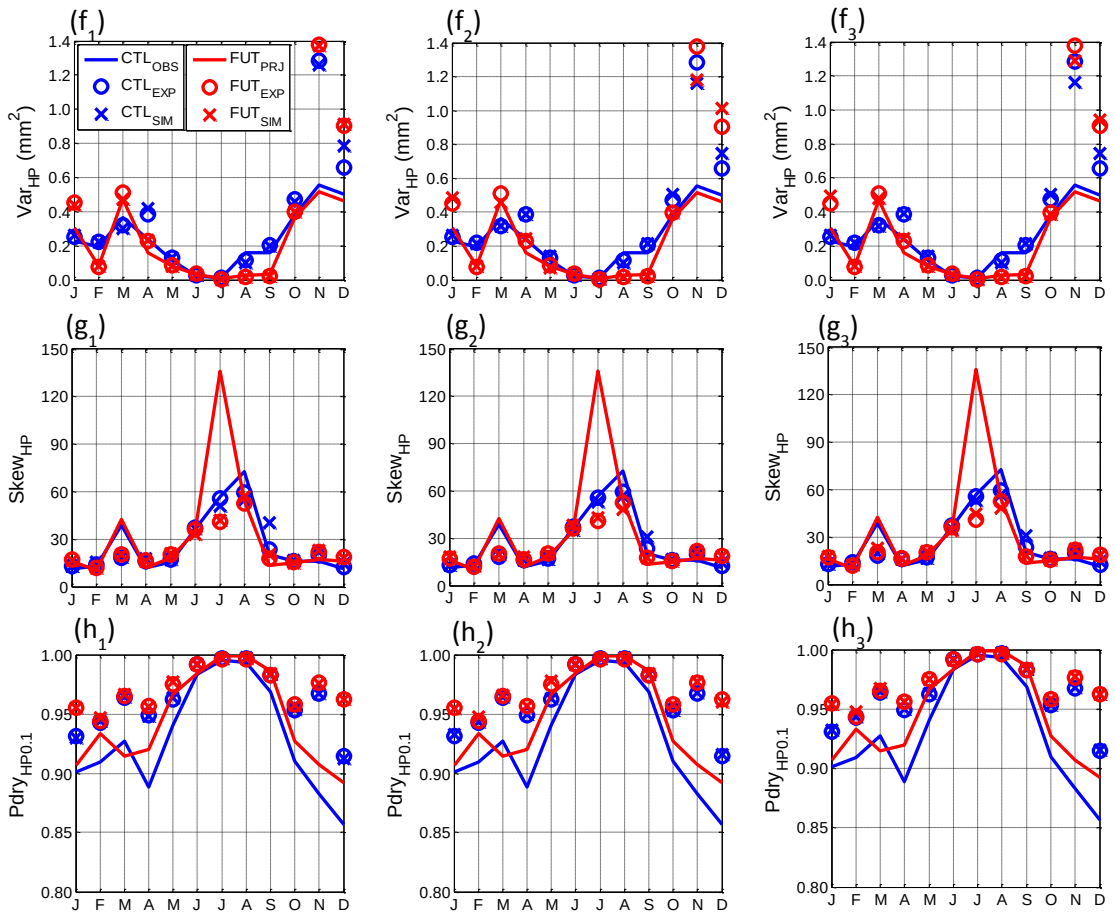

Fig. A4.1 Annual cycles of daily (a_1, a_2 and a_3) mean, (b_1, b_2 and b_3) variance, (c_1, c_2 and c_3) skewness, (d_1, d_2 and d_3) proportion of dry days and (e_1, e_2 and e_3) lag-1 autocorrelation and hourly (f_1, f_2 and f_3) variance, (g_1, g_2 and g_3) skewness and (h_1, h_2 and h_3) proportion dry hours for precipitation at the Almodôvar station from the three 1000-year simulations of the future period (2041–2070) compared to the control period (1981–2010). The observed (OBS) or projected (PRJ), fitted (EXP) and simulated (SIM) statistics are respectively shown in solid lines, circles and crosses and in respective blue and red colors for the control (CTL) and future (FUT) periods.

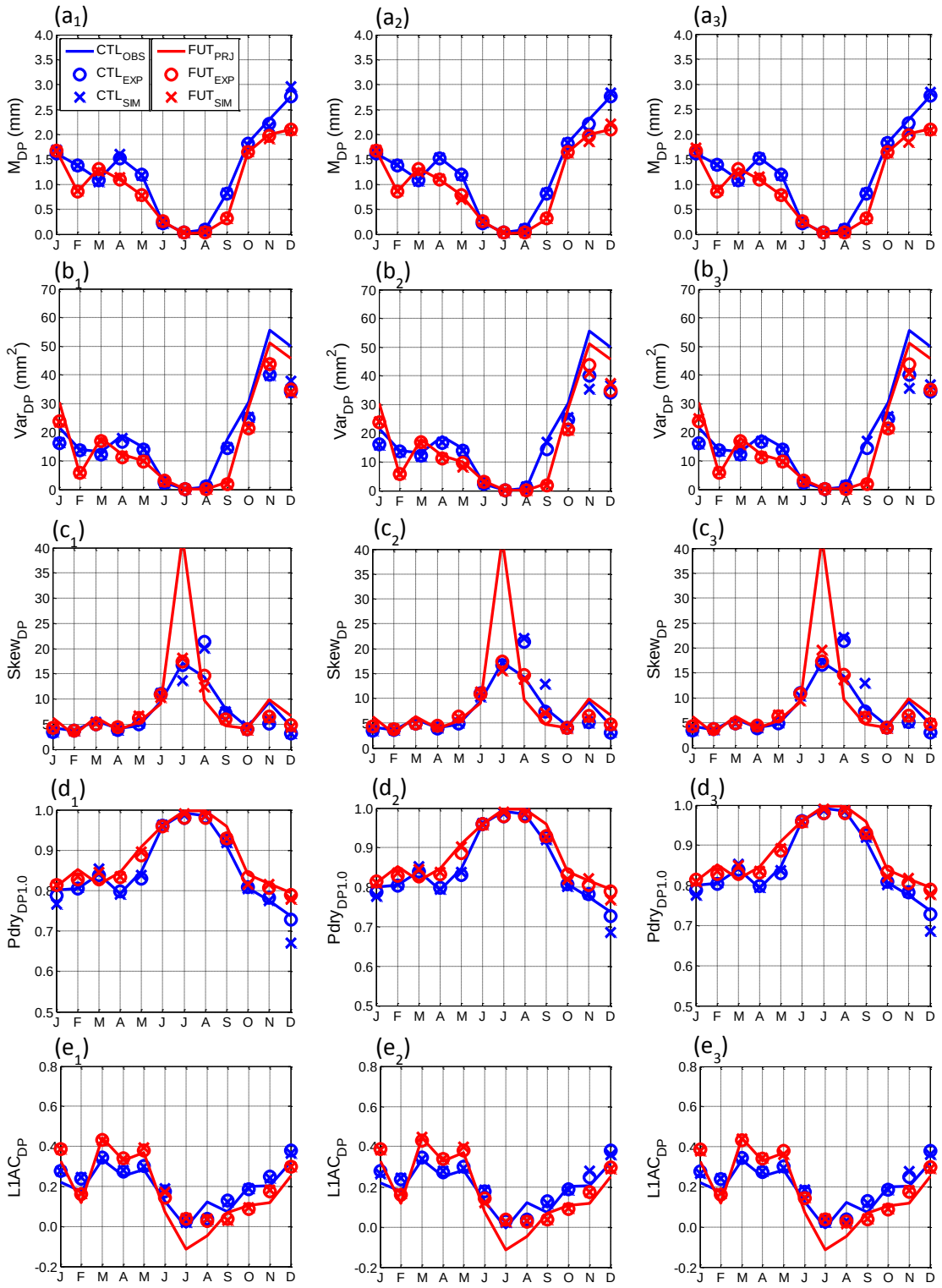
(a1)
(a2)
(a3)
(b1)
(b2)
(b3)
(c1)
(c2)
(c3)
(d1)
(d2)
(d3)
(e1)
(e2)
(e3)
CTLOBS
CTLEXP
CTLSIM
FUTPRJ
FUTEXP
FUTSIM
MDP (mm)
VarDP (mm2)
SkewDP
PdryDP1.0
L1ACDP
J F M A M J J A S O N D

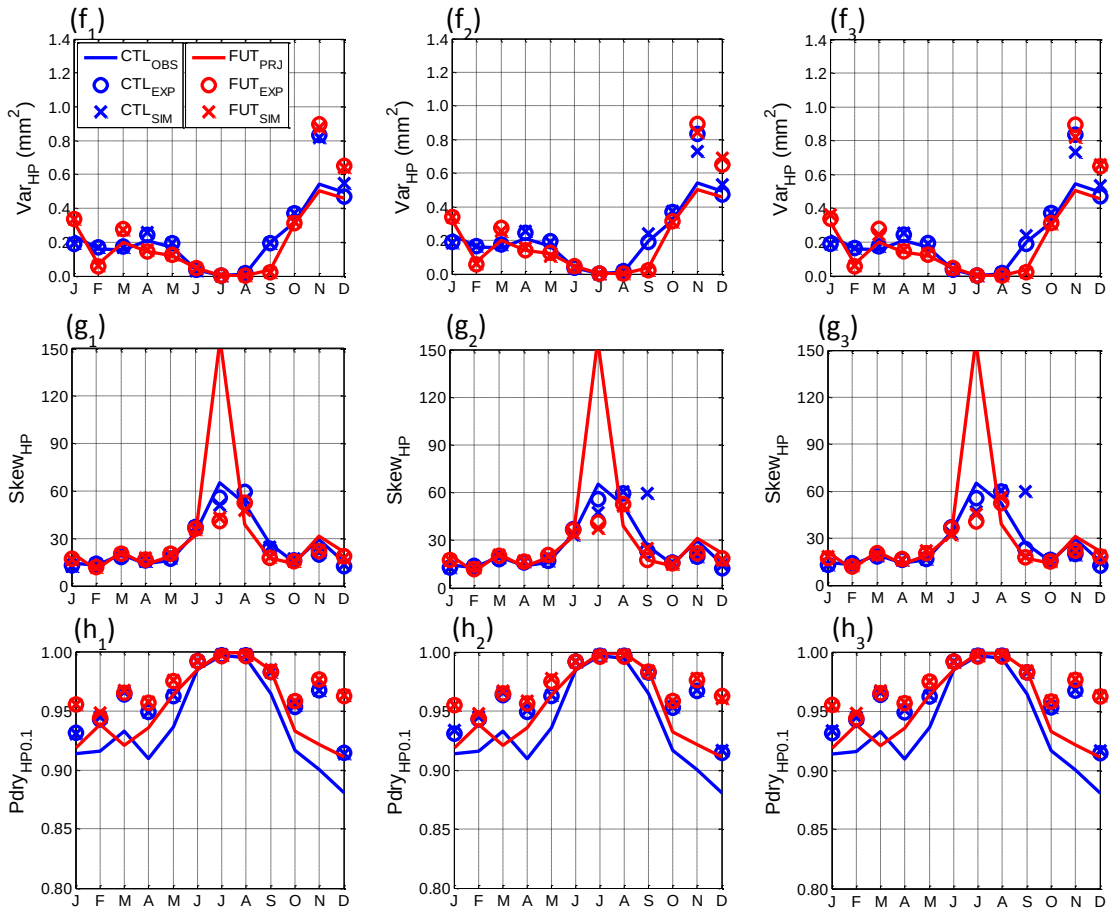

Fig. A4.2 Annual cycles of daily (a_1, a_2 and a_3) mean, (b_1, b_2 and b_3) variance, (c_1, c_2 and c_3) skewness, (d_1, d_2 and d_3) proportion of dry days and (e_1, e_2 and e_3) lag-1 autocorrelation and hourly (f_1, f_2 and f_3) variance, (g_1, g_2 and g_3) skewness and (h_1, h_2 and h_3) proportion dry hours for precipitation at the Trindade station from the three 1000-year simulations of the future period (2041–2070) compared to the control period (1981–2010). The observed (OBS) or projected (PRJ), fitted (EXP) and simulated (SIM) statistics are respectively shown in solid lines, circles and crosses and in respective blue and red colors for the control (CTL) and future (FUT) periods.

Appendix 5: Frequency Distribution of GEV, Gamma and Three-Parameter Lognormal Distributions

A5.1 GEV Distribution:

$$F(x) = \begin{cases} exp\left\{-exp\left(-\frac{x-\xi}{\alpha}\right)\right\}, & k = 0, \\ exp\left\{-\left[1-\frac{k(x-\xi)}{\alpha}\right]^{1/k}\right\}, & k \neq 0, \quad 1-k\frac{x-\xi}{\alpha} > 0 \end{cases} \tag{A5.1}$$

Where F(*x*) is a cumulative probability function of the random variable X has a value less than or equal to a particular value of *x*, *ξ* is the location parameter, *α* is the scale parameter and *k* is the shape parameter. GEV distribution is a general mathematical form which incorporates Gumbel's type I (Gumbel distribution for k = 0), II (Fréchet distribution for k<0) and III (Weibull distribution for k>0) extreme value distributions for maxima (Stedinger *et al.*, 1993). The GEV distribution is heavy tailed and its probability density function decreases at a slow rate when the shape parameter is negative; it has a finite upper tail for k > 0 and it has a "exponential-like" upper tail for k = 0 (Stedinger et al., 1993; Kharin and Zwiers 2004; Wilks 2006).

A5.2 Gamma Distribution:

$$f(x) = \frac{x^{\alpha-1}}{\beta^{\alpha}\Gamma(\alpha)} exp(-x/\beta), \quad x, \alpha, \beta > 0 \tag{A5.2}$$

Where *f*(*x*) is a probability density function for a random variable X, *α* is the shape parameter and *β* is the scale parameter. The probability density function (PDF) of gamma distribution may have a wide variety of shapes depending on the value of the shape parameter *α*. For *α* < 1 the PDF is very strongly skewed to the right; for *α* = 1 it intersects the ordinate at 1/*β* for *x* = 0 (this special case is also called the exponential distribution); for *α* > 1 the PDF begins at the origin, progressively larger values of *α* result in less skewness and for very large values of *α* it approaches the Gaussian distribution in form (Wilks 2006).

A5.3 Three-Parameter Lognormal Distribution:

$$f(y) = \frac{1}{\sqrt{2\pi}} exp\left(-\frac{y^2}{2}\right) \quad -\infty < y < +\infty \tag{A5.3}$$

Where $$y = \frac{(ln(x-\zeta)-\mu)}{\sigma} \tag{A5.4}$$

Where *f*(*x*) is a probability density function for a random variable X, *ζ* is lower bound of the three-parameter lognormal distribution, *μ* is the mean on log scale and *σ* is the standard deviation on log scale.